



Title	Photoswitchable Fluorescent Molecules with High Reversibility Assisted by Protein Surface Modification
Author(s)	鳥井, 健司
Citation	大阪大学, 2024, 博士論文
Version Type	VoR
URL	<a href="https://doi.org/10.18910/96032">https://doi.org/10.18910/96032</a>
rights	
Note	

*The University of Osaka Institutional Knowledge Archive : OUKA*

<https://ir.library.osaka-u.ac.jp/>

The University of Osaka

**Doctoral Dissertation**

**Photoswitchable Fluorescent Molecules  
with High Reversibility Assisted by  
Protein Surface Modification**

**Kenji Torii**

**January 2024**

*Laboratory of Chemical Biology*

*Division of Applied Chemistry*

*Graduate School of Engineering*

*Osaka University*



## **Acknowledgments**

I would like to thank my supervisor, Prof. Kazuya Kikuchi, for his unwavering support and encouragement during my studies in his laboratory. I was lucky to have him as my supervisor as I was blessed with great opportunities to learn the fascinating field of chemical biology.

I would like to thank Prof. Yuichiro Hori for his numerous support and helpful advice throughout my studies. He gives me valuable guidance and discussion whenever I face the challenge. I have learnt academic writing skills from his dedicated teaching.

I would like to thank Dr. Masafumi Minoshima for his helpful suggestions. I have enjoyed discussing with him not only my studies but also other concerns regarding my future career.

I would like to thank Dr. Tomoya Yamamoto for supporting me with his open mind. I was helped by his encouragement.

I would like to thank Ms. Miyako Nishiura for her sincere technical supporting including biological experiments. I was very helped by her compassionate assistance.

I am deeply grateful to Prof. Marc Vendrell and Dr. Sam Benson for giving me the wonderful opportunity to study in their group (Dynafluors™) at the University of Edinburgh for three months. After the visiting study, they continued to give me sincere support in the paper preparation.

I am grateful to the Nikon Imaging Center at Osaka University for acquiring fluorescence imaging data using their confocal laser microscopy.

I would like to thank Prof. Toshiyuki Kida and Prof. Shigeyuki Masaoka for their support in proofreading this dissertation.

I acknowledge financial support from the Japan Society for Promotion of Science (JSPS) and Interactive Materials Science Cadet (IMSC) Program.

I would like to thank Ms. Yuriko Miyata, Ms. Yukiko Nomura, and Ms. Makoto Fujimoto for their supporting regarding my financial management.

I would like to thank all the members of both Kikuchi and Hori laboratories for their helpful advice, support, and irreplaceable bonds of friendship over the years.

Last but not least, I would like to thank my family for their tremendous support and encouragement during my study.

Osaka, Japan

January 2024

**Kenji Torii**

*Laboratory of Chemical Biology*

*Division of Applied Chemistry*

*Graduate School of Engineering, Osaka University*

## List of Publications, Presentations, and Awards

### List of Publications

---

- (1) Torii, K.; Hori, Y.; Watabe, K.; Kikuchi, K. Development of Photoswitchable Fluorescent Molecules Using Arylazopyrazole. *Bull. Chem. Soc. Jpn.* **2020**, *93* (7), 821–824. <https://doi.org/10.1246/bcsj.20200077>.
- (2) Torii, K.; Hori, Y.; Kikuchi, K. Persistent Fluorescence Switching of a Probe Using a Photochromic Quencher with High Photostability Assisted by Protein-Surface Modification. *Anal. Chem.* **2023**, *95* (23), 8834–8841. <https://doi.org/10.1021/acs.analchem.3c00163>.
- (3) Torii, K.; Benson, S.; Hori, Y.; Vendrell, M.; Kikuchi, K. No-Wash Fluorogenic Labeling of Proteins for Reversible Photoswitching in Live Cells. *Chem. Sci.* **2024**, *15* (4), 1393–1401. <https://doi.org/10.1039/D3SC04953A>.

### International Conference and Symposium

---

- (1) **Kenji Torii**, Yuichiro Hori, and Kazuya Kikuchi. “Development of photoswitchable fluorescent molecules using fulgimide”, 15th International Symposium on Applied Bioinorganic Chemistry, Nara, Japan, Jun. 2019. (Poster, Peer-reviewed)
- (2) **Kenji Torii**, Yuichiro Hori, and Kazuya Kikuchi. “Development of photoswitchable fluorescent molecules using fulgimide”, The 2021 International Chemical Congress of Pacific Basin Societies, online, Dec. 2021. (Poster, Peer-reviewed)
- (3) **Kenji Torii**, Sam Benson, Yuichiro Hori, Marc Vendrell, Kazuya Kikuchi “No-wash fluorogenic labeling of proteins for reversible photoswitching in live cell imaging”, The 11<sup>th</sup> Takeda Science Foundation Symposium on PharmaSciences, Osaka, Jan. 2024. (Poster, Peer-reviewed)

### Domestic Conference

---

- (1) **鳥井健司**, 堀雄一郎, 菊地和也 “フルギミドを用いた蛍光スイッチング分子の開発”, 1P-001, 第13回バイオ関連化学シンポジウム, 宮城, 2019年9月 (ポスター, 査読有)
- (2) **鳥井健司**, 堀雄一郎, 渡部圭一郎, 菊地和也 “アリルアゾピラゾールを用いた光スイッチング蛍光分子の開発”, 1P-03, 第14回バイオ関連化学シンポジウム, オンライン開催, 2020年9月 (ポスター, 査読有)

- (3) **鳥井健司**, 堀雄一郎, 菊地和也 “フルギミドを用いた光スイッチング蛍光分子の開発”, A21-1am-01, 日本化学会第 101 回春季年会, オンライン開催, 2021 年 3 月 (口頭, 査読無)
- (4) **鳥井健司**, 堀雄一郎, 菊地和也 “フルギミドを用いた光スイッチング蛍光分子の開発”, P-45, 第 15 回日本ケミカルバイオロジー学会, オンライン開催, 2021 年 6 月 (ポスター, 査読有)
- (5) **鳥井健司**, 堀雄一郎, 菊地和也 “細胞内イメージングのためのフルギミドを用いた光スイッチング蛍光分子の開発”, B104-1pm-04, 日本化学会第 102 回春季年会, オンライン開催, 2022 年 3 月 (口頭, 査読無)
- (6) **鳥井健司**, 堀雄一郎, 菊地和也 “タンパク質表面修飾を利用した光スイッチング蛍光分子の光安定性の向上”, P42, 第 16 回バイオ関連化学シンポジウム, 愛知, 2022 年 9 月 (ポスター, 査読有)
- (7) **鳥井健司**, Sam Benson, Marc Vendrell, 堀雄一郎, 菊地和也 “フルギミドを用いた光応答性発蛍光性プローブの開発”, D1442-1am-09, 日本化学会第 103 回春季年会, 千葉, 2023 年 3 月 (口頭, 査読無)
- (8) **鳥井健司**, Sam Benson, Marc Vendrell, 堀雄一郎, 菊地和也 “タンパク質表面修飾を利用した持続可能な蛍光スイッチング戦略”, 20A-03, 第 17 回バイオ関連化学シンポジウム, 千葉, 2023 年 9 月 (口頭, 査読有)

### Domestic Symposium

---

- (1) **鳥井健司**, 堀雄一郎, 菊地和也 “Development of photoswitchable fluorescent molecules using fulgimide”, 第 4 回 A3 Young Scientist Meeting, オンライン開催, 2021 年 2 月 (口頭, 査読無)
- (2) **鳥井健司**, 堀雄一郎, 菊地和也 “Development of photoswitchable fluorescent molecules using fulgimide”, 第 4 回 A3 取りまとめシンポジウム, 仙台, 2021 年 11 月 (口頭, 査読無)

### Awards

---

- (1) RSC Organic & Biomolecular Chemistry Poster Award (第 15 回日本ケミカルバイオロジー学会ポスター賞), 2021 年 6 月

- (2) RSC Chemical Biology Poster Award (第 16 回バイオ関連シンポジウムポスター賞), 2022 年 9 月
- (3) Excellent Poster Award (The 11<sup>th</sup> Takeda Science Foundation Symposium on PharmaSciences), 2024 年 1 月

## **List of Fellowships and Grants**

- (1) JSPS (Japan Society for the Promotion of Science), Research Fellowship for Young Researchers (DC1) (日本学術振興会 特別研究員 DC1), Grants number: 21J20593, Apr. 2021 - present
- (2) IMSC (Interactive Materials Science Cadet) Program (インタラクティブ物質科学・カデットプログラム), Apr. 2020 - present

## List of Figures

Figure 1. Schematic of photoswitchable fluorescent molecules (PSFMs).....	2
Figure 2. Representative synthetic PSFMs. ....	3
Figure 3. Schematic of arylazopyrazole (AAP). ....	4
Figure 4. Schematic of furylfulgimide (FF).....	5
Figure 5. Fluorescence photoswitching principle using FF based on Förster resonance energy transfer (FRET).....	6
Figure 6. Protein-surface-assisted strategy for PSFMs and its applications. ....	7
Graphical Abstract for Chapter 1 .....	9
Figure 1-1-1. Photophysical property of AAP.....	11
Figure 1-1-2. Molecular design of SC molecules. ....	11
Figure 1-1-3. Representative calculated structures of SC molecules.....	12
Figure 1-2-1. Photoswitching properties of SC molecules. ....	13
Graphical Abstract for Chapter 2 .....	21
Figure 2-1-1. Molecular design of FF-TMR. ....	23
Figure 2-2-1. Photoswitching properties of FF-TMR. ....	24
Figure 2-2-2. Photoswitching reversibility of FF-TMR.....	25
Figure 2-2-3. Absorption spectra of FF-TMR and TMR. ....	26
Figure 2-2-4. Photoreaction tracking of FF-TMR using HPLC.....	27
Figure 2-2-5. Photodurability analysis of FF-TMR using HPLC. ....	27
Figure 2-2-6. Photoswitching rates of FF-TMR. ....	29
Figure 2-2-7. Photoswitching reversibility of FF-TMR with different concentrations.....	31
Figure 2-2-8. Absorption spectra of FF-TMR after 530 nm irradiation.....	31
Figure 2-3-1. Characterization and photoswitching property of FF-TMR-BSA.....	32
Figure 2-3-2. Photoswitching reversibility of FF-TMR-BSA.....	33
Figure 2-3-3. Photoswitching rates of FF-TMR-BSA. ....	34
Figure 2-4-1. Characterization of FF-TMR-tubBAB and ATTO655-IgG.....	35
Figure 2-4-2. Photoswitching properties of FF-TMR-tubBAB and ATTO655-IgG. ....	35
Figure 2-4-3. Fluorescence imaging of FF-TMR-tubBAB and ATTO655-IgG in fixed HeLa cells...37	
Figure 2-4-4. Ratiometric imaging of FF-TMR-tubBAB and ATTO655-IgG in fixed HeLa cells.....38	
Figure 2-5-1. Fluorescence imaging of FF-TMR and LysoTracker® Green in live HeLa cells. ....39	
Figure 2-5-2. Ratiometric imaging of FF-TMR and LysoTracker® Green in live HeLa cells.....40	
Graphical Abstract for Chapter 3 .....	54
Figure 3-1-1. Molecular design of Trp-BODIPY-FF.....	56
Figure 3-1-2. The comparison of photophysical properties of each BODIPY derivative. ....	56

Figure 3-2-1. Environmental sensitivities of Trp-BODIPY(-FF).....	58
Figure 3-2-2. Absorption spectra of Trp-BODIPY.....	58
Figure 3-2-3. Absorption spectra of Trp-BODIPY-FF. ....	60
Figure 3-2-4. Photoswitching properties of Trp-BODIPY-FF.....	61
Figure 3-2-5. Photoswitching reversibility of Trp-BODIPY-FF. ....	61
Figure 3-2-6. Quenching efficiency of Trp-BODIPY-FF over repetitive photoirradiation cycles. ....	62
Figure 3-2-7. Characterization and photoswitching reversibility of Trp-BODIPY-FF-BSA. ....	62
Figure 3-3-1. Environmental sensitivities of HTL-Trp-BODIPY-FF.....	64
Figure 3-3-2. The affinity of (HTL-)Trp-BODIPY-FF with BSA.....	65
Figure 3-3-3. Absorption spectra of HTL-Trp-BODIPY-FF. ....	66
Figure 3-3-4. Fluorogenicity of HTL-Trp-BODIPY-FF.....	67
Figure 3-3-5. Docking simulation of HTL-Trp-BODIPY-FF with Halo-tag. ....	68
Figure 3-3-6. Photoswitching properties of HTL-Trp-BODIPY-FF.....	69
Figure 3-3-7. Photoswitching reversibility of HTL-Trp-BODIPY-FF. ....	69
Figure 3-3-8. Quenching efficiency of HTL-Trp-BODIPY-FF over repetitive photoirradiation cycles. .....	70
Figure 3-4-1. Live cell imaging using HTL-Trp-BODIPY-FF.....	71
Figure 3-4-2. Extended long time live cell imaging using HTL-Trp-BODIPY-FF. ....	72
Figure 3-4-3. Ratiometric imaging of HeLa cells transfected with pcDNA3.1(+)-MBP-Halo- mCherry. ....	74
Figure 3-4-4. Live cell imaging of non-transfected and MBP-Halo-mCherry transfected HeLa cells. .....	75
Figure 3-4-5. Ratiometric imaging HEK293T cells transfected with pcDNA3.1(+)-Halo-EGFR- mCherry. ....	76
Figure 3-4-6. Ratiometric imaging of HeLa cells transfected with pcDNA3.1(+)-Tom20-Halo- mCherry. ....	77

## List of Tables and Schemes

### List of Tables

---

Table 1-2-1. Optical properties of SC molecules (SC1, SC2, and SC3). .....	13
Table 2-1-1. Optical properties of FF. ....	23
Table 2-2-1. Optical properties of FF-TMR and FF-TMR-BSA. ....	28
Table 3-1-1. Optical properties of FF in various solvents. ....	56
Table 3-2-1. Optical properties of Trp-BODIPY. ....	58
Table 3-2-2. Optical properties of Trp-BODIPY-FF. ....	59
Table 3-3-1. Optical properties of HTL-Trp-BODIPY-FF. ....	68
Table 3-3-2. Comparison of photophysical properties of representative photoswitchable fluorescent proteins and HTL-Trp-BODIPY-FF. ....	70

### List of Schemes

---

Scheme 1-1. Synthesis of SC molecules. ....	14
Scheme 2-1. Synthesis of FF. ....	41
Scheme 2-2. Synthesis of FF-TMR. ....	41
Scheme 3-1. Synthesis of Trp-BODIPY. ....	78
Scheme 3-2. Synthesis of Trp-BODIPY-FF. ....	78
Scheme 3-3. Synthesis of Halo-tag ligand. ....	79
Scheme 3-4. Synthesis of HTL-Trp-BODIPY-FF. ....	79

## List of Abbreviations

2D	two-dimensional
3D	three-dimensional
a.u.	arbitrary unit
AAP	arylazopyrazole
abs.	absorbance
BL	$\beta$ -lactamase
BOC	tert-butyloxycarbonyl
BODIPY	boron-dipyrromethene
BSA	bovine serum albumin
CBB	Coomassie brilliant blue
COMU	ethyl 2-cyano-2-((dimethyliminio)(morpholino)methoxyimino)acetate hexafluorophosphate
DAE	diarylethene
DCM	dichloromethane
DMEM	Dulbecco's modified eagle medium
DMF	<i>N,N</i> -dimethylformamide
DMSO	dimethyl sulfoxide
DNB	1,3-dinitrobenzene
EDC	1-ethyl-3-(3-dimethylaminopropyl)carbodiimide
EGFR	epidermal growth factor receptor
Eq.	equation
eq.	chemical equivalent
ESI	electrospray ionization
FAB	fast atom bombardment
FBS	fetal bovine serum
FF	furylfulgimide
FL	fluorescence
FRET	Förster resonance energy transfer
HATU	1-[bis(dimethylamino)methylene]-1 <i>H</i> -1,2,3-triazolo[4,5- <i>b</i> ]pyridinium 4-oxide hexafluorophosphate
HBSS	Hanks' balanced salt solution
hCRBPII	human cellular retinol-binding protein II
HI	hemi-indigo
HPLC	high-performance liquid chromatography

HRMS	high resolution mass spectrometry
HTI	hemi-thioindigo
HTL	Halo tag ligand
IEDDA	inverse electron demand Diels-Alder
IgG	Immunoglobulin G
LB	lysogeny broth (Luria-Bertani)
LDA	lithium diisopropylamide
LED	light emitting diode
LogP	logarithm of the partition coefficient of a solute between <i>n</i> -octanol and water
MALDI	matrix assisted laser desorption ionization
MBP	maltose binding protein
MCMM	multiconfiguration molecular mechanics
MES	2-( <i>N</i> -morpholino)ethanesulfonic acid
MINFLUX	minimal photon fluxes
MINSTED	minimal STED
MS	mass spectrometry
NA	numerical aperture
NHS	<i>N</i> -hydroxysuccinimide
NLS	nuclear localization signals
NMR	nuclear magnetic resonance
OPLS	optimized potentials for liquid simulations
PB	phosphate buffer
PCR	polymerase chain reaction
POI	protein of interest
PSFMs	photoswitchable fluorescent molecules
PSS	photostationary state
PYP	photoactive yellow protein
quant.	quantitative
RESOLFT	reversible saturable optical fluorescence transition
ROI	region of interest
SC	structural controller
SDS-PAGE	sodium dodecyl sulfate – poly-acrylamide gel electrophoresis
SEM	standard error of the mean
STED	stimulated emission depletion
Sulfo-NHS	<i>N</i> -hydroxysulfosuccinimide
TEA	triethylamine

## *List of Abbreviations*

---

TFA	trifluoroacetic acid
TLC	thin layer chromatography
TMR	tetramethylrhodamine
Tom20	translocase of outer membrane 20
Trp	tryptophan
TSTU	<i>N,N,N',N'</i> -tetramethyl- <i>O</i> -( <i>N</i> -succinimidyl)uronium tetrafluoroborate
tubBAB	anti- $\beta$ tubulin antibody
UV	ultraviolet
vis	visible

## Table of Contents

Acknowledgments .....	i
List of Publications, Presentations, and Awards .....	ii
List of Fellowships and Grants .....	iv
List of Figures.....	v
List of Tables and Schemes.....	vii
List of Abbreviations.....	viii
Table of Contents .....	xi
<b>General introduction .....</b>	<b>1</b>
Photoswitchable fluorescent molecules (PSFMs).....	1
Arylazopyrazole (AAP) as a photochromic structural controller.....	4
Furylfulgimide (FF) as a photochromic fluorescence quencher .....	5
Protein surface modification for PSFMs.....	6
Outline of the research .....	8
<b>Chapter 1. Development of photoswitchable fluorescent molecules using arylazopyrazole.....</b>	<b>9</b>
Abstract.....	9
1-1. Molecular design and synthesis of AAP-based PSFMs.....	10
1-2. Photophysical properties of AAP-based PSFMs .....	12
Synthetic Procedures.....	14
Experimental Sections .....	18
<b>Chapter 2. Persistent Fluorescence Switching Assisted by Protein-Surface Modification .....</b>	<b>21</b>
Abstract.....	21
2-1. Molecular design and synthesis of FF-TMR .....	22
2-2. Photoswitching properties of FF-TMR.....	23
2-3. Protein-surface-assisted photoswitching strategy using FF-TMR.....	32
2-4. Fluorescence imaging in fixed cells .....	34
2-5. Live-cell imaging.....	39
Synthetic Procedures.....	41
Experimental Sections .....	46
<b>Chapter 3. No-Wash Fluorogenic Labeling of Proteins for Reversible Photoswitching in Live Cells.....</b>	<b>54</b>
Abstract.....	54
3-1. Molecular design and synthesis of Trp-BODIPY-FF.....	55
3-2. Photophysical properties of Trp-BODIPY-FF .....	57
3-3. Synthesis and photophysical properties of HTL-Trp-BODIPY-FF .....	62

3-4. Live-cell imaging studies using HTL-Trp-BODIPY-FF .....	70
Synthetic Procedures.....	78
Experimental Sections .....	87
<b>Conclusions and Perspectives .....</b>	<b>98</b>
<b>References.....</b>	<b>100</b>

## General introduction

### Photoswitchable fluorescent molecules (PSFMs)

---

Photoswitchable fluorescent molecules (PSFMs) whose fluorescence intensities are reversibly changed by light irradiation are biologically important tools for fluorescence imaging. In recent years, the use of PSFMs for tracking cellular dynamics<sup>1-3</sup> and visualizing cellular components with high spatial resolution using super-resolution imaging<sup>4-8</sup> has greatly increased (Figure 1). While photoactivatable fluorophores irreversibly photoswitch from non-fluorescent to fluorescent states upon light irradiation<sup>9-21</sup>, PSFMs exhibit reversible fluorescence switching upon light irradiation allowing each PSFM to be localized multiple times. This is useful for live-cell studies where molecular dynamics can be visualized over long periods. Notably, PSFMs are also used in RESOLFT (reversible saturable optical fluorescence transition) techniques<sup>22</sup> which enable live-cell super-resolution imaging with lower-intensity light irradiation mitigating phototoxicity compared to conventional STED (stimulated emission depletion) nanoscopy<sup>23,24</sup>. In recent years, new types of super-resolution imaging technologies, namely MINFLUX (minimal photon fluxes)<sup>25-28</sup> and MINSTED (minimal STED)<sup>29,30</sup> have been demonstrated by Stefan.W.Hell and co-workers and shown to have potential to broaden the applicability of PSFMs for bioimaging. In super-resolution imaging technologies that require high-density laser irradiation, synthetic fluorophore-based PSFMs are frequently employed as imaging probes since some organic fluorophores have higher photostability and brightness than fluorescent proteins<sup>22,31-33</sup>. Although additive-dependent<sup>4,18</sup> or irreversibly caged fluorophores<sup>12,19</sup> have been widely developed as synthetic photoactivatable fluorophores or PSFMs, they are not compatible with live-cell imaging because of their phototoxicity and/or low cell-permeability. Despite the high demand for PSFMs for live-cell imaging, there have only been a few examples of reversible photoswitching in living cells, namely fluorene-based chromophore-hCRBP II (human cellular retinol-binding protein II) complexes<sup>34,35</sup>, and self-blinking fluorophores<sup>36-38</sup>. Chromophore-hCRBP II complexes exhibit fast thermal isomerization and slow photoisomerization rates from fluorescence ON to OFF states. Self-blinking fluorophores have been used for single-molecule localization nanoscopy with high spatial resolution; however, the temporal resolution is still lower than other super-resolution techniques, including STED and RESOLFT imaging.

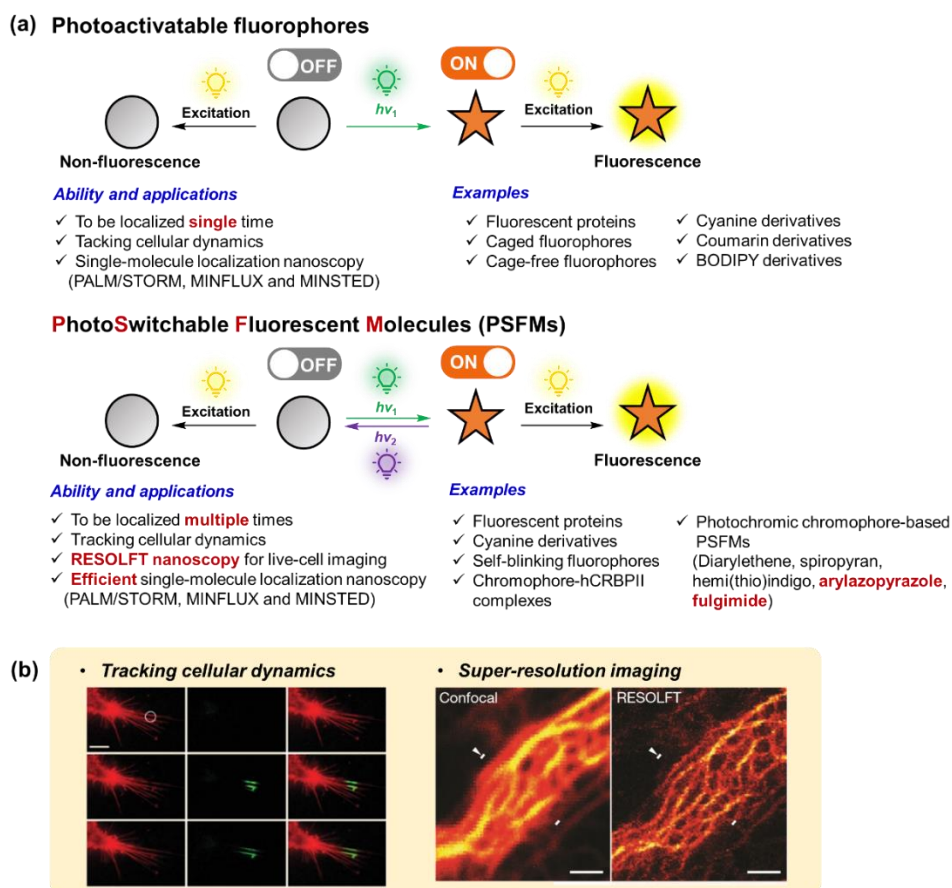


**Figure 1. Schematic of photoswitchable fluorescent molecules (PSFMs).**

**(a)** Outline of photoactivatable fluorophores vs photoswitchable fluorescent molecules (PSFMs). Photoactivatable fluorescent proteins<sup>1,2</sup>, caged fluorophore<sup>9-12,19,26</sup>, cage-free fluorophores<sup>13,28</sup>, cyanine<sup>16,17</sup>, coumarin<sup>14,15</sup>, and BODIPY<sup>20,21</sup> derivatives are reported as photoactivatable fluorophores. Photoswitchable fluorescent proteins<sup>22,31,32</sup>, cyanine derivatives<sup>4</sup>, self-blinking fluorophores<sup>36-38</sup>, chromophore-hCRBP II complexes<sup>34,35</sup>, photochromic chromophore (diarylethene<sup>5,39-42</sup>, spiropyran<sup>6-8,43,44</sup>, hemi-(thio)indigo<sup>45-47</sup>, arylazopyrazole<sup>48</sup>, and fulgimide<sup>49-51</sup>) - based PSFMs are reported as PSFMs. **(b)** General biological applications including tracking cellular dynamics<sup>1</sup> and super-resolution imaging<sup>32</sup> using PSFMs. Adapted with permission from ref 1 and 30. Copyright 2004, Springer Nature Limited. Copyright 2011, Springer Nature Limited.

Cy3-Alexa647 heterodimer<sup>4</sup> and fluorescent diarylethenes (DAE)<sup>5,39</sup> have both been developed as PSFMs for RESOLFT imaging. However, neither can be used for live-cell imaging because cyanine dyes require high concentrations of primary thiols (over 100 mM) and potassium iodide for reversible photoswitching, and DAEs contain multiple carboxylic acids to improve water solubility, resulting in poor membrane permeability (Figure 2a,b). Recently, PSFMs based on photochromic molecules that undergo reversible photoisomerization upon photoirradiation have been described. Photochromic chromophores are an attractive choice for developing PSFMs as they enable fluorescence switching

by modulating chemical and/or physical properties according to their photochromic reactions. In addition to the DAEs<sup>5,39-42</sup>, spiropyran<sup>6-8,43,44</sup>, hemi-(thio)indigo (HI and HTI)<sup>45-47</sup>, arylazopyrazole (AAP)<sup>48</sup>, and fulgimide-based PSFMs<sup>49-52</sup> have been reported in the last years. Spiropyran-based PSFMs were developed for the visualization of enzyme activity<sup>6</sup> or lipid bilayers<sup>7,8</sup> using super-resolution microscopy. These molecules show aggregation-caused quenching and are affected by thermal back isomerization and protonation of photoactivated merocyanine (Figure 2c). HI-based PSFM are strongly affected their fluorescence quantum yield and photoconversion efficiency by the presence of RNAs<sup>46</sup> or proteins<sup>47</sup>. HTI-based PSFM enables fluorescence switching in living cells utilizing proton-bridged intramolecular hydrogen bond at protonated Z isomer. However, the Z to E thermal- and photo-conversion kinetics of HTI are quite low and may be not compatible for super-resolution imaging in the current molecular designs (Figure 2d). In the dissertation, I have focused on two photochromic compounds, namely arylazopyrazole (AAP) and furylfulgimide (FF), to develop PSFMs. Except for the authors' studies, there are no examples of a PSFM using AAP<sup>48</sup> or fulgimide derivatives<sup>49,52</sup> accomplish reversible fluorescence switching in both in vitro and in living cells. Herein, I have demonstrated novel synthetic PSFMs using AAP and FF, which open up new avenues for exploring sophisticated probe designs for advanced imaging technologies including live-cell super-resolution imaging.

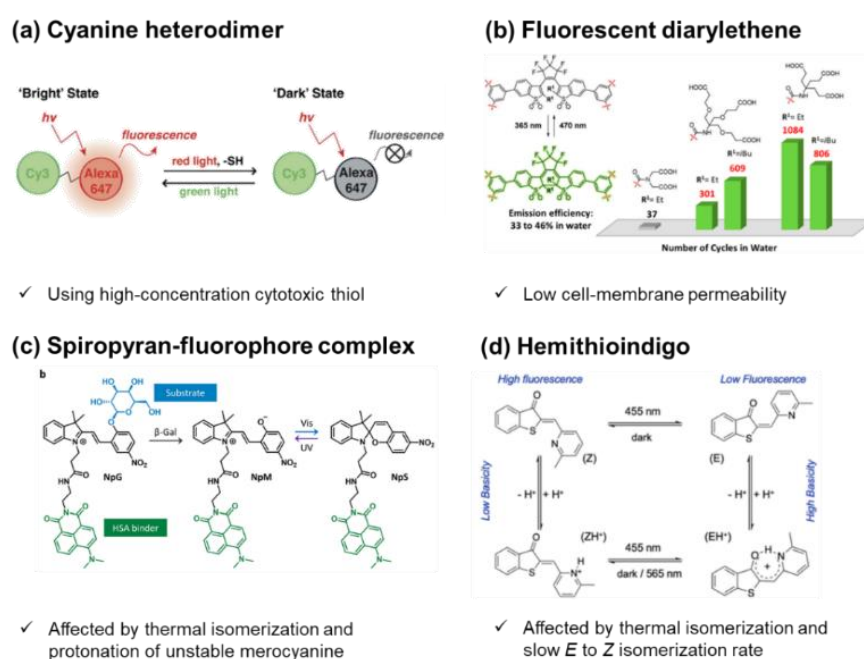


**Figure 2. Representative synthetic PSFMs.**

(a) Cyanine heterodimer<sup>4</sup>. Adapted with permission from ref 4 under CC BY. (b) Fluorescent diarylethene<sup>39</sup>. Adapted with permission from ref 39 under CC BY. Copyright 2019 American Chemical Society. (c) Spiropyran-fluorophore complex<sup>6</sup>. Adapted with permission from ref 6. Copyright 2020 American Chemical Society. (d) Hemithioindigo<sup>45</sup>. Adapted with permission from ref 45. Copyright 2023 American Chemical Society.

### Arylazopyrazole (AAP) as a photochromic structural controller

Arylazopyrazole (AAP) which is classified as an azobenzene derivative undergoes *E/Z* isomerization upon photoirradiation (Figure 3a). AAP induce *E*-to-*Z* isomerization upon UV light irradiation, whereas reverse *Z*-to-*E* isomerization is proceeded by visible light irradiation. Unlike the conventional azobenzene derivatives, AAP notably exhibits excellent thermal bistability, which allows negligible thermal back reactions and strict control of conformation by light irradiation<sup>53</sup>. Taking advantage of the large conformational changes between *E*- and *Z*- isomers, I newly designed PSFMs that fluorescence quencher and fluorophore were placed at the ends of linkers extending from both ends of AAP (Figure 3b). When AAP forms an *E*-isomer, fluorophore is oriented in the opposite direction to fluorescence quencher, resulting in fluorescence emission avoiding contact quenching (ON state). On the other hand, upon completion of *E*-to-*Z*-isomerization, fluorophore comes close to quencher, causing interaction and the resultant contact quenching (OFF state). In Chapter 1, I demonstrated that PSFMs based on this structure-dependent photoswitching strategy allow reversible control of fluorescence intensity in aqueous solution.

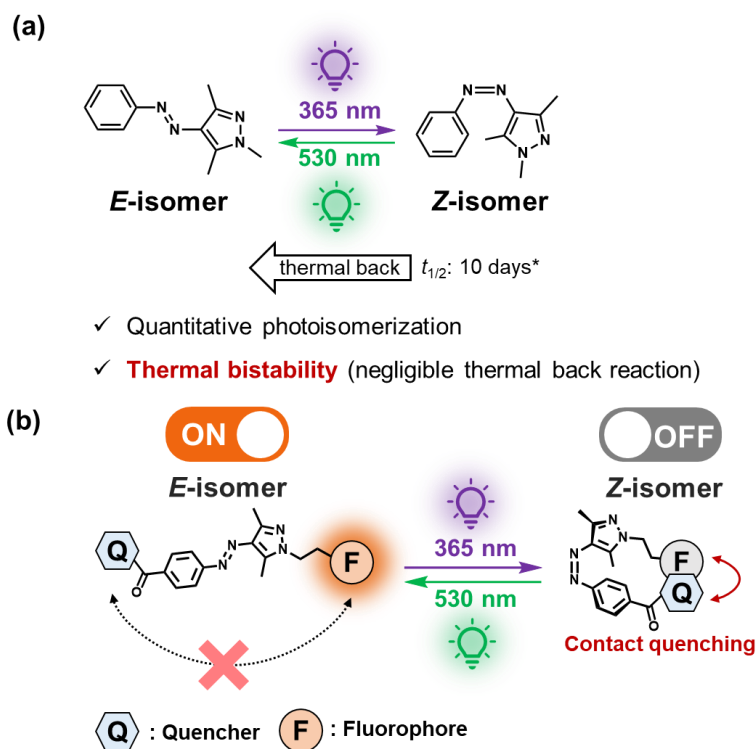


**Figure 3. Schematic of arylazopyrazole (AAP).**

(a) Chemical structure of arylazopyrazole (AAP). AAP undergoes *E*-to-*Z* isomerization upon 365 nm irradiation and *Z*-to-*E* isomerization upon 530 nm irradiation with negligible thermal back reaction (thermal half-life ( $t_{1/2}$ ) is 10 days at 25 °C). \*The thermal back reaction rate was previously reported<sup>53</sup>. (b) Fluorescence photoswitching principle using AAP using as structural controller that regulate the distance between fluorophore and quencher. Adapted with permission from ref 48. Copyright 2020 The Chemical Society of Japan.

## Furylfulgimide (FF) as a photochromic fluorescence quencher

Since the 1980s, the photochromic molecules have been vigorously developed due to their potential application in photosensitive materials including devices for optical memory. Fulgide is one of the representative molecules as a photochromic chromophore, including bis(methylene succinic anhydride) derivative whose  $\pi$ -electron conjugated system is extended by a hetero-aromatic ring namely furan, indole, and thiophene<sup>54</sup>. Furylfulgimide (FF) belongs to the class of fulgimide derivatives that allow reversible photoswitching in an aqueous solution<sup>55</sup> (Figure 4). Fulgimides undergo photoisomerization between noncolored open- and colored closed-ring forms inducing a conrotatory electrocyclization between 1,3,5-*cis*-hexatriene and 1,3-cyclohexadiene systems, referred to as the Woodward-Hoffmann rule. In general, FF induces a cyclization reaction upon UV light irradiation, whereas a cycloreversion reaction is triggered by visible light. In addition, fulgimides allow for tight photocontrol without thermal back reaction due to their high thermal bistability.

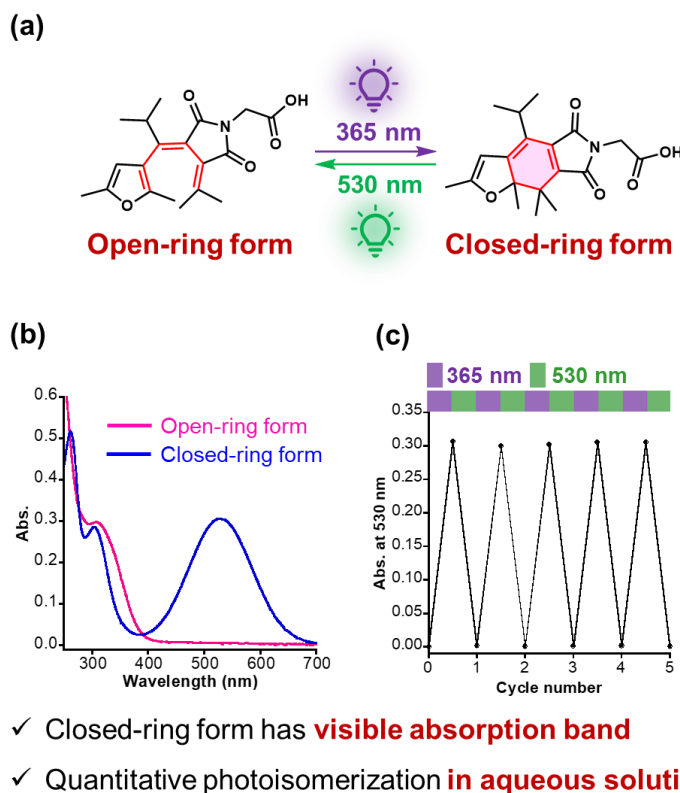


**Figure 4. Schematic of furylfulgimide (FF).**

(a) Chemical structure of furylfulgimide (FF). FF undergoes cyclization reaction upon 365 nm irradiation and cycloreversion reaction upon 530 nm irradiation. (b) Absorption spectra and (c) photoswitching reversibility of 50  $\mu$ M FF in 100 mM phosphate buffer (pH 7.4). (b) Spectra of open-ring and closed-ring forms are shown in magenta and blue lines, respectively. (c) Absorbance at 530 nm was measured after alternating irradiation at 365 and 530 nm. Light irradiation at 365 and 530 nm is indicated by the purple and green shades, respectively. Adapted with permission from ref 49. Copyright 2023 American Chemical Society.

In this molecular design of the PSFM, FF is used as a photoswitchable fluorescence quencher based on Förster resonance energy transfer (FRET) whose efficiency can be controlled by a spectral overlap integral change between the donor fluorophore and the nonfluorescent acceptor FF<sup>50,51,56–58</sup>(Figure 5). In the design principle, when FF is in an open-ring form, a donor fluorophore linked to the acceptor FF emits fluorescence without any FRET due to the absence of a spectral overlap integral between the donor and acceptor. On the other hand, photoisomerization of FF to a closed-ring form triggers FRET from the donor fluorophore to a nonfluorescent FF, resulting in fluorescence quenching. In Chapter 2 and 3, I demonstrated that PSFMs based on this FRET-dependent photoswitching strategy allow reversible fluorescence quenching not only *in vitro*, but also in fixed and living cells.

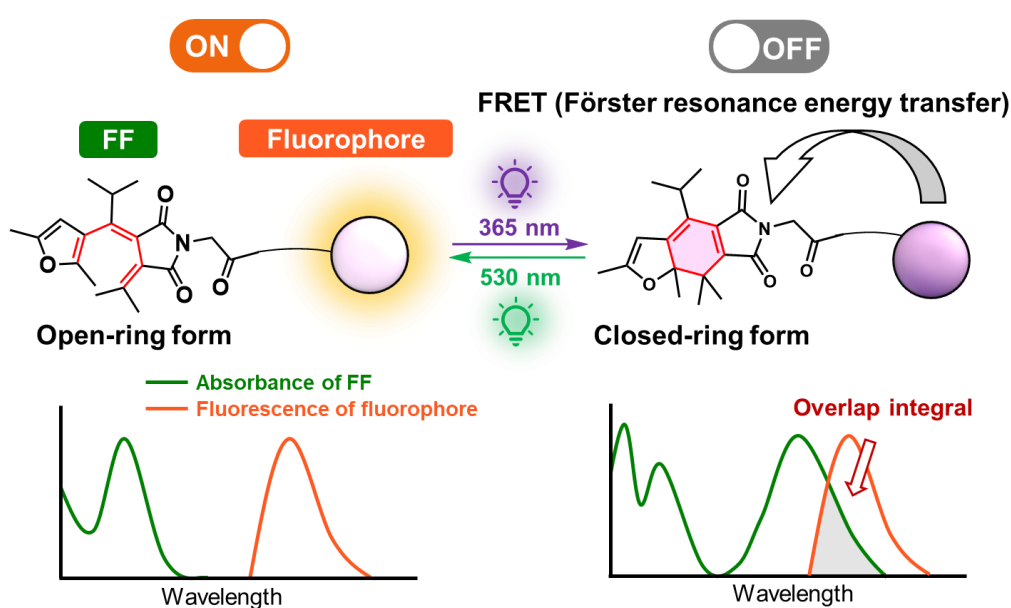


**Figure 5. Fluorescence photoswitching principle using FF based on Förster resonance energy transfer (FRET).**

Adapted with permission from ref 49. Copyright 2023 American Chemical Society.

## Protein surface modification for PSFMs

As mentioned above, synthetic PSFMs using photochromic chromophores are widely developed; however, most of them have a large molecular weight (sometimes over 1,000 g/mol) and hydrophobic molecular structure that may result in molecular aggregations exhibiting low photostability in a biological medium. More recently, DAE included by cucurbit[7]uril were reported to improve photostability compared to free diarylethene in an aqueous solution<sup>40</sup>. However, those supramolecular complexes have sterically crowded structure, and they require longer linker length to conjugate with other biomolecules. Here, to address this limitation, I established a protein-surface-assisted strategy that achieves persistent reversible fluorescence photoswitching of a PSFM in an aqueous solution (Figure 6a).

In this dissertation, I found that a PSFM labeling with a protein surface showed the persistently reversible fluorescence switching performance which allows highly-photostable optical control in cells. Modification of proteinogenic amino acids enabled PSFM-labeled antibodies to induce reversible photoswitching in a specific localization of fixed cells (Figure 6b). In recent years, modification of selective proteinogenic amino acids using a catalyst has been an attractive approach to manipulate the biological activity of a protein<sup>59,60</sup>. Protein-surface modification with a PSFM will be adapted for these modification systems. In addition to these chemoselective protein/antibody modifications, protein-tag system is one of the most attractive candidate for target-specific imaging in live cells. For example, synthetic PSFM linked to a ligand that binds to a protein tag (e.g., SNAP-tag<sup>61,62</sup>, Halo-tag<sup>63</sup>, and PYP-tag<sup>64</sup>) may have the ability to visualize any proteins of interest in live cells. I have developed Halo-tag ligand bearing PSFM that successfully recognizes and labels with Halo-tag coexpressed with protein of interest in live cells. Most importantly, the labeled PSFM exhibits reversible fluorescence switching upon light irradiation (Figure 6c). The protein-surface modification using these protein tags with a PSFM allows the persistently reversible photoswitching performance that is required for super-resolution imaging.

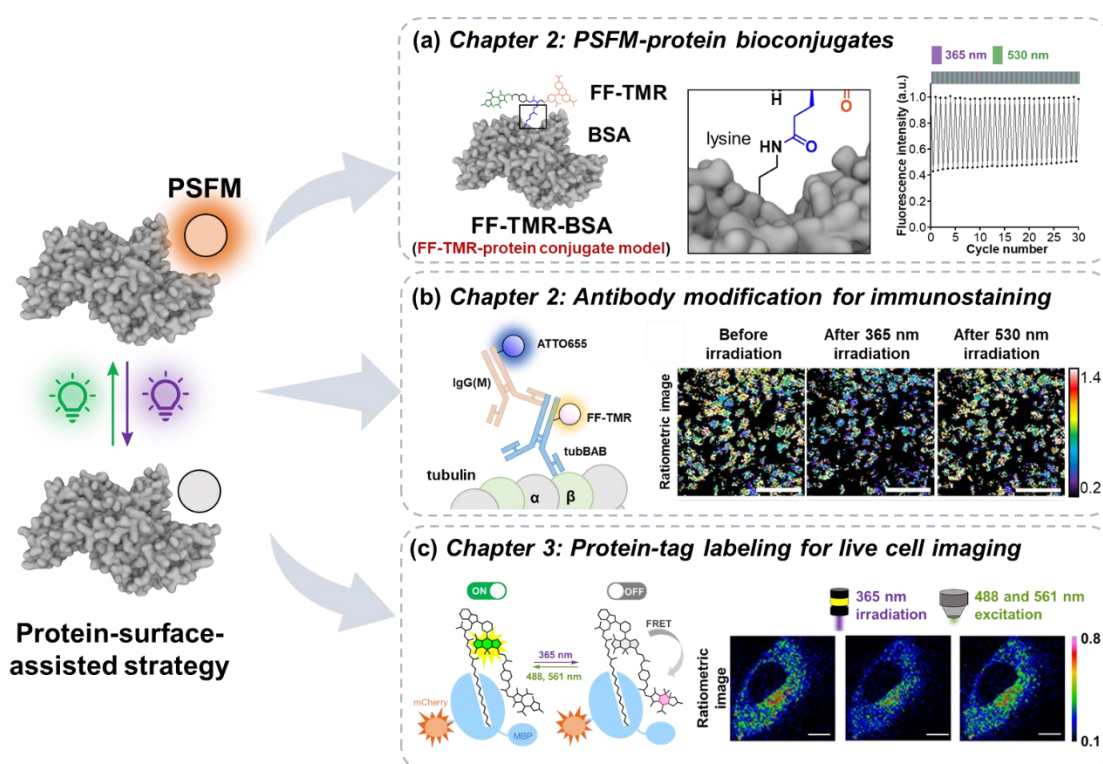


**Figure 6. Protein-surface-assisted strategy for PSFMs and its applications.**

(a) Lysine selective protein modification using PSFM (Chapter 2). (b) Antibody modification using PSFM for immunostaining and reversible fluorescence switching in fixed cells (Chapter 2). (c) Protein-tag labeling system using PSFM for reversible fluorescence switching in live cells (Chapter 3). (a,b) Adapted with permission from ref 49. Copyright 2023 American Chemical Society. (c) Adapted with permission from ref 52 under CC BY-NC.

## Outline of the research

---

In this dissertation, new PSFMs were designed and developed based on the above-mentioned strategy. The dissertation consists of following 3 chapters.

**In Chapter 1**, the new type of PSFMs using AAP were synthesized and demonstrated reversible fluorescence switching in aqueous solution. This is the first example of PSFMs utilizing the conformational change between *E*- and *Z*-isomers of AAP to regulate the quenching efficiency of the fluorophore.

**In Chapter 2**, the FRET-based PSFM using FF and synthetic fluorophore tetramethylrhodamine (TMR), named FF-TMR was developed to demonstrate the photoswitching ability. The fluorescence intensity of FF-TMR was successfully regulated by light irradiation due to the change in FRET efficiency between FF and TMR. I judiciously analyzed these photophysical properties in detail and found that their photoswitching stability is strongly affected by their surrounding environment. Taking advantage of these interesting findings, I successfully established the strategy to improve the photostability of PSFMs using proteins. The protein surface labeling allows FF-TMR to exhibit reversible and fast photoswitching supported by its surrounding environment in an aqueous solution. PSFM bound to anti-tubulin antibody surface showed a persistent reversible fluorescence switching performance which allows highly photostable optical control in fixed cells using immunostaining.

**In Chapter 3**, another FRET-based PSFM probe, named HTL-Trp-BODIPY-FF, which contains the Halo-tag ligand (HTL), the environmentally sensitive fluorophore Trp-BODIPY<sup>65-71</sup> and FF was developed for reversible fluorescence control in living cells. Halo-tag system, which is versatile for live-cell imaging applications, and Trp-BODIPY, which exhibits brighter fluorescence emission in hydrophobic environments was adapted to achieve site-specific protein labeling in living cells. Taking advantage of these abilities, HTL-Trp-BODIPY-FF showed a fluorescence intensity increase after binding Halo-tag (ON state), because it was adjacent to the hydrophobic Halo-tag protein surface. It helps to minimize the fluorescence signal derived from unlabeled HTL-Trp-BODIPY-FF and allow no-wash labeling. The labeled HTL-Trp-BODIPY-FF exhibited reversible fluorescence switching upon light irradiation with higher photostability compared to the unlabeled probe, assisted by the Halo-tag protein surface that prevents intermolecular aggregation among probes. This feature was utilized to visualize the reversible fluorescence control of HTL-Trp-BODIPY-FF to Halo-tag expressed in live cells. To the best of the authors' knowledge, this is the first example of a fluorogenic PSFM modified with a Halo-tag protein showing reversible fluorescence photoswitching and represents a valuable tool for the development of future PSFM structures.

## Chapter 1. Development of photoswitchable fluorescent molecules using arylazopyrazole

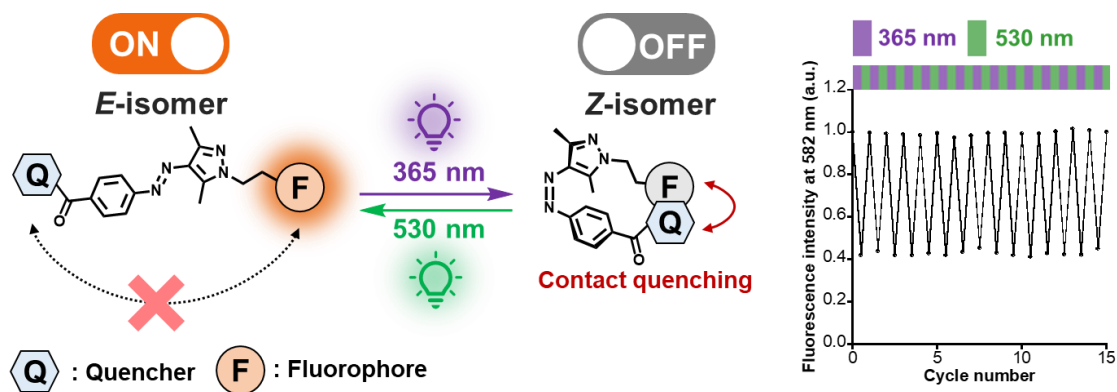
The content of this chapter has been published in:

Torii, K.; Hori, Y.; Watabe, K.; Kikuchi, K. Development of Photoswitchable Fluorescent Molecules Using Arylazopyrazole. *Bull. Chem. Soc. Jpn.* **2020**, *93* (7), 821–824.

<https://doi.org/10.1246/bcsj.20200077>.

### Abstract

Photoswitchable fluorescent molecules (PSFMs) are important tools for fluorescence imaging of biomolecules. PSFMs have been applied for pulse-chase experiments and super-resolution imaging ever before. However, most have limitations in that their fluorophores have low photostability or require cytotoxic additives for reversible photoswitching. Here, I have developed PSFMs using a photochromic compound, arylazopyrazole (AAP), to overcome these limitations. Taking advantage of the excellent photophysical properties of AAP, in this molecular design, AAP plays a key role in a structural controller, which triggers fluorophore/quencher contact quenching and its recovery upon photoirradiation. These molecules exhibited reversible changes in fluorescence intensity upon photoirradiation and high photostability in aqueous solutions.



Graphical Abstract for Chapter 1.

Adapted with permission from ref 48. Copyright 2020 The Chemical Society of Japan.

## 1-1. Molecular design and synthesis of AAP-based PSFMs

---

I designed PSFMs consisting of a fluorophore, a quencher, and a photochromic molecule, namely arylazopyrazole (AAP). I chose tetramethylrhodamine (TMR) as the fluorophore because it has excellent water-solubility and photostability<sup>33</sup>. 1,3-dinitrobenzene (DNB) has been shown to quench the fluorescence of fluorophores<sup>72,73</sup>; therefore, DNB was incorporated into the PSFMs as a quencher. AAP was used to link both the TMR and DNB. AAP undergoes *E/Z* isomerization upon photoirradiation and has excellent thermal bistability that enables strict control only by photoirradiation unlike conventional azobenzene derivatives that exhibits unignorable *Z*-to-*E* thermal back reaction<sup>53</sup>. In addition, AAP was reported to undergo almost quantitative *E/Z* photoisomerization<sup>53</sup>, which was also supported by the experiments using <sup>1</sup>H-NMR and absorption spectroscopies (Figure 1-1-1). The photostationary state (PSS) upon irradiation with 365 nm was reached 97% of *Z*-isomer, whereas the PSS at 530 nm was reduced to only 3% of *Z*-isomer (97% of *E*-isomer). In this design principle, AAP plays a fundamental role in reversibly changing the molecular structure and controlling fluorescence quenching efficiency. AAP was placed at the center of the molecule, whereas TMR and DNB were placed at the ends of linkers extending from both ends of AAP (Figure 1-1-2a). When AAP forms an *E*-isomer, TMR and DNB are oriented in the opposite direction, resulting in fluorescence emission of the fluorophore (ON state). On the other hand, upon *E*-to-*Z*-isomerization by UV irradiation, TMR and DNB come close to each other, causing intramolecular  $\pi$ - $\pi$  stacking and the resultant contact quenching of TMR (OFF state). The PSFM so designed was named structural controller (SC) molecules.

The molecular structures of different type of linkers connecting AAP with TMR or DNB were determined by molecular mechanics calculations using MacroModel software. I virtually designed five SC molecules with linkers and simulated their 3D structures when their AAP moieties became *Z*- and *E*-isomers (Figure 1-1-2b, 1-1-3), and then screened molecules, in which TMR and DNB formed a stacked structure (OFF state) in the case of the *Z*-isomer of AAP, whereas the *E*-isomer kept TMR away from DNB without forming stacked structure (ON state). The three molecules, SC1, 2, and 3, showed an ideal population, the stacked structures being higher in their *Z*-isomers, while it was lower in their *E*-isomers. Figure 1-1-3 demonstrates the representative 3D structures of both *E*- and *Z*- forms of SC molecules, indicating that TMR interacts with DNB through  $\pi$ - $\pi$  stacking only in the *Z*-isomer and not in the *E*-isomer. Therefore, the SC1, 2, and 3 were synthesized as a new series of PSFMs, and these synthetic procedures and characterization are described in the Experimental Sections and Scheme 1-1.

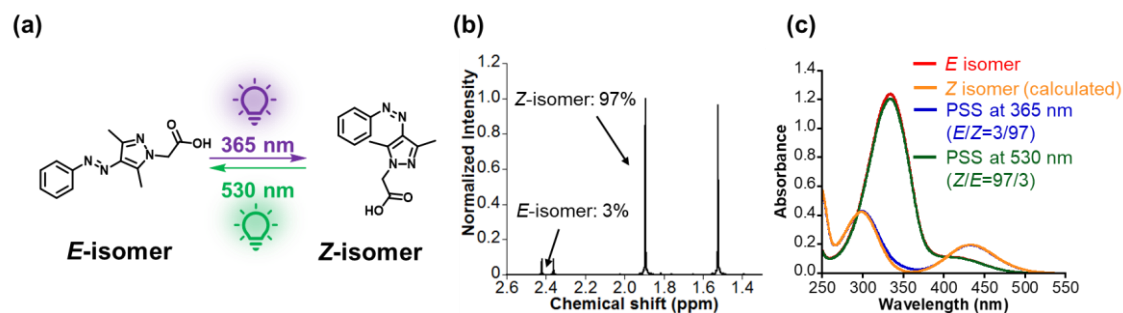


**Figure 1-1-1. Photophysical property of AAP.**

(a) Chemical structure of AAP. (b)  $^1\text{H}$  NMR spectra of methyl group protons of AAP in  $\text{D}_2\text{O}$  after 365 nm photoirradiation (Light intensity:  $8.0 \text{ mW/cm}^2$  for 24 h). (c) UV-vis absorption spectra of  $40 \mu\text{M}$  AAP in 100 mM phosphate buffer (pH 7.4). The red and blue lines show the spectra of AAP ( $E/Z = 100/0$ ) before and after 365 nm photoirradiation (Light intensity:  $4.0 \text{ mW/cm}^2$  for 5 min). The green line shows the observed spectrum of AAP in the PSS upon 530 nm photoirradiation (Light intensity:  $7.2 \text{ mW/cm}^2$  for 100 min.), while the orange line represents the calculated spectrum obtained using Eq. 1-3, 4. Adapted with permission from ref 48. Copyright 2020 The Chemical Society of Japan.

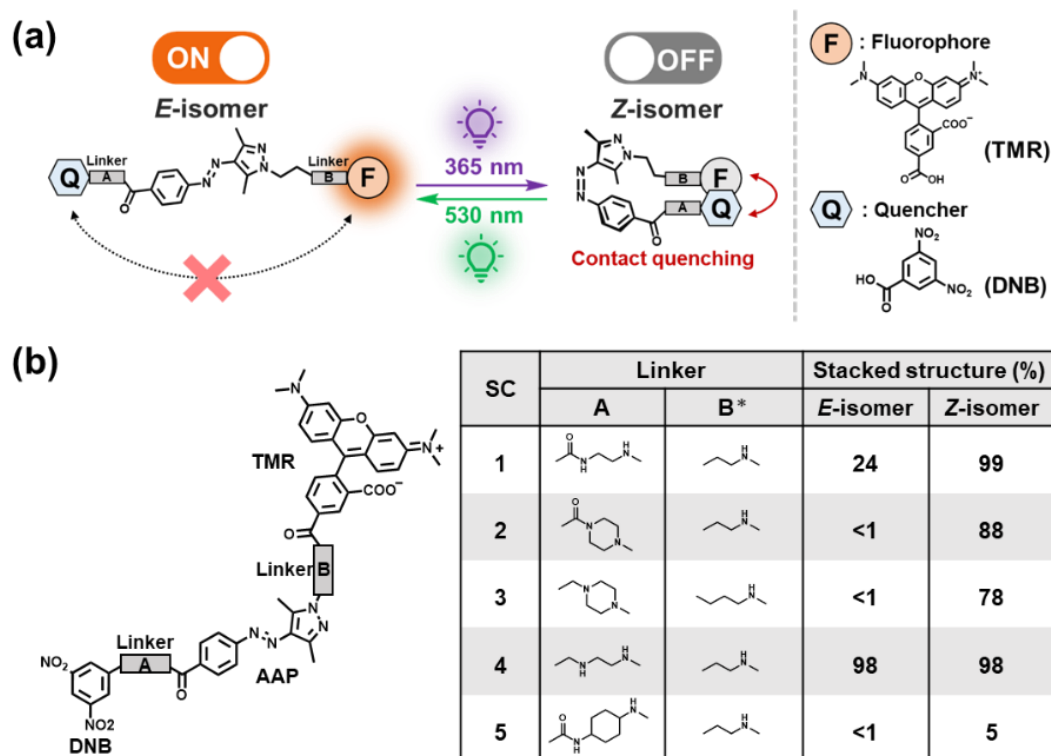


**Figure 1-1-2. Molecular design of SC molecules.**

(a) Photoswitching strategy using arylazopyrazole (AAP), fluorophore (tetramethylrhodamine (TMR)), and quencher (dinitrobenzene (DNB)). (b) Chemical structure and population of stacked structures of SC molecule candidates. Stacked structures were counted from the calculated structures using by Macromodel. \*AAP is linked to the left side and TMR is right side. Adapted with permission from ref 48. Copyright 2020 The Chemical Society of Japan.

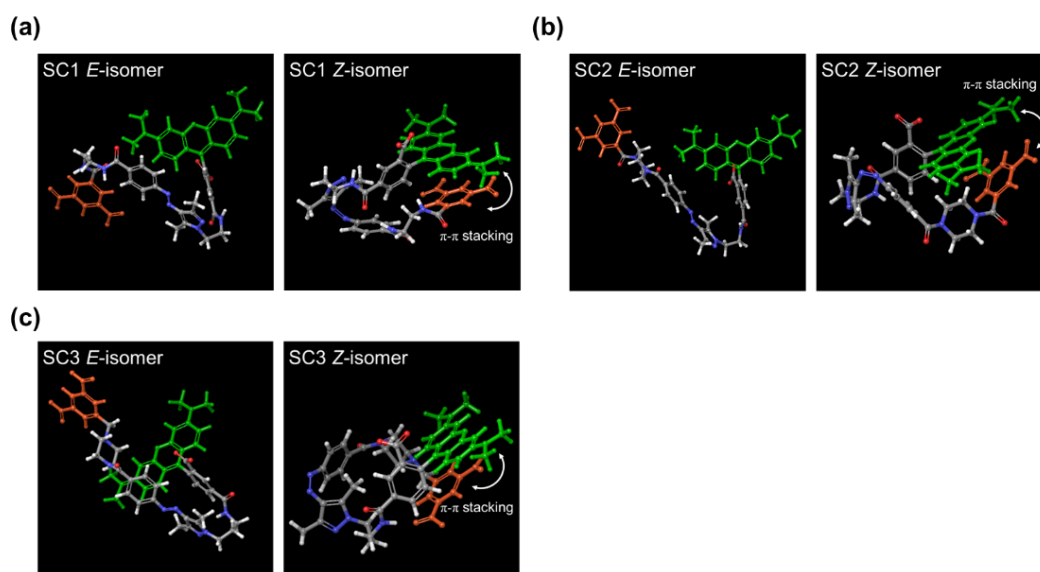


**Figure 1-1-3. Representative calculated structures of SC molecules.**

(a) SC1, (b) SC2, and (c) SC3. Green and orange parts show xanthene structural moiety of TMR and DNB, respectively.

Adapted with permission from ref 48. Copyright 2020 The Chemical Society of Japan.

## 1-2. Photophysical properties of AAP-based PSFMs

Figure 1-2-1 shows the UV-Vis absorption spectra and fluorescence spectra of the SC molecules (SC1, 2, and 3). Upon photoirradiation of the SC molecules at 365 nm, absorbance at approximately 330 nm decreased, indicating that *E*-to-*Z* isomerization of AAP had occurred in the SC molecules (Figure 1-2-1a-c). The fluorescence intensity of all the SC molecules decreased due to photoirradiation at 365 nm (Figure 1-2-1d-f). Especially, SC1 showed the largest reduction in fluorescence intensity. Table 1-2-1 shows detailed optical properties of the SC molecules. All the SC molecules showed a high extinction coefficient ( $\epsilon = 9.4 \times 10^4 \sim 1.4 \times 10^5 \text{ M}^{-1} \text{ cm}^{-1}$ ), comparable to that of unmodified TMR ( $\epsilon = 1.1 \times 10^5 \text{ M}^{-1} \text{ cm}^{-1}$ ). The SC molecules showed two-component fluorescence lifetimes ( $\tau$ ) and lower fluorescence quantum yields ( $\Phi_{\text{Fl}}$ ) than TMR before photoirradiation. Quenching probably occurred between the fluorophore and other parts of the SC molecule. Upon *E*-to-*Z* isomerization of the SC molecules, substantial changes in the length of fluorescence lifetimes were not observed, despite the decrease in  $\Phi_{\text{Fl}}$ . These results indicated that static quenching was triggered by *E*-to-*Z* isomerization, and not dynamic quenching that change in fluorescence lifetime.

I next investigated whether the fluorescence intensity of the SC molecules could be reversibly modulated by repeated photoirradiation. SC molecules were irradiated alternately at 365 and 530 nm and the fluorescence intensities were recorded each time when the isomerization process was complete (Figure 1-2-1g-i). As mentioned earlier, the first photoirradiation of SC molecules with 365 nm light decreased fluorescence intensity due to *E*-to-*Z* isomerization. Thereafter, the fluorescence intensity of SC molecules was fully recovered upon 530 nm irradiation. Moreover, the fluorescence intensity could

be switched repeatedly by photoirradiation at least 15 times. No decay of fluorescence quenching efficiency was observed after repeated cycles of photoswitching, indicating that the SC molecules had excellent reversibility between *E*- and *Z*-isomers upon 365 and 530 nm light irradiation and were resistant to photobleaching in aqueous solution.

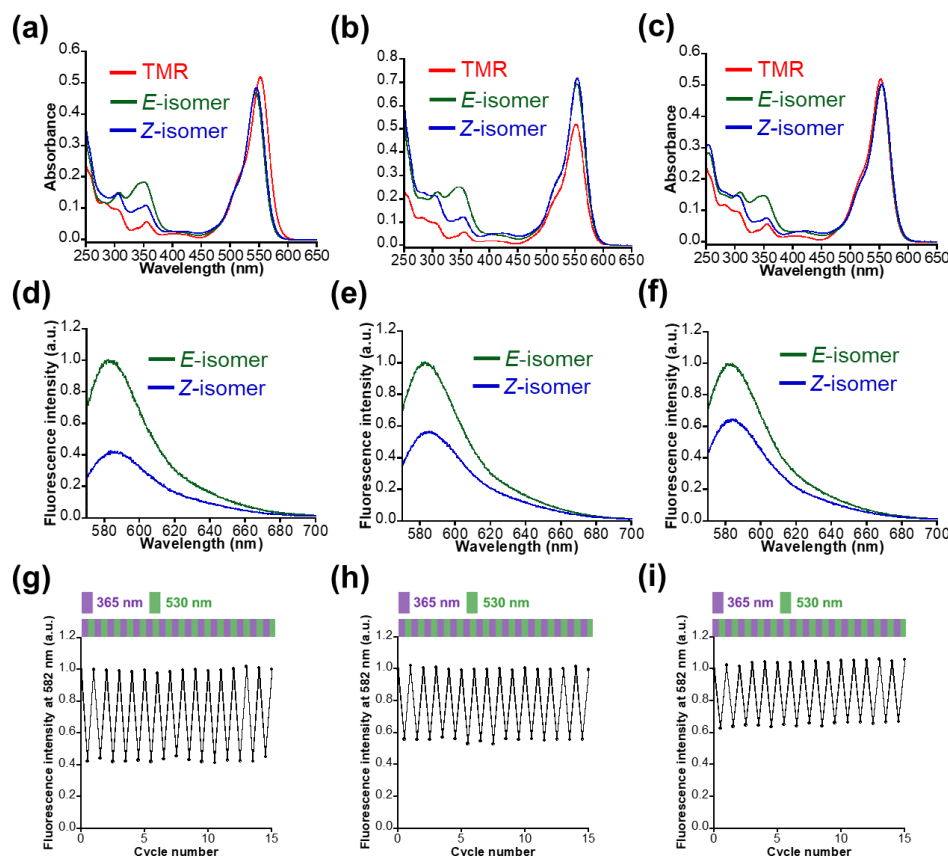


**Figure 1-2-1.** Photoswitching properties of SC molecules.

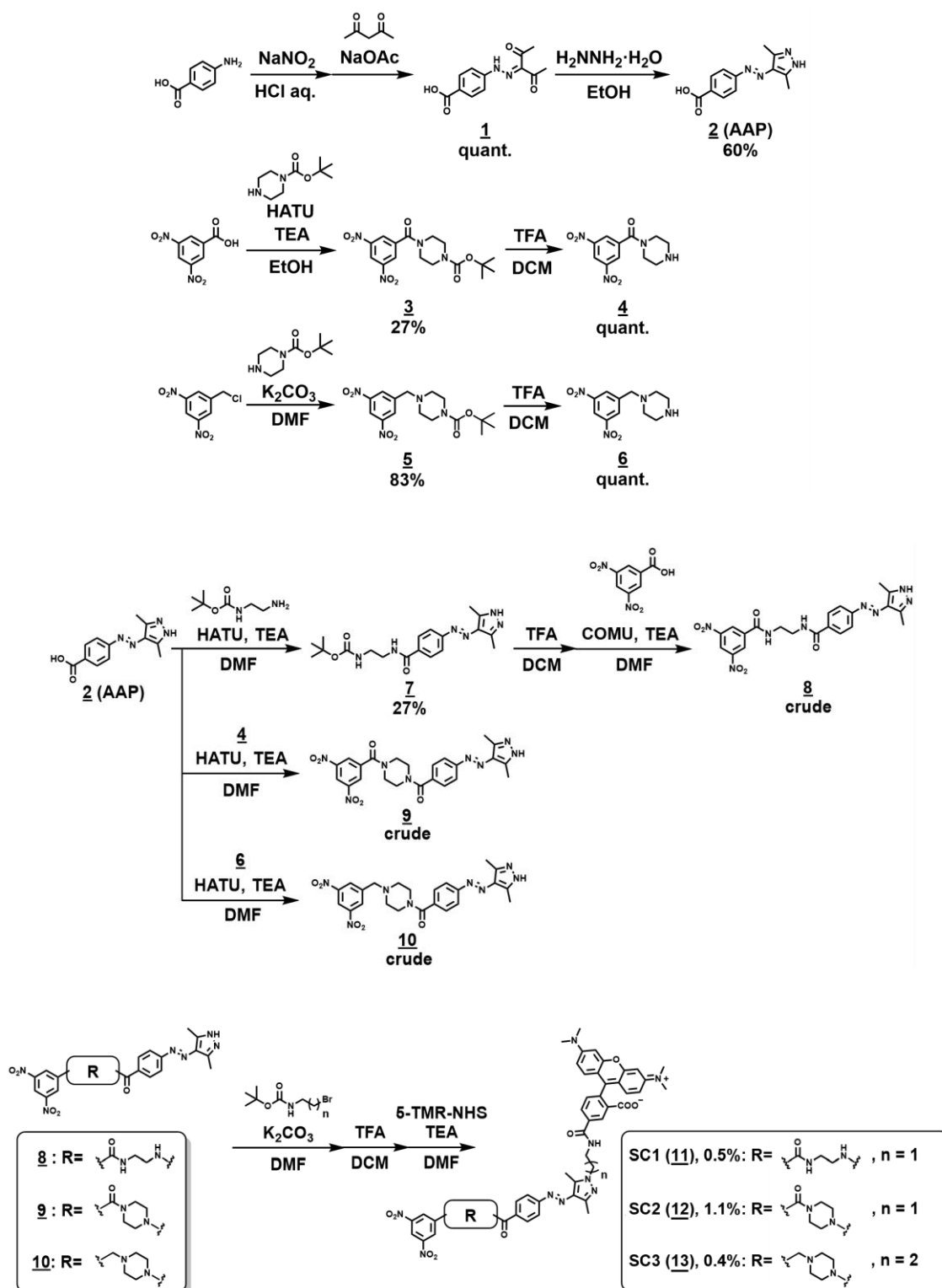
(a-c) UV-Vis absorption spectra and (d-f) fluorescence spectra (g-i) photoswitching reversibility by monitoring fluorescence intensity at 582 nm of SC molecules. (a,d,g) 5.0  $\mu\text{M}$  SC1 (15% DMSO) (b,e,h) 5.0  $\mu\text{M}$  SC2 (10% DMSO) (c,f,i) 5.0  $\mu\text{M}$  SC3 (20% DMSO) in 100 mM phosphate buffer (pH 7.4). Light intensity: 4.0  $\text{mWcm}^{-2}$  (365 nm) for 2 min. 6.2  $\text{mWcm}^{-2}$  (530 nm) for 1 min,  $\lambda_{\text{ex}} = 554 \text{ nm}$ , 25  $^{\circ}\text{C}$ . Adapted with permission from ref 48. Copyright 2020 The Chemical Society of Japan.

**Table 1-2-1.** Optical properties of SC molecules (SC1, SC2, and SC3).

		$\lambda_{\text{max abs}} [\text{nm}]/\epsilon [\text{M}^{-1}\text{cm}^{-1}]$	$\lambda_{\text{max em}} [\text{nm}]$	$\tau [\text{ns}]$	$\Phi_{\text{Fl}}$
	TMR	548/1.1 $\times 10^5$	572	2.21 <sup>*1</sup>	0.41 <sup>*1</sup>
SC1	<i>E</i> -isomer	544/9.4 $\times 10^4$	582	1.39 (70%), 2.25 (30%)	0.16
	<i>Z</i> -isomer	546/9.7 $\times 10^4$	584	1.48 (88%), 2.95 (12%)	7.6 $\times 10^{-2}$
SC2	<i>E</i> -isomer	554/1.4 $\times 10^5$	583	1.40 (75%), 2.23 (25%)	0.16
	<i>Z</i> -isomer	555/1.4 $\times 10^5$	585	1.35 (72%), 2.26 (28%)	0.10
SC3	<i>E</i> -isomer	554/1.0 $\times 10^5$	585	1.11 (51%), 2.12 (49%)	0.29
	<i>Z</i> -isomer	555/1.0 $\times 10^5$	585	1.08 (48%), 1.93 (52%)	0.19

$\tau$ , fluorescence lifetime;  $\epsilon$ , extinction coefficient;  $\Phi_{\text{Fl}}$  fluorescence quantum yield <sup>\*1</sup>; Quoted from ref <sup>33</sup>. Adapted with permission from ref 48. Copyright 2020 The Chemical Society of Japan.

## Synthetic Procedures



Scheme 1-1. Synthesis of SC molecules. Adapted with permission from ref 48. Copyright 2020 The Chemical Society of Japan.

**4-(2-(2,4-dioxopentan-3-ylidene)hydrazinyl)benzoic acid (1)**

NaNO<sub>2</sub> (1.52 g, 22.0 mmol) was dissolved in a cooled solution (0 °C) of 4-aminobenzoic acid (2.74 g, 20.0 mmol) in H<sub>2</sub>O (40 mL) and 12 M HCl aq. (6.5 mL). After stirring for 1 h at 0 °C, penta-2,4-dione (2.06 mL, 20.0 mmol) and NaOAc·3H<sub>2</sub>O (5.90 g, 70.0 mmol) in EtOH (10 mL) and H<sub>2</sub>O (100 mL) were added, forming a yellow precipitate. The suspension was stirred for 1 h at room temperature, and the precipitate was collected by filtration, washed with H<sub>2</sub>O, H<sub>2</sub>O/EtOH (1:1), and hexane. Concentration under reduced pressure and drying in vacuo afforded compound 1 as a yellow solid (5.90 g, quant.).

**<sup>1</sup>H NMR, 500 MHz, DMSO-*d*<sub>6</sub>** δ 13.69 (s, 1H), 7.98 (d, *J* = 8.5 Hz, 2H), 7.64 (d, *J* = 8.5 Hz, 2H), 2.48 (s, 3H), 2.44 (s, 3H). **<sup>13</sup>C NMR, 125 MHz, DMSO-*d*<sub>6</sub>** δ 197.81, 196.90, 167.33, 145.84, 135.34, 131.42, 127.60, 116.21, 31.72, 26.80. **HRMS (FAB+)** calculated for [M+H]<sup>+</sup> 249.0875, found 249.0871.

**(*E*)-4-((3,5-dimethyl-1H-pyrazol-4-yl)diazenyl)benzoic acid (2)**

Hydrazine monohydrate (0.552 mL, 14.2 mmol) was mixed with a solution of compound 1 (3.50 g, 14.2 mmol) in EtOH (30 mL) and refluxed for 6 h. Thereafter, concentration under reduced pressure and drying in vacuo afforded compound 2 as a yellow solid (2.07 g, 8.48 mmol, 60%).

**<sup>1</sup>H NMR, 500 MHz, DMSO-*d*<sub>6</sub>** δ 8.07 (d, *J* = 8.5 Hz, 2H), 7.79 (d, *J* = 8.5 Hz, 2H), 2.47 (s, 6H). **<sup>13</sup>C NMR, 125 MHz, DMSO-*d*<sub>6</sub>** δ 167.40, 156.04, 135.08, 131.68, 131.49, 130.95, 121.81, 113.01. **HRMS (FAB+)** calculated for [M+H]<sup>+</sup> 245.1039, found 245.1036.

***tert*-butyl 4-(3,5-dinitrobenzoyl)piperazine-1-carboxylate (3)**

HATU (4.30 g, 11.3 mmol) and TEA (2.37 mL, 17.0 mmol) were dissolved in a cooled solution (0 °C) of 3,5-dinitrobenzene (2.40 g, 11.3 mmol) in DMF (100 mL) and stirred for 1 h at 0 °C. Thereafter, *tert*-butyl piperazine-1-carboxylate (2.10 g, 11.3 mmol) was dissolved in the solution, stirred for 2 h at room temperature, and evaporated in vacuo. Subsequently, the purification of the product performed using column chromatography (hexane/AcOEt = 4/1) to afford compound 3 as a yellow solid (2.11 g, 5.55 mmol, 49%).

**<sup>1</sup>H NMR, 500 MHz, CDCl<sub>3</sub>** δ 9.12 (t, *J* = 2.0 Hz, 1H), 8.60 (d, *J* = 2.0 Hz, 2H), 3.58 (m, 8H), 1.48 (s, 9H). **<sup>13</sup>C NMR, 125 MHz, CDCl<sub>3</sub>** δ 165.47, 154.33, 148.61, 138.79, 127.50, 119.91, 80.86, 47.70, 42.56, 28.34. **MS (ESI-)** calculated for [M+HCOO]<sup>-</sup>, 425.1309, found 425.0848.

**(3,5-dinitrophenyl)(piperazin-1-yl)methanone (4)**

TFA (5 mL) was mixed with a solution of compound 3 (2.11 g, 5.55 mmol) in DCM (15 mL) and stirred for 5 h at room temperature. Thereafter, concentrating under reduced pressure and drying in vacuo afforded compound 4 as a yellow solid (3.06 g, quant.).

**<sup>1</sup>H NMR, 500 MHz, D<sub>2</sub>O** δ 9.14 (t, *J* = 2.0 Hz, 1H), 8.67 (d, *J* = 2.0 Hz, 2H), 3.98 (s, 2H), 3.69 (s, 2H), 3.37 (s, 2H), 3.23 (s, 2H). **<sup>13</sup>C NMR, 125 MHz, D<sub>2</sub>O** δ 167.74, 148.53, 136.31, 127.81, 120.90, 42.80, 42.64. **HRMS (FAB+)** calculated for [M]<sup>+</sup> 281.0880, found 281.0889.

***tert*-butyl 4-(3,5-dinitrobenzyl)piperazine-1-carboxylate (**5**)**

*tert*-Butyl piperazine-1-carboxylate (2.10 g, 11.3 mmol) and K<sub>2</sub>CO<sub>3</sub> (1.50 g, 11.3 mmol) were dissolved in a solution of 1-(chloromethyl)-3,5-dinitrobenzene (1.20 g, 5.54 mmol), diluted in CH<sub>3</sub>CN (20 mL), and stirred for 4 h at room temperature. After evaporating to dry in vacuo, the purification of the product performed using column chromatography (hexane/AcOEt = 9/1) to afford compound **5** as a yellow solid (1.68 g, 4.58 mmol, 83%).

**<sup>1</sup>H NMR, 500 MHz, CDCl<sub>3</sub>** δ 8.95 (t, *J* = 2.0 Hz, 1H), 8.56 (d, *J* = 2.0 Hz, 2H), 3.71 (s, 2H), 3.48 (t, *J* = 5.0 Hz, 4H), 2.45 (t, *J* = 5.0 Hz, 4H), 1.47 (s, 9H). **<sup>13</sup>C NMR, 125 MHz, CDCl<sub>3</sub>** δ 154.67, 148.62, 143.46, 128.69, 117.83, 79.91, 61.39, 52.95, 28.40. **HRMS (FAB+)** calculated for [M]<sup>+</sup> 366.1539, found 366.1542.

**1-(3,5-dinitrobenzyl)piperazine (**6**)**

TFA (5 mL) was mixed with a solution of compound **5** (1.32 g, 3.61 mmol) in DCM (10 mL) and stirred for 3 h at room temperature. Thereafter, concentration under reduced pressure and drying in vacuo afforded compound **6** as a pink solid (961 mg, quant.).

**<sup>1</sup>H NMR, 500 MHz, acetone-*d*<sub>6</sub>** δ 8.87 (t, *J* = 2.0 Hz, 1H), 8.73 (d, *J* = 2.0 Hz, 2H), 4.07 (s, 2H), 3.50 (t, *J* = 5.0 Hz, 4H), 3.01 (t, *J* = 5.0 Hz, 4H). **<sup>13</sup>C NMR, 125 MHz, acetone-*d*<sub>6</sub>** δ 150.50, 143.54, 131.28, 119.62, 61.50, 50.96, 45.04. **HRMS (FAB+)** calculated for [M+H]<sup>+</sup> 267.1088, found 267.1097.

***tert*-butyl (*E*)-(2-(4-((3,5-dimethyl-1H-pyrazol-4-yl)diazenyl)benzamido)ethyl)carbamate (**7**)**

HATU (4.67 g, 12.3 mmol) and TEA (2.28 mL, 19.3 mmol) were dissolved in a cooled solution (0 °C) of compound **2** (2.00 g, 8.19 mmol) in DMF (20 mL) and stirred for 1 h at 0 °C. Thereafter, *tert*-butyl (2-aminoethyl)carbamate (1.95 mL, 12.3 mmol) was mixed with the solution, stirred for 24 h at room temperature, and concentrated in vacuo. Subsequently, the purification of the product performed using column chromatography (hexane/AcOEt = 2/3) to afford compound **7** as a yellow solid (861 mg, 2.23 mmol, 27%). **<sup>1</sup>H NMR, 500 MHz, DMSO-*d*<sub>6</sub>** δ 12.93 (s, 1H), 8.55 (t, *J* = 6.0 Hz, 1H), 7.97 (d, *J* = 8.5 Hz, 2H), 7.77 (d, *J* = 8.5 Hz, 2H), 6.94 (t, *J* = 6.0 Hz, 1H), 3.31 (q, *J* = 6.0 Hz, 2H), 3.13 (q, *J* = 6.0 Hz, 2H), 2.47 (s, 6H), 1.38 (s, 9H). **<sup>13</sup>C NMR, 125 MHz, DMSO-*d*<sub>6</sub>** δ 166.24, 136.28, 154.97, 135.20, 134.94, 128.79, 121.54, 78.16, 40.40, 40.23, 40.06, 28.70. **HRMS (FAB+)** calculated for [M+H]<sup>+</sup> 387.2139, found 387.2138.

**(*E*)-N-(2-(4-((3,5-dimethyl-1H-pyrazol-4-yl)diazenyl)benzamido)ethyl)-3,5-dinitrobenzamide (**8**)**

TFA (9.5 mL) was mixed with the solution of compound **7** (412 mg, 1.04 mmol) in DCM (15 mL) and stirred for 5 h at r.t. Thereafter, it was concentrated under reduced pressure and drying in vacuo to afford BOC-protected product as a yellow solid (414 mg, quant.). COMU (608 mg, 1.42 mmol) and TEA (0.792 mL, 5.68 mmol) were dissolved in a solution of 3,5-dinitrobenzene (301 mg, 1.42 mmol) in DMF (30 mL) and stirred at 0 °C for 1 h. Thereafter, the BOC-protected product (408 mg, 1.42 mmol) was dissolved in the solution, stirred for 2 h at room temperature and the solvent was evaporated in vacuo. Subsequently, the purification of the product performed using column

chromatography (hexane/AcOEt = 2/3) to afford a crude of compound 8. The product was used without any further purification.

**(E)-(4-(4-((3,5-dimethyl-1H-pyrazol-4-yl)diazonyl)benzoyl)piperazin-1-yl)(3,5-dinitrophenyl)methanone (9)**

HATU (706 mg, 1.86 mmol) and TEA (0.518 mL, 3.72 mmol) were dissolved in a cooled solution (0 °C) of compound 2 (416 mg, 3.29 mmol) in DMF (25 mL) and stirred for 1 h at 0 °C. Thereafter, compound 4 (364 mg, 1.30 mmol) was dissolved in the solution, stirred for 8 h at room temperature, and the solvent was evaporated in vacuo. Subsequently, the purification of the product performed using column chromatography (hexane/AcOEt = 1/1) to afford compound 9 as a crude. The product was used without any further purification.

**(E)-(4-((3,5-dimethyl-1H-pyrazol-4-yl)diazonyl)phenyl)(4-(3,5-dinitrobenzyl)piperazin-1-yl)methanone (10)**

HATU (581 mg, 1.53 mmol) and TEA (0.284 mL, 2.04 mmol) were dissolved in a cooled solution (0 °C) of compound 2 (249 mg, 1.08 mmol) in DMF (25 mL) and stirred for 1 h at 0 °C. Thereafter, compound 6 (407 mg, 1.53 mmol) was dissolved in the solution, stirred for 8 h at r.t., and the solvent was evaporated in vacuo. Subsequently, the purification of the product performed using column chromatography (hexane/AcOEt = 1/1) to afford compound 10 as a crude. The product was used without any further purification.

**General synthetic procedure of SC molecules**

*tert*-butyl (2-bromoethyl)carbamate (SC1 and 2) (6.0 eq.) or *tert*-butyl (3-bromopropyl)carbamate (SC3) (6.0 eq.) and K<sub>2</sub>CO<sub>3</sub> (10 eq.) were dissolved in a solution of compound 8 (SC1), 9 (SC2), or 10 (SC3) (1.0 eq.) in DMF (1 mL) and stirred at 75-95 °C for 12-36 h. Upon the completion of the reaction, the solvent was removed, and the residue was diluted in DCM/H<sub>2</sub>O (1:1) and the aqueous layer was extracted three times with DCM. The combined organic layers were dried over anhydrous Na<sub>2</sub>SO<sub>4</sub> and the solvent was removed in vacuo. TFA (5 mL) was mixed with a solution of the crude product dissolved in DCM (15 mL), stirred for 3 h at room temperature, and concentrated in vacuo to afford a crude of BOC-deprotected product. TEA (16.9 μL, 122 μmol) and 5-TMR *N*-succinimidyl ester (1.0 eq.) were dissolved in the solution of BOC-deprotected product in DMF (1 mL), stirred for 15 h at room temperature, and concentrated in vacuo. Thereafter, the purification of the product (SC series) performed using a reversed-phase HPLC system (40-80% of 0.1% formic acid in water/acetonitrile with a linear gradient for 30 min) and detected by measuring absorbance at 550 nm. After lyophilization of the collected fraction, SC series was obtained as a deep red powder.

**SC1, (11)**

SC1 (6.7 mg, 7.2 μmol, 5 steps from compound 7, 0.5%) was obtained as a deep red powder.

**<sup>1</sup>H NMR, 500 MHz, CD<sub>3</sub>OD** δ 9.09 (t, *J* = 1.5 Hz, 1H), 9.03 (d, *J* = 1.5 Hz, 2H), 8.69 (s, 1H), 8.16 (d, *J* = 8.0 Hz, 1H), 7.92 (d, *J* = 8.5 Hz, 2H), 7.79 (d, *J* = 8.5 Hz), 7.49 (d, *J* = 8.0 Hz, 1H), 7.11 (d, *J* = 9.0 Hz, 2H), 7.02 (dd, *J* = 9.0, 2.0 Hz, 2H), 6.97 (d, *J* = 2.0 Hz, 2H), 3.88 (t, *J* = 5.5 Hz, 2H), 4.42 (t, *J* = 5.5 Hz, 2H), 3.68 (s, 4H), 3.30 (s, 12H), 2.66 (s, 3H), 2.49 (s, 3H). **<sup>13</sup>C NMR, 125 MHz, CD<sub>3</sub>OD** δ 168.62, 167.31, 164.51, 159.30, 157.64, 157.54, 155.42, 148.64,

142.55, 141.00, 137.59, 136.77, 135.97, 135.08, 134.56, 130.58, 129.70, 127.96, 127.08, 121.29, 120.52, 114.10, 113.30, 96.02, 56.07, 39.92, 39.51, 39.23, 16.03, 15.87, 15.72, 12.81, 8.53. **HRMS (FAB+)** calculated for  $[M]^+$  936.3424, found 936.3438.

### SC2, (12)

SC2 (11.4 mg, 11.9  $\mu$ mol, 4 steps from compound **4**, 1.1%) was obtained as a deep red powder.

**$^1H$  NMR, 500 MHz,  $CD_3OD$**   $\delta$  9.07 (s, 1H), 8.01 (s, 3H), 8.18 (d,  $J$  = 8.0 Hz, 1H), 7.84 (d,  $J$  = 7.0 Hz, 2H), 7.57 (s,  $J$  = 7.0 Hz, 2H), 7.51 (d,  $J$  = 8.0 Hz, 1H), 7.12 (d,  $J$  = 9.5 Hz, 2H), 7.05 (d,  $J$  = 9.5, 2.5 Hz, 2H), 6.98 (d,  $J$  = 2.5 Hz, 2H), 4.42 (t,  $J$  = 6.0 Hz, 2H), 3.88 (t,  $J$  = 6.0 Hz, 2H), 3.57 (s, 8H), 2.66 (s, 3H), 2.49 (s, 3H).  **$^{13}C$  NMR, 125 MHz,  $CD_3OD$**   $\delta$  170.85, 167.32, 166.55, 159.29, 157.65, 157.57, 154.48, 148.72, 142.51, 140.90, 138.36, 136.60, 136.00, 135.52, 135.00, 130.58, 130.53, 129.71, 127.85, 127.20, 121.60, 119.39, 114.12, 113.31, 96.03, 56.07, 39.51, 16.17, 15.87, 12.79, 8.50. **HRMS (FAB+)** calculated for  $[M]^+$  962.3580, found 962.3598.

### SC3, (13)

SC3 (6.5 mg, 6.75  $\mu$ mol, 4 steps from compound **6**, 0.4%) was obtained as a deep red powder.

**$^1H$  NMR, 500 MHz,  $CD_3OD$**   $\delta$  8.98 (t,  $J$  = 2.0 Hz, 1H), 8.74 (d,  $J$  = 1.5 Hz, 1H), 8.71 (d,  $J$  = 2.0 Hz, 2H), 8.22 (dd,  $J$  = 8.0, 2.0 Hz, 1H), 7.81 (d,  $J$  = 8.5 Hz, 2H), 7.53 (d,  $J$  = 8.5 Hz, 2H), 7.48 (d,  $J$  = 8.0 Hz, 1H), 7.09 (d,  $J$  = 9.5 Hz, 2H), 7.06 (dd,  $J$  = 9.5, 2.5 Hz, 2H), 6.97 (d,  $J$  = 2.5 Hz, 2H), 4.26 (t,  $J$  = 6.5 Hz, 2H), 4.14 (s, 2H), 3.86 (s, 4H), 3.57 (t,  $J$  = 6.5 Hz, 2H), 3.31 (s, 12H), 2.88 (s, 4H), 2.67 (s, 3H), 2.44 (s, 3H), 2.26 (m,  $J$  = 6.5 Hz, 2H).  **$^{13}C$  NMR, 125 MHz,  $CD_3OD$**   $\delta$  170.51, 166.48, 165.84, 159.25, 157.62, 157.56, 154.50, 148.73, 142.17, 140.46, 136.72, 136.04, 135.27, 134.90, 131.41, 130.82, 130.49, 129.88, 129.59, 127.84, 121.57, 118.20, 114.16, 113.27, 96.04, 59.49, 56.07, 52.08, 46.53, 39.55, 37.38, 28.70, 16.03, 15.88, 12.72, 8.50. **HRMS (FAB+)** calculated for  $[M+H]^+$  962.3944, found 962.3969.

## Experimental Sections

### Materials and Instruments

---

All chemicals were of the highest quality available and were purchased from the following four chemical suppliers: Tokyo Chemical Industries Co., Ltd. (Tokyo, Japan), Sigma-Aldrich Chemical Pvt., Ltd. (St. Louis, MO, USA), Wako Pure Chemical Corporation. (Osaka, Japan) and Funakoshi Co., Ltd. (Tokyo, Japan). All chemicals were used for syntheses without being purified. Chemical syntheses were performed according to Schemes S1-4, shown in supporting information. Analytical chromatography was carried out using 60F<sub>254</sub> silica plates (Merck Co., Inc., Kenilworth, NJ, USA) and visualized by UV light at 215 nm or 365 nm. Isolera One (Biotage Japan Ltd., Tokyo, Japan) was used for the purification of synthesized compounds. SC1, 2, and 3 were purified using a high-performance liquid chromatography (HPLC) system, equipped with an Inertsil ODS-3 column (10 mm  $\times$  250 mm, GL Sciences, Inc., Tokyo, Japan), a pump (PU-2087; JASCO Corporation, Tokyo, Japan), and a detector (MD-2010 and FP-2020; JASCO Corporation). Purity of SC1, 2, and 3 was analyzed by an HPLC system composed of an Inertsil ODS-3 column (4.6  $\times$  250 mm; GL Sciences, Inc.), a pump (PU-2080; JASCO Corporation), and a detector (MD-4010; JASCO Corporation).

During HPLC, compounds were eluted from the columns with a constant linear gradient using two solvents: water and acetonitrile, both including 0.1% formic acid. Nuclear magnetic resonance (NMR) spectra were recorded on an AVANCE 500 HD instrument (Bruker Corporation, Billerica, MA, USA) with tetramethylsilane as an internal standard, at 500 MHz for  $^1\text{H}$  NMR and at 125 MHz for  $^{13}\text{C}$  NMR. Mass spectra were obtained using the JMS-700 (JOEL Ltd., Tokyo, Japan) for fast atom bombardment or LCT-Premier XE mass spectrometer (Waters Corporation, Milford, MA, USA) for electrospray ionization. UV-Vis absorption and fluorescence spectra were measured using the V-650 (JASCO Corporation) and F4500 (Hitachi High-Tech Science Corporation, Tokyo, Japan) spectrometers, respectively. Photoirradiation experiments were conducted using home-built systems, where the light source was a xenon-lamp (MAX-302, Asahi Spectra Co., Ltd., Tokyo, Japan). Fluorescence lifetimes were recorded on the DataStation v2.4 (HORIBA Ltd, Tokyo, Japan). composed of a photon detector (TemPro-3000U-OSM1, HORIBA Ltd.) and a NanoLED source (Model: N-455, HORIBA Ltd.).

### Molecular design

---

Molecular structures were calculated using MacroModel (Schrödinger Release 2016-4: MacroModel, Schrödinger, LLC, NY, USA). These calculations were performed with OPLS3 as a force field, (solvent: water, maximum iterations: 2500, convergence threshold: 0.05). Possible structures with photoswitchable functions were obtained using torsional sampling (MCMM), (energy window for saving structures: 50 kJmol $^{-1}$ , maximum atom deviation: 0.5 Å).

### UV-Vis absorption and fluorescence measurements

---

All UV-Vis absorption and fluorescence spectra measurements were performed in 100 mM phosphate buffer (pH 7.4), including DMSO (SC1: 15%, SC2: 10%, and SC3: 20%) at 25 °C. Fluorescence measurements were conducted with excitation at 554 nm, slit width of 2.5 nm for each excitation and emission, and photomultiplier voltage at 700 V.

### Fluorescence lifetime measurements

---

Fluorescence intensity at 582 nm was measured using a light source at 454 nm. The fluorescence decay data were analyzed using the IBH DAS6 software and fitted with a sum of exponential function (Eq. 1-1), employing nonlinear least-squares deconvolution analysis.

$$I(t) = \sum_i a_i \exp\left(-\frac{t}{\tau_i}\right)$$

Equation 1-1

### Fluorescence quantum yield measurements

---

Fluorescence quantum yields of SC molecules were measured in 100 mM phosphate buffer (pH 7.4), including DMSO (20%) at 25 °C. Rhodamine B in ethanol was used as reference ( $\Phi_{\text{ref}} = 0.65^{74}$ ). Fluorescence measurements were conducted with excitation at 520 nm. Fluorescence quantum yields ( $\Phi_{\text{Fl}}$ ) were determined using Eq. 1-2:

$$\Phi_{\text{Fl}} = \Phi_{\text{ref}} \frac{A_{\text{ref}} F_{\text{s}} n_{\text{s}}^2}{A_{\text{s}} F_{\text{ref}} n_{\text{ref}}^2}$$

Equation 1-2

where  $A_s$  and  $A_{ref}$  are the absorbance at the excitation wavelength,  $F_s$  and  $F_{ref}$  are the relative sectional quadrature of fluorescence intensities, and  $n_s$  and  $n_{ref}$  are the average refractive indexes of the solvents used for the sample and reference, respectively.

#### Measurement E/Z ratio of AAP in photostationary state

---

The E/Z ratio of AAP in the photostationary state (PSS) upon irradiation at 365 nm was measured quantitatively from the integral value of the methyl group of AAP in the  $^1\text{H}$  NMR spectroscopy (Figure 1-1-1b). The ratio in the PSS upon irradiation at 530 nm was calculated from the UV-Vis absorption spectra (Figure 1-1-1c). To determine the PSS upon irradiation at 530 nm, I firstly calculated the hypothetical spectrum of AAP in 100% Z-isomer using Eq. 1-3:

$$A_Z(\lambda) = \frac{A_{365}(\lambda) - (1 - a)A_E(\lambda)}{a}$$

Equation 1-3

where  $a$  is a proportion of the Z-isomer in the PSS upon irradiation at 365 nm ( $0 \leq a \leq 1$ ), and  $A_E(\lambda)$ ,  $A_Z(\lambda)$ , and  $A_{365}(\lambda)$  are the absorbance of AAP in the E-isomer, the Z-isomer, and the PSS after irradiation at 365 nm, respectively. The ratio in the PSS upon irradiation at 530 nm was determined by Eq. 1-4:

$$b = \frac{A_{530}(\lambda) - A_Z(\lambda)}{A_E(\lambda) - A_Z(\lambda)}$$

Equation 1-4

where  $b$  is a proportion of the E-isomer in the PSS upon irradiation at 530 nm ( $0 \leq b \leq 1$ ),  $A_{530}(\lambda)$  is the absorbance of the AAP in the PSS upon irradiation at 530 nm.

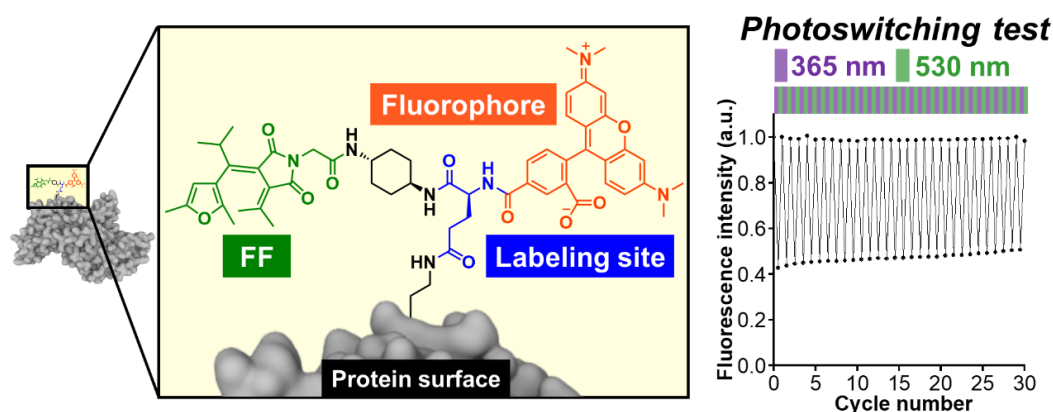
## Chapter 2. Persistent Fluorescence Switching Assisted by Protein-Surface Modification

The content of this chapter has been published in:

Torii, K.; Hori, Y.; Kikuchi, K. Persistent Fluorescence Switching of a Probe Using a Photochromic Quencher with High Photostability Assisted by Protein-Surface Modification. *Anal. Chem.* **2023**, *95* (23), 8834–8841. <https://doi.org/10.1021/acs.analchem.3c00163>.

### Abstract

Photoswitchable fluorescent molecules (PSFMs) are widely applicable in the life sciences for super-resolution imaging. Owing to the large and hydrophobic molecular structures of PSFMs that may aggregate in a biological medium, the development of synthetic PSFMs with persistent reversible photoswitching is challenging. Here, I established a protein-surface-assisted photoswitching strategy that allows for persistent reversible fluorescence photoswitching of a PSFM in an aqueous solution. As a first step, I applied the photochromic chromophore furylfulgimide (FF) as a photoswitchable fluorescence quencher and developed a Förster resonance energy transfer-based PSFM, named FF-TMR. Most importantly, the protein-surface modification strategy allows FF-TMR to exhibit persistent reversible photoswitching performance in an aqueous solution. In fixed cells, the fluorescence intensity of FF-TMR bound to anti-tubulin antibody was repetitively modulated. The protein-surface-assisted photoswitching strategy will be a useful platform to broaden the utility of functionalized synthetic chromophores enabling persistent fluorescence switching that inherits their high resistance to light irradiation.



Graphical Abstract for Chapter 2

Reprinted with permission from ref 49. Copyright 2023 American Chemical Society.

## 2-1. Molecular design and synthesis of FF-TMR

---

In Chapter 1, I have developed PSFMs, namely SC molecules to accomplish reversible fluorescence switching in aqueous solution; however, SC molecules have high hydrophobicity and require high concentrations of dimethyl sulfoxide (DMSO) to dissolve in aqueous solution making biological applications difficult. In Chapter 2, I have focused on more compact designs aiming for biological applications including intracellular imaging. For this purpose, I have newly designed a FRET-based PSFM using furylfulgimide (FF). FF exhibits photochromism in both directions between noncolored open- and colored closed-ring forms using light irradiation at two different wavelengths (365 and 530 nm). It is worth noting that closed-ring form FF has large absorption band in visible light region (around 400-700 nm) whereas open-ring form does not show absorption in this region at all (Figure 4b). Therefore, FF outperforms other photochromic compounds including AAP in the desired spectral change between two states, making it a suitable photoswitchable FRET quencher. As for the molecular design of FF, isopropyl-substituted FF was synthesized to prevent undesirable *E*-to-*Z* isomerization by increasing the bulkiness of the isopropyl group<sup>75</sup>. For preliminary testing, I confirmed that FF undergoes almost quantitative photoisomerization in an aqueous solution (Figure 4b,c, Table 2-1-1).

Here I developed a FRET-based PSFM, named FF-TMR using FF as a photochromic quencher (Figure 5). In this design principle, when FF is in an open-ring form, a donor fluorophore linked to the acceptor FF emits fluorescence without any FRET due to the absence of a spectral overlap integral between the donor and acceptor. On the other hand, photoisomerization of FF to a closed-ring form triggers FRET from the donor fluorophore to a nonfluorescent FF, resulting in fluorescence quenching. Tetramethylrhodamine (TMR) was selected as a highly water-soluble, bright, and photostable fluorophore (Figure 2-1-1a). The calculation of the overlap integral between fluorescence of TMR and absorbance of the closed-ring form of FF determined FRET distance to be 5.4 nm which is longer than the actual distance between TMR and FF, indicating sufficient FRET possibility (Figure 2-1-1b). TMR conjugated to FF through a cyclohexyl linker with a glutamic acid residue, which is used for bioconjugation. The rigid cyclohexyl group was expected to prevent fluorescence quenching caused by intramolecular interactions between FF and TMR. The energy-minimized 3D structure of FF-TMR in aqueous solution was confirmed by MacroModel simulation, which indicated that no intramolecular interaction, such as  $\pi$ - $\pi$  stacking, occurs between FF and TMR in either the open or closed-ring forms of FF (Figure 2-1-1c). FF-TMR allows for a more compact molecular design using FF as a photochromic FRET quencher than SC molecules containing three compartments (AAP, TMR, and DNB), and will improve water solubility and biological applicability. In accordance with the molecular design, I synthesized FF-TMR, whose synthetic procedures and characterization are described in the Experimental Sections and Scheme 2-1 and 2-2.

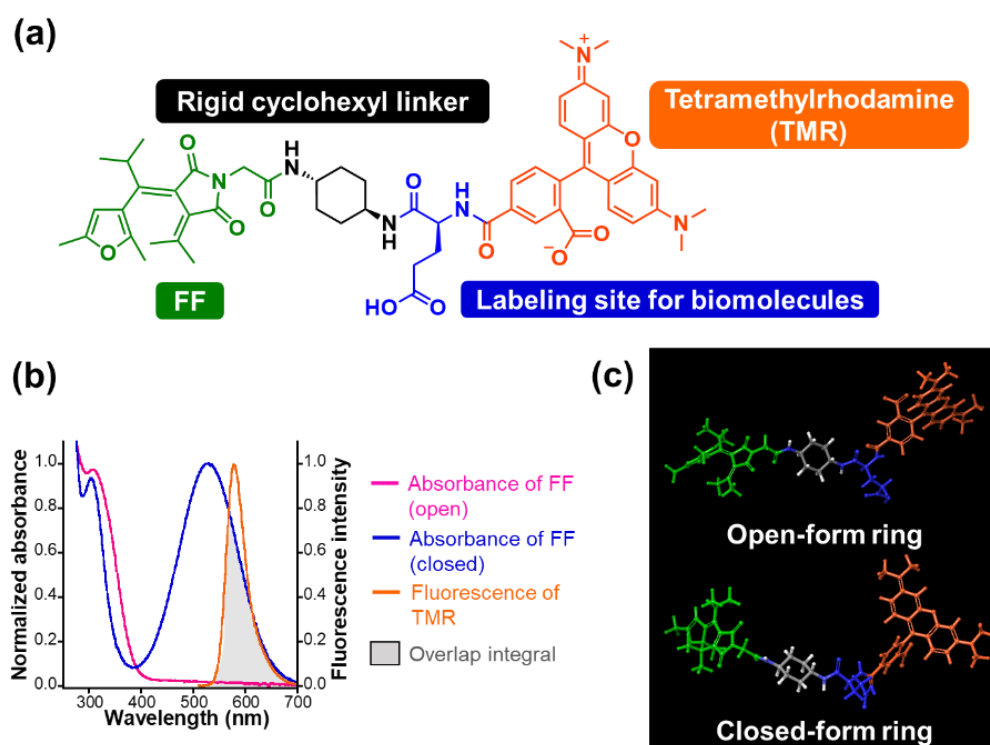


**Figure 2-1-1. Molecular design of FF-TMR.**

(a) Chemical structure of FF-TMR. (b) Absorption spectra of FF (50 μM) and fluorescence spectra of TMR (250 nM) in 100 mM phosphate buffer (pH 7.4). The area marked by gray shadow represents overlap integral of absorption of FF (closed-ring form) and fluorescence of TMR.  $\lambda_{ex}$ : 550 nm. (c) Energy-minimized structures of FF-TMR using MacroModel calculation. The green, blue, and orange parts show the FF, glutamic acid moiety, and TMR, respectively. Adapted with permission from ref 49. Copyright 2023 American Chemical Society.

**Table 2-1-1. Optical properties of FF.**

	Phosphate buffer (pH 7.4)	Ethanol
$\lambda_{max,c}$ [nm]/ $\epsilon_{max,c}$ [ $M^{-1}cm^{-1}$ ]	529/6.1 $\times 10^3$	497/6.4 $\times 10^3$
$k_{oc}/I_{irr}$ [ $s^{-1}/mW$ ]	6.44 $\times 10^{-3}$	2.78 $\times 10^{-3}$
$k_{co}/I_{irr}$ [ $s^{-1}/mW$ ]	5.72 $\times 10^{-5}$	8.54 $\times 10^{-4}$
$\Phi_{oc}$	7.2 $\times 10^{-1}$	4.9 $\times 10^{-1}$
$\Phi_{co}$	3.5 $\times 10^{-3}$	6.1 $\times 10^{-2}$
PSS [O]/[C]*	365 nm	1/99
	530 nm	>99/<1

\*PSS: photostationary state, [O]/[C] is the concentration ratio of closed/open-ring form under the PSS. Reprinted with permission from ref 49. Copyright 2023 American Chemical Society.

## 2-2. Photoswitching properties of FF-TMR

As a first step to confirm the photoswitching of FF-TMR, I investigated whether its fluorescence spectrum changes upon light irradiation. The fluorescence intensity of FF-TMR in 100 mM phosphate

buffer (pH 7.4) including 0.5% DMSO decreased by almost 80% after 365 nm irradiation, and then completely recovered after 530 nm irradiation (Figure 2-2-1a,b). To assess the repeatability of the photoswitching, FF-TMR was alternately irradiated with 365 nm and 530 nm light (Figure 2-2-1c). Opposite changes in the fluorescence intensity of FF-TMR were observed in response to light irradiation; however, the reduction in the intensity after 365 nm irradiation was gradually suppressed as the cycle number increased. I next evaluated the photoswitching properties of FF-TMR in ethanol. The fluorescence intensity of FF-TMR decreased after 365 nm irradiation, and then completely recovered after 530 nm irradiation (Figure 2-2-1d,e). Interestingly, in contrast to the result obtained using phosphate buffer, FF-TMR in ethanol showed persistent reversibility even after repeated cycles of photoswitching (Figure 2-2-1f). The number of switching cycles until the fluorescence quenching effect was attenuated by half of the initial signal reduction was measured to evaluate the photofatigue progression in each solvent. As a result, FF-TMR in phosphate buffer underwent 43 cycles, on the other hand, the FF-TMR in ethanol showed 675 cycles until half attenuation (Figure 2-2-2).

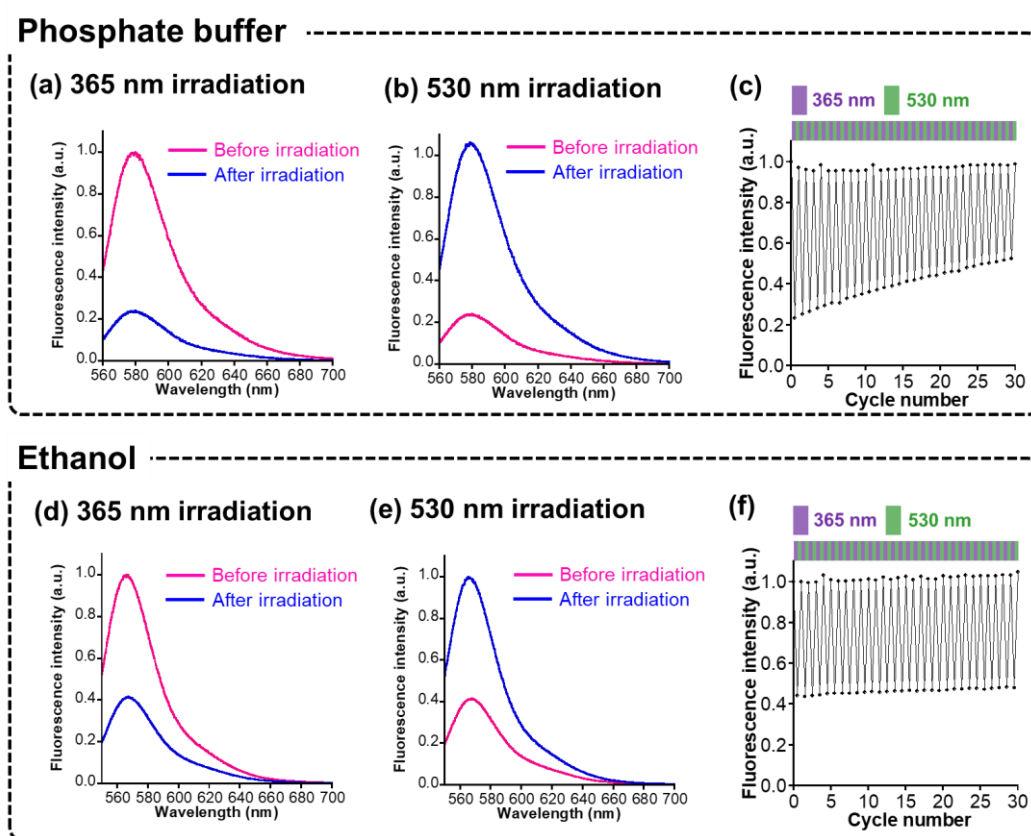


**Figure 2-2-1. Photoswitching properties of FF-TMR.**

(a,b,d,e) Fluorescence spectra and (c,f) photoswitching reversibility of 250 nM FF-TMR dissolved in (a-c) 100 mM phosphate buffer (pH 7.4) and (d-f) ethanol, including 0.5% DMSO upon (a,d) 365 nm and (b,e) 530 nm irradiation. (a,b,d,e) Spectra before and after irradiation are depicted by the magenta and blue lines, respectively. (c,f) The fluorescence intensity of FF-TMR at (c) 580 nm or (f) 570 nm was measured after alternate irradiation at 365 nm and

530 nm. Light irradiation at 365 and 530 nm is indicated by the purple and green shades, respectively. Temperature: 25 °C. Adapted with permission from ref 49. Copyright 2023 American Chemical Society.

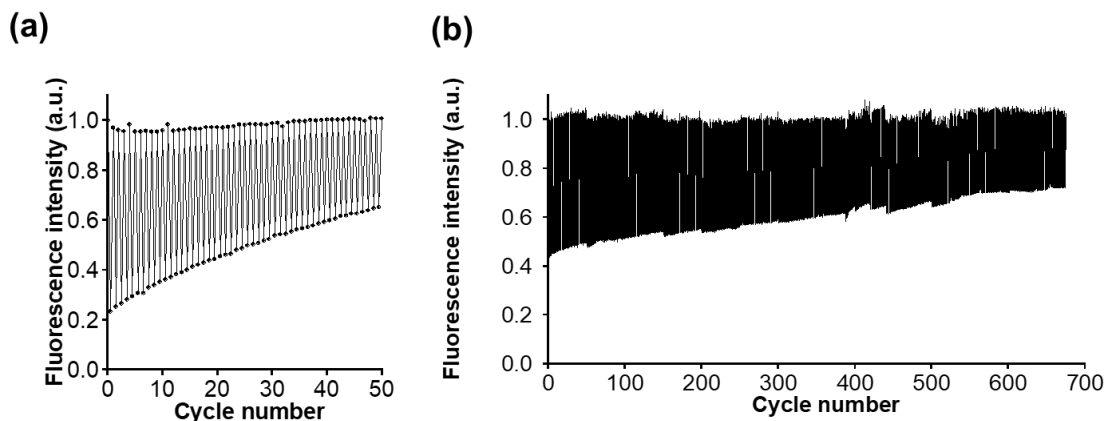


**Figure 2-2-2. Photoswitching reversibility of FF-TMR.**

FF-TMR (250 nM) dissolved in (a) 100 mM phosphate buffer (pH 7.4) and (b) ethanol including 1% DMSO. The fluorescence intensities of FF-TMR (a) at 580 nm (b) at 570 nm were measured after alternate irradiation at 365 nm and 530 nm. Temperature: 25 °C. The photoswitching durability was determined by the number of photoswitching cycles ( $N$ ) until the half-photobleaching occurs compared to the initial fluorescence contrast.  $N = 43$  obtained in 100 mM phosphate buffer, and  $N = 675$  obtained in ethanol. Adapted with permission from ref 49. Copyright 2023 American Chemical Society.

The absorption spectra and fluorescence quantum yield of FF-TMR in phosphate buffer and ethanol were also measured (Figure 2-2-3, Table 2-2-1). In both solvents, no noticeable change in the absorption spectra was detected between the open- and closed-ring forms. Because the maximum molar extinction coefficient of the ring-closed FF (about  $6 \times 10^3 \text{ M}^{-1}\text{cm}^{-1}$ ) is much smaller than that of TMR (about  $7 \times 10^4 \text{ M}^{-1}\text{cm}^{-1}$ ), the overall spectra change little upon light irradiation. Therefore, the change in fluorescence intensity depend on the change in the fluorescence quantum yield of FF-TMR in its photochromic reactions.

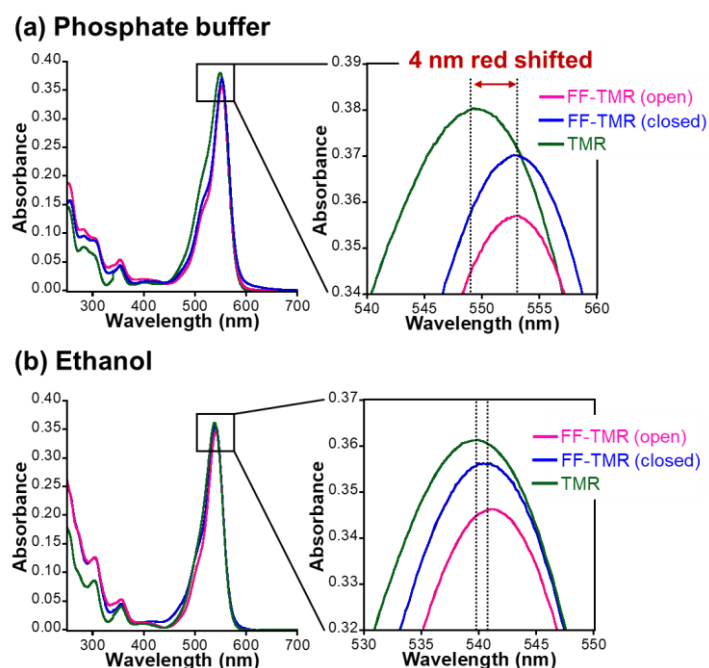


**Figure 2-2-3. Absorption spectra of FF-TMR and TMR.**

FF-TMR (5  $\mu\text{M}$ ) or TMR (5  $\mu\text{M}$ ) were dissolved in (a) 100 mM phosphate buffer (pH 7.4) and (b) ethanol including 1% DMSO. Closed-ring form of FF-TMR was obtained by irradiation at 365 nm. The enlarged spectra of the area surrounding lines are also shown in this Figure. The spectra before and after irradiation are the magenta and blue lines, respectively. Spectra of TMR are shown by the green line. Temperature: 25  $^{\circ}\text{C}$ . Adapted with permission from ref 49. Copyright 2023 American Chemical Society.

To gain insight into the difference in the photoswitching reversibility of FF-TMR between phosphate buffer and ethanol, the photoreaction of FF-TMR was quantitatively analyzed using high-performance liquid chromatography (HPLC) (Figure 2-2-4,5). The HPLC analysis revealed that irradiation of FF-TMR at 365 nm produced a ring-closed isomer, while irradiation of FF-TMR at 530 nm produced the ring-opened isomer in both phosphate buffer and ethanol (Figure 2-2-4). In phosphate buffer, however, several peaks other than that derived from the ring-opening products were observed at a retention time of 7-10 min (marked red star in Figure 2-2-4b) after 530 nm irradiation, indicating the occurrence of some undesirable side reactions. In a more detailed HPLC analysis, after continuous irradiation at 530 nm for 30 minutes, only 34% of the open-ring form of FF-TMR remained in the phosphate buffer, whereas 84% remained in ethanol (Figure 2-2-5). These results indicate that undesirable side reactions proceeded more slowly in ethanol than in phosphate buffer upon 530 nm irradiation.

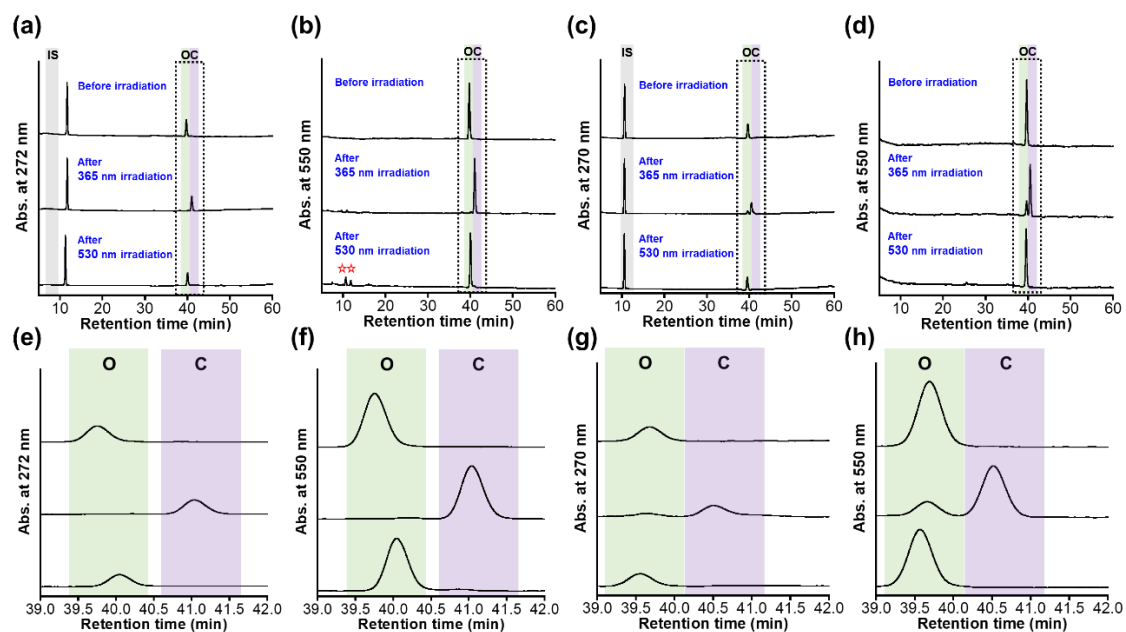


**Figure 2-2.4. Photoreaction tracking of FF-TMR using HPLC.**

FF-TMR ( $5 \mu\text{M}$ ) was dissolved in (a, b) 100 mM phosphate buffer (pH 7.4) and (c, d) ethanol containing  $500 \mu\text{M}$  benzoic acid as an internal standard and 1% DMSO, irradiated, and analyzed using HPLC. Open- and closed-ring forms of FF-TMR were irradiated at 365 nm (2 mW for 5 min) and 530 nm (4 mW for 10 min), respectively. The closed-ring form of FF-TMR was obtained by irradiation at 365 nm for 5 min.  $\lambda_{\text{abs}}$ : (a) 272 nm, (c) 270 nm, (b, d) 550 nm. (e-h) The enlarged spectra of the area are surrounded by the dot lines of (a-d). IS: internal standard (gray), O: open-ring form (green), C: closed-ring form (purple). The red stars represent peaks derived from undesirable side reactions. Adapted with permission from ref 49. Copyright 2023 American Chemical Society.

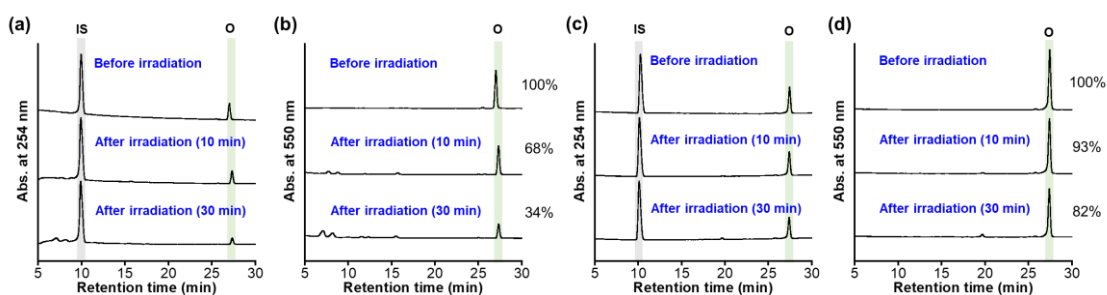


**Figure 2-2.5. Photodurability analysis of FF-TMR using HPLC.**

FF-TMR ( $5 \mu\text{M}$ ) was dissolved in (a, b) 100 mM phosphate buffer (pH 7.4) and (c, d) ethanol including  $500 \mu\text{M}$  benzoic acid as an internal standard and 1% DMSO, irradiated, and analyzed using HPLC. The open-ring form of FF-TMR was irradiated at 530 nm (4 mW) for 10 and 30 min. The percentage shows the ratio of the amount of ring-opening form before and after irradiation.  $\lambda_{\text{abs}}$ : (a, c) 254 nm, and (b, d) 530 nm. IS: internal standard (gray); O: open-ring form (green). Adapted with permission from ref 49. Copyright 2023 American Chemical Society.

Table 2-2-1. Optical properties of FF-TMR and FF-TMR-BSA.

Solvent		Phosphate buffer	Ethanol	Bioconjugate (FF-TMR-BSA)
$\lambda_{\text{ex,max}}$ [nm]/ $\epsilon_{\text{max}}$ [M <sup>-1</sup> cm <sup>-1</sup> ]	O* <sup>1</sup>	553/7.1×10 <sup>4</sup>	541/6.9×10 <sup>4</sup>	557/7.1×10 <sup>4</sup> * <sup>2</sup>
	C* <sup>1</sup>	553/7.4×10 <sup>4</sup>	541/7.1×10 <sup>4</sup>	557/7.4×10 <sup>4</sup> * <sup>2</sup>
$\Phi_{\text{FL}}$	O	3.7×10 <sup>-1</sup>	9.4×10 <sup>-1</sup>	1.3×10 <sup>-1</sup>
	C	9.0×10 <sup>-2</sup>	3.8×10 <sup>-1</sup>	5.2×10 <sup>-2</sup>
$k_{\text{oc}}/I_{\text{irr}}$ [s <sup>-1</sup> /mW]		4.33×10 <sup>-3</sup>	2.71×10 <sup>-3</sup>	2.88×10 <sup>-3</sup>
$k_{\text{co}}/I_{\text{irr}}$ [s <sup>-1</sup> /mW]		6.97×10 <sup>-4</sup>	6.92×10 <sup>-3</sup>	2.04×10 <sup>-3</sup>
$\Phi_{\text{OC}}$		2.2×10 <sup>-2</sup>	6.4×10 <sup>-3</sup>	1.5×10 <sup>-2</sup> * <sup>3</sup>
$\Phi_{\text{CO}}$		1.3×10 <sup>-4</sup>	6.4×10 <sup>-4</sup>	2.8×10 <sup>-4</sup> * <sup>3</sup>
PSS	365 nm	6/94	22/78	n.a.
[O]/[C]* <sup>4</sup>	530 nm	n.a.* <sup>5</sup>	>99/<1	n.a.

\*<sup>1</sup>O: open-ring form, C: closed-ring form obtained by irradiation at 365 nm for 300 s. \*<sup>2</sup>The molar extinction coefficient of FF-TMR-BSA was approximated by using the coefficient value of FF-TMR, since the absorbance was not changed so significantly after conjugation and ununiform numbers of FF-TMR conjugated to individual BSA proteins prevented determination of the precise value of the coefficient. \*<sup>3</sup>The quantum yield of FF-TMR-BSA was determined by using the coefficient value of FF-TMR in place of FF-TMR-BSA for the reason mentioned above. \*<sup>4</sup>PSS: photostationary state, [O]/[C] is the concentration ratio of closed/open-ring form under the PSS (Figure 2-2-4). \*<sup>5</sup>The value is not determined owing to competing for undesired photoreactions. Adapted with permission from ref 49. Copyright 2023 American Chemical Society.

To investigate the relationship between photostability and the photoswitching rates of FF-TMR, I next measured the kinetics of FF-TMR in both solvents (phosphate buffer vs. ethanol). Both the fluorescent turn-off and -on rates followed first-order kinetics (Figure 2-2-6a,b). I investigated the dependency of photoswitching kinetics and irradiated light intensities, revealing linear relationships between kinetic constants  $k$  [s<sup>-1</sup>] and irradiated light intensities  $I_{\text{irr}}$  [mW] (Figure 2-2-6c,d). The results provide slopes  $k/I_{\text{irr}}$  [s<sup>-1</sup>/mW], which are independent values of irradiated light intensities and can be compared among the different experiments. The turn-off rate per irradiated light intensity ( $k_{\text{off}}/I_{\text{irr}}$ ) was not substantially different between the two solvents, whereas the turn-on rate per irradiated light intensity in ethanol was about 10 times faster than that in phosphate buffer ( $k_{\text{on}}/I_{\text{irr}}$ : 6.97 × 10<sup>-4</sup> s<sup>-1</sup>/mW in phosphate buffer vs. 6.92 × 10<sup>-3</sup> s<sup>-1</sup>/mW in ethanol) (Table 2-2-1). In addition, the ring-opening rate of FF in ethanol was about 15 times faster than in phosphate buffer ( $k_{\text{oc}}/I_{\text{irr}}$ : 5.72 × 10<sup>-4</sup> s<sup>-1</sup>/mW in phosphate buffer vs. 8.54 × 10<sup>-3</sup> s<sup>-1</sup>/mW in ethanol) (Table 2-2-1). The quantum yields of the ring-opening reactions of FF ( $\Phi_{\text{co}}$ ) were determined 7-fold higher values in ethanol than in phosphate buffer (6.1 × 10<sup>-2</sup> in phosphate buffer vs. 4.9 × 10<sup>-1</sup> in ethanol) (Table 2-1-1). It was previously reported that the low  $\Phi_{\text{CO}}$  was due to interactions between the excited state of fulgimide and the solvent<sup>76</sup>. This interaction can be strengthened in polar solvents, increasing the activation energy for the ring-opening reaction and accordingly decreasing the transformation efficiency. Therefore, FF has a lower  $\Phi_{\text{CO}}$  in phosphate buffer, with higher polarity than ethanol. In this context, it is reasonable to assume that FF-

TMR has a higher  $\phi_{CO}$  in ethanol than in phosphate buffer so that the fluorescence turn-on kinetics is faster in ethanol than in phosphate buffer, as shown in Figure 2-2-6b,d, and Table 2-2-1. In addition, because FF itself shows reversible and quantitative photoisomerization in phosphate buffer, the photoreaction kinetics are not considered to affect the photostability of FF-TMR, and another factor must affect photostability depending on the solvents.

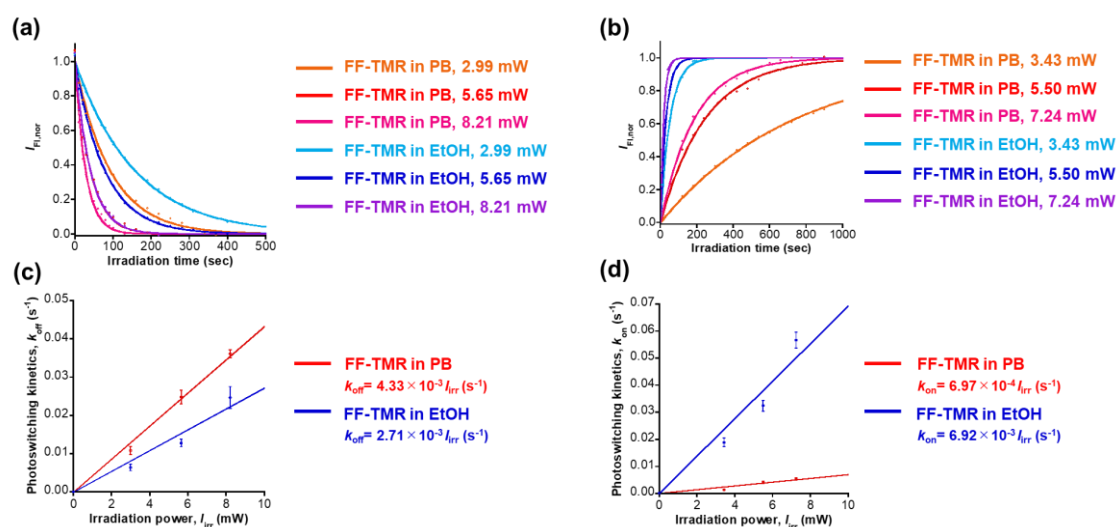


**Figure 2-2-6. Photoswitching rates of FF-TMR.**

(a,b) Time course of fluorescence intensities ( $I_{Fl,nor}$ ) upon (a) 365 nm (2.99, 5.65, and 8.21 mW) and (b) 530 nm (3.43, 5.50, and 7.24 mW) irradiation. (c,d) Linear relationship between photoswitching kinetics of (c) fluorescence turn-off ( $k_{off}$ ) or (d) turn-on ( $k_{on}$ ) and irradiated light intensities ( $I_{irr}$ ) at (c) 365 nm or (d) 530 nm. Red and blue lines show FF-TMR in 100 mM phosphate buffer (pH 7.4) and ethanol, respectively. Temperature: 25 °C.  $\lambda_{ex}$  = 550 nm (in PB),  $\lambda_{ex}$  = 540 nm (in EtOH). PB: 100 mM phosphate buffer (pH 7.4), EtOH: ethanol. Adapted with permission from ref 49. Copyright 2023 American Chemical Society.

To evaluate the intra- or intermolecular interactions of FF-TMR, I compared the absorption spectra of FF-TMR and TMR itself. In absorption measurements, the maximum absorption wavelength of FF-TMR is red-shifted compared with that of TMR in phosphate buffer (553 nm for FF-TMR vs. 549 nm for TMR) (Figure 2-2-3), indicating that the hydrophobic intra- or intermolecular aggregation of FF-TMR occurs in phosphate buffer<sup>77,78</sup>. To evaluate the hydrophobicity of FF-TMR, the LogP of TMR and FF-TMR were measured respectively. The LogP is defined as the partition coefficient between water and *n*-octanol, with higher values indicating a greater degree of hydrophobicity. The logP of FF-TMR is higher than that of TMR (1.08 vs -0.75). It indicates that FF-TMR shows more hydrophobicity than TMR, and FF-TMR can easily form aggregates compared to TMR in aqueous solution, resulting in red-shifted absorption of FF-TMR (Figure 2-2-3). According to the calculated 3D structure of FF-TMR, it is unlikely that the FF and TMR moieties have intramolecular interactions due to the

molecular rigidity of FF-TMR; therefore, the intermolecular interactions may be more favorable than the intramolecular interactions (Figure 2-1-1c). On the other hand, the redshift of FF-TMR was negligible in ethanol, indicating that the intermolecular interactions are reduced in ethanol (Figure 2-2-3). These analyses suggest that intermolecular aggregation might be responsible for the irreversible photoreactions of FF-TMR in phosphate buffer, while such interactions are significantly suppressed in ethanol, resulting in reversible photoswitching. As a supplementary experiment, the fluorescence reversibility test of FF-TMR was performed with different concentrations (250 nM, 2.5  $\mu$ M, and 25  $\mu$ M) in phosphate buffer and ethanol, respectively (Figure 2-2-7). As a result, the quenching effect of the fulgimide moiety was more rapidly lost in higher concentration of FF-TMR in phosphate buffer during the repeated photocycles of FF-TMR, clearly demonstrating that higher concentrations cause promotion of the photo fatigue of the fulgimide moiety. On the other hand, in ethanol, only subtle effect of photofatigue was observed even when the concentration of FF-TMR was increased. In general, intermolecular aggregation of hydrophobic compounds in higher concentrations is more easily induced in an aqueous solution rather than ethanol. Thus, the concentration-dependency in phosphate buffer strongly indicates that intermolecular aggregation causes the facilitation of photo fatigue process. In addition, the absorption spectra do not change upon irradiation at 530 nm (Figure 2-2-8), suggesting that these undesirable photoreactions cause photo fatigue in the FF moiety rather than the TMR moiety. As a result, FF-TMR at 530 nm irradiation maintains its fluorescence intensity even upon repeated light irradiation (Figure 2-2-1c,f). The detailed mechanism is currently under investigation. As a solution to this problem, I expected that conjugation of FF-TMR with a biomolecule would suppress intermolecular interactions among FF-TMRs, thereby improving the photoswitching repeatability.

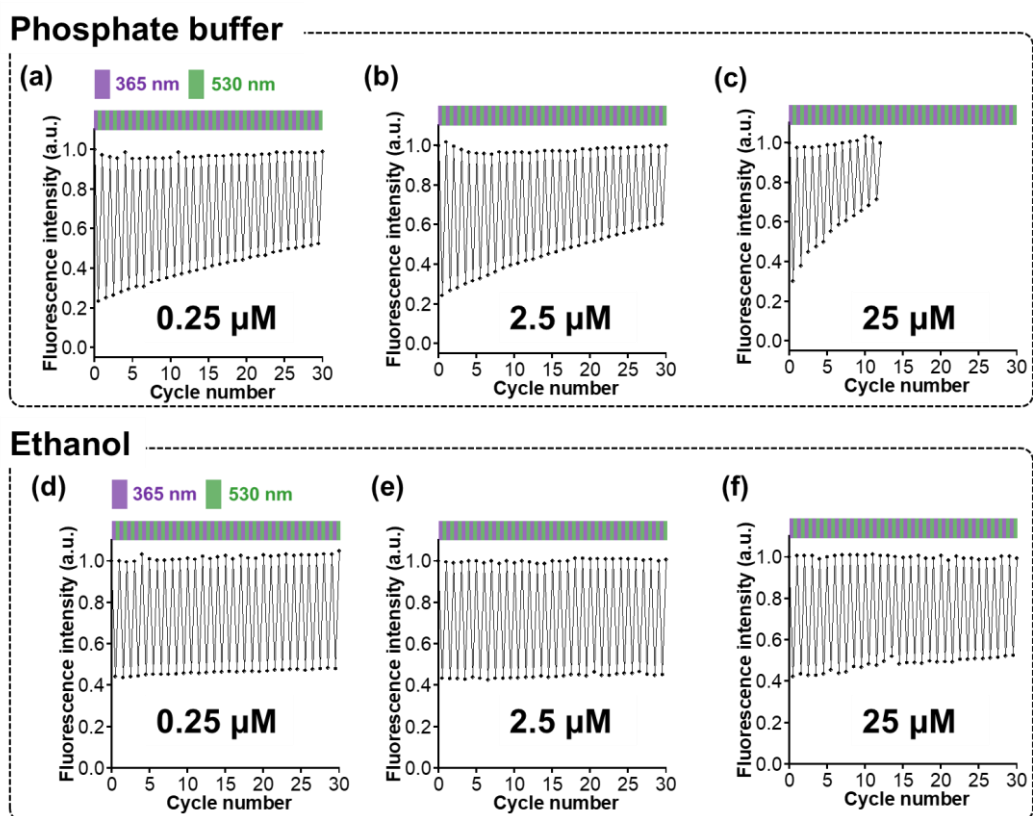


**Figure 2-2-7. Photoswitching reversibility of FF-TMR with different concentrations.**

FF-TMR ((a,d): 250 nM, ((b,e): 2.5  $\mu$ M, and (c,f): 25  $\mu$ M) dissolved in (a-c) 100 mM phosphate buffer (pH 7.4) and (d-f) ethanol including 1% DMSO. The fluorescence intensities of FF-TMR (a-c) at 580 nm (d-f) at 570 nm were measured after alternate irradiation at 365 nm and 530 nm. Adapted with permission from ref 49. Copyright 2023 American Chemical Society.

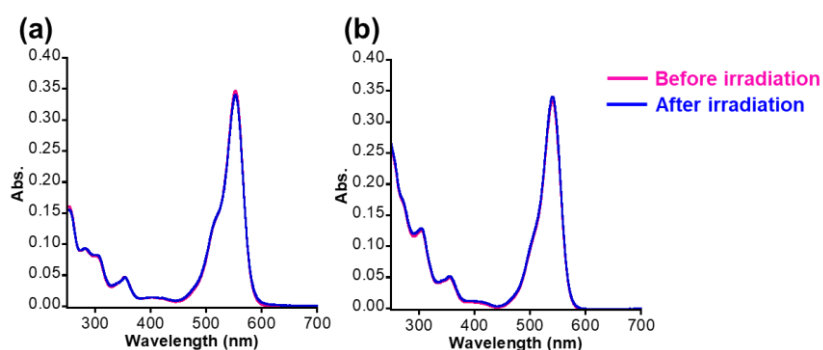


**Figure 2-2-8. Absorption spectra of FF-TMR after 530 nm irradiation.**

FF-TMR (5  $\mu$ M) or TMR (5  $\mu$ M) dissolved in (a) 100 mM phosphate buffer (pH 7.4) and (b) ethanol (in 1% DMSO) upon 530 nm (4 mW, 30 min) irradiation. The spectra before and after irradiation are shown by the magenta and blue lines, respectively. Temperature: 25  $^{\circ}$ C. Adapted with permission from ref 49. Copyright 2023 American Chemical Society.

### 2-3. Protein-surface-assisted photoswitching strategy using FF-TMR

I prepared a bioconjugate of FF-TMR with bovine serum albumin (BSA), named FF-TMR-BSA, as described in the Experimental Sections and examined its photoswitching performance in an aqueous solution. The purity of FF-TMR-BSA was demonstrated by SDS-PAGE analysis. (Figure 2-3-1a). As shown in Figure 2-3-1b and c, I confirmed that the fluorescence intensity of FF-TMR-BSA decreased upon 365 nm irradiation, and fully recovered upon 530 nm irradiation. As expected, FF-TMR-BSA showed persistent reversible photoswitching after repeated cycles of light irradiation even in phosphate buffer (Figure 2-3-1d). The number of switching cycles of FF-TMR-BSA until the fluorescence quenching effect was attenuated by half of the initial signal reduction was measured. FF-TMR-BSA in phosphate buffer showed increase in the cycle number to 222, which is more than 5 times larger compared to that of FF-TMR in phosphate buffer. This result supports that FF-TMR improves photostability by modification on protein-surface (Figure 2-3-2).

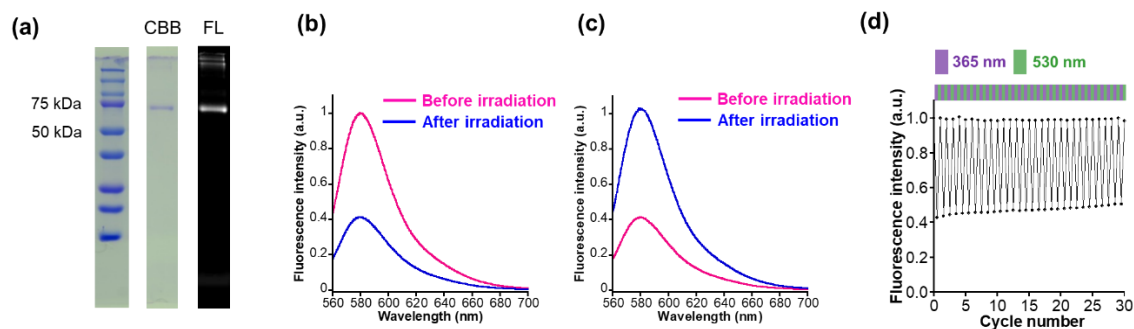


**Figure 2-3-1. Characterization and photoswitching property of FF-TMR-BSA.**

(a) The results of SDS-PAGE of FF-TMR-BSA. The left and right image shows CBB-stained and fluorescence images, respectively. The first column at the left represents a ladder to confirm protein size (BSA: 66.5 kDa). Fluorescence images were obtained with excitation at 525 nm. (b,c) Fluorescence spectra and (d) photoswitching reversibility of 250 nM FF-TMR-BSA dissolved in 100 mM phosphate buffer (pH 7.4) upon (b) 365 nm and (c) 530 nm irradiation. (b,c) Spectra before and after irradiation are depicted by the magenta and blue lines, respectively. (d) The fluorescence intensity of FF-TMR at 580 nm was measured after alternate irradiation at 365 nm and 530 nm. Light irradiation at 365 nm and 530 nm is indicated by the purple and green shades, respectively. Temperature: 25 °C. Adapted with permission from ref 49. Copyright 2023 American Chemical Society.

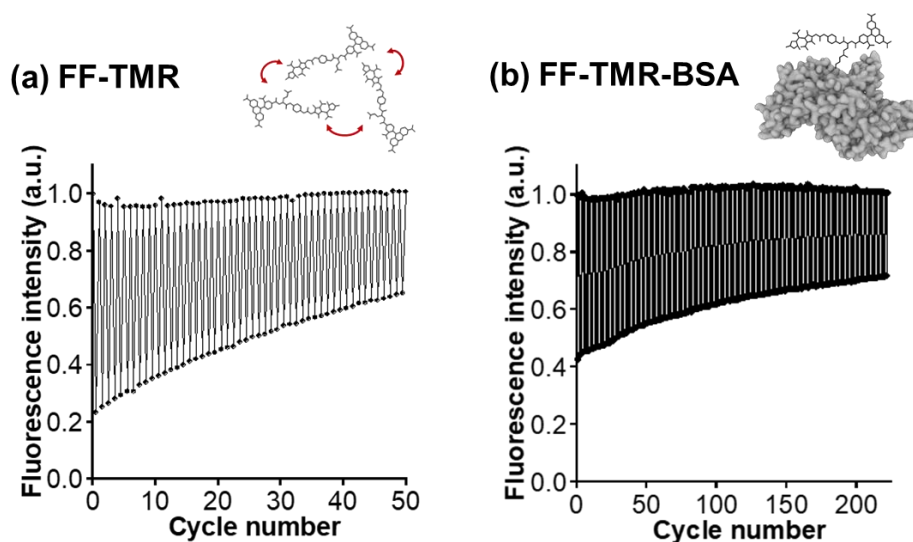


**Figure 2-3-2. Photoswitching reversibility of FF-TMR-BSA.**

(a) FF-TMR (250 nM) and (b) FF-TMR-BSA (250 nM) dissolved in 100 mM phosphate buffer (pH 7.4) including 1% DMSO. The fluorescence intensities at 580 nm were measured after alternate irradiation at 365 nm and 530 nm. (a) is a replication of Figure 2-2-2a. The number of switching cycles ( $N$ ) of FF-TMR-BSA, in which the fluorescence quenching effect was attenuated by half of the initial signal reduction is  $N = 222$ . Adapted with permission from ref 49. Copyright 2023 American Chemical Society.

In addition, I also measured the photoswitching rates of FF-TMR-BSA in phosphate buffer. The photoswitching rates in both directions of FF-TMR-BSA followed first-order kinetics, as seen in FF-TMR (Figure 2-3-3a,b). There was no large difference in fluorescence turn-off kinetics per irradiated light intensity ( $k_{\text{off}}/I_{\text{irr}}$ ) between FF-TMR-BSA and FF-TMR in phosphate buffer, whereas the fluorescence turn-on rate per irradiated light intensity ( $k_{\text{on}}/I_{\text{irr}}$ ) of FF-TMR-BSA was 3 times faster than that of FF-TMR ( $2.04 \times 10^{-3} \text{ s}^{-1}/\text{mW}$  for FF-TMR-BSA vs.  $6.97 \times 10^{-4} \text{ s}^{-1}/\text{mW}$  for FF-TMR) (Figure 2-3-3c,d, Table 2-2-1). It is an intermediate value between those of FF-TMR in phosphate buffer and ethanol, suggesting that the FF-TMR binding site of BSA is less polar than that of phosphate buffer. Taken together, the protein-surface-assisted photoswitching strategy was shown to be useful to create a PSFM with FF-TMR that shows durable reversible and fast photoswitching in an aqueous buffer as in ethanol, which provides an aggregation-free environment.

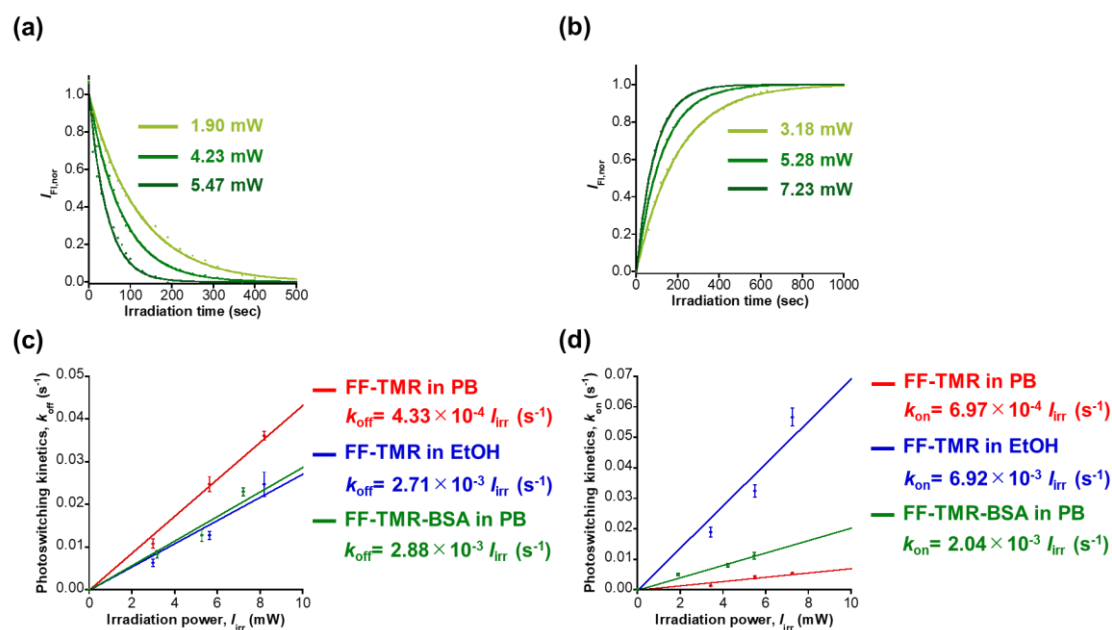


**Figure 2-3-3. Photoswitching rates of FF-TMR-BSA.**

(a,b) Time course of fluorescence intensities ( $I_{Fl,nor}$ ) upon (a) 365 nm (1.90, 4.27, and 5.47 mW) and (b) 530 nm (3.18, 5.28, and 7.23 mW) irradiation. (c,d) Linear relationship between photoswitching kinetics of (c) fluorescence turn-off ( $k_{off}$ ) or (d) turn-on ( $k_{on}$ ) and irradiated light intensities ( $I_{irr}$ ) at (c) 365 nm or (d) 530 nm. Red and blue lines show FF-TMR in PB and EtOH, respectively. The green line shows FF-TMR-BSA in PB. Temperature: 25 °C.  $\lambda_{ex} = 550$  nm (in PB),  $\lambda_{ex} = 540$  nm (in EtOH). PB: 100 mM phosphate buffer (pH 7.4), EtOH: ethanol. Adapted with permission from ref 49. Copyright 2023 American Chemical Society.

## 2-4. Fluorescence imaging in fixed cells

The protein-surface-assisted strategy has been applied to an antibody for fluorescence imaging of cellular molecules. I prepared antibodies labeled with FF-TMR. As described in the Experimental Sections, mouse anti- $\beta$  tubulin antibodies (tubBAB) were conjugated with FF-TMR, creating FF-TMR-tubBAB, to stain microtubules. The purity of FF-TMR-tubBAB was demonstrated by SDS-PAGE analysis. (Figure 2-4-1a). FF-TMR-tubBAB exhibited reversible photoswitching of its fluorescence intensity upon light irradiation as seen in FF-TMR-BSA (Figure 2-4-2a-c). These observations indicate that the protein-surface-assisted strategy can be utilized for general purposes.

I next conducted immunostaining of microtubules with FF-TMR-tubBAB to verify photoswitching in fixed cells. After FF-TMR-tubBAB staining, further staining was performed with an ATTO655-labeled secondary antibody (ATTO655-IgG) as an internal control for ratiometric imaging with FF-TMR-tubBAB. The purity of ATTO655-IgG was demonstrated by SDS-PAGE analysis. (Figure 2-4-1b). Ratiometric imaging enables quantitative analysis of fluorescence photoswitching performance of FF-TMR-tubBAB in cells. Before immunostaining imaging, I confirmed that the fluorescence

intensity of ATTO655-IgG was not affected by light irradiation (Figure 2-4-2d,e) and FF-TMR-tubBAB, indicating that no FRET occurs from FF-TMR-tubBAB to ATTO655-IgG. Next, the fluorescence intensity ratio of FF-TMR-tubBAB to ATTO655-IgG reversibly changed upon light irradiation (Figure 2-4-2f).

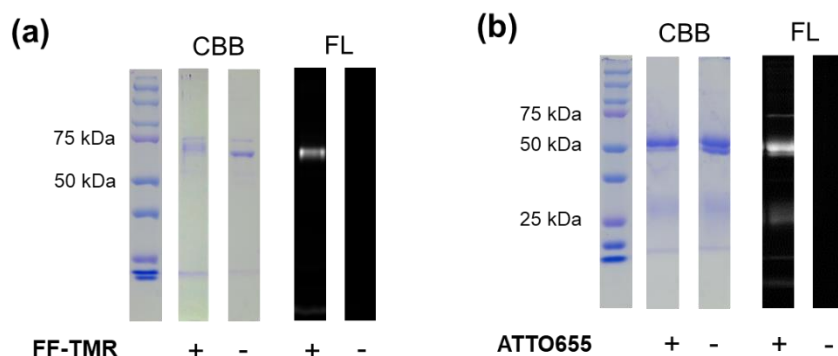


**Figure 2-4-1. Characterization of FF-TMR-tubBAB and ATTO655-IgG.**

The results of SDS-PAGE of (a) FF-TMR-tubBAB and (b) ATTO655-IgG. The left and right image shows CBB-stained and fluorescence images, respectively. The first column at the left represents a ladder to confirm antibody-fluorophore complex size. Fluorescence images were obtained with excitation at (a) 525 nm and (b) 643 nm. Adapted with permission from ref 49. Copyright 2023 American Chemical Society.

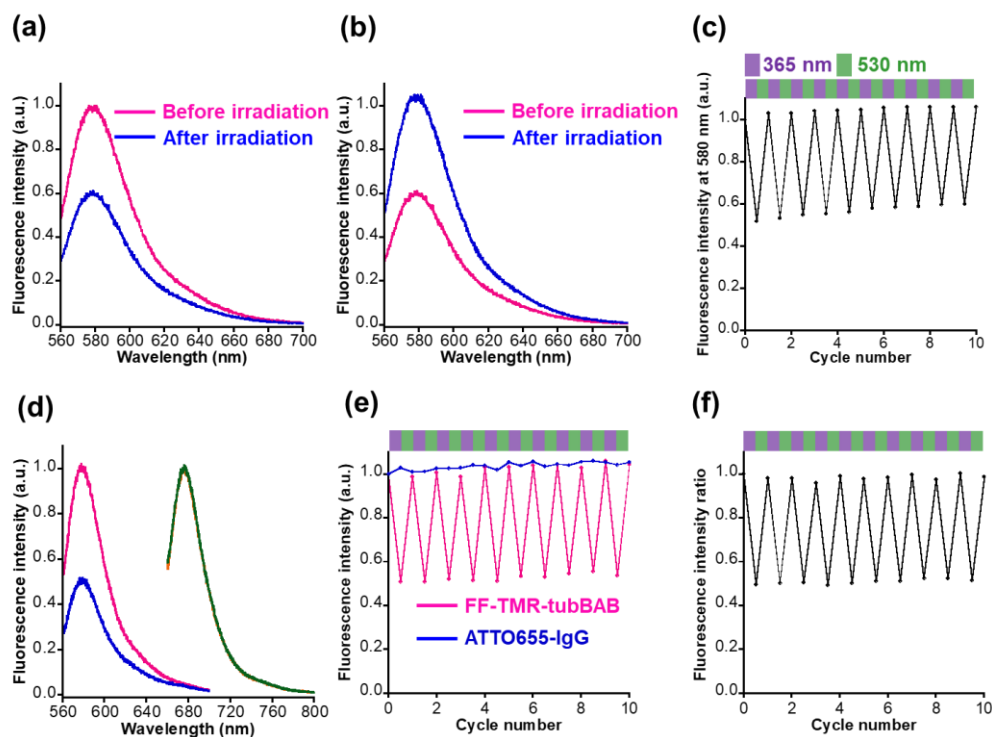


**Figure 2-4-2. Photoswitching properties of FF-TMR-tubBAB and ATTO655-IgG.**

(a, b) Fluorescence spectra of 180 nM FF-TMR-tubBAB in 100 mM phosphate buffer (pH 7.4). Open- and closed ring

form of FF-TMR-tubBAB was irradiated at **(a)** 365 nm and **(b)** 530 nm for 300 sec, respectively. Closed-ring form of FF-TMR-tubBAB was obtained by irradiation at 365 nm for 300 sec. Spectra before and after irradiation are shown by the magenta and blue lines, respectively. **(c)** The fluorescence intensity of FF-TMR-tubBAB at 580 nm was measured after alternate irradiation at 365 and 530 nm. **(d)** Fluorescence spectra of 180 nM FF-TMR-tubBAB and 120 nM ATTO655-IgG in 100 mM phosphate buffer (pH 7.4). Open-ring form of FF-TMR-tubBAB and ATTO655-IgG was irradiated at 365 nm for 300 sec. Spectra of FF-TMR-tubBAB (ATTO655-IgG) before and after irradiation are shown by the magenta (orange) and blue (green) lines, respectively. **(e)** Fluorescence intensity of 180 nM FF-TMR-tubBAB at 580 nm (the magenta line) and 120 nM ATTO655-IgG at 670 nm (the blue line) in 100 mM phosphate buffer (pH 7.4) were measured after alternate irradiation at 365 nm and 530 nm. **(f)** The fluorescence intensity ratio of FF-TMR-tubBAB to ATTO655-IgG. **(c, e, f)** Light irradiation at 365 and 530 nm are shown in purple and green shades, respectively. Light intensity: 365 nm (2 mW/cm<sup>2</sup>), 530 nm (4 mW/cm<sup>2</sup>). FF-TMR-tubBAB:  $\lambda_{\text{ex}} = 550$  nm, ATTO655-IgG:  $\lambda_{\text{ex}} = 640$  nm. Adapted with permission from ref 49. Copyright 2023 American Chemical Society.

Fluorescence imaging of FF-TMR-tubBAB and ATTO655-IgG in fixed HeLa cells was performed using a confocal microscope. Both FF-TMR-tubBAB and Atto655-IgG show the same staining patterns, which were detected as tubulin in cells. (Figure 2-4-3). Furthermore, using these images, the Pearson's correlation coefficient was determined to be 0.84 indicating that the two antibodies are highly colocalized. In addition, the line profile analysis was performed to verify the localization of each antibody in a single cell (Figure 2-4-3b). It also shows that FF-TMR-tubBAB and ATTO655-IgG have similar localization in a single cell. To confirm the photoswitching of FF-TMR-tubBAB in cells, ratiometric imaging was conducted using the fluorescence intensity of FF-TMR-tubBAB and ATTO655-IgG (Figure 2-4-4). The fluorescence intensity ratio of FF-TMR-tubBAB to ATTO655-IgG was decreased after 365 nm irradiation and recovered after 530 nm irradiation (Figure 2-4-4a). Furthermore, the alternating decrease and increase in the ratio were repeatedly observed in response to light irradiation (Figure 2-4-4b,c). To the best of the authors' knowledge, this is the first example of intracellular fluorescence photoswitching using a bioconjugated PSFM with a fulgimide chromophore.

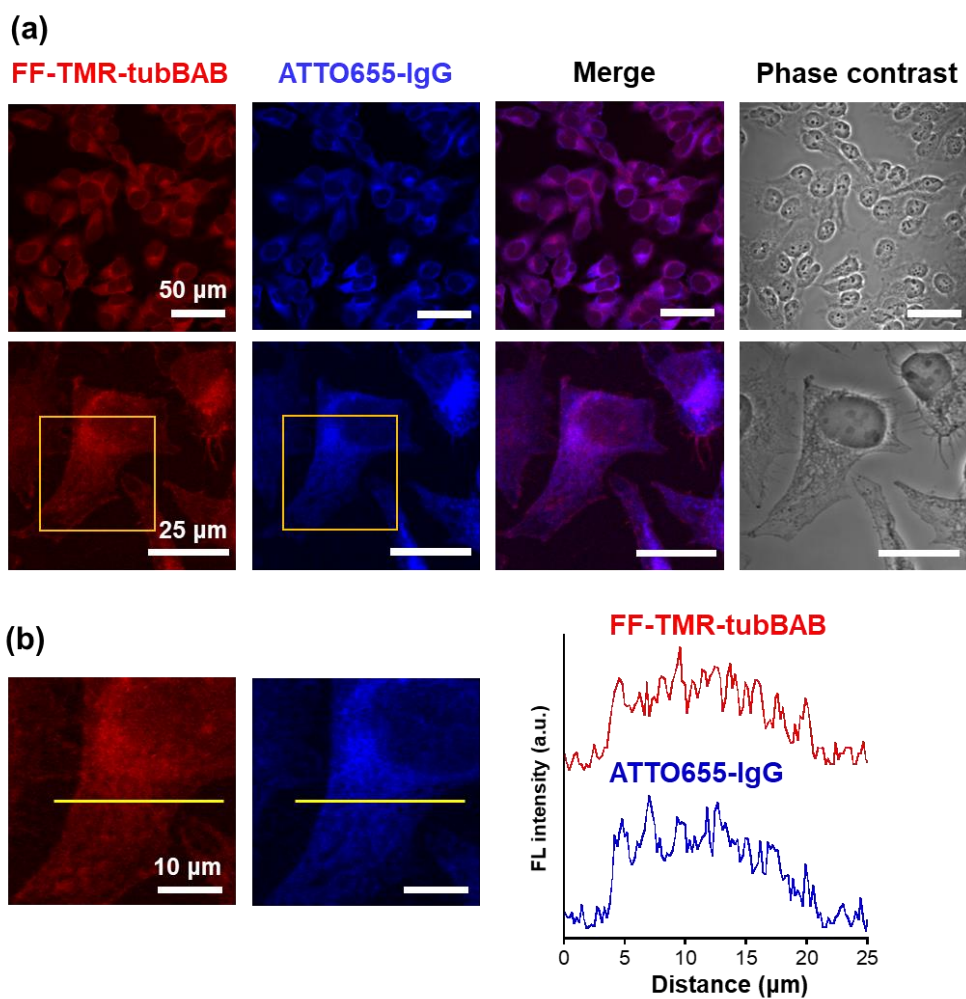


**Figure 2-4-3. Fluorescence imaging of FF-TMR-tubBAB and ATTO655-IgG in fixed HeLa cells.**

(a) Scale bars: 50  $\mu\text{m}$  and 25  $\mu\text{m}$ . (b) Enlarged images surrounded by the yellow squares on (a) and line profile analysis along the yellow line on the image. Scale bars: 10  $\mu\text{m}$ . FF-TMR-tubBAB:  $\lambda_{\text{ex}}/\lambda_{\text{em}} = 559/570\text{-}670$  nm, ATTO655-IgG:  $\lambda_{\text{ex}}/\lambda_{\text{em}} = 635/660\text{-}760$  nm. Pearson's correlation coefficient ( $R=0.84$ ). Adapted with permission from ref 49. Copyright 2023 American Chemical Society.

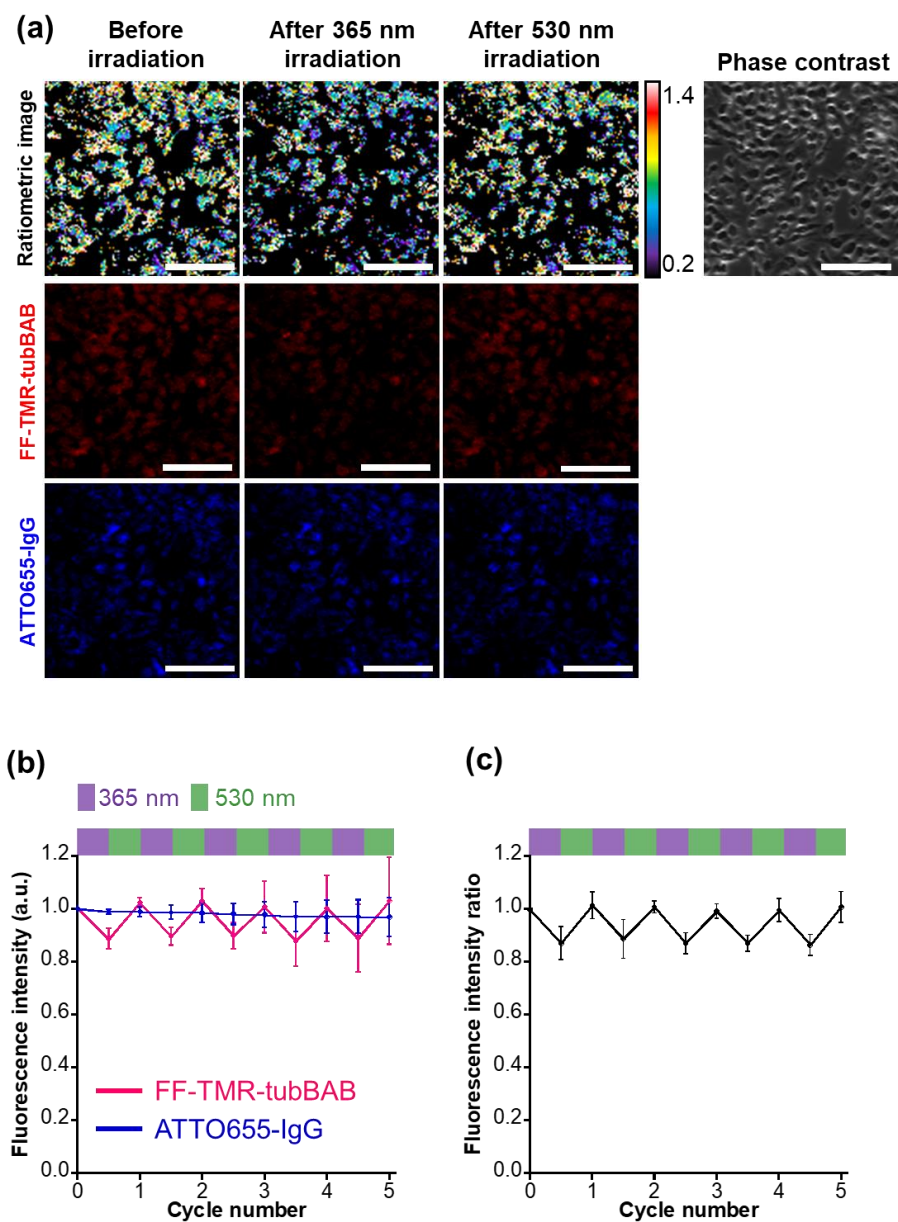


**Figure 2-4-4. Ratiometric imaging of FF-TMR-tubBAB and ATTO655-IgG in fixed HeLa cells.**

(a) Scale bar: 300  $\mu\text{m}$ . FF-TMR-tubBAB:  $\lambda_{\text{ex}}/\lambda_{\text{em}} = 559/570\text{-}670$  nm, ATTO655-IgG:  $\lambda_{\text{ex}}/\lambda_{\text{em}} = 635/660\text{-}760$  nm. Samples were irradiated at 365 nm (15  $\text{mW}/\text{cm}^2$ ) and 530 nm (20  $\text{mW}/\text{cm}^2$ ) for 1 min alternately. Ratiometric images were obtained by dividing the intensity of FF-TMR-tubBAB by that of ATTO655-IgG in each pixel. Maximum ratio: 1.4, Minimum ratio: 0.2. (c) The fluorescence intensity ratio was obtained by dividing the intensity of FF-TMR-tubBAB by that of ATTO655-IgG. (b,c) The error bars indicate the mean  $\pm$  the standard error of the mean (SEM);  $N=3$  from independent experiments. The fluorescence intensities of FF-TMR-tubBAB and ATTO655-IgG are shown by the magenta and blue lines, respectively. Adapted with permission from ref 49. Copyright 2023 American Chemical Society.

## 2-5. Live-cell imaging

Finally, I applied FF-TMR for live-cell fluorescence imaging. Fluorescence photoswitching of FF-TMR in live cells was measured, although the protein-surface-assisted strategy was not utilized. HeLa cells were incubated with FF-TMR, and confocal fluorescence imaging was performed. Co-staining with LysoTracker<sup>®</sup> Green showed that fluorescence signals of FF-TMR overlapped with those of LysoTracker<sup>®</sup> Green (Figure 2-5-1), indicating that FF-TMR localized in the lysosome. To assess the switching capacity of FF-TMR in live cells, ratiometric imaging was conducted using the fluorescence intensity ratio of FF-TMR to LysoTracker<sup>®</sup> Green. While irradiation at 365 nm reduced the ratio, an increase in the ratio was observed after 530 nm irradiation. This signal conversion occurred repeatedly as seen in immunostained fixed cells (Figure 2-5-2). These results indicate that the fluorescence intensity of FF-TMR can be controlled in live cells by light irradiation.

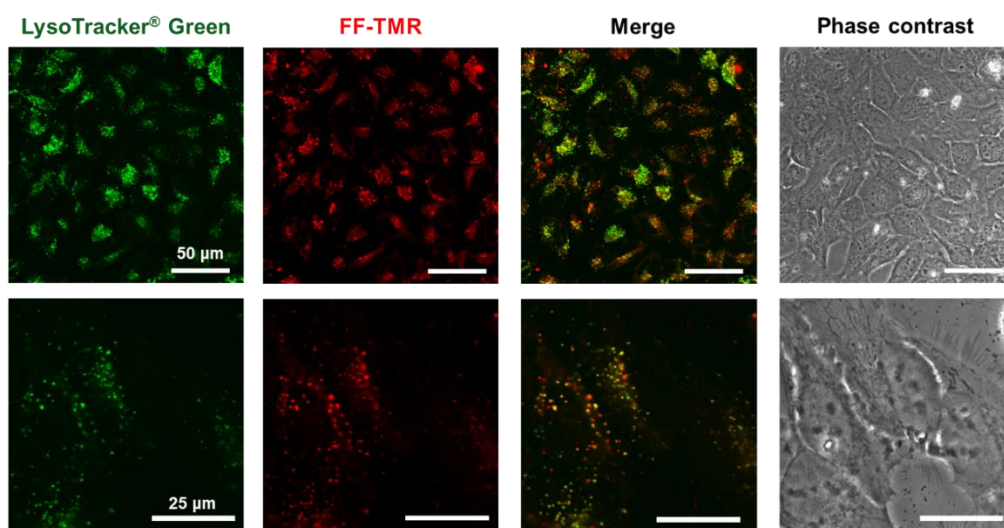


**Figure 2-5-1. Fluorescence imaging of FF-TMR and LysoTracker<sup>®</sup> Green in live HeLa cells.**

Scale bar: 50 μm, 25 μm. LysoTracker<sup>®</sup> Green:  $\lambda_{ex}/\lambda_{em} = 473/490-540$  nm, FF-TMR:  $\lambda_{ex}/\lambda_{em} = 559/570-670$  nm. Pearson's correlation coefficient ( $R=0.79$ ). Adapted with permission from ref 49. Copyright 2023 American Chemical Society.

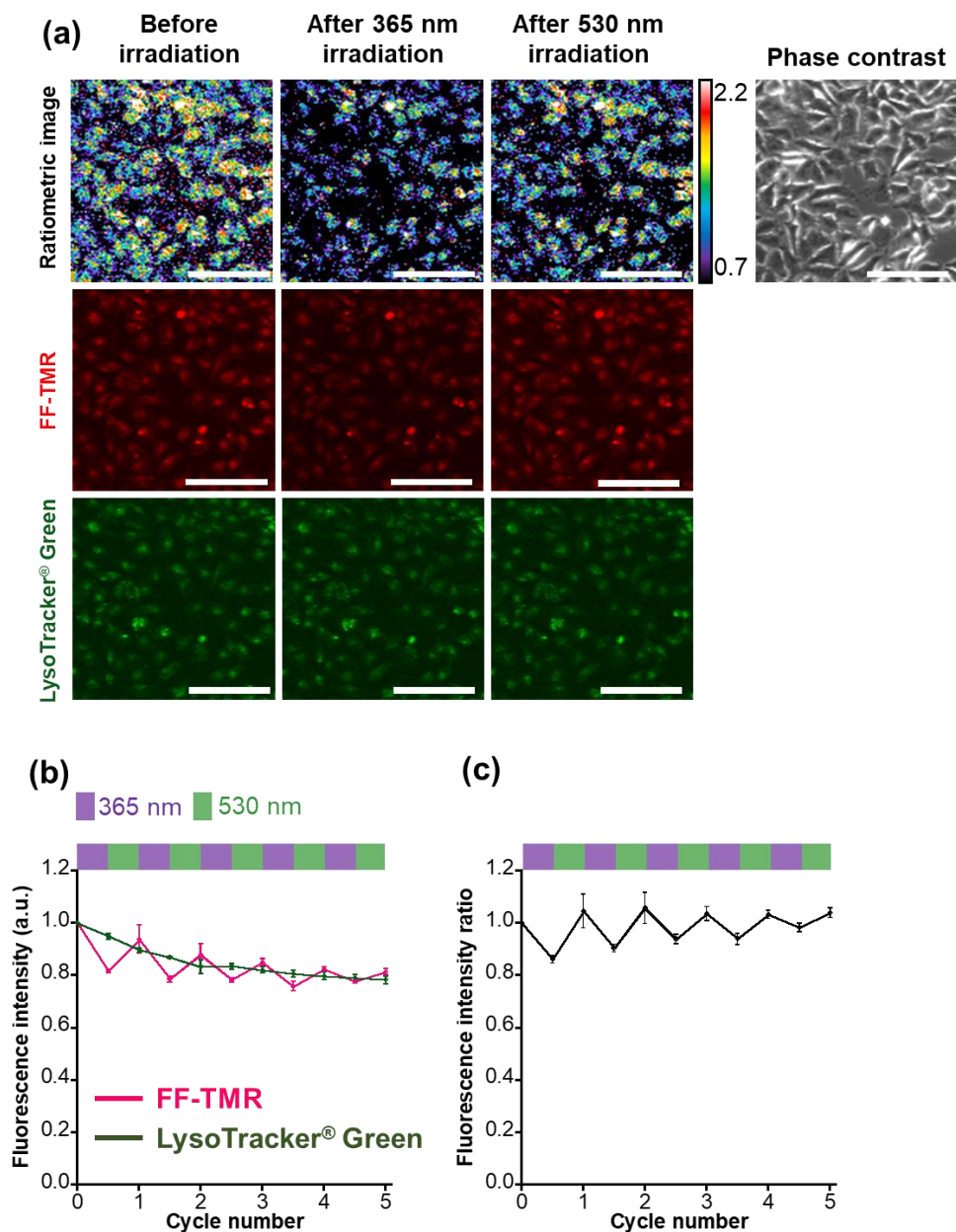
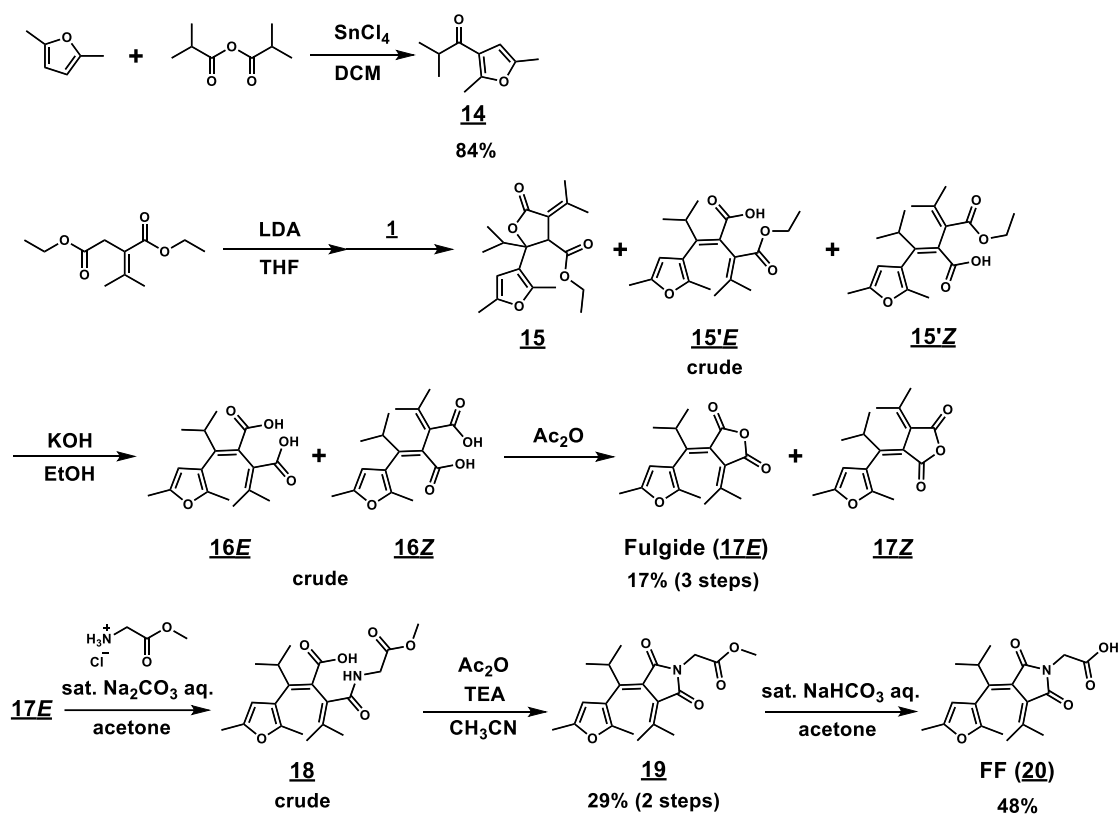


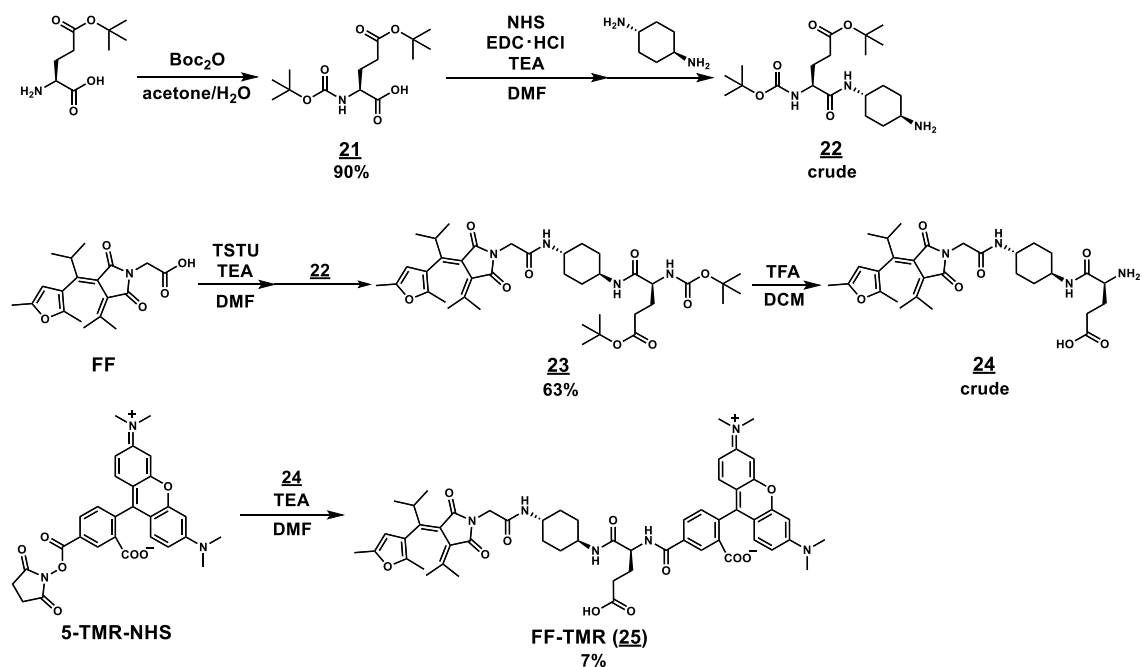
**Figure 2-5-2. Ratiometric imaging of FF-TMR and LysoTracker® Green in live HeLa cells.**

Scale bar: 300  $\mu\text{m}$ . LysoTracker® Green:  $\lambda_{\text{ex}}/\lambda_{\text{em}} = 473/490\text{-}540$  nm, FF-TMR:  $\lambda_{\text{ex}}/\lambda_{\text{em}} = 559/570\text{-}670$  nm. Samples were irradiated at 365 nm (15 mW/cm<sup>2</sup>) and 530 nm (20 mW/cm<sup>2</sup>) for 1 min alternately. Ratiometric images were obtained by dividing the intensity of FF-TMR by that of LysoTracker® Green in each pixel. Maximum ratio: 2.2, Minimum ratio: 0.7. **(b)** The fluorescence intensity ratio was obtained by dividing the intensity of FF-TMR by that of LysoTracker® Green. **(c)** The error bars indicate the mean  $\pm$  the standard error of the mean (SEM);  $N = 3$  from independent experiments. The fluorescence intensities of FF-TMR and LysoTracker® Green are shown by the magenta and green lines, respectively. Adapted with permission from ref 49. Copyright 2023 American Chemical Society.

## Synthetic Procedures



Scheme 2-1. Synthesis of FF. Adapted with permission from ref 49. Copyright 2023 American Chemical Society.



Scheme 2-2. Synthesis of FF-TMR. Adapted with permission from ref 49. Copyright 2023 American Chemical Society.

**1-(2,5-dimethylfuran-3-yl)-2-methylpropan-1-one, (14)**

A solution of 2,5-dimethylfuran (5.56 mL, 52.0 mmol, 1.0 eq.) in DCM (10 mL) was cooled to 0 °C and 2-methylpropanoic anhydride (9.53 mL, 57.2 mmol, 1.1 eq.) was added. Tin (IV) chloride (1 M in DCM, 57 mL, 1.1 eq.) was added dropwise with stirring for 1 h, and the temperature of the solution was maintained at 0 °C. The deep red solution was stirred for a further 30 min and acidified with aqueous HCl (2 M). The organic phase was separated, washed with water, saturated NaHCO<sub>3</sub> aqueous solution, and water again, dried over Na<sub>2</sub>SO<sub>4</sub>, and evaporated to remove the solvent. The crude product was purified using column chromatography (ethyl acetate/hexane = 1/5) to obtain 14 as a yellow solid (7.25 g, 43.4 mmol, 84%).

<sup>1</sup>H NMR, 500 MHz, CDCl<sub>3</sub> δ 6.19 (s, 1H), 3.04 (sept, *J* = 7 Hz, 1H), 2.54 (s, 3H), 2.26 (s, 3H), and 1.15 (d, *J* = 7 Hz, 6H); MS (FAB<sup>+</sup>): calculated for [M]<sup>+</sup> 166.0994, found: 166.0991.

**Ethyl 2-(2,5-dimethylfuran-3-yl)-2-isopropyl-5-oxo-4-(propan-2-ylidene)tetrahydrofuran-3-carboxylate, (15)  
(*E*, *Z*)-3-(2,5-dimethylfuran-3-yl)-2-(1-ethoxy-3-methyl-1-oxobut-2-en-2-yl)-4-methylpent-2-enoic acid, (15'*E*, 15'*Z*)**

A solution of diethyl isopropylidenesuccinate (481 μL, 2.33 mmol, 1.0 eq.) in anhydrous THF (5 mL) was cooled to -78 °C under N<sub>2</sub> atmosphere and a solution of LDA (1.5 M, 2.0 mL, 1.3 eq.) was added dropwise at -78 °C and kept stirring for 1 h. A solution of compound 14 (420 mg, 2.33 mmol, 1.0 eq.) in anhydrous THF (3 mL) was added to the reaction mixture, and the solution was warmed to room temperature with stirring for 18 h. The solution was acidified with aqueous HCl (2 M), and the aqueous phase was extracted with ethyl acetate three times. The organic phase was washed with brine and dried over Na<sub>2</sub>SO<sub>4</sub>. After removing the solvent under vacuum, the crude product was purified using column chromatography (ethyl acetate/hexane = 1/5) to afford three fractions - 15 (extremely small amount), 15'*E* (98.9 mg, 296 μmol, 13%), and 15'*Z* (24.7 mg, 74.0 μmol, 3%) as brown oil.

**Compound 15**; <sup>1</sup>H NMR, 500 MHz, CDCl<sub>3</sub> δ 5.74 (s, 1H), 3.96 (s, 1H), 3.87 (m, 1H), 3.78 (m, 1H), 2.31 (s, 3H), 2.30 (s, 3H), 2.17 (s, 3H), 2.05 (sept, *J* = 7 Hz, 1H), 1.88 (s, 3H), 0.96 (t, *J* = 7 Hz, 3H), 0.89 (d, *J* = 7 Hz, 3H), and 0.88 (d, *J* = 7 Hz, 3H); MS (ESI<sup>+</sup>): calculated for [M + H]<sup>+</sup> 335.18, found: 335.19. **Compound 15'*E***; <sup>1</sup>H NMR, 500 MHz, CDCl<sub>3</sub> δ 5.62 (s, 1H), 4.23 (q, *J* = 7 Hz, 2H), 3.58 (sept, *J* = 7 Hz, 1H), 2.17 (s, 3H), 2.02 (s, 3H), 1.98 (s, 3H), 1.80 (s, 3H), 1.29 (t, *J* = 7 Hz, 3H), and 0.99 (d, *J* = 7 Hz, 6H); MS (ESI<sup>+</sup>): calculated for [M + H]<sup>+</sup> 335.18, found: 335.13. **Compound 15'*Z***; <sup>1</sup>H NMR, 500 MHz, CDCl<sub>3</sub> δ 5.62 (s, 1H), 4.03 (s (br), 2H), 2.83 (sept, *J* = 7 Hz, 1H), 2.25 (s, 3H), 2.20 (s, 3H), 2.10 (s, 3H), 1.90 (s, 3H), 0.99 (t, *J* = 7 Hz, 3H), and 0.95 (s (br), 6H); MS (ESI<sup>+</sup>): calculated for [M + H]<sup>+</sup> 335.18, found: 335.13.

**(*E*, *Z*)-2-(1-(2,5-dimethylfuran-3-yl)-2-methylpropylidene)-3-(propan-2-ylidene)succinic acid, (16E, 16Z)**

The mixture of compounds 15'*E* and 15Z (124 mg, 370 μmol, *E/Z* = 4/1) was dissolved in ethanol (16 mL) and a saturated aqueous solution of KOH (10 mL) was added. After stirring at 70 °C for 3 h, the reaction mixture was cooled to room temperature and acidified with aqueous HCl (2 M). The reaction product was extracted thrice with ethyl acetate. The organic layer was washed with brine and dried over Na<sub>2</sub>SO<sub>4</sub> and evaporated to remove the solvent. The crude

product was purified using reversed-phase chromatography (0.1% formic acid of acetonitrile/water) to obtain two fractions - 16E (46.4 mg, 152, 41%) and 16Z (11.6 mg, 37.9  $\mu$ mol, 10%) as white powders.

**Compound 16E**;  $^1\text{H NMR}$ , 500 MHz,  $\text{CDCl}_3$   $\delta$  5.61 (s, 1H), 3.71 (sept,  $J = 7$  Hz, 1H), 2.18 (s, 3H), 2.03 (s, 3H), 1.99 (s, 3H), 1.84 (s, 3H), and 0.99 (d,  $J = 7$  Hz, 6H); **MS (ESI $^-$ )**: calculated for  $[\text{M} - \text{H}]^-$  305.15, found 305.16; **Compound 16Z**;  $^1\text{H NMR}$ , 500 MHz,  $\text{CDCl}_3$   $\delta$  5.83 (s, 1H), 2.81 (sept,  $J = 7$  Hz, 1H), 2.26 (s, 3H), 2.24 (s, 3H), 2.14 (s, 3H), 1.94 (s, 3H), and 0.90 (s (br), 6H); **MS (ESI $^-$ )**: calculated for  $[\text{M} - \text{H}]^-$  305.15, found: 305.16.

**(*E, Z*)-3-(1-(2,5-dimethylfuran-3-yl)-2-methylpropylidene)-4-(propan-2-ylidene)dihydrofuran-2,5-dione, (17E, 17Z)**

The mixture of compound 16E and 16Z (30.0 mg, 97.8  $\mu$ mol,  $E/Z = 4/1$ ) was dissolved in  $\text{Ac}_2\text{O}$  (20 mL) and the mixture was heated to 80  $^\circ\text{C}$  overnight. After removing the solvent under vacuum, the crude product was purified using column chromatography (ethyl acetate/hexane = 1/10) to obtain 17E (22.0 mg, 76.4  $\mu$ mol, 78, and red solid) and 17Z (yellow solid).

**Compound 17E (Fulgide)**;  $^1\text{H NMR}$ , 500 MHz,  $\text{CDCl}_3$   $\delta$  5.93 (s, 1H), 4.28 (sept,  $J = 7$  Hz, 1H), 2.28 (s, 3H), 2.26 (s, 3H), 1.89 (s, 3H), 1.37 (s, 3H), 1.31 (s (br), 3H), and 0.89 (s (br), 3H);  $^{13}\text{C NMR}$ , 125 MHz,  $\text{CDCl}_3$   $\delta$  163.2, 163.1, 158.0, 154.1, 150.7, 147.1, 120.8, 120.1, 119.2, 105.7, 30.9, 27.1, 22.6, 22.6, 20.5, 13.3, and 12.9; **HRMS (FAB $^+$ )**: calculated for  $[\text{M} + \text{H}]^+$  289.1440, found 289.1438. **Compound 17Z**;  $^1\text{H NMR}$ , 500 MHz,  $\text{CDCl}_3$   $\delta$  5.88 (s, 1H), 2.83 (sept,  $J = 7$  Hz, 1H), 2.40 (s, 3H), 2.28 (s, 3H), 2.15 (s, 3H), 2.06 (s, 3H), 1.19 (d,  $J = 7$  Hz, 3H), and 0.99 (d,  $J = 7$  Hz, 3H);  $^{13}\text{C NMR}$ , 125 MHz,  $\text{CDCl}_3$   $\delta$  163.4, 161.3, 155.6, 153.3, 151.8, 149.8, 121.2, 120.0, 115.3, 106.3, 34.2, 26.6, 22.2, 21.8, 19.1, 13.4, and 12.7; **MS (FAB $^+$ )**: calculated for  $[\text{M} + \text{H}]^+$  289.1440, found: 289.1444.

**(*E*)-3-(2,5-dimethylfuran-3-yl)-2-(1-((2-methoxy-2-oxoethyl)amino)-3-methyl-1-oxobut-2-en-2-yl)-4-methylpent-2-enoic acid, (18)**

A solution of compound 17E (30.0 mg, 104  $\mu$ mol, 1.0 eq.) in acetone (10 mL) was added to L-glycine methyl ester hydrochloride (54.1 mg, 431  $\mu$ mol, 4.1 eq.) in a saturated  $\text{Na}_2\text{CO}_3$  aqueous solution (10 mL). The mixture was stirred at room temperature for 2 h and then acidified with aqueous HCl (2 M). The reaction product was extracted thrice with ethyl acetate. The organic layer was washed with brine and dried over  $\text{Na}_2\text{SO}_4$  and removed the solvent under vacuum. Compounds 18a or 18b (11.7 mg, 31.0  $\mu$ mol, 30%) were obtained as red oil.

$^1\text{H NMR}$ , 500 MHz,  $\text{CDCl}_3$   $\delta$  5.59 (s, 1H), 4.12 (d,  $J = 5.5$  Hz, 2H), 3.77 (s, 3H), 3.23 (sept,  $J = 7$  Hz, 1H), 2.19 (s, 3H), 2.01 (s, 3H), 1.99 (s, 3H), 1.92 (s, 3H), and 0.99 (d,  $J = 7$  Hz, 6H);  $^{13}\text{C NMR}$ , 125 MHz,  $\text{CDCl}_3$   $\delta$  171.5, 170.2, 170.0, 152.2, 149.2, 147.0, 146.6, 131.4, 124.5, 115.9, 107.7, 52.4, 41.2, 32.3, 24.6, 22.5, 22.5, 21.2, 13.4, and 12.5; **MS (ESI $^+$ )**: calculated for  $[\text{M} + \text{H}]^+$  378.18, found: 378.14.

**methyl (*E*)-2-(3-(1-(2,5-dimethylfuran-3-yl)-2-methylpropylidene)-2,5-dioxo-4-(propan-2-ylidene)pyrrolidin-1-yl)acetate, (19)**

A solution of compound 18 (11.7 mg, 31.0  $\mu$ mol, 1.0 eq.) in MeCN (10 mL) was added to triethylamine (200  $\mu$ L, 1.44

mmol, 46.5 eq.) and Ac<sub>2</sub>O (200 μL, 2.11 mmol, 68.1 eq.) and stirred at 60 °C for 3 h. After evaporating the solvent under vacuum, the crude product was purified using column chromatography (ethyl acetate/hexane = 1/3) to get compound 19 (2.0 mg, 5.57 μmol, 18%) as a red solid. **<sup>1</sup>H NMR, 500 MHz, CDCl<sub>3</sub>** δ 5.94 (s, 1H), 4.48 (sept, *J* = 7 Hz, 1H), 4.35 (m, 2H), 3.77 (s, 3H), 2.19 (s, 3H), 2.01 (s, 3H), 1.99 (s, 3H), 1.92 (s, 3H), and 0.99 (d, *J* = 7 Hz, 6H); **<sup>13</sup>C NMR, 125 MHz, CDCl<sub>3</sub>** δ 170.18, 170.35, 170.11, 151.30, 149.24, 147.28, 146.56, 131.03, 124.45, 115.62, 107.63, 60.41, 52.43, 41.24, 32.40, 24.32, 22.33, 21.20, 21.06, 14.20, 13.39, and 12.52; **MS (FAB+)**: calculated for [M + H]<sup>+</sup> 360.1811, found: 360.1807.

#### **FF, (20)**

A solution of compound 19 (10.9 mg, 30.4 μmol, 1.0 eq.) in acetone (10 mL) was added to a saturated Na<sub>2</sub>CO<sub>3</sub> aqueous solution (10 mL). The mixture was stirred at room temperature for 2 h and then acidified with aqueous HCl (2 M). The reaction product was extracted thrice with ethyl acetate. The organic layer was washed with brine and dried over Na<sub>2</sub>SO<sub>4</sub>. After removing the solvent in vacuo, the crude product was purified using column chromatography (ethyl acetate/hexane = 1/3) to get compound 20 (5.1 mg, 14.8 μmol, 48%) as a red solid.

**<sup>1</sup>H NMR, 500 MHz, CD<sub>3</sub>OD** δ 6.05 (s, 1H), 4.49 (sept, *J* = 7 Hz, 1H), 4.27 (m, 2H), 2.25 (s, 3H), 2.23 (s, 3H), 1.87 (s, 3H), 1.39 (s, 3H), 1.30 (d, *J* = 7 Hz, 3H), and 0.83 (d, *J* = 7 Hz, 3H); **<sup>13</sup>C NMR, 125 MHz, CD<sub>3</sub>OD** δ 169.6, 167.7, 167.5, 152.7, 150.2, 148.3, 146.9, 123.5, 123.2, 119.4, 106.1, 29.6, 28.2, 25.8, 21.4, 20.5, 19.5, 11.8, and 11.3; **MS (FAB+)**: calculated for [M + H]<sup>+</sup> 346.1654, found: 346.1659.

#### **5-(*tert*-butoxy)-2-((*tert*-butoxycarbonyl)amino)-5-oxopentanoic acid, (21)**

A solution of 5-*tert*-butyl L-glutamate (99.7 mg, 491 μmol, 1.0 eq.) in acetone (10 mL) and water (10 mL) was added to triethylamine (120 μL, 863 μmol, 1.8 eq.) and Boc<sub>2</sub>O (140 μL, 610 μmol, 1.2 eq.) The mixture was stirred overnight at room temperature. After removing the solvent in vacuo, the residue was acidified with aqueous HCl (2 M) and extracted thrice with DCM. The organic layer was washed with brine and dried over Na<sub>2</sub>SO<sub>4</sub>, and the solvent was removed in vacuo. Compound 21 (135.2 mg, 446 μmol, 90%) was obtained as a white solid.

**<sup>1</sup>H NMR, 500 MHz, CD<sub>3</sub>OD** δ 5.25 (s, 1H), 4.30 (s, 1H), 2.37 (m, 2H), 2.17 (m, 1H), 1.98 (m, 1H), 1.45 (s, 9H), and 1.45 (s, 9H); **MS (ESI-)**: calculated for [M - H]<sup>+</sup> 302.17, found: 302.13.

#### ***tert*-butyl 5-(((1*r*,4*r*)-4-aminocyclohexyl)amino)-4-((*tert*-butoxycarbonyl)amino)-5-oxopentanoate, (22)**

A solution of compound 21 (95.1 mg, 314 μmol, 1.0 eq.) and triethylamine (50.0 μL, 360 μmol, 1.1 eq.) was added in anhydrous DMF (10 mL), EDC·HCl (61.6 mg, 395 μmol, 1.3 eq.), and NHS (45.2 mg, 399 μmol, 1.3 eq.) in anhydrous DMF (10 mL) and stirred at room temperature for 2 h. A solution of trans-1,4-diaminocyclohexane (348 mg, 3.05 mmol, 9.7 eq.) in anhydrous DMF (15 mL) was added dropwise to this solution and stirred at room temperature for 3 h. After evaporating the solvent in vacuo, the residue was added to DCM and H<sub>2</sub>O and extracted with DCM three times. The organic layer was washed with brine and dried over Na<sub>2</sub>SO<sub>4</sub>, and the solvent was removed under vacuum. Compound 22 (101.6 mg, 254 μmol, 81 %) was obtained as a yellow solid.

**<sup>1</sup>H NMR, 500 MHz, CDCl<sub>3</sub>** δ 6.08 (s, 1H), 5.26 (s, 1H), 4.04 (s, 1H), 2.66 (m, 1H), 2.38 (m, 2H), 2.28 (m, 1H), 2.02 (m, 2H), 2.00-1.80 (m, 4H), 1.45 (s, 9H), 1.45 (s, 9H), and 1.25-1.10 (m, 4H); **MS (FAB<sup>+</sup>)**: calculated for [M + H]<sup>+</sup> 400.2811, found: 400.2806.

***tert*-butyl 4-((*tert*-butoxycarbonyl)amino)-5-(((1*r*,4*r*)-4-(2-((*E*)-3-(1-(2,5-dimethylfuran-3-yl)-2-methylpropylidene)-2,5-dioxo-4-(propan-2-ylidene)pyrrolidin-1-yl)acetamido)cyclohexyl)amino)-5-oxopentanoate, (**23**)**

A solution of compound **20** (47.9 mg, 139 μmol, 1.0 eq.) in anhydrous DMF (6 mL) was added to a solution of TEA (30.4 μL, 219 μmol, 1.6 eq.) and TSTU (53.0 mg, 176 μmol, 1.3 eq.) in anhydrous DMF (6 mL) and stirred overnight at room temperature. The mixture was then added to a solution of compound **22** (102 mg, 254 μmol, 1.8 eq.) in anhydrous DMF (10 mL) and stirred overnight at room temperature. After evaporating the solvent in vacuo, the residue was dissolved in DCM and H<sub>2</sub>O and extracted with DCM three times. The organic layer was washed with brine and dried over Na<sub>2</sub>SO<sub>4</sub>. After concentrating the solution under vacuum, the crude product was purified using column chromatography (ethyl acetate/DCM = 1/1) to get compound **23** (63.5 mg, 87.4 μmol, 63%) as a red solid.

**<sup>1</sup>H NMR, 500 MHz, CDCl<sub>3</sub>** δ 6.17 (s, 1H), 5.93 (s, 1H), 5.70 (d, *J* = 8 Hz, 1H), 5.26 (d, *J* = 7 Hz, 1H), 4.47 (sept, *J* = 7 Hz, 1H), 4.27 (m, 2H), 4.03 (m, 1H), 3.80-3.67 (m, 2H), 2.36 (m, 2H), 2.25 (s, 3H), 2.25 (s, 3H), 2.10-2.00 (m, 4H), 1.92-1.83 (m, 2H), 1.87 (s, 3H), 1.45 (s, 9H), 1.43 (s, 9H), 1.35 (s, 3H), 1.28 (d, *J* = 7 Hz, 3H), 1.30-1.15 (m, 4H), and 0.84 (d, *J* = 7 Hz, 3H); **<sup>13</sup>C NMR, 125 MHz, CDCl<sub>3</sub>** δ 172.8, 170.9, 167.8, 167.7, 165.7, 155.8, 153.3, 149.9, 148.9, 147.0, 123.2, 123.1, 119.5, 106.3, 80.1, 54.1, 47.9, 47.5, 40.8, 38.6, 31.8, 29.9, 28.3, 28.1, 27.7, 27.1, 22.9, 22.0, 20.6, 13.3, and 12.8; **MS (FAB<sup>+</sup>)**: calculated for [M + Na]<sup>+</sup> 749.4102, found: 749.4106.

**4-amino-5-(((1*r*,4*r*)-4-(2-((*E*)-3-(1-(2,5-dimethylfuran-3-yl)-2-methylpropylidene)-2,5-dioxo-4-(propan-2-ylidene)pyrrolidin-1-yl)acetamido)cyclohexyl)amino)-5-oxopentanoic acid, (**24**)**

Compound **23** (50.0 mg, 68.8 μmol, 1.0 eq.) was dissolved in a mixed solution of TFA/DCM (3.13 mL, TFA/DCM = 1/4) and stirred at room temperature for 2 h. After evaporating the solvent under vacuum, compound **24** was obtained as a purple solid.

**HRMS (FAB<sup>+</sup>)**: calculated for [M + Na]<sup>+</sup> 593.2951, found: 593.2962. The full characterization of **24** is not provided. Compound **24** was used in the subsequent reaction without further purification.

**FF-TMR, (**25**)**

A solution of 5-TMR-NHS (14.8 mg, 28.1 μmol, 1.0 eq.) in anhydrous DMF (10 mL) was added to a solution of compound **24** (17.6 mg, 30.9 μmol, 1.1 eq.) and triethylamine (300 μL, 2.16 mmol, 76.9 eq.) in anhydrous DMF (10 mL) and stirred at 30 °C for 12 h. After concentrating the solution under vacuum, the crude product was purified using reversed-phase chromatography (0.1% formic acid acetonitrile/water) to get compound **25** (2.4 mg, 2.4 μmol, 7%) as a purple powder.

**<sup>1</sup>H NMR, 500 MHz, CD<sub>3</sub>OD** δ 8.70 (s, 1H), 8.17 (m, 1H), 7.43 (m, *J* = 8 Hz, 1H), 7.19 (d, *J* = 9.3 Hz, 2H), 7.02 (d, *J*

= 9.3 Hz, 2H), 6.95 (d, 2H), 6.05 (s, 1H), 4.60 (m, 1H), 4.49 (sept,  $J = 7$  Hz, 1H), 4.20 (d, 2H), 3.66 (m, 2H), 3.29 (s, 12H), 2.50 (m, 2H), 2.25 (s, 3H), 2.23 (s, 3H), 2.20-2.10 (m, 2H), 2.00-1.90 (m, 4H), 1.88 (s, 3H), 1.40-1.30 (m, 4H), 1.39 (s, 3H), 1.30 (d,  $J = 7$  Hz, 3H), and 0.84 (d,  $J = 7$  Hz, 3H);  $^{13}\text{C}$  NMR, 125 MHz,  $\text{CD}_3\text{OD}$   $\delta$  171.72, 167.97, 167.75, 167.24, 166.94, 166.86, 159.92, 157.64, 157.44, 152.54, 150.15, 148.13, 146.93, 136.34, 135.52, 130.92, 129.67, 129.32, 123.50, 123.26, 119.45, 113.89, 113.35, 106.07, 96.00, 53.93, 39.49, 39.33, 30.84, 30.74, 30.66, 30.23, 29.61, 27.11, 25.87, 21.87, 20.49, 19.48, 11.78, and 11.43; MS (FAB+): calculated for  $[\text{M} + \text{H}]^+$  983.4555, found: 983.4551.

## Experimental Sections

### Materials and Instrument

---

All chemicals for the synthesis were purchased from Tokyo Chemical Industries Co., Ltd. (Tokyo, Japan), Wako Pure Chemical Corp. (Osaka, Japan), Sigma-Aldrich Chemicals Pvt., Ltd. (St. Louis, MO, USA), or Funakoshi Co., Ltd. (Tokyo, Japan) and were used as received without further purification. Chemical reaction progresses were monitored by thin-layer chromatography using 60F254 silica gel glass plates (Merck Co., Inc., Kenilworth, NJ, USA). Isolera One (Biotage Japan Ltd., Tokyo, Japan) was utilized for reversed-phase chromatography to purify the synthesized products. The purification of FF and FF-TMR was conducted using a high-performance liquid chromatography (HPLC) system composed of a reversed-phase column (Inertsil ODS-3,  $250 \times 10$  mm; GL Sciences, Inc., Tokyo, Japan), a detector (MD-2010; JASCO Corp., Tokyo, Japan), and a pump (PU-2087; JASCO Corp.). The purity of all samples was confirmed using an HPLC system including a reversed-phase column (Inertsil ODS-3,  $250 \times 4.6$  mm; GL Sciences, Inc.), a detector (MD-4010; JASCO Corp.), and a pump (PU-2080; JASCO Corp.). For HPLC analysis, compounds were eluted through a column with a linear gradient of acetonitrile/water containing 0.1% formic acid.  $^1\text{H}$  (500 MHz) and  $^{13}\text{C}$  (125 MHz) nuclear magnetic resonance (NMR) spectroscopic data were measured utilizing an AVANCE III HD 500 (Bruker Corp., Billerica, MA, USA). Mass spectra (MS) were measured utilizing an electrospray ionization (ESI) (LCT-Premier XE; Waters Corp., Milford, MA, USA) or a fast atom bombardment (FAB) spectrometry (JMS-700; JOEL Ltd., Tokyo, Japan). Absorption and emission spectroscopic data were recorded on a V-650 (JASCO Corp.) and an F-4500 spectrometer (Hitachi High-Tech Science Corp., Tokyo, Japan), respectively. Light irradiation of samples was conducted using a MAX-302 xenon light source (Asahi Spectra Co., Ltd., Tokyo, Japan).

### Molecular Simulation of FF-TMR

---

Molecular structures of FF-TMR were simulated using MacroModel (Schrödinger Release 2019-1: Maestro, Schrödinger, LLC, NY, USA). The computations were conducted on the OPLS3 force field (solvent model: water). Energy-minimized structures of FF-TMR were searched using Monte Carlo multiple minimum sampling (energy window for keeping structures:  $50 \text{ kJmol}^{-1}$ ).

### Preparation of Bioconjugates

---

#### FF-TMR-BSA

FF-TMR was added to 200 mM 2-(*N*-morpholino)ethanesulfonic acid (MES) buffer (pH 6.0) containing 50 mM *N*-hydroxysulfosuccinimide sodium salt (Sulfo-NHS) and 5 mM 1-ethyl-3-(3-dimethylaminopropyl)-carbodiimide hydrochloride (EDC·HCl) and stirred at 25 °C for 1 h. The reaction solution was then incubated with BSA (A0281; Sigma-Aldrich Chemicals Pvt., Ltd.) in 200 mM MES buffer (pH 6.0) at 37 °C for 1 h. Unconjugated FF-TMR was excluded using Nanosep® centrifugal devices with an Omega™ membrane 30 K (OD030C34; Pall Corp., Port Washington, NY, USA). After ultrafiltration, the conjugates were dissolved in 200 μL of 100 mM phosphate buffer (pH 7.4). An aliquot of the solution (10 μL) was added to the loading buffer including 100 mM dithiothreitol (10 μL), heated at 103 °C for 3 min, and subsequently analyzed using sodium dodecyl sulfate-polyacrylamide gel electrophoresis (SDS-PAGE). After the fluorescent gel images were obtained using a Typhoon FLA 9500 (GE Healthcare, Chicago, IL, USA), the gel was stained with Coomassie Brilliant Blue. The BSA concentration was determined using the Bradford assay on a multilabel counter (ARVOTM MX; PerkinElmer, Waltham, MA, USA) with BSA as a standard reagent. The UV-vis absorption of the FF-TMR-BSA solution was measured to estimate the conjugated FF-TMR concentrations.

#### FF-TMR-tubBAB

FF-TMR was added to 200 mM MES buffer (pH 5.0) containing 50 mM sulfo-NHS and 5 mM EDC·HCl, and 0.5% polyoxyethylene octylphenyl ether and stirred at 25 °C for 1 h. The reaction solution was then incubated with anti-β-tubulin antibody (tubBAB) (T4026; Sigma-Aldrich Chemicals Pvt., Ltd.) in 100 M phosphate buffer (pH 8.0) at 37°C for 1 h. FF-TMR were purified using gel filtration chromatography on Superose™ 6 10/300 GL (Cytiva, Tokyo, Japan). Characterization was conducted in the same manner as that for FF-TMR-BSA.

#### ATTO655-IgG

ATTO655 was added to 200 mM MES buffer (pH 6.0) containing 50 mM sulfo-NHS and 5 mM EDC·HCl and stirred at 25°C for 1 h. The reaction solution was then incubated with anti-mouse IgG (whole molecule) antibody (M7023; Sigma-Aldrich Chemicals Pvt., Ltd.,) in 0.2 M MES buffer (pH 6.0) at 37 °C for 1 h. The purification and characterization were conducted in the same manner as that for FF-TMR-BSA.

### Determination of photon flux using chemical actinometers

---

For determining photoconversion quantum yields of FF and photoswitching kinetics of FF, FF-TMR, and FF-TMR-BSA, 4,4'-dimethylazobenzene in acetonitrile and Aberchrome 540 in toluene were used as chemical actinometers. The photon flux at 365 nm was determined from the *E*-to-*Z* photoisomerization kinetics of 1,4-dimethyl azobenzene at 365 nm irradiation following a previous report<sup>79</sup>. The photon flux at 530 nm was determined using Aberchrome 540. The procedure is described below.

The ring-closure reaction rate of Aberchrome 540 is determined following Eq. 2-1.

$$\frac{d[C]}{dt} = -\frac{\phi_{co}q_0}{V} \frac{\epsilon_{c,\lambda_i}[C]f}{\epsilon_{c,\lambda_i}[C] + \epsilon_{o,\lambda_i}[O]} + \frac{\phi_{oc}q_0}{V} \frac{\epsilon_{o,\lambda_i}[O]f}{\epsilon_{c,\lambda_i}[C] + \epsilon_{o,\lambda_i}[O]}$$

Equation 2-1

Here,  $[C]$ ,  $\phi_{co}$ ,  $q_0$ ,  $V$ , and  $\varepsilon_{\lambda_i}$  are the concentration of the closed-ring form, ring-opening reaction quantum yield, photon flux, the sample volume, and the molar absorption coefficient at the irradiation wavelength ( $\lambda_i = 530$  nm), respectively. The absorption coefficient of open-ring form  $\varepsilon_{o,\lambda_i}$  was regarded as 0 and the Eq. 2-1 reduced to Eq. 2-2.

$$\frac{d[C]}{dt} = -\frac{\phi_{co}q_0}{V}f$$

Equation 2-2

$f$  is a fraction of light absorbed by Aberchrome 540, estimated from the absorbance at 494 nm, because the molar absorption coefficient at 494 nm is widely known as  $\varepsilon_{494} = 8200 \text{ M}^{-1}\text{cm}^{-1}$ <sup>57</sup>.

$$f = 1 - 10^{-\varepsilon_{c,\lambda_i}[C]l} = 1 - 10^{-\frac{\varepsilon_{c,\lambda_i}A_{494}}{\varepsilon_{494}}} = 1 - 10^{-A'(t)}$$

Equation 2-3

Following Lambert-Beer equation, Eq. 2-4 is described.

$$d[C] = -\frac{dA_{494}}{\varepsilon_{494}l}$$

Equation 2-4

The combination of Eq. 2-2, 2-3, and 2-4 provides Eq. 2-5.

$$\frac{dA_{494}}{\varepsilon_{494}l} \frac{1}{dt} = \frac{\phi_{co}q_0}{V}(1 - 10^{-A'(t)})$$

Equation 2-5

The integral of Eq. 5 gives the following Eq. 2-6.

$$\ln(10^{A'(t)} - 1) = \ln(10^{A'(0)} - 1) - \frac{\phi_{co}q_0\varepsilon_{c,\lambda_i}l \ln 10}{V}t$$

Equation 2-6

Here, the linear relationship between  $\ln(10^{A'(t)} - 1)$  and  $t$  provides the slope  $m$  which determines photon flux  $q_0$ . (Eq. 2-7)

$$q_0 = -\frac{mV}{\phi_{co}\varepsilon_{494}l \ln 10} \text{ [mol/s]}$$

Equation 2-7

The ring-opening reaction quantum yield of Aberchrome 540 in toluene is known as  $\phi_{co} = 0.051$  at 530 nm<sup>80</sup>.

Irradiated light intensity  $I_{irr}$ [mW] is provided following Eq. 2-8.

$$I_{irr} = \frac{q_0 N_A h c}{\lambda_i} \times 10^3 \text{ [mW]}$$

Equation 2-8

Here,  $N_A$ ,  $h$ , and  $c$ , are the Avogadro constant, Planck constant, and light speed, respectively.

---

#### Determination of photoswitching rate constants of FF, FF-TMR and FF-TMR-BSA

---

Both the ring-closure and ring-opening reactions of FF followed the first-order kinetics. The ring-closure reaction rate constants ( $k_{oc}$ ) and the ring-opening reaction rate constants ( $k_{co}$ ) were determined by following Eq. 2-9 and 2-10, respectively.

$$A(t) = A_{\text{PSS at 530 nm}}(1 - \exp(-k_{oc}t))$$

Equation 2-9

$$A(t) = A_{\text{PSS at 530 nm}} \exp(-k_{co}t)$$

Equation 2-10

Both the fluorescence turning-off and turning-on processes of FF-TMR and FF-TMR-BSA also followed the first-order kinetics. The turning-off rate constant ( $k_{off}$ ) and turning-on rate constants ( $k_{on}$ ) were determined by following Eq. 11 and 12, respectively.

$$I_{\text{Fl,nor}}(t) = \exp(-k_{off}t)$$

Equation 2-11

$$I_{\text{Fl,nor}}(t) = 1 - \exp(-k_{on}t)$$

Equation 2-12

$I_{\text{Fl,nor}}(t)$  is normalized fluorescence intensity, in which fluorescence intensity of FF-TMR or FF-TMR-BSA is at 365 nm photostationary state and at 530 nm photostationary state is normalized to 0 and 1, respectively. These kinetic constants depend on irradiated light intensities. The linear relation between kinetic constants  $k$  [ $\text{s}^{-1}$ ] and irradiated light intensities  $I_{\text{irr}}$  [mW] provides the slope  $k/I_{\text{irr}}$  [ $\text{s}^{-1}/\text{mW}$ ] which is an independent value of irradiated light intensities and can be compared with each kinetic constant.

### Photoconversion quantum yield measurements of FF, FF-TMR, and FF-TMR-BSA

---

The photoconversion quantum yields of FF, FF-TMR and FF-TMR-BSA were measured in 100 mM phosphate buffer (pH 7.4) and ethanol (FF and FF-TMR) upon light irradiation at 365 nm and 530 nm, respectively. Each quantum yield of FF was obtained by measuring the time evolution of the absorbance of the FF under light irradiation. The ring-closure reaction of FF is determined following Eq. 2-13 which is provided by combining Eq. 2-2 and 2-3.

$$\frac{d[C]}{dt} = -\frac{\phi_{co}q_0}{V}(1 - 10^{-\epsilon_{c,\lambda_i}[C]l})$$

Equation 2-13

Following Lambert-Beer equation, Eq. 2-14 is described.

$$d[C] = -\frac{dA_{\lambda_i}}{\epsilon_{c,\lambda_i}l}$$

Equation 2-14

The combination of Eq. 2-13 and 2-14 provides Eq. 2-15.

$$\frac{dA_{\lambda_i}}{\epsilon_{c,\lambda_i}l} \frac{1}{dt} = \frac{\phi_{co}q_0}{V}(1 - 10^{-A_{\lambda_i}(t)})$$

Equation 2-15

The integral of Eq 2-15 gives Eq. 2-16<sup>81</sup>.

$$\ln(10^{A_{\lambda_i}(t)} - 1) = \ln(10^{A_{\lambda_i}(0)} - 1) - \frac{\phi_{co} q_0 \varepsilon_{c,\lambda_i} l \ln 10}{V} t$$

Equation 2-16

where  $A_{\lambda_i}(t)$ ,  $\varepsilon_{c,\lambda_i}$ ,  $l$ ,  $V$  are the absorbance at 530 nm, the molar extinction coefficient at 530 nm, the optical length of the sample, and the sample volume, respectively.  $A_{\lambda_i}(t)$  was regarded as the absorbance of the closed-ring form because the open-ring form has no absorption in the visible region. Here, the linear relation between  $\ln(10^{-A_{\lambda_i}(t)} - 1)$  and  $t$  provides the slope  $m$  which determines the quantum yield for the ring-opening reaction  $\phi_{co}$ (Eq. 2-17).

$$\phi_{co} = -\frac{mV}{q_0 \varepsilon_{c,\lambda_i} l \ln 10}$$

Equation 2-17

The quantum yield of the ring-closure reaction  $\phi_{oc}$  was determined using Eq. 2-18.

$$\frac{d[O]}{dt} = -\frac{\phi_{oc} q_0}{V} \frac{\varepsilon_{o,\lambda_i} [O] f}{\varepsilon_{c,\lambda_i} [C] + \varepsilon_{o,\lambda_i} [O]} + \frac{\phi_{co} q_0}{V} \frac{\varepsilon_{c,\lambda_i} [C] f}{\varepsilon_{c,\lambda_i} [C] + \varepsilon_{o,\lambda_i} [O]}$$

Equation 2-18

$f$  is a fraction of light absorbed by a sample, estimated from the absorbance at 365 nm (Eq. 2-19).

$$f = 1 - 10^{-\varepsilon_{c,\lambda_i} [C] l + \varepsilon_{o,\lambda_i} [O] l}$$

Equation 2-19

In general, when the absorbance of the closed-ring form is 20 times lower than that of the open-ring form (Eq. 2-20), Equation 2-18 can be reduced and convened in Eq. 2-21.

$$\varepsilon_{o,\lambda_i} [O] \geq 20 \varepsilon_{c,\lambda_i} [C]$$

Equation 2-20

$$\frac{d[O]}{dt} = -\frac{\phi_{oc} q_0}{V} (1 - 10^{-\varepsilon_{o,\lambda_i} [O] l})$$

Equation 2-21

Following Lambert-Beer equation, Eq. 2-22 is described.

$$d[O] = -\frac{dA_{\lambda_i}}{\varepsilon_{o,\lambda_i} l}$$

Equation 2-22

The combination of Eq. 2-19, 2-20, and 2-22 provides Eq. 2-23.

$$\frac{dA_{\lambda_i}}{\varepsilon_c l} \frac{1}{dt} = \frac{\phi_{co} q_0}{V} (1 - 10^{-\varepsilon_{c,\lambda_i} [C] l})$$

Equation 2-23

The integral of Eq. 2-23 gives Eq. 2-24.

$$\ln(10^{A_{\lambda_i}(t)} - 1) = \ln(10^{A_{\lambda_i}(0)} - 1) - \frac{\phi_{oc} q_0 \varepsilon_{o,\lambda_i} l \ln 10}{V} t$$

Equation 2-24

Here, the linear relationship between  $\ln(10^{A_{\lambda_i}(t)} - 1)$  and  $t$  provides the slope  $m$  which determines the quantum yield for the ring-closure reaction  $\phi_{oc}$ (Eq. 2-25).

$$\phi_{oc} = -\frac{mV}{q_0 \epsilon_{o,\lambda_i} l \ln 10}$$

Equation 2-25

To determine the photoconversion quantum yields of FF-TMR and FF-TMR-BSA, I estimated each value of absorbance  $A_{est,\lambda_i}(t)$  using  $I_{Fl,nor}(t)$ . The absorbance  $A_{est,\lambda_i}(t)$  were calculated to determine the quantum yield for the ring-closure/opening reaction using Eq. 2-26 and 2-27, respectively.

$$A_{est,\lambda_i}(t) = cl(\epsilon_{o,\lambda_i} - (\epsilon_{o,\lambda_i} - \epsilon_{c,\lambda_i})(1 - I_{Fl,nor}(t))), \lambda_i = 365 \text{ nm}$$

Equation 2-26

$$A_{est,\lambda_i}(t) = cl(\epsilon_{c,\lambda_i} - (\epsilon_{c,\lambda_i} - \epsilon_{o,\lambda_i})I_{Fl,nor}(t)), \lambda_i = 530 \text{ nm}$$

Equation 2-27

Since the ring-closure/opening reaction follows the first-order kinetics (Eq. 11 and 12), Eq 2-26 and 2-27 provide Eq 2-28 and 2-29, respectively.

$$A_{est,\lambda_i}(t) = cl(\epsilon_{o,\lambda_i} - (\epsilon_{o,\lambda_i} - \epsilon_{c,\lambda_i})(1 - \exp(-kt))), \lambda_i = 365 \text{ nm}$$

Equation 2-28

$$A_{est,\lambda_i}(t) = cl(\epsilon_{c,\lambda_i} - (\epsilon_{c,\lambda_i} - \epsilon_{o,\lambda_i})(1 - \exp(-kt))), \lambda_i = 530 \text{ nm}$$

Equation 2-29

From the Eq. 2-13 and 2-21, following equations are obtained (Eq. 2-30 and 2-31)

$$\ln(10^{A_{est,\lambda_i}(t)} - 1) = \ln(10^{A_{est,\lambda_i}(0)} - 1) - \frac{\phi_{oc} q_0 \epsilon_{o,\lambda_i} l \ln 10}{V} t, \lambda_i = 365 \text{ nm}$$

Equation 2-30

$$\ln(10^{A_{est,\lambda_i}(t)} - 1) = \ln(10^{A_{est,\lambda_i}(0)} - 1) - \frac{\phi_{co} q_0 \epsilon_{c,\lambda_i} l \ln 10}{V} t, \lambda_i = 530 \text{ nm}$$

Equation 2-31

Here, the linear relation between  $\ln(10^{A_{est,\lambda_i}(t)} - 1)$  and  $t$  provides the slope  $m$  which determines the quantum yield for the ring-closure/opening reaction respectively (Eq. 2-32 and 2-33).

$$\phi_{oc} = -\frac{mV}{q_0 \epsilon_{o,\lambda_i} l \ln 10}, \lambda_i = 365 \text{ nm}$$

Equation 2-32

$$\phi_{co} = -\frac{mV}{q_0 \epsilon_{c,\lambda_i} l \ln 10}, \lambda_i = 530 \text{ nm}$$

Equation 2-33

**Förster's distance between the closed-ring form of FF and TMR**

---

Förster's distance ( $R_0$ ) between the closed-ring form of FF and TMR was calculated by following Förster's equation (Eq. 2-34).

$$R_0^6 = \frac{9000 (\ln 10) \kappa^2 Q_D}{128 \pi^5 n^4 N_A} J = 8.79 \times 10^{-25} n^{-4} \kappa^2 Q_D J \text{ (cm}^6\text{)}$$

Equation 2-34

Here,  $n$ ,  $N_A$ ,  $\kappa^2$ , and  $Q_D$  are the solvent refractive index, Avogadro constant, orientation factor, and fluorescence quantum yield of the donor fluorophore.  $J$  is a spectral overlap integral between absorption of the acceptor, FF ( $\epsilon_A(\lambda)$ ) and donor emission ( $F_D(\lambda)$ ), and determine the value ( $J = 3.21 \times 10^{-7} \text{ mol} \cdot \text{cm}^6$ ) following Eq. 2-35<sup>82</sup>.

$$J = \frac{\int_0^\infty \epsilon_A(\lambda) F_D(\lambda) \lambda^4 d\lambda}{\int_0^\infty F_D(\lambda) d\lambda}$$

Equation 2-35

Since the linker between donor and acceptor has multiple single bonds with free rotation, the orientation factor was approximated to  $\kappa^2 = 2/3$ .  $Q_D$  is the value of the fluorescence quantum yield of TMR ( $Q_D = 0.41$ <sup>33</sup>). Förster's distance was calculated as  $R_0 = 5.4 \text{ nm}$  using the Eq. 3. It is enough distance to cause FRET from TMR to the closed-ring form of FF because the simulated distance of FF and TMR in FF-TMR is small (maximum 1.5 nm).

#### Fluorescence quantum yields measurements of FF-TMR and FF-TMR-BSA

---

Fluorescence quantum yields of FF-TMR and FF-TMR-BSA were measured in 100 mM phosphate buffer (pH 7.4) and ethanol (only FF-TMR), containing 0.5% DMSO at 25 °C. Rhodamine B in ethanol ( $\Phi_{\text{ref}} = 0.49$ <sup>83</sup>) was used as a reference. Fluorescence measurements were performed at 500 nm excitation. Fluorescence quantum yields ( $\Phi_{\text{FL}}$ ) were determined following Eq. 2-36<sup>84</sup>.

$$\Phi_{\text{FL}} = \Phi_{\text{ref}} \frac{A_{\text{ref}} F_s n_s^2}{A_s F_{\text{ref}} n_{\text{ref}}^2}$$

Equation 2-36

Here,  $A_s$  and  $A_{\text{ref}}$  are the absorbances at the excitation wavelength,  $F_s$  and  $F_{\text{ref}}$  are the relative fluorescence intensities, and  $n_s$  and  $n_{\text{ref}}$  are the solvent refractive indices of the sample and reference, respectively.

#### Measurement of photostationary state at 365/530 nm of FF and FF-TMR

---

Photostationary state (PSS) of FF and FF-TMR were measured by obtained peaks area using HPLC monitored at isosbestic points. Isosbestic points at 260 nm (FF in phosphate buffer), 269 nm (FF in ethanol), 272 nm (FF-TMR in phosphate buffer), and 270 nm (FF-TMR in ethanol) was determined by absorption spectra.

#### Measurement of LogP of 5-carboxy tetramethylrhodamine (TMR) and FF-TMR

---

The LogP of TMR and FF-TMR were experimentally measured following a previous report<sup>85</sup>. UV-vis spectroscopy

was used to determine the concentration of each solute in water and *n*-octanol.

#### **Immunostaining procedure and Fluorescence imaging**

---

HeLa cells were cultured in Dulbecco's modified Eagle's medium (DMEM) on cover glasses in a 24-well plate. After washing thrice with PBS buffer, the cells were incubated with 10% formalin solution (250  $\mu$ L/well) at room temperature for 15 min for cell fixation. After another washing step (thrice with PBS buffer), the cells were incubated in PBS buffer (250  $\mu$ L/well) containing 0.2% Triton<sup>®</sup> X-100 for 10 min for permeabilization. Then, HeLa cells were washed twice with PBS and blocked by 10% BSA in PBS buffer (250  $\mu$ L/well) at room temperature for 30 min. After removal of the blocking buffer, HeLa cells were incubated with 1  $\mu$ M FF-TMR-tubBAB in 3% BSA/PBS buffer (250  $\mu$ L/well) at room temperature for 1 h. HeLa cells were then washed thrice with PBS buffer (for 5 min each) and incubated with 1  $\mu$ M ATTO655-IgG in 3% BSA/PBS buffer (250  $\mu$ L/well) at room temperature for 1 h. After washing step (thrice with PBS buffer for 5 min each), the cells were mounted on glass slides using mounting reagent (Mowiol<sup>®</sup>4-88/*p*-phenylenediamine=9/1, 16  $\mu$ L/well). Microscopic images of the immunostained HeLa cells were recorded on a confocal laser-scanning microscope (FV10i; Olympus Corp., Tokyo, Japan) with excitation/emission at 559/570–670 nm for FF-TMR-tubBAB detection, and the excitation/emission at 635/660–760 nm for ATTO655-IgG detection.

#### **Live-cells imaging**

---

HeLa cells were washed thrice with Hanks' balanced salt solution (HBSS). The cells were incubated with 2.0  $\mu$ M FF-TMR and 0.05% LysoTracker<sup>®</sup> Green in DMEM containing 0.2% DMSO at 37 °C and 5% CO<sub>2</sub> for 30 min. The cells were then washed with HBSS three times and added DMEM. Microscopic images of the FF-TMR/LysoTracker<sup>®</sup> Green-treated cells were recorded using a FV10i microscope with excitation/emission at 473/490–590 nm for LysoTracker<sup>®</sup> Green detection and at 559/570–670 nm for FF-TMR detection.

#### **Image analysis**

---

Image analyses were done with commercial software ImageJ (Fiji)<sup>86</sup> and MetaMorph (Molecular Devices, LLC; SanJose, CA, USA). Pearson's correlation coefficients were determined using a Coloc2 Fiji plugin in ImageJ software. The fluorescence signal of images was processed with the ImageJ software. Ratiometric images were generated using a MetaMorph.

## Chapter 3. No-Wash Fluorogenic Labeling of Proteins for Reversible Photoswitching in Live Cells

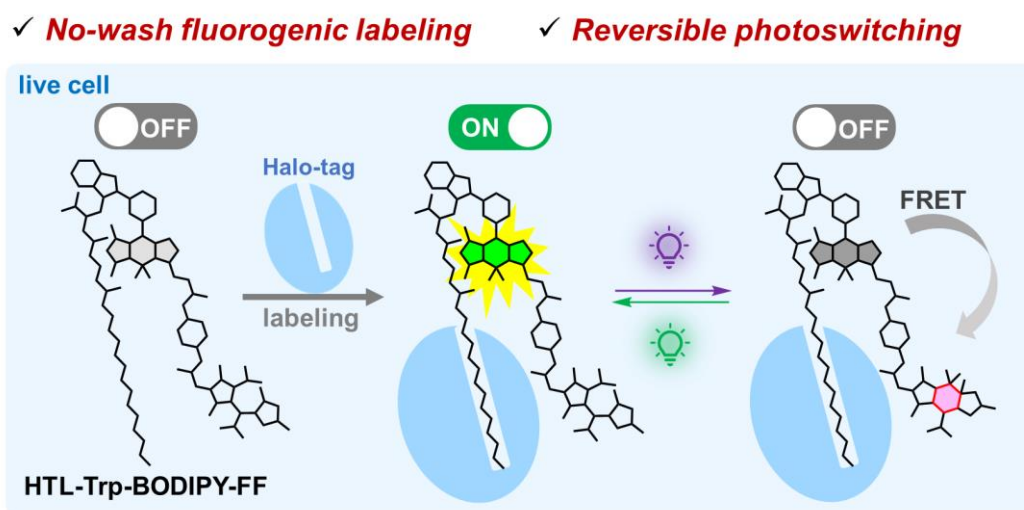
The content of this chapter has been published in:

Torii, K.; Benson, S.; Hori, Y.; Vendrell, M.; Kikuchi, K. No-Wash Fluorogenic Labeling of Proteins for Reversible Photoswitching in Live Cells. *Chem. Sci.* **2024**, *15* (4), 1393-1401.

<https://doi.org/10.1039/D3SC04953A>.

### Abstract

Photoswitchable fluorescent molecules (PSFMs) are positioned as valuable tools for biomolecule localization tracking and super-resolution imaging technologies due to their unique ability to reversibly control fluorescence intensity upon light irradiation. Despite the high demand for PSFMs that are suitable for live-cell imaging, no general method has been reported that enables reversible fluorescence control on proteins of interest in living cells. Herein, I have established a platform to realize reversible fluorescence switching in living cells by adapting a protein labeling system. I have developed a new PSFM, named HTL-Trp-BODIPY-FF, which exhibits strong fluorogenicity upon recognition of Halo-tag protein and reversible fluorescence photoswitching in living cells. This is the first example of a PSFM that can be applicable to a general-purpose Halo-tag protein labeling system for no-wash live-cell imaging.



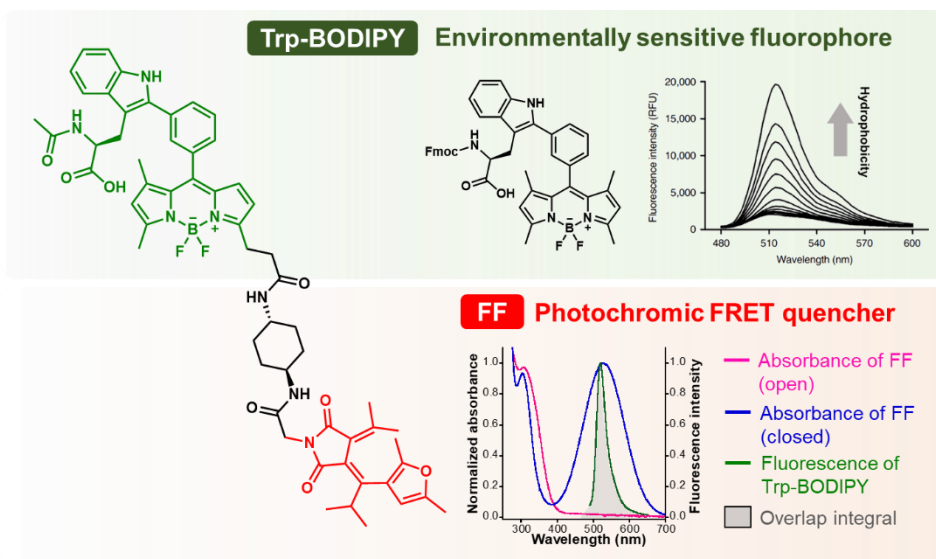
Graphical Abstract for Chapter 3

Adapted with permission from ref 52 under CC BY-NC.

### 3-1. Molecular design and synthesis of Trp-BODIPY-FF

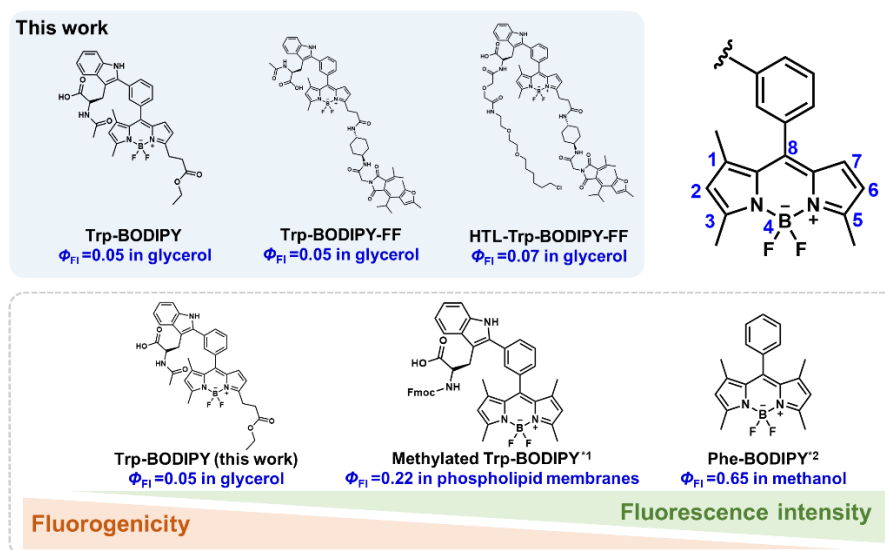
First, I designed the photoswitchable fluorogenic molecule Trp-BODIPY-FF to scrutinize its photophysical properties, including both environmental sensitivity and photoswitching performance (Figure 3-1-1). Trp-BODIPY<sup>65-71</sup> is an environmentally sensitive fluorophore that emits green fluorescence in high viscosity or hydrophobic environments. In the previous study, the authors' group optimized the core structure of Trp-BODIPY, which has high environmental sensitivity and ease of synthesis<sup>66</sup>. Trp-BODIPY has lower fluorescence quantum yields ( $\phi_{FL}=0.22$  in phospholipid membranes<sup>65</sup>) compared to the conventional meso-phenyl BODIPY ( $\phi_{FL}=0.65$  in methanol<sup>87</sup>) (Figure 3-1-2). This may be due to photoinduced electron transfer from donor tryptophan to the acceptor BODIPY core<sup>69</sup>. In addition, the introduction of tryptophan can lower the transition energy barrier to access non-radiative decay, which improves fluorogenicity<sup>69</sup>. Considering this advantage of tryptophan, I speculate that Trp-BODIPY exhibits significant fluorogenic ability in hydrophobic environments, and it is suitable for the purpose of fluorogenic protein labeling.

FF is known to exhibit quantitative photoisomerization to the closed-ring form upon irradiation at 365 nm and to the open-ring form upon irradiation at 530 nm as shown in Chapter 2 (Table 3-1-1). The open-ring form of FF has no visible absorption and doesn't show any FRET with Trp-BODIPY (Figure 3-1-1); therefore, Trp-BODIPY is able to fluoresce in a hydrophobic environment (ON state). While the closed-ring form has a large absorption band in the visible region and functions as a FRET-based fluorescence quencher for Trp-BODIPY (OFF state). In addition, a rigid cyclohexyl linker between Trp-BODIPY and FF was incorporated to prevent intramolecular quenching<sup>49,58</sup>. Taken together, Trp-BODIPY-FF was designed to exhibit its fluorogenic nature after interacting with the protein surface, and the fluorescence intensity was regulated by light irradiation (Graphical Abstract). The detailed synthetic scheme and full characterization data are described in the Experimental Sections (Scheme 3-2).



**Figure 3-1-1. Molecular design of Trp-BODIPY-FF.**

Chemical structure of Trp-BODIPY-FF. The upper fluorescence spectra were modified from the previous study<sup>65</sup>. The bottom spectra represent absorption spectra of FF (50  $\mu\text{M}$ ) and fluorescence spectra of Trp-BODIPY (1.0  $\mu\text{M}$ ) in 100 mM phosphate buffer (pH 7.4). The area marked by gray shadow represents overlap integral of absorption of FF (closed-ring form) and fluorescence of TMR.  $\lambda_{\text{ex}}$ : 550 nm. Adapted with permission from ref 65 under CC BY. Adapted with permission from ref 52 under CC BY-NC.

**Figure 3-1-2. The comparison of photophysical properties of each BODIPY derivative.**

The introduction of tryptophan or the absence of a methyl group at 1 or 7 position in the BODIPY core improves the fluorogenicity because the transition energy barrier to access non-radiative decay is decreased. On the other hands, it facilitates non-radiative decay instead of the radiative decay as fluorescence. This tendency has already investigated in the previous report<sup>69</sup>.  $\Phi_{\text{Fl}}$ : fluorescence quantum yield \*1: the value of  $\Phi_{\text{Fl}}$  was cited from previous work<sup>87</sup>. \*2: the value of  $\Phi_{\text{Fl}}$  was cited from previous work<sup>65</sup>. Adapted with permission from ref 52 under CC BY-NC.

**Table 3-1-1. Optical properties of FF in various solvents.**

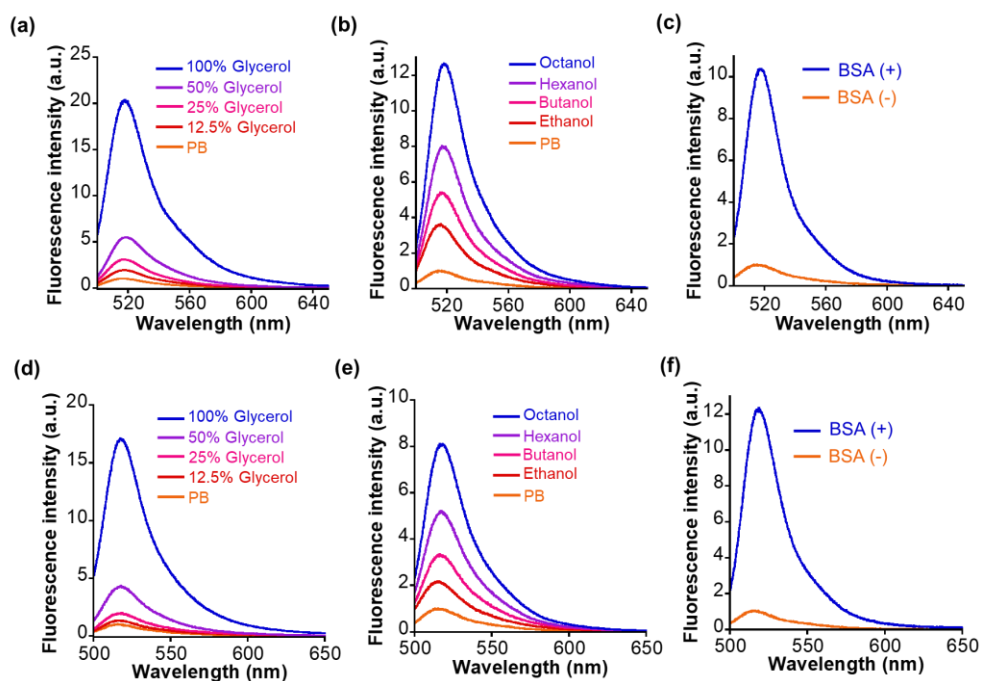
Solvent	PB, BSA(-) <sup>*1</sup>	Glycerol	Octanol	PB, BSA(+)
$\lambda_{\text{max,c}}$ [nm] <sup>*2</sup>	529	529	500	514
$\epsilon_{\text{max,c}}$ [ $\text{M}^{-1}\text{cm}^{-1}$ ] <sup>*2</sup>	$6.1 \times 10^3$	$5.1 \times 10^3$	$6.4 \times 10^3$	$6.4 \times 10^3$
$k_{\text{oc}}/I_{\text{IRR}}$ [ $\text{s}^{-1}/\text{mW}$ ]	$6.4 \times 10^{-3}$	$5.2 \times 10^{-3}$	$4.3 \times 10^{-3}$	$5.9 \times 10^{-4}$
$k_{\text{co}}/I_{\text{IRR}}$ [ $\text{s}^{-1}/\text{mW}$ ]	$5.7 \times 10^{-5}$	$2.8 \times 10^{-4}$	$9.4 \times 10^{-4}$	$8.4 \times 10^{-4}$
$\Phi_{\text{OC}}$	0.72	0.24	0.42	0.91
$\Phi_{\text{CO}}$	$3.5 \times 10^{-3}$	$1.6 \times 10^{-2}$	$6.8 \times 10^{-2}$	$5.2 \times 10^{-2}$

\*<sup>1</sup>Quoted from previous work<sup>49</sup>. \*<sup>2</sup>maximum absorption wavelength ( $\lambda_{\text{max,c}}$ ) and molar extinction coefficient ( $\epsilon_{\text{max,c}}$ ) of closed-ring form was recorded after light irradiation at 365 nm (10  $\text{mW}/\text{cm}^2$ ) for 10 min. Adapted with permission from ref 52 under CC BY-NC.

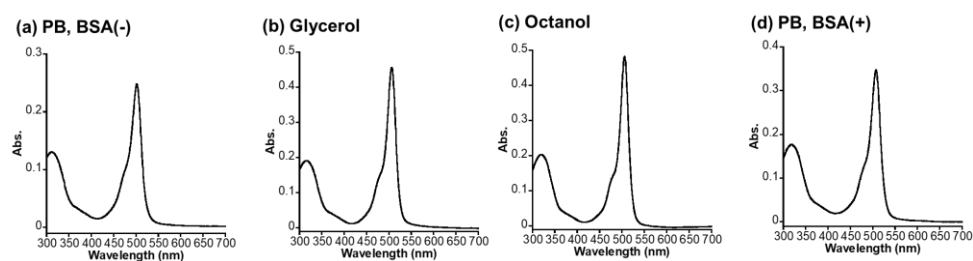
### 3-2. Photophysical properties of Trp-BODIPY-FF

---

Next, I measured the photophysical properties of Trp-BODIPY-FF. The fluorescence intensity of Trp-BODIPY-FF is significantly higher with increasing glycerol concentration in phosphate buffer (PB) and displays its strongest fluorescence emission in high viscosity environments (Figure 3-2-1a). This viscosity sensitivity is consistent with the previously reported Trp-BODIPY derivatives<sup>65-71</sup>. The viscosity sensitivity is closely related to the C-C bond rotation between the BODIPY core and the phenyl group. In high viscosity environments, this rotation is restricted, while the fluorescence intensity is enhanced because the nonradiative decay is inactivated<sup>88</sup>. The fluorescence intensity also increased upon its dissolution in low polarity alcohols with longer carbon numbers (*n*-octanol > *n*-hexanol > *n*-butanol > ethanol > PB), indicating that BODIPY-FF shows strong fluorescence in low polarity environments (Figure 3-2-1b). The reason that higher polarity environments cause loss of fluorescence may be partially due to photoinduced electron transfer from the benzene moiety to the BODIPY core, as some phenyl BODIPY derivatives have previously reported<sup>89</sup>. In addition, the fluorescence intensity was significantly enhanced in PB containing bovine serum albumin (BSA) as a model protein, indicating that the fluorogenic behavior was triggered on the hydrophobic binding cavities within BSA (Figure 3-2-1c). The reason for the increase in fluorescence intensity of Trp-BODIPY-FF surrounded by BSA is considered to be two factors: (1) a decrease in polarity by being adjacent to the hydrophobic protein surface, and (2) the sterically inhibited C-C bond rotation between BODIPY and phenyl groups. These photophysical properties were also confirmed in the control Trp-BODIPY without FF, indicating that its fluorogenicity was not affected by the introduction of FF (Figure 3-2-1d-f). The absorption spectra and fluorescence quantum yield of Trp-BODIPY and Trp-BODIPY-FF were also measured (Figure 3-2-2,3 and Table 3-2-1,2). The fluorescence quantum yields in each solvent between Trp-BODIPY and Trp-BODIPY-FF are almost the same value, indicating that open-ring form of FF does not affect the fluorescence intensity of Trp-BODIPY. The fluorescence quantum yield of Trp-BODIPY-FF is lower than previously reported Trp-BODIPY derivatives. This is mainly due to the absence of the methyl group at the 7-position in the BODIPY cores (Figure 3-1-2).


**Figure 3-2-1. Environmental sensitivities of Trp-BODIPY(-FF).**

Fluorescence spectra of 1  $\mu\text{M}$  (a-c) Trp-BODIPY-FF and (d-f) Trp-BODIPY in (a,d) 100 mM phosphate buffer (PB) (pH 7.4) with increasing glycerol concentrations (from top to bottom: 100, 50, 25, 12.5, and 0%), in (b,e) *n*-octanol (blue line), *n*-hexanol (purple line), *n*-butanol (magenta line), ethanol (red line), and PB (orange line) in (c,f) 100 mM PB (pH 7.4) with/without 5  $\mu\text{M}$  BSA (blue/orange line).  $\lambda_{\text{ex}}$ : 470 nm, 37  $^{\circ}\text{C}$ . Adapted with permission from ref 52 under CC BY-NC.


**Figure 3-2-2. Absorption spectra of Trp-BODIPY.**

10  $\mu\text{M}$  Trp-BODIPY dissolved in (a) 100 mM phosphate buffer (pH 7.4), (b) glycerol, (c) *n*-octanol, and (d) 100 mM phosphate buffer (pH 7.4) with 250  $\mu\text{M}$  BSA including 1% DMSO. Temperature: 37  $^{\circ}\text{C}$ . Adapted with permission from ref 52 under CC BY-NC.

**Table 3-2-1. Optical properties of Trp-BODIPY.**

Solvent	PB, BSA(-)	Glycerol	Octanol	PB, BSA(+)
$\lambda_{\text{ex,max}}$ [nm]	502	506	506	507
$\varepsilon_{\text{max}}$ [ $\text{M}^{-1}\text{cm}^{-1}$ ]	$2.5 \times 10^4$	$4.6 \times 10^4$	$4.8 \times 10^4$	$3.5 \times 10^4$
$\lambda_{\text{em,max}}$ [nm]	516	517	518	518
$\Phi_{\text{FL}}$	$4.5 \times 10^{-3}$	$4.2 \times 10^{-2}$	$2.6 \times 10^{-2}$	$2.7 \times 10^{-2}$

Adapted with permission from ref 52 under CC BY-NC.

Table 3-2-2. Optical properties of Trp-BODIPY-FF.

Solvent		PB, BSA(-)	Glycerol	Octanol	PB, BSA(+)
$\lambda_{\text{ex,max}}$ [nm]	O*1	508	507	507	509
	C*1	507	507	507	509
$\epsilon_{\text{max}}$ [ $\text{M}^{-1}\text{cm}^{-1}$ ]	O	$2.3 \times 10^4$	$5.3 \times 10^4$	$5.2 \times 10^4$	$4.7 \times 10^4$
	C	$2.4 \times 10^4$	$5.5 \times 10^4$	$5.6 \times 10^4$	$5.0 \times 10^4$
$\lambda_{\text{em,max}}$ [nm]	O	517	518	519	518
	C	517	518	519	518
$\Phi_{\text{FL}}$	O	$4.4 \times 10^{-3}$	$4.9 \times 10^{-2}$	$3.2 \times 10^{-2}$	$2.9 \times 10^{-2}$
	C	$2.2 \times 10^{-3}$	$2.2 \times 10^{-2}$	$1.1 \times 10^{-2}$	$7.4 \times 10^{-3}$
$k_{\text{oc}}/I_{\text{irr}}$ [ $\text{s}^{-1}/\text{mW}$ ]		$7.0 \times 10^{-3}$	$6.5 \times 10^{-3}$	$9.2 \times 10^{-3}$	$1.2 \times 10^{-2}$
$k_{\text{co}}/I_{\text{irr}}$ [ $\text{s}^{-1}/\text{mW}$ ]		$2.3 \times 10^{-3}$	$3.7 \times 10^{-4}$	$4.0 \times 10^{-3}$	$1.6 \times 10^{-3}$
$\Phi_{\text{OC}}$		$4.3 \times 10^{-2}$	$3.1 \times 10^{-2}$	$4.8 \times 10^{-2}$	$5.0 \times 10^{-2}$
$\Phi_{\text{CO}}$		$5.1 \times 10^{-3}$	$6.2 \times 10^{-2}$	0.11	0.16

\*1O: open-ring form, C: closed-ring form obtained by irradiation at 365 nm ( $10 \text{ mW}/\text{cm}^2$ ) for 3 min. Adapted with permission from ref 52 under CC BY-NC.

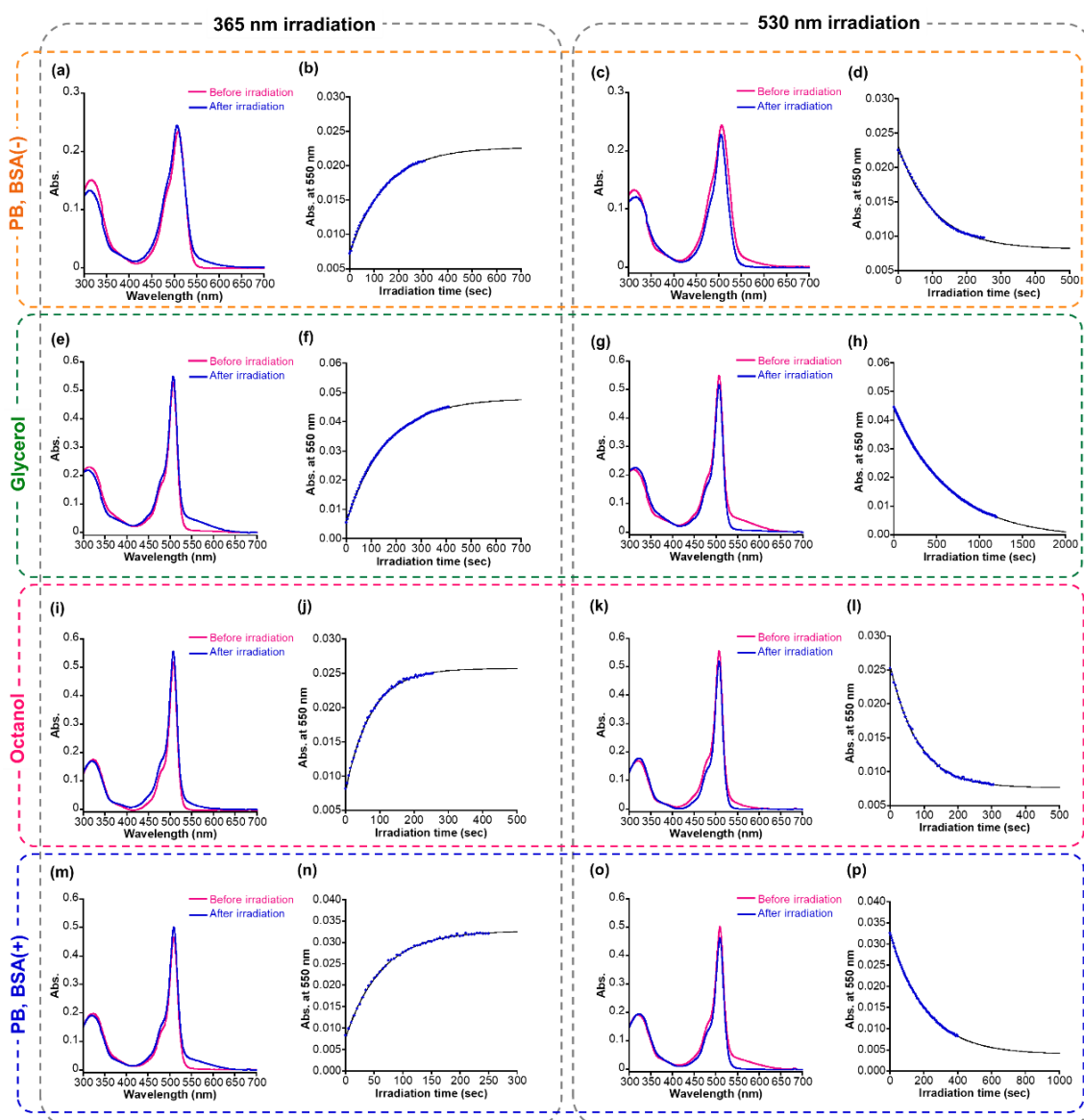


**Figure 3-2-3. Absorption spectra of Trp-BODIPY-FF.**

10  $\mu\text{M}$  Trp-BODIPY-FF dissolved in (a,b) 100 mM phosphate buffer (pH 7.4), (c,d) glycerol, (e,f) *n*-octanol, and (g,h) 100 mM phosphate buffer (pH 7.4) with 50  $\mu\text{M}$  (5 eq.) BSA including 1% DMSO. (a,c,e,g) The spectra before and after 365 nm (10 mW/cm<sup>2</sup>, 3 min) irradiation are shown by the magenta and blue lines, respectively. (b,d,f,h) The spectra before and after 530 nm (10 mW/cm<sup>2</sup>, 3 min) irradiation are shown by the magenta and blue lines, respectively. Temperature: 37 °C. Adapted with permission from ref 52 under CC BY-NC.

Light irradiation experiments were performed for each solution in PB, glycerol, *n*-octanol, and PB in the presence of BSA. In all samples, the absorbance at 550 nm was increased following first-order kinetics upon 365 nm irradiation and decreased following first-order kinetics after 530 nm irradiation (Figure 3-2-3). It clearly indicated that Trp-BODIPY-FF undergoes cyclization and cycloreversion reactions at 365 and 530 nm irradiation. The detailed photophysical parameters including cyclization/cycloreversion reaction kinetics per light irradiation intensity ( $k_{\text{oc/co}}/I_{\text{irr}}$ ) and quantum yields ( $\Phi_{\text{oc/co}}$ ) are determined following Experimental Sections (Table 3-2-2). More importantly, the fluorescence intensity of Trp-BODIPY-FF was decreased after 365 nm irradiation and completely recovered after 530 nm irradiation (Figure 3-2-4), indicating that FF works as a photoswitchable FRET quencher. However, in PB and glycerol, the fluorescence intensity after 365 nm irradiation was gradually suppressed with increasing cycle number (Figure 3-2-5a,b). Meanwhile, Trp-BODIPY-FF in both *n*-octanol and PB including BSA showed persistent repeatability (Figure 3-2-5c,d).

The difference in the photostability in each solution is due to the ease of aggregate formation. Dissolution in low-polarity solvent (*n*-octanol) or solution containing hydrophobic protein surfaces circumvent the formation of aggregate, while in higher-polarity solvents (PB or glycerol), Trp-BODIPY-FF readily aggregates to reduce its photostability during light irradiation. To quantify the photofatigue progress over repetitive photoirradiation cycles, I calculated quenching efficiency of Trp-BODIPY-FF in each solvent conditions. Quenching efficiency was determined by dividing the difference in fluorescence intensity before and after 365 nm irradiation by the fluorescence intensity before 365 nm irradiation. Trp-BODIPY-FF in both *n*-octanol and PB including BSA showed no photofatigue over 30 photoirradiation cycles (Figure 3-2-6). In addition, the bioconjugate of Trp-BODIPY-FF with BSA, named Trp-BODIPY-FF-BSA, was prepared by conjugating with the carboxylic acid of Trp-BODIPY-FF and lysine residues on the BSA surface. A detailed preparation procedure and characterization are described in Experimental Sections and Figure 3-2-7a. Trp-BODIPY-FF-BSA also shows persistent reversibility even after 10 cycles of photoswitching (Figure 3-2-7b). These results are consistent with the findings that showed improved photostability of PSFM in hydrophobic environments, including protein surfaces, thus circumventing intermolecular aggregation among PSFMs as discussed in Chapter 2. As a next step, I conjugated Trp-BODIPY-FF to a Halo-tag ligand to evaluate whether Trp-BODIPY-FF would display fluorescence switching upon

binding to the Halo-tag protein.

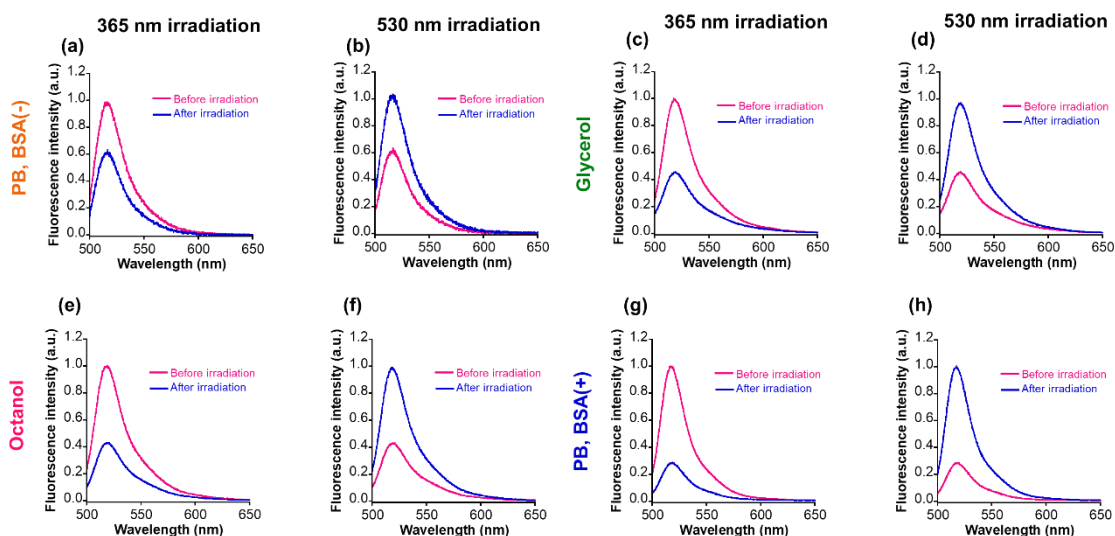


**Figure 3-2-4. Photoswitching properties of Trp-BODIPY-FF.**

Fluorescence spectra of 1  $\mu\text{M}$  Trp-BODIPY-FF dissolved in (a,b) 100 mM phosphate buffer (pH 7.4), (c,d) glycerol, (e,f) *n*-octanol, and (g,h) 100 mM phosphate buffer (pH 7.4) with 5  $\mu\text{M}$  (5 eq.) BSA including 1% DMSO. (a,c,e,g) The spectra before and after 365 nm (10 mW/cm<sup>2</sup>, 3 min) irradiation are shown by the magenta and blue lines, respectively. (b,d,f,h) The spectra before and after 530 nm (10 mW/cm<sup>2</sup>, 3 min) irradiation are shown by the magenta and blue lines, respectively.  $\lambda_{\text{ex}}$ : 470 nm, 37 °C. Adapted with permission from ref 52 under CC BY-NC.

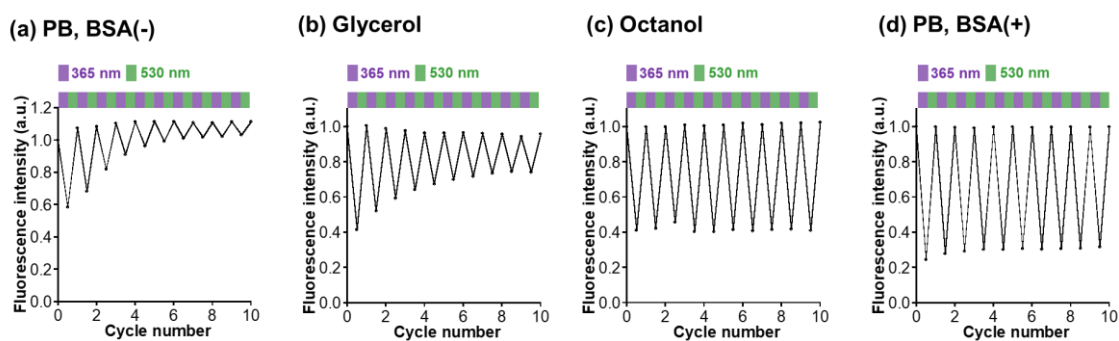


**Figure 3-2-5. Photoswitching reversibility of Trp-BODIPY-FF.**

Fluorescence intensity of 1  $\mu\text{M}$  Trp-BODIPY-FF in (a) PB (pH 7.4), (b) glycerol, (c) *n*-octanol, and (d) PB (pH 7.4) including 5  $\mu\text{M}$  BSA.  $\lambda_{\text{ex/em}}$ : 490/520 nm, 37 °C. 365/530 nm irradiations are indicated by purple/green shades, respectively. Adapted with permission from ref 52 under CC BY-NC.

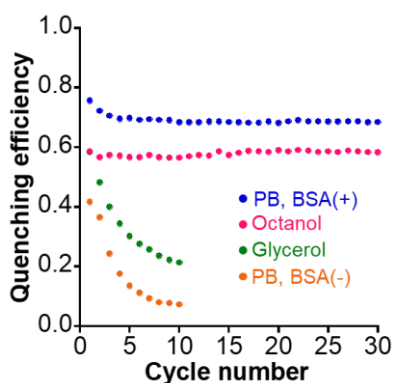


**Figure 3-2-6. Quenching efficiency of Trp-BODIPY-FF over repetitive photoirradiation cycles.**

1  $\mu$ M Trp-BODIPY-FF in PB (orange), glycerol (green), octanol (magenta), and PB with 5  $\mu$ M BSA (blue).  $\lambda_{\text{ex/em}}$ : 490/520 nm, 37  $^{\circ}$ C. Adapted with permission from ref 52 under CC BY-NC.

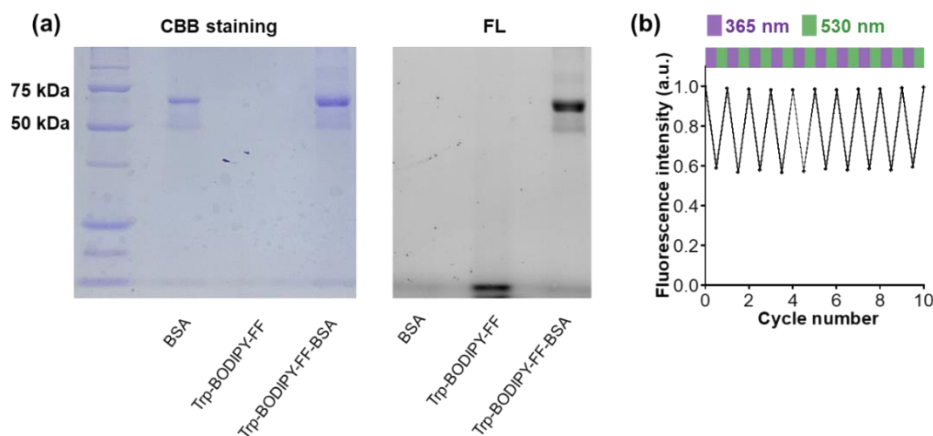


**Figure 3-2-7. Characterization and photoswitching reversibility of Trp-BODIPY-FF-BSA.**

(a) The results of SDS-PAGE of Trp-BODIPY-FF-BSA. The left and right image shows CBB-stained and fluorescence images, respectively. The first column at the left represents a ladder to confirm protein size (BSA: 66.5 kDa). Fluorescence images were obtained with excitation at 488 nm. (b) Fluorescence reversibility of 1  $\mu$ M Trp-BODIPY-FF-BS in PB (pH 7.4),  $\lambda_{\text{ex/em}}$ : 490/520 nm, 37  $^{\circ}$ C. 365/530 nm irradiations are indicated by purple/green shades, respectively. Adapted with permission from ref 52 under CC BY-NC.

### 3-3. Synthesis and photophysical properties of HTL-Trp-BODIPY-FF

The compound, HTL-Trp-BODIPY-FF, was synthesized by conjugation of the chloroalkane Halo-tag ligand to the terminal amine of Trp-BODIPY-FF. The detailed synthetic scheme and characterization data are included in the Experimental Sections and Scheme 3-3 and 3-4. I verified that HTL-Trp-BODIPY-FF had increased fluorescence intensity in high viscosity environments as with its precursor compound, Trp-BODIPY-FF (Figure 3-3-1a, Table 3-3-1). I further measured the viscosity dependence of HTL-Trp-BODIPY-FF and compared it to Trp-BODIPY and Trp-BODIPY-

FF by plotting the fluorescence intensity against dynamic viscosity (Figure 3-3-1c). HTL-Trp-BODIPY-FF clearly showed a strong fluorescence emission with increasing dynamic viscosity, consistent with the results of Trp-BODIPY and Trp-BODIPY-FF. I corroborated that the fluorescence intensity of HTL-Trp-BODIPY-FF was enhanced in non-polar environments in the same manner as Trp-BODIPY-FF (Figure 3-3-1b, Table 3-3-1). The affinity of Trp-BODIPY-FF and HTL-Trp-BODIPY-FF with BSA (Figure 3-3-2) was also measured. The dissociation constant of Trp-BODIPY-FF and HTL-Trp-BODIPY-FF were determined to be  $6.9 \pm 2.8 \mu\text{M}$  and  $11.8 \pm 3.9 \mu\text{M}$ , respectively and the fluorescence increase of HTL-Trp-BODIPY-FF was suppressed compared to Trp-BODIPY-FF in higher concentrations of BSA. It may be due to the Halo-tag ligand (HTL) bypassing the interaction of Trp-BODIPY moiety with BSA.

The absorption spectrum and fluorescence quantum yield of HTL-Trp-BODIPY-FF were also determined (Figure 3-3-3, Table 3-3-1). The photophysical properties including excitation maximum, extinction coefficient, and fluorescence quantum yield between Trp-BODIPY-FF and HTL-Trp-BODIPY-FF are almost the same value. Importantly, in the presence of Halo-tag in PB, the fluorescence intensity increased 12-fold as shown in Figure 3-3-4a and Table 3-3-1. Furthermore, SDS-PAGE gel analysis was performed and a fluorescent band between 25 and 37 kDa was observed, indicating that Halo-tag (34 kDa) had been coupled to HTL-Trp-BODIPY-FF (Figure 3-3-4b). Fluorogenicity has great advantages for live cell imaging because it suppresses background fluorescence derived from free probes and allows for no-wash labelling.

I further described the optimized conformation of HTL-Trp-BODIPY-FF labeled with Halo-tag using computational calculation software (Macromodel: Schrödinger Maestro v13.1) as presented in the Experimental Sections. As shown in Figure 3-3-5, no specific binding interaction was observed except for the HTL region and Trp-BODIPY was partially exposed in hydrophobic environments surrounded by several hydrophobic residues. It is reported that the crystal structure of HTL-bearing tetramethylrhodamine demonstrates multiple interaction modes at the protein surface<sup>44</sup>. Although I do not exclude the possibility that HTL-Trp-BODIPY-FF may have similar interactions, the result of the simulation indicates that Trp-BODIPY is confined in hydrophobic environments, supporting the mechanism that fluorogenic enhancement is induced by hydrophobic interaction and steric suppression of phenyl ring rotation.

The labeling rate constant  $k_2$  was determined to be  $1.5 \times 10^3 \text{ M}^{-1}\text{s}^{-1}$  by the second-order approximation, and the increase in fluorescence intensity was mostly completed within 20 min of the addition of  $1.0 \mu\text{M}$  HTL-Trp-BODIPY-FF to  $2.0 \mu\text{M}$  Halo-tag solution (Figure 3-3-4c). The labeling kinetics of common Halo-tag ligands conjugated with fluorophores show different values (around  $10^3 \sim 10^8 \text{ M}^{-1}\text{s}^{-1}$  order) because the affinity is strongly influenced by the substrate structure<sup>90</sup>. The labeling kinetics of HTL-Trp-BODIPY-FF with Halo-tag is relatively slow compared to other fluorophores bearing HTL. Thus, it may be partly due to the negative charge on the carboxylic acid of HTL-Trp-

BODIPY-FF, which has less affinity to the Halo-tag protein surface, resulting in low labeling kinetics<sup>90</sup>. In the molecular simulation, no interactions were observed, and the carboxylic acid was exposed to the solvent (water) away from the Halo-tag residues as shown in Figure 3-3-5. According to the latest reviews on bioorthogonal click chemistry, one of the fastest click reactions is the inverse electron demand Diels-Alder (IEDDA) reaction<sup>91</sup>. The kinetics of IEDDA reactions used for protein labeling reach about  $10^4 \text{ M}^{-1}\text{s}^{-1}$ <sup>191-93</sup>. The rate constant is higher than that of HTL-Trp-BODIPY-FF with Halo-tag; however, IEDDA reactions have been reported that fluorophore-tetrazine conjugates shows slow labeling and takes more than 1 hour until the completion in living cells<sup>94,95</sup>. On the other hand, HTL-Trp-BODIPY-FF completed Halo-tag labeling within 20 min in live cells, which is comparable to the result of the in vitro experiment, as discussed in the next section 3-4.

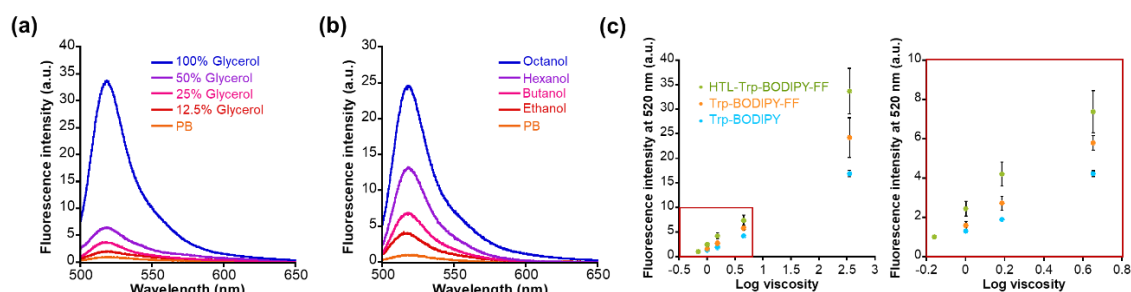


**Figure 3-3-1. Environmental sensitivities of HTL-Trp-BODIPY-FF.**

**(a,b)** Fluorescence spectra of  $1 \mu\text{M}$  HTL-Trp-BODIPY-FF in **(a)** 100 mM phosphate buffer (PB) (pH 7.4), increasing glycerol/sample volume (from top to bottom: 100, 50, 25, 12.5, and 0%), in **(b)** *n*-octanol (blue line), *n*-hexanol (purple line), *n*-butanol (magenta line), ethanol (red line), and 100 mM PB (pH 7.4) (orange line), respectively. **(c)** The relationship between the fluorescence intensity of HTL-Trp-BODIPY-FF (green), Trp-BODIPY-FF (orange), and Trp-BODIPY (sky blue) and Log viscosity. Dynamic viscosity was calculated using the equations described in ref 96.  $\lambda_{\text{ex/em}}$ : 470/520 nm, 37 °C. Adapted with permission from ref 52 under CC BY-NC.

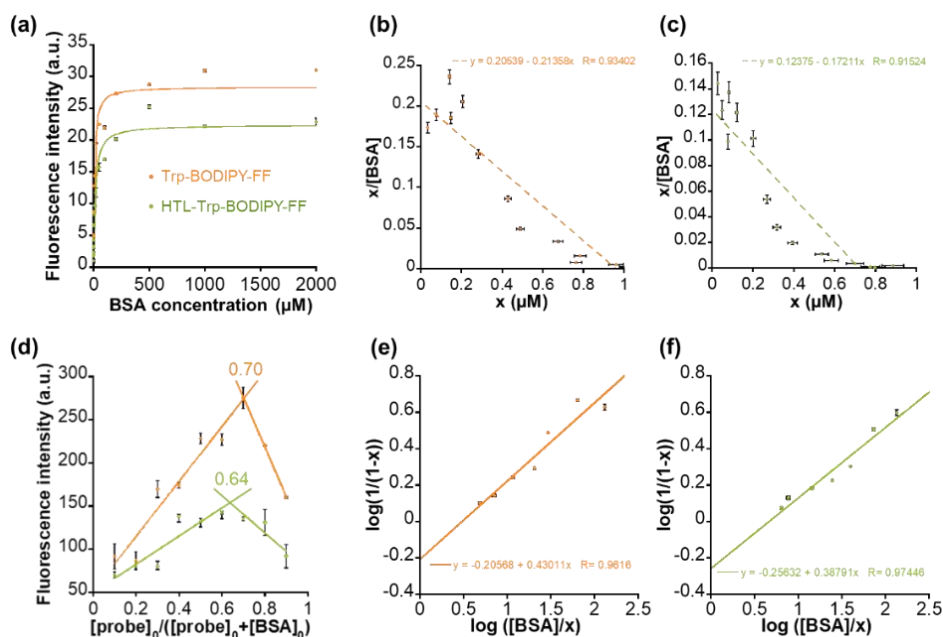


**Figure 3-3-2. The affinity of (HTL-)Trp-BODIPY-FF with BSA.**

(a) Fluorescence intensity at 520 nm of 1.0  $\mu\text{M}$  Trp-BODIPY-FF (orange) or 1.0  $\mu\text{M}$  HTL-Trp-BODIPY-FF (green) in 100 mM phosphate buffer (pH 7.4) containing varying concentrations of BSA (from 0 to 2000  $\mu\text{M}$ ).  $N=3$ . (b,c) Scatchard plot for (b) Trp-BODIPY-FF or (c) HTL-Trp-BODIPY-FF vs BSA in 100 mM phosphate buffer.  $x$  is concentrations of BSA-probe complex estimated from fluorescent intensity at 520 nm using Eq. 21. The probe concentration is fixed at 1.0  $\mu\text{M}$ .  $N=3$ . Both plots do not give a proper linear approximation, and show a downward convex-like curve, suggesting the presence of multiple different binding sites. (d) Job's plot for Trp-BODIPY-FF (orange) or HTL-Trp-BODIPY-FF (green) vs BSA in 100 mM phosphate buffer (pH 7.4) monitoring the fluorescence intensity at 520 nm. The concentration of the probe varied from 100 to 900 nM as the BSA concentration decreased from 900 to 100 nM.  $N=3$ . Both Job's plots exhibited maximum mole fractions ( $[\text{probe}]_0 / ([\text{probe}]_0 + [\text{BSA}]_0)$ ) around 0.70 (Trp-BODIPY-FF) and 0.64 (HTL-Trp-BODIPY-FF), implicating that the binding ratio of the probe to BSA is 2. (e,f) The modified Hill plot for (e) Trp-BODIPY-FF or (f) HTL-Trp-BODIPY-FF vs BSA in 100 mM phosphate buffer (pH 7.4) monitoring the fluorescence intensity at 520 nm. The concentration of the probe is fixed at 1.0  $\mu\text{M}$ . BSA concentration varied from 1.0 to 100  $\mu\text{M}$ .  $N=3$ . The plot of Trp-BODIPY-FF vs BSA gives  $K_D = 6.9 \pm 2.8 \mu\text{M}$ , and HTL-Trp-BODIPY-FF vs BSA gives  $K_D = 11.8 \pm 3.9 \mu\text{M}$ , respectively. Adapted with permission from ref 52 under CC BY-NC.

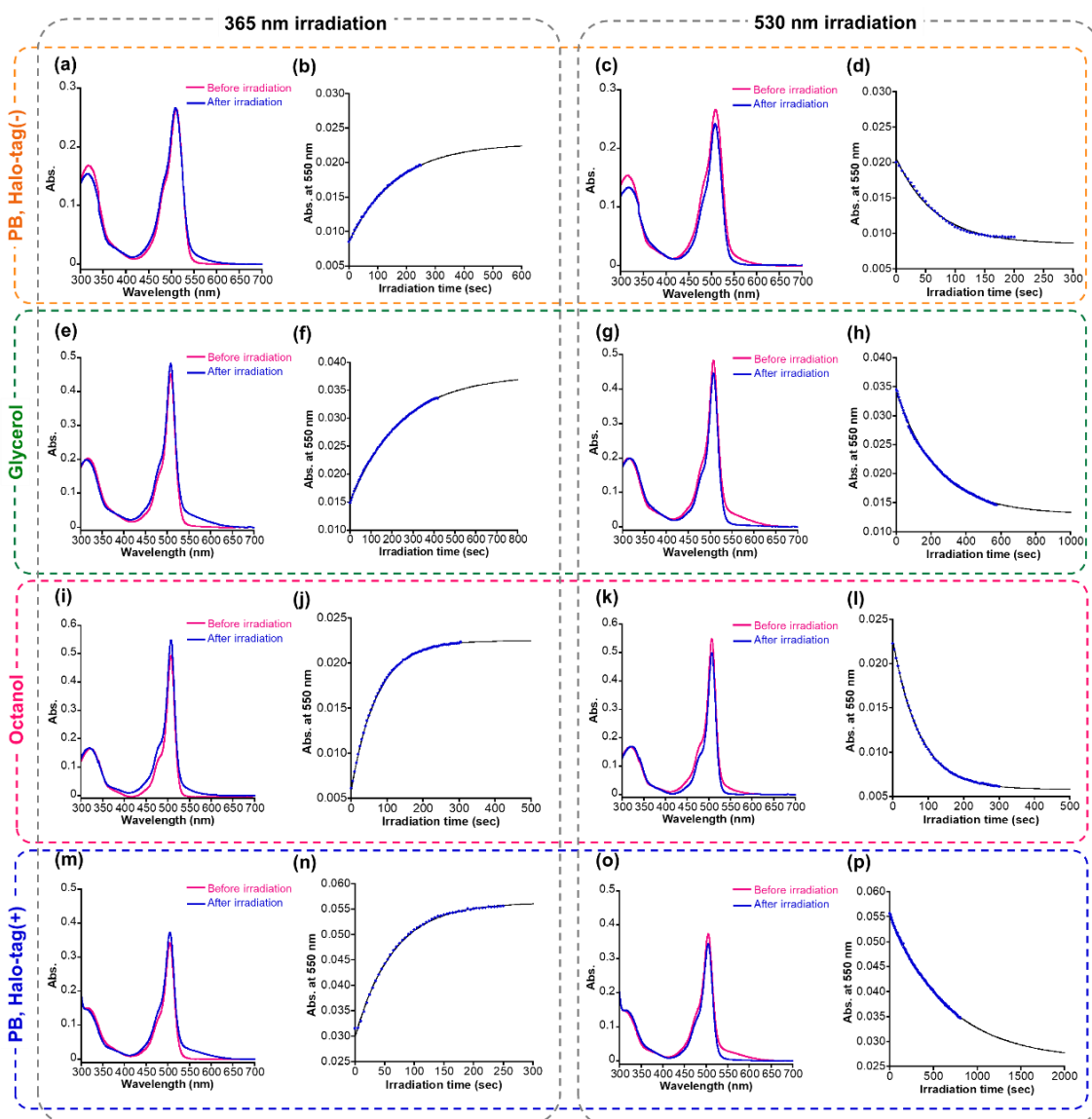


**Figure 3-3-3. Absorption spectra of HTL-Trp-BODIPY-FF.**

10  $\mu\text{M}$  HTL-Trp-BODIPY-FF dissolved in (a,b) 100 mM phosphate buffer (pH 7.4), (c,d) glycerol, (e,f) *n*-octanol, and (g,h) 100 mM phosphate buffer (pH 7.4) after incubated with 20  $\mu\text{M}$  (2 eq.) Halo-tag for 1 h. All samples contain 1% DMSO. (a,c,e,g) The spectra before and after 365 nm (10 mW/cm<sup>2</sup>, 3 min) irradiation are shown by the magenta and blue lines, respectively. (b,d,f,h) The spectra before and after 530 nm (10 mW/cm<sup>2</sup>, 3 min) irradiation are shown by the magenta and blue lines, respectively. Temperature: 37 °C. Adapted with permission from ref 52 under CC BY-NC.

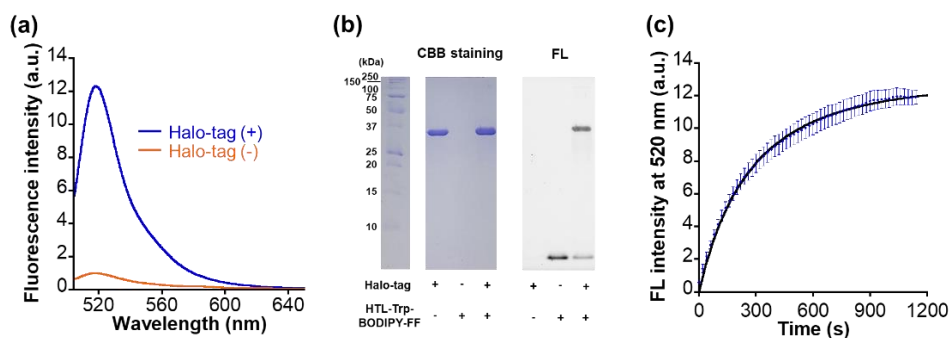


**Figure 3-3-4. Fluorogenicity of HTL-Trp-BODIPY-FF.**

**(a)** Fluorescence spectra of 1.0  $\mu\text{M}$  HTL-Trp-BODIPY-FF in PB (pH 7.4), after (blue) before (orange) incubating with 2.0  $\mu\text{M}$  Halo-tag for 20 min.  $\lambda_{\text{ex}}$ : 490 nm, 37  $^{\circ}\text{C}$ . **(b)** The results of SDS-PAGE of HTL-Trp-BODIPY-FF with Halo-tag. The left and right image shows CBB-stained and fluorescence images, respectively. 2.0  $\mu\text{M}$  HTL-Trp-BODIPY-FF was incubated with 4.0  $\mu\text{M}$  Halo-tag at 37  $^{\circ}\text{C}$  for 1 h. The first column at the left represents a ladder to confirm protein size (Halo-tag: 34 kDa). Fluorescence images were obtained with excitation at 488 nm. **(c)** Time course of fluorescence intensities of 1.0  $\mu\text{M}$  HTL-Trp-BODIPY-FF after incubating with 2.0  $\mu\text{M}$  Halo-tag in PB (pH 7.4). Adapted with permission from ref 52 under CC BY-NC.

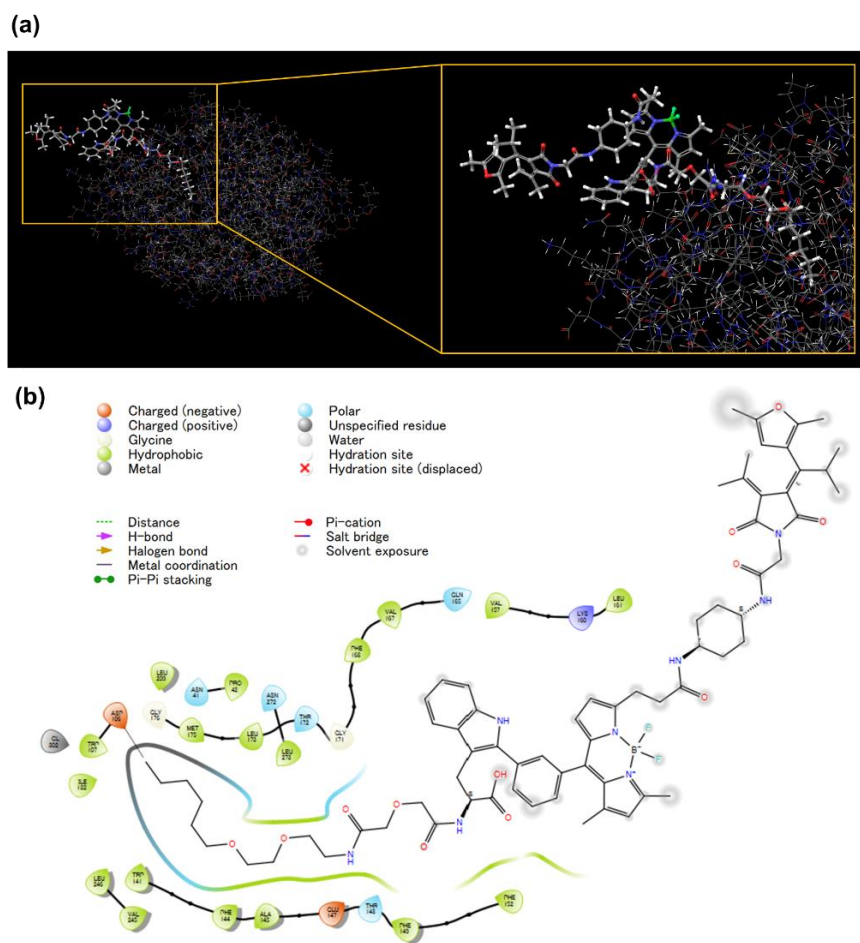


**Figure 3-3-5. Docking simulation of HTL-Trp-BODIPY-FF with Halo-tag.**

(a) Optimized three-dimensional (3D) structure on HTL-Trp-BODIPY-FF with Halo-tag (PDB ID: 6u32) using MacroModel software. (b) The two-dimensional (2D) ligand interaction map of HTL-Trp-BODIPY-FF with Halo-tag created from (a). Adapted with permission from ref 52 under CC BY-NC.

**Table 3-3-1. Optical properties of HTL-Trp-BODIPY-FF.**

Solvent		PB, Halo-tag(-)	Glycerol	Octanol	PB, Halo-tag(+)
$\lambda_{\text{ex,max}}$ [nm]	O*1	511	508	508	505
	C*1	510	508	508	505
$\epsilon_{\text{max}}$ [ $\text{M}^{-1}\text{cm}^{-1}$ ]	O	$2.6 \times 10^4$	$4.5 \times 10^4$	$5.0 \times 10^4$	$3.4 \times 10^4$
	C	$2.7 \times 10^4$	$4.8 \times 10^4$	$5.5 \times 10^4$	$3.7 \times 10^4$
$\lambda_{\text{em,max}}$ [nm]	O	517	519	518	520
	C	517	519	518	520
$\Phi_{\text{FL}}$	O	$2.8 \times 10^{-3}$	$6.5 \times 10^{-2}$	$2.8 \times 10^{-2}$	$3.0 \times 10^{-2}$
	C	$1.5 \times 10^{-3}$	$2.3 \times 10^{-2}$	$1.1 \times 10^{-2}$	$1.1 \times 10^{-2}$
$k_{\text{co}}/I_{\text{IRR}}$ [ $\text{s}^{-1}/\text{mW}$ ]		$6.2 \times 10^{-3}$	$4.2 \times 10^{-3}$	$9.5 \times 10^{-3}$	$1.1 \times 10^{-2}$
$k_{\text{co}}/I_{\text{IRR}}$ [ $\text{s}^{-1}/\text{mW}$ ]		$3.5 \times 10^{-3}$	$1.0 \times 10^{-3}$	$4.4 \times 10^{-3}$	$5.1 \times 10^{-4}$
$\Phi_{\text{OC}}$		$3.2 \times 10^{-2}$	$1.5 \times 10^{-2}$	$2.6 \times 10^{-2}$	$7.1 \times 10^{-2}$
$\Phi_{\text{CO}}$		$9.9 \times 10^{-3}$	$8.5 \times 10^{-2}$	0.12	0.14

\*1O: open-ring form, C: closed-ring form obtained by irradiation at 365 nm ( $10 \text{ mW}/\text{cm}^2$ ) for 3 min. Adapted with permission from ref 52 under CC BY-NC.

Light irradiation experiments were performed for each solution in glycerol, octanol, and before and after Halo-tag binding in PB. In all samples, the absorbance at 550 nm was increased following first-order kinetics upon 365 nm irradiation and decreased following first-order kinetics after 530 nm irradiation (Figure 3-3-3), and the fluorescence intensity was decreased after 365 nm irradiation followed by recovery after 530 nm irradiation (Figure 3-3-6). The detailed photoswitching parameters were determined following Experimental Sections (Table 3-3-1). The photophysical properties of HTL-Trp-BODIPY-FF labeled with Halo-tag were compared with other representative green photoswitchable fluorescent proteins applicable for super-resolution imaging (rsEGFP2<sup>97</sup>, Dronpa<sup>98</sup>, and Padron2<sup>99</sup>) in Table 3-3-2. Although, the fluorescence quantum yield and brightness of HTL-Trp-BODIPY-FF are lower than those of photoswitchable fluorescent proteins, both OFF-to-ON and ON-to-OFF photoswitching quantum yields ( $\Phi_{\text{OFF-ON}}$  and  $\Phi_{\text{ON-OFF}}$ ) are higher than those of proteins ( $\Phi_{\text{OFF-ON}}$  of Dronpa shows higher value; however,  $\Phi_{\text{ON-OFF}}$  is over 200 times lower than that of HTL-Trp-BODIPY-FF.  $\Phi_{\text{ON-OFF}}$  of Padron2 shows a slightly higher value; however,  $\Phi_{\text{OFF-ON}}$  is 10 times lower than that of HTL-Trp-BODIPY-FF). Overall, the photoswitching efficiency of HTL-Trp-BODIPY-FF is superior to photoswitchable fluorescent proteins. The photofatigue progress was observed in glycerol over 10 cycles of photoirradiation, while not in *n*-octanol even after 30 cycles of photoirradiation (Figure 3-3-7 and 3-3-8). Most importantly, the pre-labeled HTL-Trp-BODIPY-FF showed a rapid reduction of quenching efficiency over repeated light irradiation cycles, whereas the labeled HTL-Trp-BODIPY-FF obtains persistent fluorescence switching performance maintaining

over 50% quenching efficiency after repeated 30 cycles of light irradiation (Figure 3-3-8). It was demonstrated that the protein surface-assisted strategy is effective for site-specific labeling with Halo-tag and contributes to the improved photostability of a PSFM.

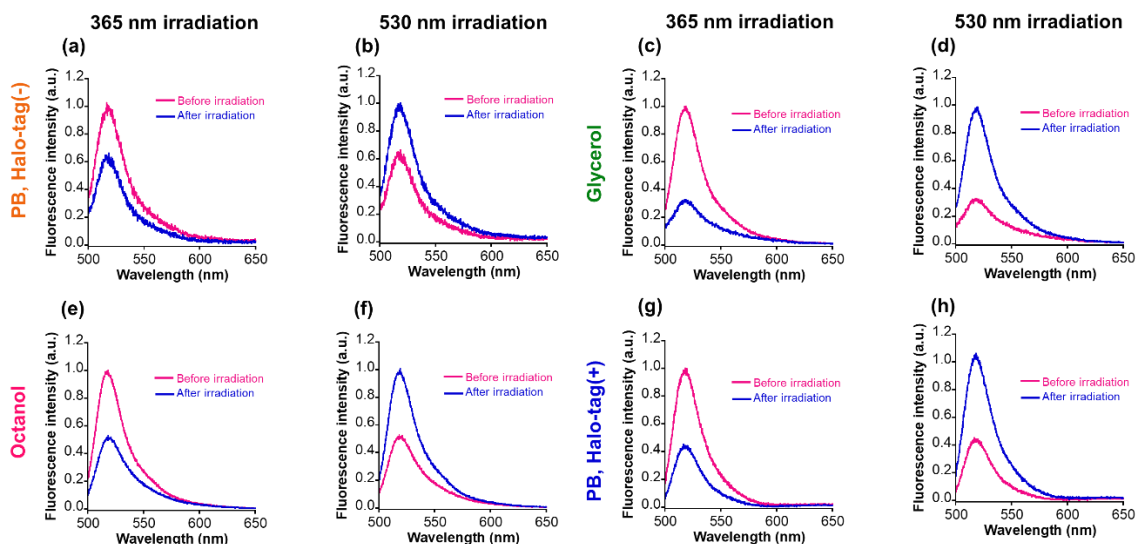


**Figure 3-3-6. Photoswitching properties of HTL-Trp-BODIPY-FF.**

Fluorescence spectra of 1  $\mu\text{M}$  HTL-Trp-BODIPY-FF dissolved in (a,b) 100 mM phosphate buffer (pH 7.4), (c,d) glycerol, (e,f) *n*-octanol, and (g,h) 100 mM phosphate buffer (pH 7.4) after incubating with 2  $\mu\text{M}$  (2 eq.) Halo-tag for 30 min. All samples contain 1% DMSO. (a,c,e,g) The spectra before and after 365 nm (10 mW/cm<sup>2</sup>, 3 min) irradiation are shown by the magenta and blue lines, respectively. (b,d,f,h) The spectra before and after 530 nm (10 mW/cm<sup>2</sup>, 3 min) irradiation are shown by the magenta and blue lines, respectively.  $\lambda_{\text{ex}}$ : 470 nm, 37 °C. Adapted with permission from ref 52 under CC BY-NC.

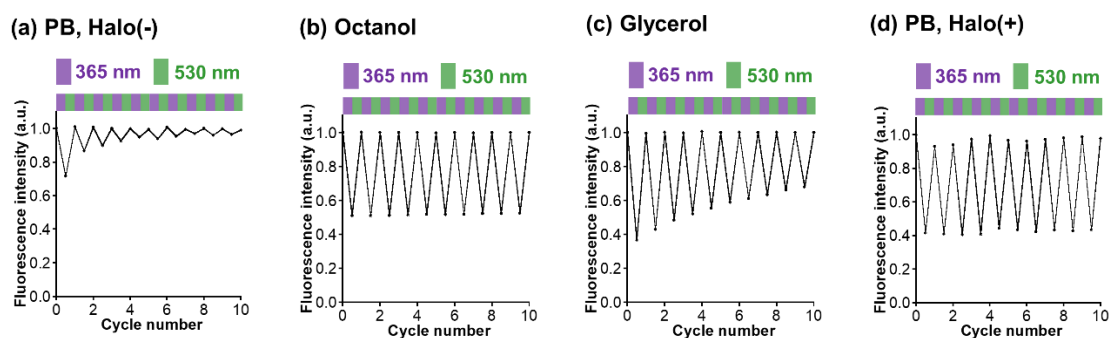


**Figure 3-3-7. Photoswitching reversibility of HTL-Trp-BODIPY-FF.**

Fluorescence intensity of 1  $\mu\text{M}$  HTL-Trp-BODIPY-FF in (a) PB (pH 7.4), (b) glycerol, (c) *n*-octanol, and (d) PB (pH 7.4) after incubating with 2  $\mu\text{M}$  (2 eq.) Halo-tag for 30 min. All samples contain 1% DMSO.  $\lambda_{\text{ex/em}}$ : 490/520 nm, 37 °C. 365/530 nm irradiations are indicated by purple/green shades, respectively. Adapted with permission from ref 52 under CC BY-NC.

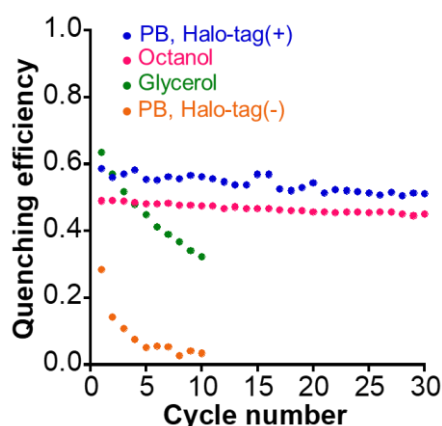


**Figure 3-3-8. Quenching efficiency of HTL-Trp-BODIPY-FF over repetitive photoirradiation cycles.**

1  $\mu\text{M}$  HTL-Trp-BODIPY-FF in PB (orange), glycerol (green), *n*-octanol (magenta), and PB after incubating with 2  $\mu\text{M}$  Halo-tag for 30 min (blue).  $\lambda_{\text{ex/em}}$ : 490/520 nm, 37  $^{\circ}\text{C}$ . Adapted with permission from ref 52 under CC BY-NC.

**Table 3-3-2. Comparison of photophysical properties of representative photoswitchable fluorescent proteins and HTL-Trp-BODIPY-FF.**

	rsEGFP2 <sup>*1</sup>	Dronpa <sup>*2</sup>	Padron2 <sup>*3</sup>	HTL-Trp-BODIPY-FF <sup>*4</sup>
$\lambda_{\text{ex,max}}$ [nm] <sup>*5</sup>	478	503	495	505
$\epsilon_{\text{max}}$ [ $\text{M}^{-1}\text{cm}^{-1}$ ] <sup>*5</sup>	$6.1 \times 10^4$	$9.5 \times 10^4$	$2.4 \times 10^4$	$3.4 \times 10^4$
$\lambda_{\text{em,max}}$ [nm] <sup>*5</sup>	503	518	513	520
$\Phi_{\text{FL}}$ <sup>*5</sup>	0.30	0.85	0.49	$3.0 \times 10^{-2}$
Brightness [ $\text{M}^{-1}\text{cm}^{-1}$ ]	$1.7 \times 10^4$	$8.1 \times 10^4$	$1.2 \times 10^4$	$1.0 \times 10^3$
$\Phi_{\text{ON-OFF}}$ <sup>*6</sup>	$8.9 \times 10^{-3}$	$3.2 \times 10^{-4}$	$8.9 \times 10^{-2}$	$7.1 \times 10^{-2}$
$\Phi_{\text{OFF-ON}}$ <sup>*6</sup>	0.12	0.37	$1.5 \times 10^{-2}$	0.14

\*1: Cited from ref 97. \*2: Cited from ref 98. \*3: Cited from ref 99. \*4: After labeling with Halo-tag. \*5: ON state. \*6: photoswitching quantum yield from ON to OFF state ( $\Phi_{\text{ON-OFF}}$ ) and from OFF to ON state ( $\Phi_{\text{OFF-ON}}$ ).  $\Phi_{\text{ON-OFF}}$  and  $\Phi_{\text{OFF-ON}}$  of HTL-Trp-BODIPY-FF are  $\Phi_{\text{OC}}$  and  $\Phi_{\text{CO}}$  respectively. Adapted with permission from ref 52 under CC BY-NC.

### 3-4. Live-cell imaging studies using HTL-Trp-BODIPY-FF

As a next step, I performed live cell imaging with HTL-Trp-BODIPY-FF. The fluorescence signals of HTL-Trp-BODIPY-FF were visualized in HeLa cells transfected with maltose binding protein (MBP) fused to Halo-tag in order to stain intracellular cytosol. The constructs were also fused with the red fluorescent protein, mCherry, to both confirm the colocalization of Halo-tag and HTL-Trp-BODIPY-FF and to quantitatively evaluate the fluorescence intensity changes of HTL-Trp-BODIPY-FF during light irradiation experiments. The plasmids used for live-cell imaging (pcDNA3.1(+)-MBP-Halo-mCherry) were prepared according to the procedures described in the Experimental Sections. After incubation of the cells with HTL-Trp-BODIPY-FF for 20 min, fluorescence images were acquired under a confocal laser scanning microscope. The green fluorescence signals from HTL-Trp-BODIPY-FF co-localized with the red fluorescence signal from mCherry in the cytosol of HeLa cells

expressing Halo-MBP-mCherry, (Figure 3-4-1a). In contrast, cells transfected with an empty vector (pcDNA3.1(+)) were devoid of fluorescent signals (Figure 3-4-1b). To demonstrate the stability of HTL-Trp-BODIPY-FF in living cells, I have performed extended live cell imaging and monitored fluorescence signals in transfected cells and background signals in non-transfected cells, which show no signal from mCherry in the same field of view with multiple cells. After 20 min of incubation from probe addition, the fluorescence signal from HTL-Trp-BODIPY-FF was fully enhanced in transfected cells (Figure 3-4-2). Importantly, as seen in Figure 3-4-2b, the fluorescence signals in transfected cells were maintained without any attenuation even after prolonged incubation time (up to 600 min after probe addition), while the background signal from non-transfected cells (surrounded by yellow circles in Figure 3-4-2b) was negligible in this visualization.

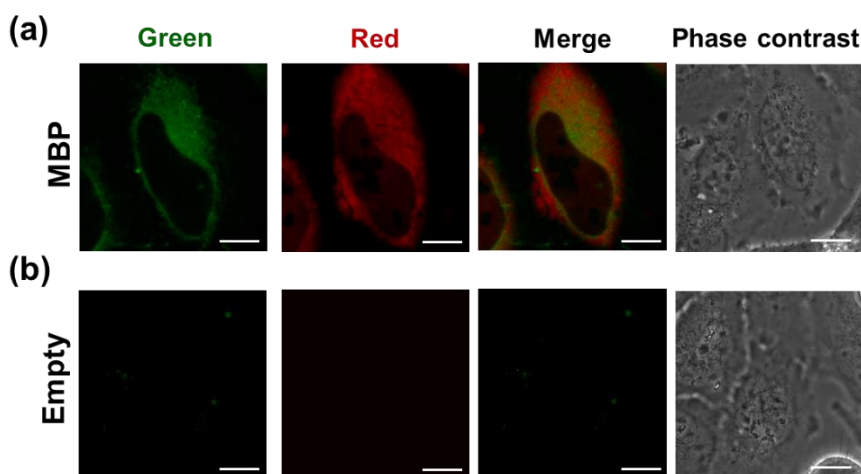


**Figure 3-4-1. Live cell imaging using HTL-Trp-BODIPY-FF.**

(a) MBP-Halo-mCherry and (b) empty vector (pcDNA3.1(+)) fused HeLa cells. Before observation, 1  $\mu$ M HTL-Trp-BODIPY-FF (0.1% DMSO) was added into the cell culture for 20 min. Scale bar 25  $\mu$ m. Green channel:  $\lambda_{ex/em}$ : 473/490-540 nm; Red channel:  $\lambda_{ex/em}$ : 559/570-620 nm. Adapted with permission from ref 52 under CC BY-NC.

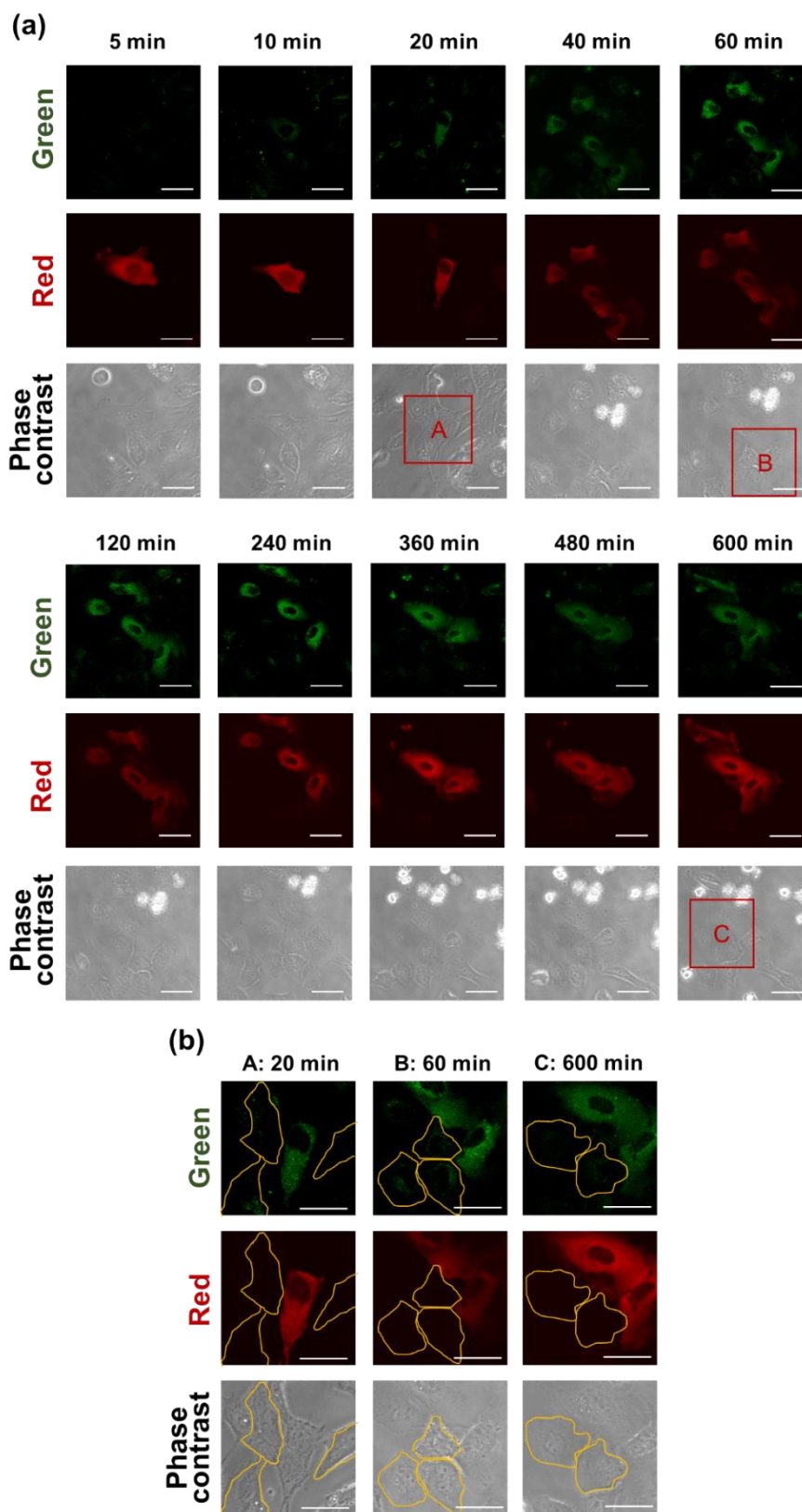
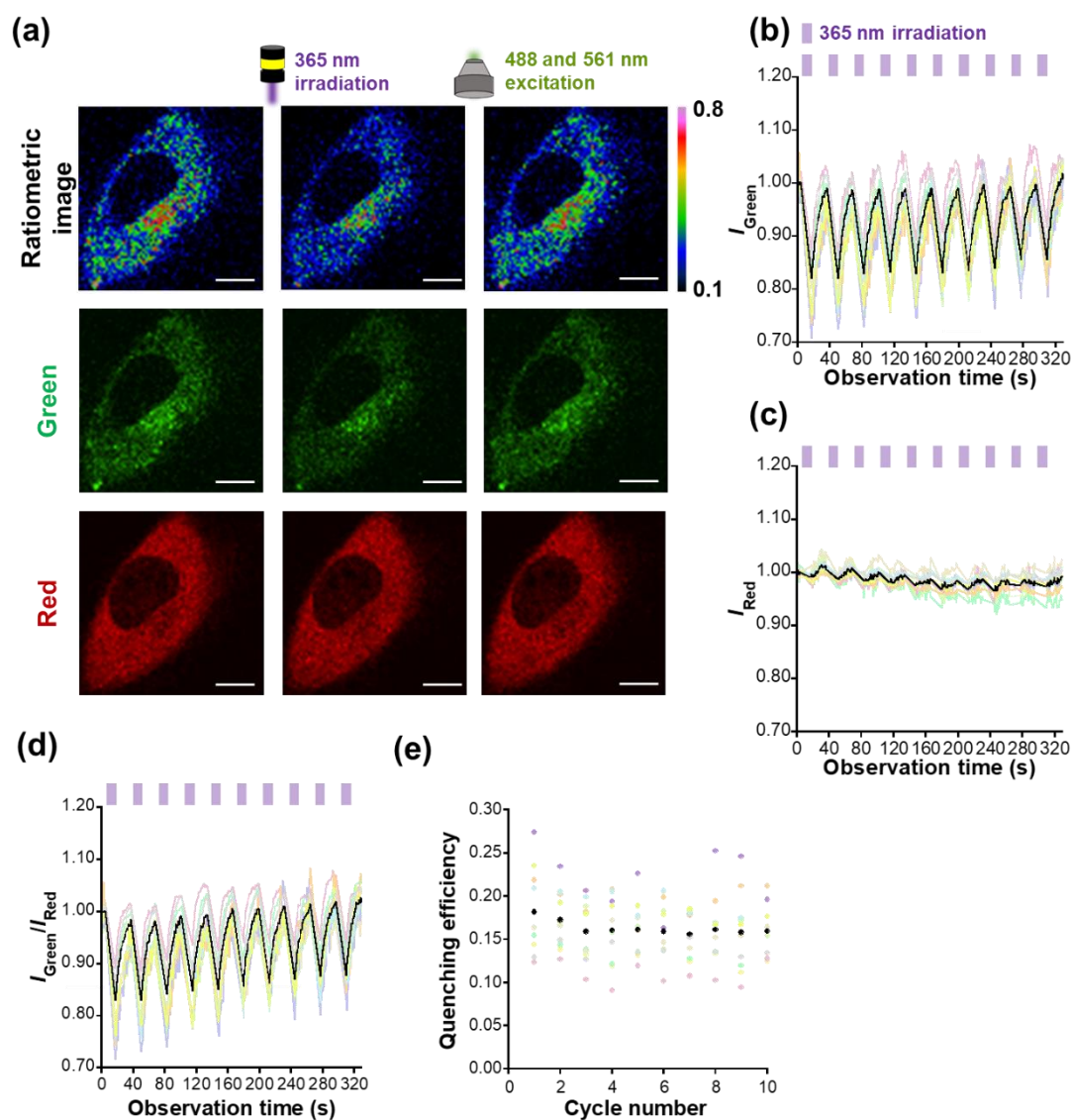


Figure 3-4-2. Extended long time live cell imaging using HTL-Trp-BODIPY-FF.

**(a)** HeLa cells were transfected with pcDNA3.1(+)-MBP-Halo-mCherry. Before observation, 1.0  $\mu$ M HTL-Trp-BODIPY-FF (0.1% DMSO) was added into the cell culture for 5, 10, 20, 40, 60, 120, 240, 360, 480, and 600 min, respectively. Scale bar 50  $\mu$ m. Green channel:  $\lambda_{ex/em}$ : 473/490-540 nm; Red channel:  $\lambda_{ex/em}$ : 559/570-620 nm. **(b)** The enlarged images of A, B, and C are marked as red squares in **(a)**. The non-transfected cells, which do not show any expression of mCherry, are surrounded by yellow circles. Scale bar 25  $\mu$ m. Adapted with permission from ref 52 under CC BY-NC.

I performed light irradiation experiments in Halo-MBP-mCherry expressing HeLa cells after treatments with HTL-Trp-BODIPY-FF. Cells were repeatedly irradiated at 365 nm for 10 sec and 488 and 561 nm for 20 sec, respectively, using LED light and excitation light from confocal microscopy. Although the 488- and 561-nm lasers were set up for excitation in the green channel (HTL-Trp-BODIPY-FF) and the red channel (mCherry), these light sources are sufficient to induce the cycloreversion reaction because the closed-ring form of FF has a large absorption band in the visible region (Figure 4) that covers both 488 and 561 nm. Detailed experimental conditions are described in the Experimental Sections. Under these conditions, the fluorescence intensity of HTL-Trp-BODIPY-FF decreased upon 365 nm irradiation and rapidly recovered upon 488 and 561 nm light stimulation, whereas the fluorescence intensity of mCherry showed little changes during light irradiation (Figure 3-4-3a-c). It indicates that the effect of FRET from HTL-Trp-BODIPY-FF to mCherry was negligible. This resulted in the fluorescence intensity ratio of HTL-Trp-BODIPY-FF to mCherry to decrease after 365 nm irradiation followed by recovery after 488 and 561 nm excitation light (Figure 3-4-3a,d). As shown in Figure 3-4-3d, it was confirmed that changes in fluorescence intensity induced by light stimulation were repeated over more than 10 cycles in a random selection of 10 cells. Moreover, I calculated the quenching efficiency of HTL-Trp-BODIPY-FF in living cells transfected with Halo-MBP-mCherry by dividing the difference in fluorescence intensity ratio before and after 365 nm irradiation by the fluorescence intensity ratio before 365 nm irradiation. It showed persistent reversibility even after 10 cycles of photoswitching, maintaining over 15% averaged quenching efficiency (Figure 3-4-3e).



**Figure 3-4-3. Ratiometric imaging of HeLa cells transfected with pcDNA3.1(+)-MBP-Halo-mCherry.**

(a) After adding 1  $\mu\text{M}$ , HTL-Trp-BODIPY-FF (0.1% DMSO), cells were incubated for more than 20 min. Samples were alternately irradiated at 365 nm (10 mW/cm<sup>2</sup> for 10 s) and 488 and 561 nm excitation light exposure (20 s). Scale bar: 10  $\mu\text{m}$ . Green channel:  $\lambda_{\text{ex}} = 488 \text{ nm}$ ,  $\lambda_{\text{em}} = 499\text{-}551 \text{ nm}$ . Red channel:  $\lambda_{\text{ex}} = 561 \text{ nm}$ ,  $\lambda_{\text{em}} = 571\text{-}625 \text{ nm}$ . Ratiometric images were generated by dividing the intensity of green channel by that of red channel in each pixel. Maximum ratio: 0.8; minimum ratio: 0.1. (b-d) Time course of the fluorescence intensities of (b) green channel and (c) red channel upon 365/488 and 561 nm irradiation (10 cycles). (d) The fluorescence intensity ratio was obtained by dividing the intensity of green channel by that of red channel ( $I_{\text{Green}}/I_{\text{Red}}$ ). The data were collected from a random selection of 10 cells. (e) Quenching efficiency calculated from the data of (d). The black (b-d) line and (e) dots represent the average ratio intensity and quenching efficiency from ten different cells. Other pale-colored (b-d) lines and (e) dots describe each ratio intensity/quenching efficiency from each cell. Adapted with permission from ref 52 under CC BY-NC.

The photoswitching behavior of unlabeled HTL-Trp-BODIPY-FF in non-transfected cells was also investigated (Figure 3-4-4). The signal intensity of non-transfected cells is about 3 times lower than that of non-transfected cells (Figure 3-4-4c). Figure 3-4-4d shows representative photoswitching behavior of transfected and non-transfected cells in the same field of view (Figure 3-4-4a,b). As seen in Figure 3-4-4e, the fluorescence signals from non-transfected cells were repeatedly changed upon light irradiation. To confirm the photoswitching performance for other targets in living cells, I have visualized both plasma membrane and mitochondria using the plasmids of pcDNA3.1(+)-Halo-EGFR-mCherry and pcDNA3.1(+)-Tom20-Halo-mCherry, respectively. I confirmed that the HTL-Trp-BODIPY-FF localized to the plasma membrane and mitochondria, respectively. Moreover, the photoirradiation experiments were performed as with cytosol imaging. Both plasma membrane and mitochondria imaging shows reputative fluorescence switching upon light irradiations (Figure 3-4-5 and 3-4-6). These experiments demonstrated that the protein-surface-assisted strategy can be applied to live cell imaging and enables reversible fluorescence photoswitching in living cells.

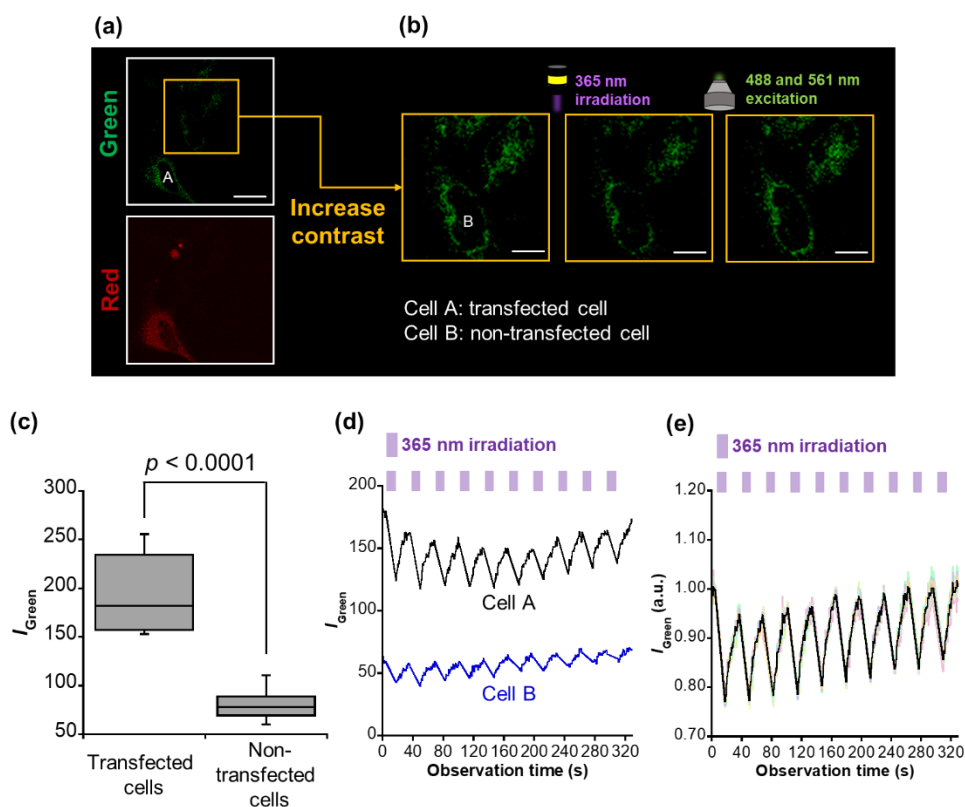


**Figure 3-4-4. Live cell imaging of non-transfected and MBP-Halo-mCherry transfected HeLa cells.**

(a,b) After adding 1.0  $\mu\text{M}$ , HTL-Trp-BODIPY-FF (0.1% DMSO), cells were incubated for 20 min. Scale bar 50  $\mu\text{m}$ . (b) Enlarged images of (a) that show fluorescence signals from non-transfected cells are modified for visualization by increasing image contrast. Scale bar 25  $\mu\text{m}$ . Samples were alternately irradiated at 365 nm (10 mW/cm<sup>2</sup> for 10 s) and

488 and 561 nm excitation light exposure (20 s). Scale bar: 10  $\mu\text{m}$ . Green channel:  $\lambda_{\text{ex}} = 488 \text{ nm}$ ,  $\lambda_{\text{em}} = 499\text{-}551 \text{ nm}$ . Red channel:  $\lambda_{\text{ex}} = 561 \text{ nm}$ ,  $\lambda_{\text{em}} = 571\text{-}625 \text{ nm}$ . **(c)** Comparison of green fluorescence intensity between transfected and non-transfected cells. Data presents as box plot ( $N=10$ ). P values were obtained from two-tailed t tests. **(d,e)** Time course of the fluorescence intensity of green channel with 365 nm irradiation (10 cycles) of transfected cells (cell A in **(a)**) and non-transfected cells (cell B in **(b)**), **(d)** a random selection of 10 non-transfected cells in three different cell plates (the number of replicates:  $N=3$ ). The black line represents the average intensity from 10 different cells. Other pale-colored lines describe the intensity of each cell. Adapted with permission from ref 52 under CC BY-NC.

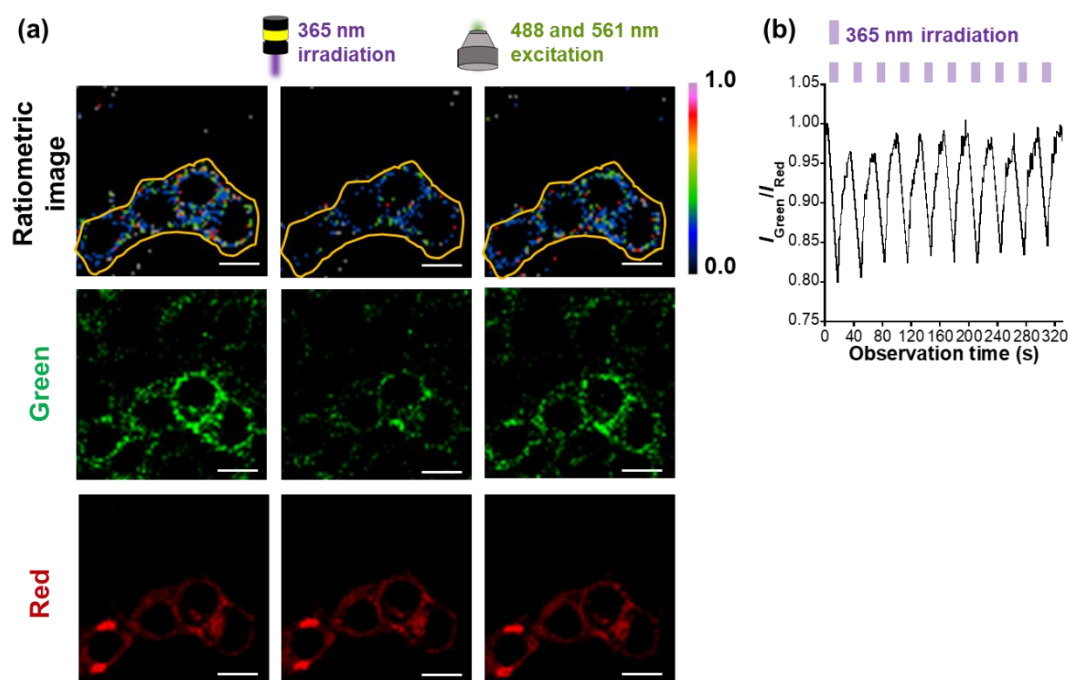


**Figure 3-4-5. Ratiometric imaging of HEK293T cells transfected with pcDNA3.1(+)-Halo-EGFR-mCherry.**

**(a)** After adding 100 nM, HTL-Trp-BODIPY-FF (0.1% DMSO), cells were incubated for 20 min. Samples were alternately irradiated at 365 nm (10 mW/cm<sup>2</sup> for 10 s) and 488 and 561 nm excitation light exposure (20 s). Scale bar: 10  $\mu\text{m}$ . Green channel:  $\lambda_{\text{ex}} = 488 \text{ nm}$ ,  $\lambda_{\text{em}} = 499\text{-}551 \text{ nm}$ . Red channel:  $\lambda_{\text{ex}} = 561 \text{ nm}$ ,  $\lambda_{\text{em}} = 571\text{-}625 \text{ nm}$ . Ratiometric images were generated by dividing the intensity of green channel by that of red channel in each pixel. Maximum ratio: 0.8; minimum ratio: 0.1. **(b)** Time course of the ratio for fluorescence intensities of green channel to red channel with 365 nm irradiation (10 cycles). The fluorescence intensity ratio ( $I_{\text{Green}}/I_{\text{Red}}$ ) was obtained from the selected region of interest (ROI) surrounded by the yellow circle. Adapted with permission from ref 52 under CC BY-NC.

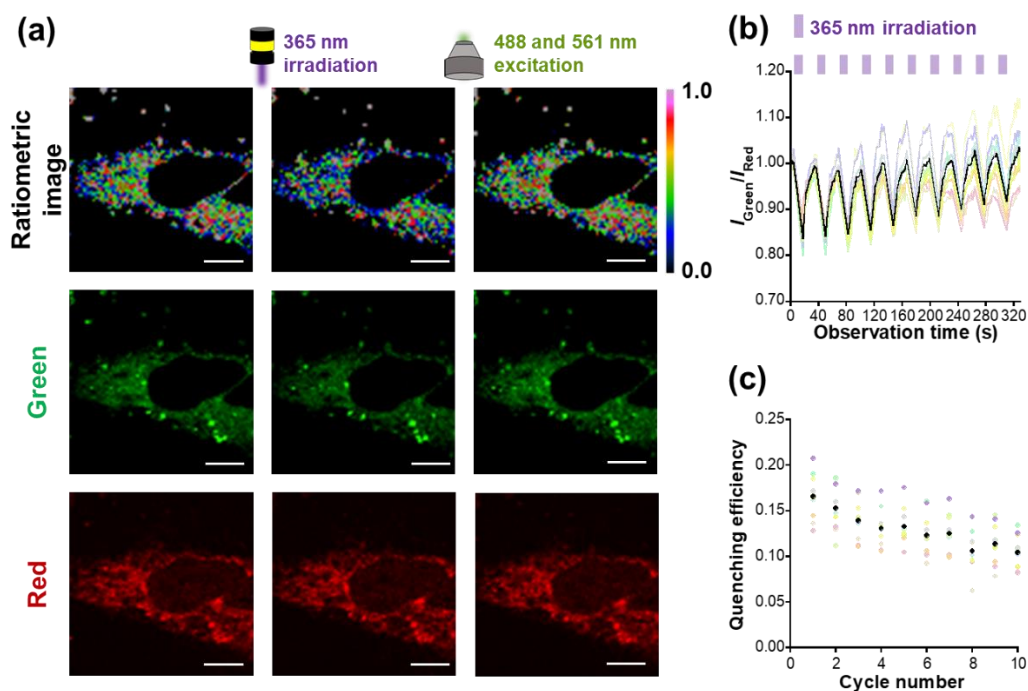
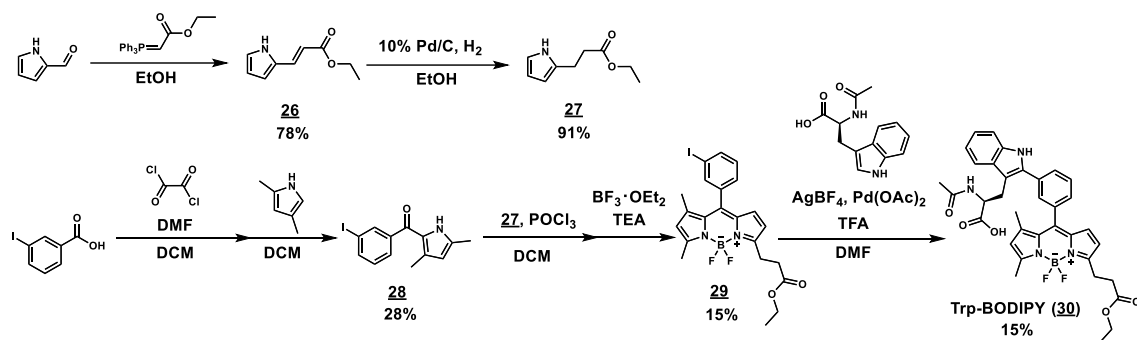


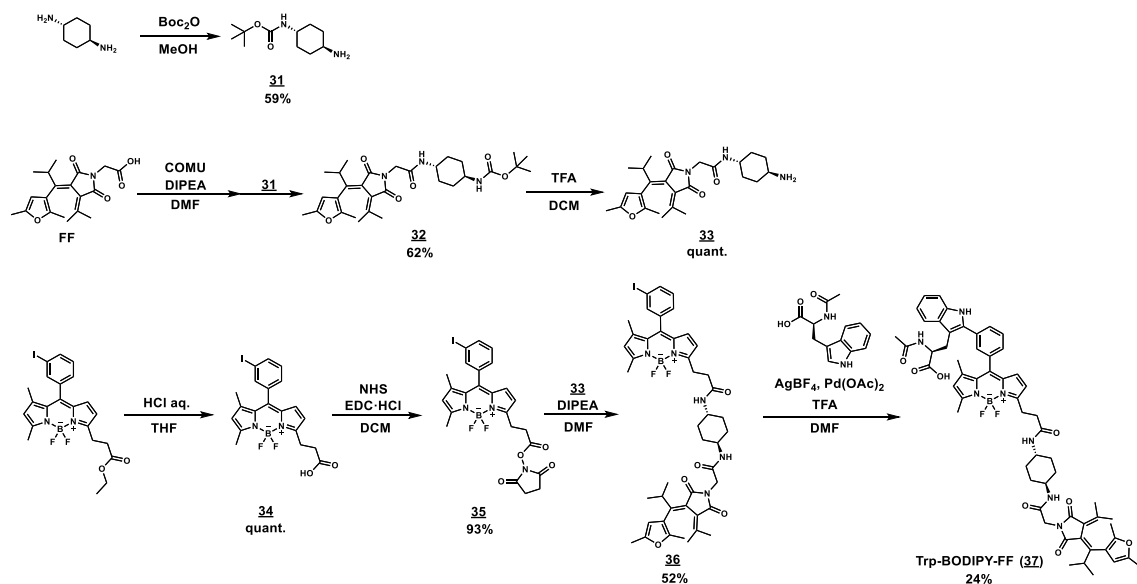
**Figure 3-4-6. Ratiometric imaging of HeLa cells transfected with pcDNA3.1(+)-Tom20-Halo-mCherry.**

(a) After adding 1.0  $\mu\text{M}$ , HTL-Trp-BODIPY-FF (0.1% DMSO), cells were incubated for 20 min. Samples were alternately irradiated at 365 nm (10 mW/cm<sup>2</sup> for 10 s) and 488 and 561 nm excitation light exposure (20 s). Scale bar: 10  $\mu\text{m}$ . Green channel:  $\lambda_{\text{ex}} = 488 \text{ nm}$ ,  $\lambda_{\text{em}} = 499\text{-}551 \text{ nm}$ . Red channel:  $\lambda_{\text{ex}} = 561 \text{ nm}$ ,  $\lambda_{\text{em}} = 571\text{-}625 \text{ nm}$ . Ratiometric images were generated by dividing the intensity of green channel by that of red channel in each pixel. Maximum ratio: 0.8; minimum ratio: 0.1. (b) Time course of the ratio for fluorescence intensities of green channel to red channel with 365 nm irradiation (10 cycles). The fluorescence intensity ratio ( $I_{\text{Green}}/I_{\text{Red}}$ ) was obtained from a random selection of 10 cells in three different cell plates (the number of replicates:  $N=3$ ). (c) Quenching efficiency calculated from the data of (b). The black (b) line and (c) dots represent the average ratio intensity and quenching efficiency from 10 different cells. Other pale-colored (b) lines and (c) dots describe each ratio intensity/quenching efficiency from each cell. Adapted with permission from ref 52 under CC BY-NC.

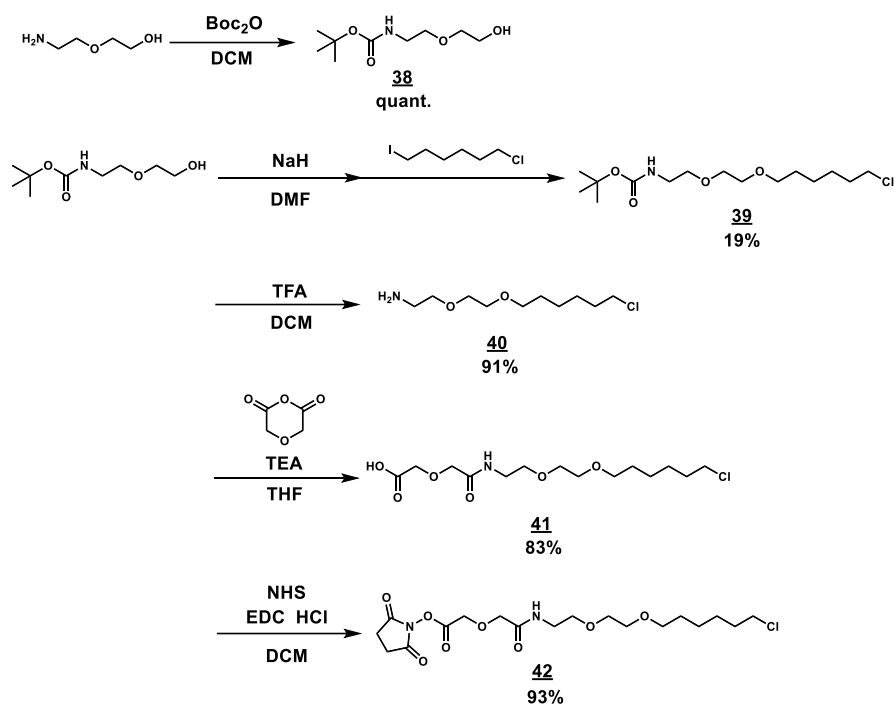
### Synthetic Procedures



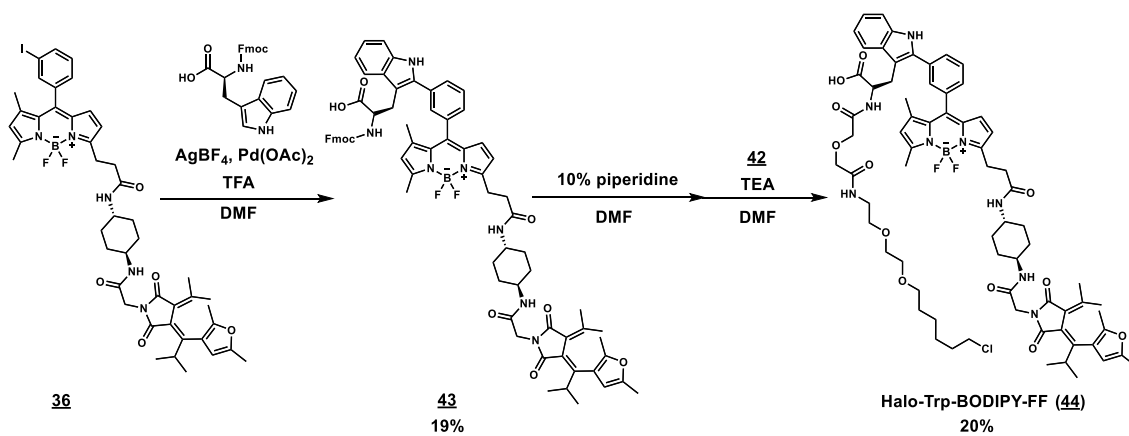
Scheme 3-1. Synthesis of Trp-BODIPY. Adapted with permission from ref 52 under CC BY-NC.



Scheme 3-2. Synthesis of Trp-BODIPY-FF. Adapted with permission from ref 52 under CC BY-NC.



Scheme 3-3. Synthesis of Halo-tag ligand. Adapted with permission from ref 52 under CC BY-NC.



Scheme 3-4. Synthesis of HTL-Trp-BODIPY-FF. Adapted with permission from ref 52 under CC BY-NC.

**ethyl (*E*)-3-(1*H*-pyrrol-2-yl)acrylate, (26)**

1*H*-pyrrole-2-carbaldehyde (800mg, 8.4 mmol, 1.0 eq) and ethyl (triphenylphosphoranylidene)acetate (3.70 g, 10.6 mmol, 1.3 eq.) were dissolved in ethanol (35 mL). The reaction mixture was heated to 80 °C and stirred for 36 h. After evaporating the solvent under vacuum, the crude product was purified using column chromatography (methanol/dichloromethane (DCM) = 1/200) to get compound 26 (1.08 g, 6.5 mmol, 78%) as a pale-yellow needle crystal.

**<sup>1</sup>H NMR, 500 MHz, CDCl<sub>3</sub>** δ 8.84 (s(br), 1H), 7.55 (d, *J* = 15 Hz, 1H), 6.92 (m, 1H), 6.56 (m, 1H), 6.28 (m, 1H), 6.02 (d, *J* = 15 Hz, 1H), 4.24 (q, *J* = 15 Hz, 2H), 1.32 (t, *J* = 15 Hz, 3H). **<sup>13</sup>C NMR, 125 MHz, CDCl<sub>3</sub>** δ 167.78, 134.26, 128.47, 122.38, 114.29, 111.32, 110.96, 60.31, 14.37. **HRMS (ESI+)** [*M* + Na<sup>+</sup>] found: 188.0680, calculated: 188.0682.

**ethyl 3-(1*H*-pyrrol-2-yl)propanoate, (27)**

Palladium-activated carbon (Pd 10%) (100 mg) was added to a solution of compound 26 (1.08 g, 6.5 mmol, 1.0 eq.) in ethanol (15 mL). After performing three vacuum and nitrogen purging cycles, the reaction vessel was filled with hydrogen gas. The reaction mixture was stirred vigorously at room temperature for 5 h. Upon completion, celite filtration was conducted to remove palladium-activated carbon. The filtrate was evaporated to dryness by a rotary evaporator, and compound 27 (982 mg, 5.88 mmol, 91%) was obtained as a colorless oil without further purification.

**<sup>1</sup>H NMR, 500 MHz, CDCl<sub>3</sub>** δ 8.54 (s(br), 1H), 6.67 (m, 1H), 6.10 (m, 1H), 5.92 (m, 1H), 4.16 (q, *J* = 7.0 Hz, 2H), 2.91 (t, *J* = 7.0 Hz, 2H), 2.63 (t, *J* = 6.8 Hz, 2H), 1.26 (t, *J* = 6.8 Hz, 3H). **<sup>13</sup>C NMR, 125 MHz, CDCl<sub>3</sub>** δ 174.17, 131.07, 116.78, 107.98, 105.50, 60.70, 34.61, 22.54, 14.19. **HRMS (EI+)** [*M*<sup>+</sup>] found: 167.0942, calculated: 167.0946.

**(3,5-dimethyl-1*H*-pyrrol-2-yl)(3-iodophenyl)methanone, (28)**

A solution of 3-iodobenzoic acid (3.0 g, 12.1 mmol, 1.0 eq.) in anhydrous DCM (80 mL) including 100 μL *N,N*-dimethylformamide (DMF) was added dropwise oxalyl chloride (1.5 mL, 17.5 mmol, 1.4 eq.) at 0 °C with stirring for 1 h. The solution was allowed to warm to room temperature with stirring for 4 h and then removed solvent using a rotary evaporator to afford crude 3-iodobenzoyl chloride which was used for the next reaction without further purification. The solution of 3-iodobenzoyl chloride in anhydrous DCM (40 mL) was added dropwise 2,4-dimethylpyrrole (1.2 mL, 12.1 mmol, 1.0 eq.) for 5 min. The mixture was stirred for 3 h and quenched with saturated NaHCO<sub>3</sub> aqueous solution. The organic layer was extracted with DCM three times. After washing the organic layer with brine and drying over Na<sub>2</sub>SO<sub>4</sub>, the residue was concentrated under reduced pressure. The crude product was purified using column chromatography (DCM/hexane = 2/5-4/5) to afford compound 28 (1.12 g, 3.44 mmol, 28%) as a pale-red powder.

**<sup>1</sup>H NMR, 500 MHz, CDCl<sub>3</sub>** δ 8.95 (s(br), 1H), 7.96 (m, 1H), 7.84 (m, 1H), 7.59 (m, 1H), 7.20 (m, 1H), 5.89 (m, 1H), 2.31(s, 3H), 1.93 (s, 3H). **<sup>13</sup>C NMR, 125 MHz, CDCl<sub>3</sub>** δ 183.64, 141.85, 139.67, 137.02, 136.09, 131.00, 130.04, 127.36, 127.21, 113.28, 93.93, 14.15, 13.23. **HRMS (MALDI)** [*M*+H<sup>+</sup>] found: 326.0037, calculated: 326.0036.

**ethyl 3-(5,5-difluoro-10-(3-iodophenyl)-7,9-dimethyl-5*H*-4λ<sup>4</sup>,5λ<sup>4</sup>-dipyrrolo[1,2-*c*:2',1'-*f*][1,3,2]diazaborinin-3-**

**yl)propanoate, (29)**

Compound 27 (860 mg, 5.15 mmol, 1.5 eq.) and compound 28 (1.12 g, 3.44 mmol, 1.0 eq.) were dissolved in anhydrous DCM (10 mL) and cooled to 0 °C under a nitrogen atmosphere. The reaction mixture was then added dropwise phosphoryl chloride (320 µL, 3.43 mmol, 1.0 eq.) and kept at 0 °C for 1 h. The solution was allowed to warm to room temperature with stirring for 18 h. After cooling the solution to 0 °C again, the mixture was then added to boron trifluoride - ethyl ether complex (5.2 mL, 41.2 mmol, 12 eq.) and triethylamine (4.8 mL, 34.3 mmol, 10 eq.) and gradually warmed to room temperature with stirring for 1 h. Upon completion, the reaction was quenched by adding a saturated NaHCO<sub>3</sub> aqueous solution, and the organic layer was extracted with DCM three times. After washing the organic layer with brine and drying it using Na<sub>2</sub>SO<sub>4</sub>, the solvent was removed under reduced pressure. The crude product was purified using column chromatography (DCM/hexane = 1/1) to get compound 29 (264 mg, 506 µmol, 15%) as a red-brown oil.

**<sup>1</sup>H NMR, 500 MHz, CDCl<sub>3</sub>** δ 7.83 (ddd, *J* = 7.5 Hz, *J* = 1.5 Hz, *J* = 1.0 Hz, 1H), 7.71 (dd, *J* = 1.5 Hz, *J* = 1.5 Hz, 1H), 7.31 (ddd, *J* = 7.5 Hz, *J* = 1.5 Hz, *J* = 1.5 Hz, 1H), 7.21 (dd, *J* = 1.5 Hz, *J* = 1.5 Hz, 1H), 6.36 (d, *J* = 4.0 Hz, 1H), 6.23 (d, *J* = 4.0 Hz, 1H), 6.09 (s, 1H), 4.15 (q, *J* = 7.5 Hz, 2H), 3.31 (t, *J* = 7.5 Hz, 2H), 2.77 (t, *J* = 7.5 Hz, 2H), 2.60 (s, 3H), 1.54 (s, 3H), 1.26 (t, *J* = 7.5 Hz, 3H). **<sup>13</sup>C NMR, 125 MHz, CDCl<sub>3</sub>** δ 172.53, 160.11, 157.14, 144.93, 139.81, 138.24, 137.51, 136.12, 134.60, 132.22, 130.00, 128.42, 128.11, 122.74, 116.68, 93.76, 60.58, 33.45, 23.92, 14.99, 14.22. **HRMS (MALDI) [M+Na<sup>+</sup>]** found: 545.0682, calculated: 545.0679.

**Trp-BODIPY, (30)**

Acetyl-*L*-tryptophan (9.5 mg, 38.3 µmol, 1.0 eq.), palladium(II) acetate (1.8 mg, 7.7 µmol, 0.2 eq.), silver(I) tetrafluoroborate (7.6 mg, 38.3 µmol, 1.0 eq.), compound 29 (20.0 mg, 38.3 µmol, 1.0 eq.), and trifluoroacetic acid (2.9 µL, 38.3 µmol, 1.0 eq.) were dissolved in DMF (2 mL). The reaction mixture was placed under microwave irradiation at 80 °C for 30 min. After the reaction, celite filtration was conducted to remove metal complexes. The filtrate was evaporated to dryness using a rotary evaporator and purified using reverse-phase chromatography (0.1% formic acid acetonitrile/water = 50/50-95/5). After lyophilization, compound 30 (8.9 mg, 13.9 µmol, 36%) was obtained as an orange powder.

**<sup>1</sup>H NMR, 500 MHz, acetone-*d*<sub>6</sub>** δ 10.49 (s, 1H), 7.96 (m, 1H), 7.76 (m, 2H), 7.69 (m, 1H), 7.46 (m, 1H), 7.38 (m, 1H), 7.23 (m, 1H), 7.13 (m, 1H), 7.05 (m, 1H), 6.58 (d, *J* = 5.0 Hz, 1H), 6.35 (d, *J* = 5.0 Hz, 1H), 6.27 (s, 1H), 4.82 (m, 2H), 4.13 (q, *J* = 7.5 Hz, 2H), 3.48 (m, 2H), 3.28 (t, *J* = 7.5 Hz, 2H), 2.78 (t, *J* = 7.5 Hz, 2H), 2.58 (s, 3H), 1.76 (d, 3H), 1.70 (d, 3H), 1.63 (s, 3H), 1.23 (dt, *J* = 7.5 Hz, 3H). **<sup>13</sup>C NMR, 125 MHz, CD<sub>3</sub>OD** δ 173.48, 172.71, 170.04, 160.52, 157.62, 146.34, 142.98, 137.36, 135.73, 135.61, 135.44, 134.63, 133.18, 130.29, 130.10, 129.97, 129.89, 129.63, 129.16, 128.83, 123.44, 122.94, 120.10, 117.40, 111.94, 109.36, 60.90, 53.88, 33.67, 28.30, 24.57, 22.72, 15.15, 14.94, 14.55. **HRMS (MALDI) [M+Na<sup>+</sup>]** found: 663.2569, calculated: 663.2561.

**tert-butyl ((1*r*,4*r*)-4-aminocyclohexyl)carbamate, (31)**

A solution of *trans*-1,4-cyclohexanediamine (500 mg, 4.39 mmol, 3.6 eq.) in methanol (15 mL) was added dropwise

di-*tert*-butyl decarbonate (280  $\mu$ L, 1.22 mmol, 1.0 eq.) at room temperature with stirring for 2 h. The solvent was removed under reduced pressure and dissolved in ethyl acetate and water. The organic layer was extracted with ethyl acetate three times, washed with brine, and dried over by  $\text{Na}_2\text{SO}_4$ . After removing the solvent, compound **31** (157 mg, 715  $\mu$ mol, 59%) was afforded as a white powder.

**$^1\text{H}$  NMR, 500 MHz,  $\text{CDCl}_3$**   $\delta$  4.35 (m, 1H), 3.38 (s(br), 1H), 2.62 (s(br), 1H), 1.90 (m, 4H), 1.43 (s, 9H), 1.18 (s, 4H).  **$^{13}\text{C}$  NMR, 125 MHz,  $\text{CDCl}_3$**   $\delta$  155.27, 79.15, 49.95, 49.25, 35.39, 32.22, 28.42. **HRMS (MALDI)**  $[\text{M}+\text{Na}^+]$  found: 237.1579, calculated: 237.1574.

***tert*-butyl ((1*r*,4*r*)-4-(2-((*E*)-3-(1-(2,5-dimethylfuran-3-yl)-2-methylpropylidene)-2,5-dioxo-4-(propan-2-ylidene)pyrrolidin-1-yl)acetamido)cyclohexyl)carbamate, (**32**)**

A solution of FF (543 mg, 1.57 mmol, 1.0 eq.) in anhydrous DMF (12 mL) was added a solution of 1-[(1-(Cyano-2-ethoxy-2-oxoethylideneaminoxy) dimethylaminomorpholino)] uronium hexafluorophosphate (1.01 g, 2.36 mmol, 1.5 eq.) and *N,N*-diisopropylethylamine (543  $\mu$ L, 3.12 mmol, 2.0 eq.) in DMF (10 mL) and stirred at room temperature for 30 min. The mixture was then added to a solution of compound **31** (337 mg, 1.57 mmol, 1.0 eq.) at room temperature with stirring for 1 h under a nitrogen atmosphere. After confirming the reaction was completely proceeded by TLC plate monitoring, the solvent was removed by a rotary evaporator. The crude product was washed with water and then extracted with DCM three times, washed with brine, and dried over  $\text{Na}_2\text{SO}_4$ . After removing the solvent, the crude product was purified using column chromatography (ethyl acetate/hexane = 1/10-1/1) to get compound **32** (510 mg, 943  $\mu$ mol, 62%) as a white powder.

**$^1\text{H}$  NMR, 500 MHz,  $\text{CDCl}_3$**   $\delta$  5.93 (d, 1H), 5.64 (d, 1H), 4.47 (sept,  $J=7.0$  Hz, 1H), 4.43 (m, 1H), 4.21 (m, 2H), 3.73 (m, 1H), 3.40 (s(br), 1H), 2.25 (s, 3H), 2.25 (s, 3H), 2.00 (m, 4H), 1.87 (s, 3H), 1.43 (s, 9H), 1.35 (s, 3H), 1.29 (d,  $J=7.5$  Hz, 3H), 1.21 (m, 4H), 0.84 (d,  $J=7.5$  Hz, 3H).  **$^{13}\text{C}$  NMR, 125 MHz,  $\text{CDCl}_3$**   $\delta$  167.82, 167.74, 165.68, 155.24, 153.33, 149.93, 149.93, 148.97, 147.01, 123.20, 123.07, 119.48, 106.29, 48.82, 48.05, 40.81, 31.90, 31.57, 29.93, 28.41, 27.08, 22.84, 21.96, 20.64, 13.34, 12.75. **HRMS (MALDI)**  $[\text{M}+\text{Na}^+]$  found: 564.3047, calculated: 564.3044.

***N*-((1*r*,4*r*)-4-aminocyclohexyl)-2-((*E*)-3-(1-(2,5-dimethylfuran-3-yl)-2-methylpropylidene)-2,5-dioxo-4-(propan-2-ylidene)pyrrolidin-1-yl)acetamide, (**33**)**

A solution of compound **32** (255 mg, 471  $\mu$ mol) in DCM (10 mL) was added dropwise trifluoroacetic acid (2 mL) and stirred at room temperature for 1 h. After removing the solvent, compound **33** (208 mg, 471  $\mu$ mol, quant.) was afforded as a red oil which was used for the next reaction without further purification.

**HRMS (MALDI)**  $[\text{M}+\text{Na}^+]$  found: 464.2520, calculated: 464.2520.

**3-(5,5-difluoro-10-(3-iodophenyl)-7,9-dimethyl-5*H*-4 $\lambda^4$ ,5 $\lambda^4$ -dipyrrolo[1,2-*c*:2',1'-*f*][1,3,2]diazaborinin-3-yl)propanoic acid, (**34**)**

A solution of compound **29** (264 mg, 506  $\mu$ mol) in tetrahydrofuran (30 mL) was added to 2M HCl aqueous solution (30 mL). The mixture was stirred at room temperature for 60 h. After confirming the hydrolysis was completely

proceeded by TLC plate monitoring, the organic layer was extracted with DCM three times. After washing the organic layer with brine and drying it using Na<sub>2</sub>SO<sub>4</sub>, the solvent was removed under reduced pressure. The hydrolysis product, compound **34** (248 mg, 502 μmol, quant.) was obtained as a red oil without further purification.

**<sup>1</sup>H NMR, 500 MHz, CDCl<sub>3</sub>** δ 7.84 (ddd, *J*=7.5 Hz, *J*=1.5 Hz, *J*=1.0 Hz, 1H), 7.71 (dd, *J*=1.5 Hz, *J*=1.5 Hz, 1H), 7.32 (ddd, *J*=7.5 Hz, *J*=1.5 Hz, *J*=1.5 Hz, 1H), 7.21 (d, *J*=7.5 Hz, *J*=7.5 Hz, 1H), 6.36 (d, *J*=4.0 Hz, 1H), 6.24 (d, *J*=4.0 Hz, 1H), 6.10 (s, 1H), 3.32 (t, *J*=7.5 Hz, 2H), 2.84 (t, *J*=7.5 Hz, 2H), 2.60 (s, 3H), 1.55 (s, 3H). **<sup>13</sup>C NMR, 125 MHz, CDCl<sub>3</sub>** δ 176.05, 160.47, 156.37, 145.17, 139.92, 138.60, 138.29, 137.52, 136.09, 134.65, 132.38, 130.02, 128.35, 128.12, 122.88, 116.64, 93.78, 32.77, 23.66, 15.01. **HRMS (MALDI) [M+Na<sup>+</sup>]** found: 517.0362, calculated: 517.0366.

**2,5-dioxopyrrolidin-1-yl 3-(5,5-difluoro-10-(3-iodophenyl)-7,9-dimethyl-5*H*-4λ<sup>4</sup>,5λ<sup>4</sup>-dipyrrolo[1,2-*c*:2',1'-*f*][1,3,2]diazaborinin-3-yl)propanoate, (**35**)**

A solution of compound **34** (161 mg, 327 μmol, 1.0 eq.) in anhydrous DCM (10 mL) was added *N*-hydroxysuccinimide (56.4 mg, 490 μmol, 1.5 eq.) and 1-(3-dimethylaminopropyl)-3-ethylcarbodiimide hydrochloride (74.9 mg, 392 μmol, 1.2 eq.) at room temperature and stirred for 1 h under the nitrogen atmosphere. Upon completion of the reaction, the mixture was washed with water three times. The organic layer was then washed with brine and dried over Na<sub>2</sub>SO<sub>4</sub>. After removing the solvent under reduced pressure, compound **35** (179 mg, 304 μmol, 93%) was afforded as a red oil. **<sup>1</sup>H NMR, 500 MHz, CDCl<sub>3</sub>** δ 7.84 (ddd, *J*=7.5 Hz, *J*=1.5 Hz, *J*=1.0 Hz, 1H), 7.72 (dd, *J*=1.5 Hz, *J*=1.5 Hz, 1H), 7.32 (ddd, *J*=7.5 Hz, *J*=1.5 Hz, *J*=1.5 Hz, 1H), 7.22 (dd, *J*=7.5 Hz, *J*=7.5 Hz, 1H), 6.37 (d, *J*=4.0 Hz, 1H), 6.30 (d, *J*=4.0 Hz, 1H), 6.11 (s, 1H), 3.40 (t, *J*=7.5 Hz, 2H), 3.10 (t, *J*=7.5 Hz, 2H), 2.84 (s, 4H), 2.60 (s, 3H), 1.55 (s, 3H). **<sup>13</sup>C NMR, 125 MHz, CDCl<sub>3</sub>** δ 169.49, 169.03, 168.99, 167.83, 160.94, 154.61, 145.52, 140.09, 138.32, 137.48, 135.99, 134.68, 132.54, 130.03, 128.29, 128.10, 123.06, 116.78, 93.79, 30.36, 25.59, 23.33, 15.06. **HRMS (MALDI) [M+Na<sup>+</sup>]** found: 614.0535, calculated: 614.0530.

**3-(5,5-difluoro-10-(3-iodophenyl)-7,9-dimethyl-5*H*-4λ<sup>4</sup>,5λ<sup>4</sup>-dipyrrolo[1,2-*c*:2',1'-*f*][1,3,2]diazaborinin-3-yl)-*N*-((1*r*,4*r*)-4-(2-((*E*)-3-(1-(2,5-dimethylfuran-3-yl)-2-methylpropylidene)-2,5-dioxo-4-(propan-2-ylidene)pyrrolidin-1-yl)acetamido)cyclohexyl)propenamide, (**36**)**

A solution of compound **35** (210 mg, 355 μmol, 1.0 eq.) in anhydrous DCM (10 mL) was added to a solution of compound **33** (208 mg, 471 μmol, 1.3 eq.), and *N,N*-diisopropylethylamine (500 μL, 2.87 mmol, 8.1 eq.) in anhydrous DCM (5 mL) at room temperature under nitrogen atmosphere. The reaction mixture was stirred at 40 °C for 1 h. Upon completion of the reaction, the residue was concentrated by using a rotary evaporator. The crude product was purified using column chromatography (ethyl acetate/hexane= 1/1-3/1) to obtain compound **36** (168 mg, 183 μmol, 52%) as a red solid.

**<sup>1</sup>H NMR, 500 MHz, CDCl<sub>3</sub>** δ 7.83 (ddd, *J*=7.5 Hz, *J*=1.5 Hz, *J*=1.0 Hz, 1H), 7.69 (dd, *J*=1.0 Hz, *J*=1.5 Hz, 1H), 7.30 (ddd, *J*=7.5 Hz, *J*=1.5 Hz, *J*=1.5 Hz, 1H), 7.23 (dd, *J*=7.5 Hz, *J*=7.5 Hz, 1H), 6.35 (d, *J*=4.0 Hz, 1H), 6.23 (d, *J*=4.0 Hz, 1H), 6.11 (s, 1H), 5.93 (s, 1H), 5.63 (s, 2H), 4.47 (sept, *J*=7.0 Hz, 1H), 4.20 (m, 2H), 3.70 (m, 2H), 3.26 (t, *J*=7.5 Hz, 2H), 2.72 (s, 3H), 2.63 (t, *J*=7.5 Hz, 2H), 2.59 (s, 3H), 2.25 (s, 3H), 2.24 (s, 3H), 2.00-1.80 (m, 4H), 1.87

(s, 3H), 1.35 (s, 3H), 1.28 (d,  $J=7.0$  Hz, 3H), 1.25-1.10 (m, 4H), 0.84 (d,  $J=7.0$  Hz, 3H).  $^{13}\text{C}$  NMR, 125 MHz,  $\text{CDCl}_3$   $\delta$  171.68, 171.30, 167.84, 165.79, 160.27, 156.73, 153.39, 149.94, 149.03, 147.02, 145.30, 139.88, 138.33, 137.48, 135.96, 134.60, 132.24, 130.10, 128.51, 128.07, 123.17, 119.48, 117.46, 106.29, 93.83, 60.43, 47.94, 47.36, 40.81, 35.97, 31.43, 29.93, 27.09, 25.41, 24.79, 22.85, 21.97, 21.07, 20.65, 15.05, 14.20, 13.94, 12.76. HRMS (FAB+)  $[\text{M}+\text{Na}^+]$  found: 940.2898, calculated: 940.2888.

#### Trp-BODIPY-FF, (37)

Acetyl-*L*-tryptophan (16 mg, 65.4  $\mu\text{mol}$ , 1.0 eq.), palladium(II) acetate (3.0 mg, 13.1  $\mu\text{mol}$ , 0.2 eq.), silver(I) tetrafluoroborate (13 mg, 65.4  $\mu\text{mol}$ , 1.0 eq.), compound 36 (60 mg, 65.4  $\mu\text{mol}$ , 1.0 eq.), and trifluoroacetic acid (5.0  $\mu\text{L}$ , 65.4  $\mu\text{mol}$ , 1.0 eq.) were dissolved in DMF (2 mL). The reaction mixture was placed under microwave irradiation at 80 °C for 30 min. After the reaction, celite filtration was conducted to remove metal complexes. The filtrate was evaporated to dryness using a rotary evaporator and purified using reverse-phase chromatography (0.1% formic acid acetonitrile/water= 60/40-95/5). After lyophilization, compound 37 (16.3 mg, 15.7  $\mu\text{mol}$ , 24%) was obtained as an orange powder.

$^1\text{H}$  NMR, 500 MHz, acetone- $\text{d}_6$   $\delta$  10.50 (d, 1H), 7.95 (m, 1H), 7.75 (m, 2H), 7.68 (dd,  $J=7.5$  Hz,  $J=7.5$  Hz, 1H), 7.45 (m, 1H), 7.38 (d,  $J=4.0$  Hz, 1H), 7.27 (d,  $J=4.0$  Hz, 1H), 7.25 (m, 1H), 7.12 (m, 2H), 7.05 (ddd,  $J=7.5$  Hz,  $J=7.5$  Hz,  $J=1.5$  Hz, 1H), 6.56 (dd, 1H), 6.32 (t, 1H), 6.25 (s, 1H), 6.10 (s, 1H), 4.81 (m, 1H), 4.54 (sept,  $J=7.0$  Hz, 1H), 4.18 (m, 2H), 3.70-3.60 (m, 2H), 3.55-3.35 (m, 2H), 3.26 (m, 2H), 2.58 (t,  $J=7.5$  Hz, 2H), 2.56 (s, 3H), 2.25 (s, 3H), 2.22 (s, 3H), 2.00-1.80 (m, 4H), 1.88 (s, 3H), 1.75 (d,  $J=6.5$  Hz, 3H), 1.62 (s, 3H), 1.36 (s, 3H), 1.29 (m,  $J=7.0$  Hz, 3H), 1.35-1.20 (m, 4H), 0.82 (d,  $J=7.0$  Hz, 3H).  $^{13}\text{C}$  NMR, 125 MHz, acetone- $\text{d}_6$   $\delta$  173.49, 171.19, 170.06, 168.29, 166.10, 159.87, 159.12, 152.10, 150.85, 147.80, 147.57, 145.87, 142.81, 137.38, 135.68, 135.52, 134.63, 132.95, 130.31, 129.97, 129.85, 129.27, 128.91, 125.04, 124.51, 123.20, 122.94, 120.24, 120.10, 117.82, 111.97, 109.46, 107.33, 53.93, 48.85, 48.44, 40.71, 35.50, 32.20, 32.17, 28.32, 28.29, 27.00, 25.19, 23.14, 22.74, 21.63, 20.91, 15.13, 15.10, 114.93, 13.28, 12.78. MS (MALDI)  $[\text{M}-\text{F}^-]$  found: 1016.4957, calculated: 1016.4893,  $[\text{M}+\text{Na}^+]$  found: 1058.4830, calculated: 1058.4775.

#### tert-butyl (2-(2-hydroxyethoxy)ethyl)carbamate, (38)

A solution of 2-(2-aminoethoxy)ethan-1-ol (10.0 g, 95.1 mmol, 1.0 eq.) in DCM (40 mL) was added dropwise di-*tert*-butyl decarbonate (22.8 g, 105 mmol, 1.1 eq.) at room temperature with stirring for 18 h. After concentrating the residue using a rotary evaporator, the crude product was washed with water and extracted with ethyl acetate three times. The organic layer was washed with brine and dried over  $\text{Na}_2\text{SO}_4$ . The solvent was removed under reduced pressure, and compound 38 (19.5 g, 94.9 mmol, quant.) was afforded as a colorless oil.

$^1\text{H}$  NMR, 500 MHz,  $\text{CDCl}_3$   $\delta$  3.73 (m, 2H), 3.56 (m, 4H), 3.32 (t,  $J=5.5$  Hz, 2H), 1.44 (s, 9H)  $^{13}\text{C}$  NMR, 125 MHz,  $\text{CDCl}_3$   $\delta$  156.11, 79.43, 72.18, 70.32, 61.77, 40.37, 28.55, 28.40. HRMS (FAB+)  $[\text{M}+\text{Na}^+]$  found: 228.1208, calculated: 228.1212.

***tert*-butyl (2-(2-((6-chlorohexyl)oxy)ethoxy)ethyl)carbamate, (39)**

Compound **38** (2.20 g, 10.7 mmol, 1.0 eq.) was dissolved in anhydrous tetrahydrofuran (8 mL) and DMF (4 mL) and cooled to 0 °C. The mixture was added sodium hydride, 60% oil dispersion (470 mg, 11.8 mmol, 1.1 eq.), and stirred at 0 °C for 30 min under a nitrogen atmosphere. The mixture was added 1-chloro-6-iodohexane (2.63 g, 10.7 mmol, 1.0 eq.) and gradually warmed to room temperature with stirring for 18 h. The reaction was quenched by adding saturated NH<sub>4</sub>Cl aqueous solution. The organic layer was extracted with ethyl acetate three times. After drying over Na<sub>2</sub>SO<sub>4</sub>, the solvent was removed under reduced pressure. The crude product was purified using column chromatography (ethyl acetate/hexane = 1/10-1/3) to afford compound **39** (660 mg, 2.04 mmol, 19%) as a colorless oil. **<sup>1</sup>H NMR, 500 MHz, CDCl<sub>3</sub>** δ 4.99 (s(br), 1H), 3.65-3.50 (m, 8H), 3.49 (t, *J* = 7.0 Hz, 2H), 3.34 (t, 2H), 1.80 (m, 2H), 1.64 (m, 4H (including H<sub>2</sub>O)), 1.44 (s, 9H), 1.50-1.35 (m, 4H). **<sup>13</sup>C NMR, 125 MHz, CDCl<sub>3</sub>** δ 156.01, 71.30, 70.29, 70.23, 70.04, 45.05, 40.38, 32.54, 29.44, 28.43, 26.69, 25.54. **HRMS (FAB+)** [M+Na<sup>+</sup>] found: 346.1751, calculated: 346.1761.

**2-(2-((6-chlorohexyl)oxy)ethoxy)ethan-1-amine, (40)**

Compound **39** (200 mg, 619 μmol) was dissolved in DCM (10 mL) at 0 °C. The solution was added dropwise trifluoroacetic acid (2 mL) and allowed to warm to room temperature and stirred for 2 h. Upon completion, the reaction was quenched by adding 1M sodium hydroxide aqueous solution (1 mL). The crude product was washed with water and brine. After drying over Na<sub>2</sub>SO<sub>4</sub>, the solvent was removed under reduced pressure, and compound **40** (127 mg, 566 μmol, 91%) was obtained as a colorless oil.

**<sup>1</sup>H NMR, 500 MHz, CDCl<sub>3</sub>** δ 3.60-3.55 (m, 4H), 3.55-3.50 (m, 4H), 3.47 (t, 2H), 2.87 (m, 2H), 1.78 (m, 2H), 1.61 (m, 2H), 1.52 (s(br), 2H (including H<sub>2</sub>O)), 1.45-1.35 (m, 4H). **<sup>13</sup>C NMR, 125 MHz, CDCl<sub>3</sub>** δ 73.46, 71.27, 70.35, 70.09, 45.06, 41.80, 32.55, 29.47, 26.70, 25.44. **HRMS (FAB+)** [M+H<sup>+</sup>] found: 224.1416 (<sup>35</sup>Cl), calculated: 224.1412.

**18-chloro-5-oxo-3,9,12-trioxa-6-azaoctadecanoic acid, (41)**

A solution of compound **40** (138 mg, 614 μmol, 1.0 eq.) and triethylamine (112 μL, 805 μmol, 1.3 eq.) in anhydrous tetrahydrofuran (10 mL) was added 1,4-dioxane-2,6-dione (86 mg, 743 μmol, 1.2 eq.) at room temperature with stirring for 2 h. Upon completion, the residue was concentrated by using a rotary evaporator and washed with saturated NaHCO<sub>3</sub> aqueous solution three times. The water layer was added to 2 M HCl aqueous solution until the pH=1 and then extracted with ethyl acetate three times. After washing with brine and drying over Na<sub>2</sub>SO<sub>4</sub>, the solvent was removed under reduced pressure and compound **41** (174 mg, 513 μmol, 83%) was obtained as a colorless oil.

**<sup>1</sup>H NMR, 500 MHz, CDCl<sub>3</sub>** δ 7.72 (s, 1H), 4.18 (s, 2H), 4.15 (s, 2H), 3.65-3.50 (m, 12H), 1.78 (m, 2H), 1.67 (m, 2H), 1.45-1.35 (m, 4H). **<sup>13</sup>C NMR, 125 MHz, CDCl<sub>3</sub>** δ 171.29, 169.93, 72.71, 71.50, 70.58, 70.25, 69.97, 69.80, 60.42, 45.00, 38.96, 32.45, 28.77, 26.58, 25.16, 21.06, 20.43, 14.20. **HRMS (FAB+)** [M+H<sup>+</sup>] found: 340.1524 (<sup>35</sup>Cl), calculated: 340.1528.

**2,5-dioxopyrrolidin-1-yl 18-chloro-5-oxo-3,9,12-trioxa-6-azaoctadecanoate, (42)**

A solution of compound **41** (174 mg, 513  $\mu\text{mol}$ , 1.0 eq.) in anhydrous DCM (5 mL) was added *N*-hydroxysuccinimide (89 mg, 769  $\mu\text{mol}$ , 1.5 eq.) and 1-(3-dimethylaminopropyl)-3-ethylcarbodiimide hydrochloride (118 mg, 616  $\mu\text{mol}$ , 1.2 eq.) at room temperature and stirred for 2 h under nitrogen atmosphere. Upon completion of the reaction, the mixture was washed with water three times. The organic layer was then washed with brine and dried over  $\text{Na}_2\text{SO}_4$ . After removing the solvent under reduced pressure, compound **42** (209 mg, 477  $\mu\text{mol}$ , 93%) was afforded as a colorless oil.  **$^1\text{H}$  NMR, 500 MHz,  $\text{CDCl}_3$**   $\delta$  6.92 (s, 1H), 4.52 (s, 2H), 4.16 (s, 2H), 3.65-3.50 (m, 10H), 3.46 (t, 2H), 2.87 (s, 4H), 1.78 (m, 2H), 1.60 (m, 4H (including  $\text{H}_2\text{O}$ )), 1.45-1.35 (m, 4H).  **$^{13}\text{C}$  NMR, 125 MHz,  $\text{CDCl}_3$**   $\delta$  168.51, 168.00, 165.14, 71.28, 71.16, 70.36, 70.04, 69.66, 66.26, 45.10, 38.72, 32.53, 29.45, 26.69, 25.58, 25.42. **HRMS (FAB+)** [ $\text{M}+\text{H}^+$ ] found: 437.1705 ( $^{35}\text{Cl}$ ), calculated: 437.1691.

**(*S*)-2-(((9*H*-fluoren-9-yl)methoxy)carbonyl)amino)-3-(2-(3-(7-(3-(((1*r*,4*r*)-4-(2-((*E*)-3-(1-(2,5-dimethylfuran-3-yl)-2-methylpropylidene)-2,5-dioxo-4-(propan-2-ylidene)pyrrolidin-1-yl)acetamido)cyclohexyl)amino)-3-oxopropyl)-5,5-difluoro-1,3-dimethyl-5*H*-4 $\lambda^4$ ,5 $\lambda^4$ -dipyrrolo[1,2-*c*:2',1'-*f*][1,3,2]diazaborinin-10-yl)phenyl)-1*H*-indol-3-yl)propanoic acid, (**43**)**

(((9*H*-fluoren-9-yl)methoxy)carbonyl)-*L*-tryptophan (49.5 mg, 116  $\mu\text{mol}$ , 1.0 eq.), palladium(II) acetate (5.5 mg, 24.4  $\mu\text{mol}$ , 0.2 eq.), silver(I) tetrafluoroborate (22.8 mg, 116  $\mu\text{mol}$ , 1.0 eq.), compound **36** (107 mg, 116  $\mu\text{mol}$ , 1.0 eq.), and trifluoroacetic acid (9.0  $\mu\text{L}$ , 116  $\mu\text{mol}$ , 1.0 eq.) were dissolved in DMF (4 mL). The reaction mixture was placed under microwave irradiation at 80  $^\circ\text{C}$  for 30 min. After the reaction, celite filtration was conducted to remove metal complexes. The filtrate was evaporated to dryness using a rotary evaporator and purified using reverse phase chromatography (0.1% formic acid acetonitrile/water= 75/25-95/5). After lyophilization, compound **43** (26.4 mg, 21.7  $\mu\text{mol}$ , 19%) was obtained as an orange powder.

**$^1\text{H}$  NMR, 500 MHz, acetone- $\text{d}_6$**   $\delta$  10.53 (d, 1H), 7.96 (m, 1H), 7.81 (m, 4H), 7.65 (dd,  $J=3.0$  Hz,  $J=3.0$  Hz, 1H), 7.58 (m, 2H), 7.40 (m, 4H), 7.26 (m, 3H), 7.13 (dd,  $J=7.5$  Hz,  $J=7.5$  Hz, 1H), 7.05 (m, 2H), 6.56 (m, 2H), 6.29 (d,  $J=4.0$  Hz, 1H), 6.20 (d,  $J=12$  Hz, 1H), 6.10 (s, 1H), 4.63 (q, 1H), 4.54 (sept,  $J_{\text{dc}}=7.0$  Hz, 1H), 4.18 (m, 2H), 4.14 (m, 3H), 3.70-3.60 (m, 3H), 3.50 (dt, 1H), 3.25 (m, 2H), 2.55 (m, 5H), 2.25 (s, 3H), 2.22 (s, 3H), 2.00-1.80 (m, 4H), 1.88 (s, 3H), 1.61 (d,  $J=5.0$  Hz, 3H), 1.36 (s, 3H), 1.35-1.20 (m, 7H), 0.82 (d,  $J=7.0$  Hz, 3H).  **$^{13}\text{C}$  NMR, 125 MHz, acetone- $\text{d}_6$**   $\delta$  173.55, 171.05, 168.28, 166.07, 159.77, 159.11, 156.69, 152.08, 150.83, 147.78, 147.54, 145.78, 144.99, 142.76, 141.99, 137.42, 135.70, 135.56, 134.55, 132.92, 130.30, 129.89, 129.19, 128.87, 128.47, 127.93, 126.23, 125.04, 124.50, 123.15, 122.98, 120.73, 120.39, 120.21, 120.09, 117.78, 112.01, 109.51, 107.32, 67.24, 55.77, 55.66, 48.85, 48.38, 47.89, 40.69, 35.51, 32.20, 32.16, 29.21, 28.22, 26.99, 25.16, 23.12, 21.62, 20.90, 15.11, 14.90, 13.27, 12.77. **HRMS (ESI+)** [ $\text{M}^+$ ] found: 1238.5356, calculated: 1238.5345.

**HTL-Trp-BODIPY-FF, (**44**)**

A solution of compound **43** (15.0 mg, 12.3  $\mu\text{mol}$ , 1.0 eq.) in anhydrous DMF (100  $\mu\text{L}$ ) was added to a solution of piperidine (20  $\mu\text{L}$ , 203  $\mu\text{mol}$ , 16.5 eq.) in anhydrous DMF (100  $\mu\text{L}$ ) at room temperature with stirring for 5 min. Upon completion, the reaction was quenched by adding a saturated  $\text{NH}_4\text{Cl}$  aqueous solution. The organic layer was extracted

with ethyl acetate three times, washed with brine, and dried over Na<sub>2</sub>SO<sub>4</sub>. The solvent was removed using a rotary evaporator and the crude deprotected product (H<sub>2</sub>N-Trp-BODIPY-FF) was used for the next reaction without further purification. H<sub>2</sub>N-Trp-BODIPY-FF was dissolved in anhydrous DMF (3 mL) and then added a solution of compound 17 (9.0 mg, 20.6 μmol, 1.7 eq.) and *N,N*-diisopropylethylamine (100 μL, 574 μmol, 47 eq.) under nitrogen atmosphere. The mixture was stirred at 40 °C for 2 h. Upon completion, the residue was concentrated under reduced pressure, and purified using reversed-phase chromatography (0.1% formic acid acetonitrile/water=65/35-95/5). After lyophilization, compound 44 (3.3 mg, 2.47 μmol, 20%) was obtained as an orange powder.

**<sup>1</sup>H NMR, 500 MHz, acetone-d<sub>6</sub>** δ 10.53 (s, 1H), 7.95 (m, 1H), 7.75 (dd, 1H, *J* = 4.0 Hz, *J* = 4.0 Hz), (ddd, *J* = 7.5 Hz, *J* = 1.5 Hz, *J* = 1.5 Hz, 1H), 7.70 (ddd, *J* = 7.5 Hz, *J* = 7.5 Hz, *J* = 1.0 Hz, 1H), 7.53 (dd, 1H), 7.45 (m, 1H), 7.39 (m, 1H), 7.29 (m, 2H), 7.16 (ddd, *J* = 7.5 Hz, *J* = 7.5 Hz, *J* = 1.5 Hz, 1H), 7.09 (m, 2H), 6.58 (m, 1H), 6.34 (m, 1H), 6.25 (s, 1H), 6.11 (s, 1H), 4.81 (m, 1H), 4.54 (sept, *J* = 7.0 Hz, 1H), 4.18 (m, 2H), 3.90-3.75 (m, 4H), 3.70-3.45 (m, 12H), 3.40 (m, 1H), 3.26 (m, 2H), 2.58 (t, *J* = 7.5 Hz, 2H), 2.56 (s, 3H), 2.25 (s, 3H), 2.22 (s, 3H), 2.00-1.80 (m, 4H), 1.88 (s, 3H), 1.72 (m, 2H), 1.63 (d, *J* = 2.5 Hz, 3H), 1.52 (m, 2H), 1.43-1.37 (m, 2H), 1.36 (s, 3H), 1.35-1.25 (m, 9H), 0.82 (d, *J* = 7.0 Hz, 3H). **<sup>13</sup>C NMR, 125 MHz, acetone-d<sub>6</sub>** δ 173.09, 171.11, 171.07, 169.36, 168.28, 166.03, 159.80, 159.16, 152.08, 150.84, 147.78, 147.53, 145.77, 142.73, 137.37, 135.69, 135.54, 134.51, 132.97, 130.25, 129.99, 129.22, 128.89, 125.03, 124.50, 122.99, 120.39, 120.17, 120.03, 117.94, 122.04, 109.24, 107.32, 71.59, 71.53, 71.35, 70.92, 70.82, 70.26, 53.63, 53.50, 48.85, 48.39, 45.76, 40.68, 39.38, 35.51, 33.35, 32.20, 32.16, 29.20, 28.00, 27.36, 26.99, 26.16, 25.19, 23.14, 21.61, 20.90, 15.09, 14.93, 13.27, 12.77. **HRMS (ESI+)** [M+Na<sup>+</sup>] found: 1337.6008, calculated: 1337.6007.

## Experimental Sections

### Materials and instruments

---

All chemical reagents for the synthesis were purchased from Tokyo Chemical Industries Co., Ltd. (Tokyo, Japan), Wako Pure Chemical Corp. (Osaka, Japan), or Sigma-Aldrich Chemicals Pvt., Ltd. (St. Louis, MO, USA) and used as received. Thin-layer chromatography (TLC) was performed to judge the reaction completion using aluminum 60F254 silica gel sheets (Merck Co., Inc., Kenilworth, NJ, USA). The microwave reactions were completed using a microwave synthesizer (Initiator; Biotage). The purification and purity analysis of Trp-BODIPY, Trp-BODIPY-FF, and HTL-Trp-BODIPY-FF were carried out using a high-performance liquid chromatography (HPLC) system composed of a reversed-phase column (Inertsil ODS-3, 250 × 10 mm (for semi-prep), 250 × 4.6 mm (for analysis); GL Sciences, Inc., Tokyo, Japan), a detector (MD-4010; JASCO Corp., Tokyo, Japan), and a pump (PU-2080; JASCO Corp.). For HPLC analysis, samples were eluted through a column with a linear gradient of acetonitrile/water containing 0.1% formic acid. <sup>1</sup>H (500 MHz) and <sup>13</sup>C (125 MHz) nuclear magnetic resonance (NMR) spectroscopic data were recorded and analyzed using an AVANCE III HD 500 (Bruker Corp., Billerica, MA, USA) with a software (TopSpin 4.3.0; Bruker Corp.). Mass spectra (MS) were collected using an electrospray ionization (ESI) (LCT-Premier XE; Waters Corp., Milford, MA, USA), a fast atom bombardment (FAB), a electron ionization (JMS-700; JOEL Ltd., Tokyo, Japan), or a matrix assisted laser

desorption ionization (MALDI) spectrometry (JMS-S300; JOEL Ltd.). Absorption and fluorescence spectroscopic data were recorded on a V-650 (JASCO Corp.) and an F-4500 spectrometer (Hitachi High-Tech Science Corp., Tokyo, Japan).

#### Light irradiation setup for in vitro analysis

---

Light irradiation of samples in a cuvette was conducted by a home-built system using a MAX-302 xenon light source (Asahi Spectra Co., Ltd., Tokyo, Japan) equipped with two band-pass filters LX0365 (Asahi Spectra Co., Ltd.) for 365 nm irradiation and LX0530 (Asahi Spectra Co., Ltd.) for 530 nm irradiation. The light was irradiated to the orthogonal side of the cuvette from the detector in the V-650 or F-4500 spectrometer. The concentration of Trp-BODIPY-FF or HTL-Trp-BODIPY-FF was optimized at 10  $\mu\text{M}$  to obtain absorption spectra and extinction coefficients and at 1.0  $\mu\text{M}$  to obtain fluorescence spectra and intensities. Each spectroscopic data was recorded in 100 mM phosphate buffer (pH 7.4), *n*-octanol and glycerol containing 1% dimethyl sulfoxide (DMSO) at 37 °C. The photoswitching performance of Trp-BODIPY-FF including 5.0 eq. BSA, or HTL-Trp-BODIPY-FF with 2.0 eq. Halo-tag (previously incubated for 20 minutes at 37 °C to complete labeling) were also evaluated in this system.

#### Measurement of fluorescence quantum yields and brightness of Trp-BODIPY, Trp-BODIPY-FF, and HTL-Trp-BODIPY-FF

---

Fluorescence quantum yields of Trp-BODIPY, Trp-BODIPY-FF, and HTL-Trp-BODIPY-FF were measured in 100 mM phosphate buffer (pH 7.4), *n*-octanol, and glycerol containing 1% DMSO at 37 °C. Fluorescence quantum yields of Trp-BODIPY and Trp-BODIPY-FF in 100 mM phosphate buffer (pH 7.4) including 5.0  $\mu\text{M}$  BSA were also measured. The fluorescence quantum yield of Halo-tag binding HTL-Trp-BODIPY-FF was measured by incubating with a 2.0  $\mu\text{M}$  Halo tag at 37 °C for 20 min beforehand. Fluorescein in basic ethanol ( $\Phi_{\text{ref}} = 0.92^{100}$ ) was used as a reference. Fluorescence measurements were performed at 470 nm excitation. Fluorescence quantum yields ( $\Phi_{\text{FL}}$ ) were determined following Eq. 3-1.

$$\Phi_{\text{FL}} = \Phi_{\text{ref}} \frac{A_{\text{ref}} F_s n_s^2}{A_s F_{\text{ref}} n_{\text{ref}}^2}$$

Equation 3-1

Here,  $A_s$  and  $A_{\text{ref}}$  are the absorbances at the excitation wavelength,  $F_s$  and  $F_{\text{ref}}$  are the relative fluorescence intensities, and  $n_s$  and  $n_{\text{ref}}$  are the solvent refractive indices of the sample and reference, respectively. Brightness is calculated as the product of the fluorescence quantum yield ( $\Phi_{\text{FL}}$ ) and extinction coefficient at the maximum absorption wavelength ( $\epsilon_{\text{max}}$ ) (Eq. 3-2).

$$\text{Brightness} = \Phi_{\text{FL}} \times \epsilon_{\text{max}} [\text{M}^{-1}\text{cm}^{-1}]$$

Equation 3-2

#### Determination of photon flux

---

For determining photoconversion quantum yields and kinetics of FF, Trp-BODIPY-FF, and HTL-Trp-BODIPY-FF in various conditions, 4,4'-dimethylazobenzene in acetonitrile and Aberchrome 540 in toluene were used as chemical actinometers. The photon flux at 365 nm was determined from the *E*-to-*Z* photoisomerization kinetics of 1,4-dimethyl azobenzene at 365 nm irradiation following a previous report<sup>79</sup>. The photon flux at 530 nm was determined from the cycloreversion reaction kinetics of Aberchrome 540 at 530 nm irradiation following the previous report<sup>49</sup>.

### Determination of photoconversion quantum yield

To measure the photoconversion quantum yield, the time courses of absorption change of 50  $\mu\text{M}$  FF (at 530 nm), 10  $\mu\text{M}$  Trp-BODIPY-FF (at 550 nm), and 10  $\mu\text{M}$  HTL-Trp-BODIPY-FF (at 550 nm) in each condition upon 365 or 530 nm photoirradiation were recorded. Judging from these results of measurement, both the cyclization and cycloreversion reactions of FF, Trp-BODIPY-FF, and HTL-Trp-BODIPY-FF proceed by first-order kinetics. The cyclization reaction rate constants ( $k_{oc}$ ) and the cycloreversion reaction rate constants ( $k_{co}$ ) were determined by following Eq. 3-3 and 3-4, respectively.

$$A(t) = A_{\text{PSS at 530 nm}} - (A_{\text{PSS at 365 nm}} - A_{\text{PSS at 530 nm}}) \exp(-k_{oc}t) \text{ [s}^{-1}\text{]}$$

Equation 3-3

$$A(t) = A_{\text{PSS at 365 nm}} - (A_{\text{PSS at 530 nm}} - A_{\text{PSS at 365 nm}}) \exp(-k_{co}t) \text{ [s}^{-1}\text{]}$$

Equation 3-4

The  $A(t)$  is recorded absorbance at 530 nm (FF) and 550 nm (Trp-BODIPY-FF and HTL-Trp-BODIPY-FF).  $A_{\text{PSS at 365 nm}}$  and  $A_{\text{PSS at 530 nm}}$  is the absorbance in the photostationary state at 365 and 530 nm, respectively. The value of  $A_{\text{PSS at 365 nm}}$ ,  $A_{\text{PSS at 530 nm}}$ ,  $k_{oc}$  and  $k_{co}$  was approximated from the collected data of  $A(t)$ .

In principle, the cyclization and cycloreversion reaction rate are defined as following Eq. 3-5 and 3-6, respectively.

$$\frac{d[\text{O}]}{dt} = -\frac{\phi_{oc}q_{\lambda_i}}{V} \frac{\varepsilon_{o,\lambda_i}[\text{O}]f}{\varepsilon_{c,\lambda_i}[\text{C}] + \varepsilon_{o,\lambda_i}[\text{O}]} + \frac{\phi_{co}q_{\lambda_i}}{V} \frac{\varepsilon_{c,\lambda_i}[\text{C}]f}{\varepsilon_{c,\lambda_i}[\text{C}] + \varepsilon_{o,\lambda_i}[\text{O}]}$$

Equation 3-5

$$\frac{d[\text{C}]}{dt} = -\frac{\phi_{co}q_0}{V} \frac{\varepsilon_{c,\lambda_i}[\text{C}]f}{\varepsilon_{c,\lambda_i}[\text{C}] + \varepsilon_{o,\lambda_i}[\text{O}]} + \frac{\phi_{oc}q_0}{V} \frac{\varepsilon_{o,\lambda_i}[\text{O}]f}{\varepsilon_{c,\lambda_i}[\text{C}] + \varepsilon_{o,\lambda_i}[\text{O}]}$$

Equation 3-6

Here,  $[\text{C}]$ ,  $[\text{O}]$ ,  $\phi_{co}$ ,  $\phi_{oc}$ ,  $q_{\lambda_i}$ ,  $V$ , and  $\varepsilon_{\lambda_i}$  are the concentration of the closed-ring and open-ring form, cyclization and cycloreversion reaction quantum yield, photon flux determined using chemical actinometers, the sample volume, and the molar absorption coefficient at the irradiation wavelength ( $\lambda_i = 365$  and 530 nm).  $f$  is a fraction of light absorbed by a sample, estimated from the absorbance at 365 and 530 nm (Eq. 3-7).

$$f = 1 - 10^{-(\varepsilon_{c,\lambda_i}[\text{C}] + \varepsilon_{o,\lambda_i}[\text{O}])l}$$

Equation 3-7

In the initial stage of the cyclozation reaction, when the absorbance of the closed-ring form is 20 times lower than that of the open-ring form (Eq. 3-8), Equation 3-5 and 3-7 can be reduced and convened in Eq. 3-9.

$$\varepsilon_{o,\lambda_i}[\text{O}] \geq 20\varepsilon_{c,\lambda_i}[\text{C}]$$

Equation 3-8

$$\frac{d[O]}{dt} = -\frac{\phi_{oc}q_{\lambda_i}}{V}(1 - 10^{-\varepsilon_{o,\lambda_i}[O]l})$$

Equation 3-9

The integral of Eq. 3-9 gives Eq. 3-10.

$$\ln(10^{\varepsilon_{o,\lambda_i}[O]l} - 1) = \ln(10^{\varepsilon_{o,\lambda_i}[O]_0l} - 1) - \frac{\phi_{oc}q_{\lambda_i}\varepsilon_{o,\lambda_i}l \ln 10}{V}t$$

Equation 3-10

Following Lambert-Beer equation, Eq. 3-11 is described.

$$\ln(10^{A_{\lambda_i}(t)} - 1) = \ln(10^{A_{\lambda_i}(0)} - 1) - \frac{\phi_{oc}q_{\lambda_i}\varepsilon_{o,\lambda_i}l \ln 10}{V}t$$

Equation 3-11

Since the cyclization reaction follows the first-order kinetics (Eq. 3-3),  $A_{\lambda_i}(t)$  are calculated following Eq. 3-12.

$$A_{\lambda_i}(t) = A_{\lambda_i}(\infty) - (A_{\lambda_i}(\infty) - A_{\lambda_i}(0)) \exp(-k_{oc}t)$$

Equation 3-12

Here,  $A_{\lambda_i}(\infty)$  and  $A_{\lambda_i}(0)$  is the absorbance at  $\lambda_i = 365$  nm in the photostationary state at 365 and 530 nm, respectively. Here, the linear relation between  $\ln(10^{A_{\lambda_i}(t)} - 1)$  and  $t$  provides the slope  $m$  and determines the quantum yield for the cyclization reaction.

$$\phi_{oc} = -\frac{mV}{q_{\lambda_i}\varepsilon_{o,\lambda_i}l \ln 10}$$

Equation 3-13

In the initial stage of the cycloreversion reaction, when the absorbance of the open-ring form is 20 times lower than that of the closed-ring form (Eq. 3-14), Equation 3-6 and 3-7 can be reduced and convened in Eq. 3-15.

$$\varepsilon_{c,\lambda_i}[C] \geq 20\varepsilon_{o,\lambda_i}[O]$$

Equation 3-14

$$\frac{d[C]}{dt} = -\frac{\phi_{co}q_{\lambda_i}}{V}(1 - 10^{-\varepsilon_{c,\lambda_i}[C]l})$$

Equation 3-15

The integral of Eq. 3-15 gives Eq. 3-16.

$$\ln(10^{-\varepsilon_{c,\lambda_i}[C]l} - 1) = \ln(10^{-\varepsilon_{c,\lambda_i}[C]_0l} - 1) - \frac{\phi_{co}q_{\lambda_i}\varepsilon_{c,\lambda_i}l \ln 10}{V}t$$

Equation 3-16

Following Lambert-Beer equation, Eq. 3-17 is described.

$$\ln(10^{A_{\lambda_i}(t)} - 1) = \ln(10^{A_{\lambda_i}(0)} - 1) - \frac{\phi_{co}q_{\lambda_i}\varepsilon_{c,\lambda_i}l \ln 10}{V}t$$

Equation 3-17

Since the cycloreversion reaction follows the first-order kinetics (Eq. 3-4),  $A_{\lambda_i}(t)$  are measured or calculated following Eq. 3-18.

$$A_{\lambda_i}(t) = A_{\lambda_i}(\infty) - (A_{\lambda_i}(\infty) - A_{\lambda_i}(0)) \exp(-k_{co}t)$$

Equation 3-18

Here,  $A_{\lambda_i}(\infty)$  and  $A_{\lambda_i}(0)$  is the absorbance at  $\lambda_i = 530$  nm in the photostationary state at 365 and 530 nm, respectively. Here, the linear relation between  $\ln(10^{A_{\lambda_i}(t)} - 1)$  and  $t$  provides the slope  $m$  and determines the quantum yield for the cycloreversion reaction.

$$\phi_{co} = -\frac{mV}{q_{\lambda_i} \epsilon_{c,\lambda_i} l \ln 10}$$

Equation 3-19

### Quenching efficiency calculation

---

The quenching efficiencies of 1.0  $\mu$ M Trp-BODIPY-FF and 1.0  $\mu$ M HTL-Trp-BODIPY-FF in 100 mM phosphate buffer (pH 7.4) (PB), glycerol, *n*-octanol, PB including 5.0  $\mu$ M BSA (for Trp-BODIPY-FF), and PB including 2  $\mu$ M Halo-tag (for HTL-Trp-BODIPY-FF) were quantified using following Eq. 3-20.

$$\text{Quenching efficiency, } E(n) = \frac{I_{\text{Fl,on}}(n) - I_{\text{Fl,off}}(n)}{I_{\text{Fl,on}}(n)}$$

Equation 3-20

Here,  $I_{\text{Fl,on}}(n)$  and  $I_{\text{Fl,off}}(n)$  are the fluorescence intensity before and after the  $n$  th 365 nm irradiation.

### Preparation of Trp-BODIPY-FF-BSA bioconjugate

---

A solution of Trp-BODIPY-FF (10 mM) in DMSO (2  $\mu$ L) was added to 200 mM 2-(*N*-morpholino)ethanesulfonic acid (MES) buffer (pH 6.0) (200  $\mu$ L) containing *N*-hydroxysulfosuccinimide sodium salt (50 mM) and 1-ethyl-3-(3-dimethylaminopropyl)-carbodiimide hydrochloride (5 mM) and shook vigorously at 25  $^{\circ}$ C for 1 h. The mixture was then incubated with BSA (A0281; Sigma-Aldrich Chemicals Pvt., Ltd.) (10  $\mu$ M) in MES buffer (pH 6.0) (200  $\mu$ L) at 37  $^{\circ}$ C for 1 h. Unconjugated Trp-BODIPY-FF was excluded using Nanosep<sup>®</sup> centrifugal devices with an Omega<sup>TM</sup> membrane 30 K (OD030C34; Pall Corp., Port Washington, NY, USA). After ultrafiltration, the conjugates were dissolved in 100 mM phosphate buffer (pH 7.4) (200  $\mu$ L). An aliquot of the solution (10  $\mu$ L) was added to the loading buffer including 100 mM dithiothreitol (10  $\mu$ L), heated at 103  $^{\circ}$ C for 3 min, and subsequently analyzed using sodium dodecyl sulfate-polyacrylamide gel electrophoresis (SDS-PAGE). The molecular marker (Precision Plus Protein Unstained Standards; BioRad Laboratories, Inc., Hercules, CA, USA) was also loaded onto the same gel plate. After the fluorescent gel images were obtained using a Typhoon FLA 9500 (GE Healthcare, Chicago, IL, USA), the gel was stained with Coomassie Brilliant Blue. The BSA concentration was determined using the Bradford assay on a multilabel counter (ARVOTM MX; PerkinElmer, Waltham, MA, USA) with BSA as a standard reagent.

### Analysis of the affinity of Trp-BODIPY-FF and HTL-Trp-BODIPY-FF with BSA

---

Scatchard plot for Trp-BODIPY-FF and HTL-Trp-BODIPY-FF vs BSA in 100 mM phosphate buffer is analyzed from the fluorescence intensities with increasing the concentration of BSA ( $[BSA]_0$ ) varied from 0 to 2000  $\mu\text{M}$ . The concentrations of the BSA-probe complex ( $x$ ) were estimated from the fluorescent intensity at 520 nm using Eq. 3-21. The value of  $n$  represents the binding ratio of the probe to BSA. In the Scatchard plot,  $n$  was estimated as 1. The probe concentration ( $[probe]_0$ ) is fixed at 1.0  $\mu\text{M}$ .  $F$  is the fluorescence intensity at 520 nm of probe containing BSA of each concentration.  $F_{\text{max}}$  is the approximated maximum fluorescence intensity at 520 nm of probe using the quadratic equation (Eq. 3-22) which is derived from Eq. 3-23.  $F_{\text{min}}$  was defined as to be 1. Both plots do not give a proper linear approximation, and show a downward convex-like curve, suggesting the presence of multiple different binding sites.

$$x = \frac{[probe]_0}{n} \frac{F - F_{\text{min}}}{F_{\text{max}} - F_{\text{min}}}$$

Equation 3-21

$$F = F_{\text{min}} + \frac{F_{\text{max}} - F_{\text{min}}}{2[probe]_0} \left( ([probe]_0 + [BSA]_0 + K_D) - \sqrt{([probe]_0 + [BSA]_0 + K_D)^2 - 4n[probe]_0[BSA]_0} \right)$$

Equation 3-22

$$x = \frac{([probe]_0 + [BSA]_0 + K_D) - \sqrt{([probe]_0 + [BSA]_0 + K_D)^2 - 4[probe]_0[BSA]_0}}{2}$$

Equation 3-23

Although the dissociation constant ( $K_D$ ) was also approximated by Eq. 3-22,  $K_D$  was determined using the modified Hill plot. When the binding ratio is unknown, the Hill plot is more appropriate because Eq. 3-22 assumes that the binding ratio of the probe to BSA ( $n$ ) is 1 (Eq. 3-24).

$$K_D = \frac{([probe] - x)([BSA] - x)}{x}$$

Equation 3-24

Job's plot for Trp-BODIPY-FF and HTL-Trp-BODIPY-FF vs BSA in 100 mM phosphate buffer (pH 7.4) was analyzed by monitoring the fluorescence intensity at 520 nm. The concentration of the probe varied from 100 to 900 nM as the BSA concentration decreased from 900 to 100 nM. Both Job's plots exhibited maximum mole fractions ( $[probe]_0/[probe]_0+[BSA]_0$ ) around 0.70 (Trp-BODIPY-FF) and 0.64 (HTL-Trp-BODIPY-FF), implicating that the binding ratio of the probe to BSA is 2. To analyze the affinity with BSA, the fluorescence intensities of both probes (1.0  $\mu\text{M}$ ) were measured in 100 mM phosphate buffer (pH 7.4) containing varying concentrations of BSA (from 1 to 100  $\mu\text{M}$ ). When the binding ratio is unknown, the dissociation constant ( $K_D$ ) was defined as Equation 3-25.

$$K_D = \frac{[probe]^n [BSA]}{x}$$

Equation 3-25

Herein, the  $[probe]$  and  $[BSA]$  are the concentration of probe and BSA at equilibrium. The value of  $n$  represents the

binding ratio of the probe to BSA (equivalent to Hill coefficient). Eq. 3-26 is provided by taking the logarithm of Eq. 3-25.

$$\log \frac{1}{[\text{probe}]} = \frac{1}{n} \log \frac{[\text{BSA}]}{x} - \frac{1}{n} \log K_D$$

Equation 3-26

The initial concentration of the probe is fixed at 1.0  $\mu\text{M}$  (Eq. 3-27).

$$[\text{probe}] = 1 - nx \quad (\mu\text{M})$$

Equation 3-27

The combination of Eq 3-21, 3-26 and 3-27 gives Equation for linear plot (modified Hill plot). (Eq. 3-28).

$$\log \frac{F_{\max} - F_{\min}}{F_{\max} - F} = \frac{1}{n} \log \frac{[\text{BSA}](F_{\max} - F_{\min})}{F - F_{\min}} - \frac{1}{n} \log \frac{K_D}{n}$$

Equation 3-28

Here, the linear relation between  $\log \frac{F_{\max} - F_{\min}}{F_{\max} - F}$  and  $\log \frac{[\text{BSA}](F_{\max} - F_{\min})}{F - F_{\min}}$  provides the slope  $\frac{1}{n}$  and the intercept  $-\frac{1}{n} \log \frac{K_D}{n}$ . In this plot,  $[\text{BSA}]$  is approximated to  $[\text{BSA}]_0$ . The modified Hill plot of Trp-BODIPY-FF vs BSA gives  $n = 2.3 \pm 0.2$  and  $K_D = 6.9 \pm 2.8 \mu\text{M}$ , and HTL-Trp-BODIPY-FF vs BSA gives  $n = 2.6 \pm 0.2$  and  $K_D = 11.8 \pm 3.9 \mu\text{M}$ , respectively.

### Computational simulation of HTL-Trp-BODIPY-FF with Halo-tag

---

Computational simulation study on HTL-Trp-BODIPY-FF with Halo-tag was carried out using MacroModel (Schrödinger Maestro v13.1). The protein data bank (PDB ID: 6u32) was used for determining the protein structure and Halo-tag ligand (HTL) binding mode. The conformational structure of HTL-Trp-BODIPY-FF was searched and optimized using OPLS4 as a force field (solvent: water, maximum iterations: 2500, convergence threshold: 0.05) followed by torsional sampling MCMM (energy window for saving structures: 21  $\text{kJmol}^{-1}$ , maximum atom deviation cut off: 0.5 Å). The energy-minimized structure of HTL-Trp-BODIPY-FF was manually docked with Halo-tag and optimized the structure of the complex by OPLS4 (solvent: water, maximum iterations: 5000, convergence threshold: 0.1). The range of minimization was set to all atoms within 5 Å of HTL-Trp-BODIPY-FF.

### Protein expression and purification

---

*Escherichia coli* BL21 (DE3) (Novagen) was transformed with pET21b (+)-Halo-His and cultured in Luria-Bertani (LB) medium containing 100 ng/ $\mu\text{L}$  ampicillin at 37 °C. The recombinant Halo-tag protein was expressed and purified according to the previously reported protocol.<sup>72</sup> The purified Halo-tag protein was stored in a pH 7.4 phosphate buffered saline buffer (prepared using PBS Tablets; Takara Bio Inc., Shiga, Japan) at -80 °C by flash freezing. The assay of Halo-tag protein was performed by dissolving the appropriate solutions after thawing the stock solution on ice.

### Protein labeling assay using SDS-PAGE

---

To confirm the labeling of HTL-Trp-BODIPY-FF with Halo-tag, SDS-PAGE analysis was performed. HTL-Trp-

BODIPY-FF (1.0, 2.0, and 4.0  $\mu\text{M}$ ) were incubated with Halo-tag (2.0, 4.0, and 8.0  $\mu\text{M}$ ), respectively, in 100 mM phosphate buffer (pH 7.4) at 37°C for 1 h. After incubation, each solution (10  $\mu\text{L}$ ) was added to loading buffer containing 100 mM dithiothreitol (10  $\mu\text{L}$ ), heated at 103°C for 3 min, and then analyzed by SDS-PAGE. The molecular marker (Precision Plus Protein Unstained Standards) was also loaded onto the same gel plate. The fluorescence image was obtained using a Typhoon FLA 9500, and the gel was then stained with Coomassie Brilliant Blue.

### Labeling kinetics analysis

To determine the labeling kinetics of HTL-Trp-BODIPY-FF to Halo-tag, the time course of the fluorescence intensity of 1.0  $\mu\text{M}$  HTL-Trp-BODIPY-FF incubated with 2.0  $\mu\text{M}$  Halo-tag in 100 mM phosphate buffer (pH 7.4) at 37 °C was monitored. The rate of formation of Halo-tag and probe conjugate follows second-order kinetics and is defined as the rate constants  $k_2$  using Eq. 3-29.

$$-\frac{d[\text{probe}]}{dt} = k_2[\text{probe}][\text{protein}]$$

Equation 3-29

The value of [probe] and [protein] is the concentration of probe (HTL-Trp-BODIPY-FF) and protein (Halo-tag), respectively (Here,  $[\text{probe}]_0 = 1.0 \mu\text{M}$ ,  $[\text{protein}]_0 = 2.0 \mu\text{M}$ ). Additionally, when determining the value of  $[\text{probe}]_0$  and  $[\text{protein}]_0$  as the initial concentration of HTL-Trp-BODIPY-FF and Halo-tag respectively, the concentration of conjugate [conjugate] was expressed (Eq. 3-30).

$$[\text{conjugate}] = [\text{probe}]_0 - [\text{probe}] = [\text{protein}]_0 - [\text{protein}]$$

Equation 3-30

The combination of Eq. 3-29 and 3-30 provides Eq. 3-31.

$$[\text{probe}] = \frac{[\text{probe}]_0([\text{probe}]_0 - [\text{protein}]_0)}{[\text{probe}]_0 - [\text{protein}]_0 \exp(([\text{protein}]_0 - [\text{probe}]_0)k_2t)}$$

Equation 3-31

When the initial concentration of HTL-Trp-BODIPY-FF is lower than that of Halo-tag ( $[\text{probe}]_0 < [\text{protein}]_0$ ), the concentration of conjugate [conjugate] was described using the fluorescence intensity of the reaction mixture as Eq. 3-32.

$$[\text{conjugate}] = \frac{F(t) - F(0)}{\Delta F} [\text{probe}]_0$$

Equation 3-32

$F(t)$  is the fluorescence intensity of the reaction mixture and  $\Delta F$  is the difference in fluorescence intensity between the initial and final state (Eq. 3-33).

$$\Delta F = F(\infty) - F(0)$$

Equation 3-33

The combination of Eq. 3-30, 3-31, 3-32, and 3-33 provides Eq. 3-34.

$$F(t) = \left( \frac{[\text{protein}]_0 - [\text{protein}]_0 \exp(([\text{protein}]_0 - [\text{probe}]_0)k_2t)}{[\text{probe}]_0 - [\text{protein}]_0 \exp(([\text{protein}]_0 - [\text{probe}]_0)k_2t)} \right) \Delta F + F(0)$$

Equation 3-34

The value of  $k_2$  was approximated using the recorded data of  $F(t)$  following Eq.3-34.

### **Construction of plasmid**

---

#### pcDNA3.1(+)-MBP-Halo-mCherry

The DNA fragment of MBP was separately prepared from pcDNA3.1(+)-MBP-PYP-NLS<sup>101</sup> by PCR amplification using a forward primer 5'-GCACTCGCTAGCCACCATGAAAATCGAAGAAG-3' and a reverse primer 5'-TCATCCGGATCCCCTTCCCTCGATCCCG -3'. The fragments were digested using restriction enzymes *NheI* and *BamHI* and were separately ligated into pcDNA3.1(+)-4xCox8-Halo-mCherry plasmid that underwent similar restriction enzyme digestion to generate the title plasmid.

#### \*pcDNA3.1(+)-Tom20-Halo-mCherry

The DNA fragment of Tom20 was separately prepared from pcDNA3.1(+)-Tom20-BL which was gifted from Prof. Miyawaki's group by PCR amplification using a forward primer 5'-GCATTCGCTAGCCACCATGGTG-3' and a reverse primer 5'-TCATAGGGATCC TTCCACATCATCTTCAGCC-3'. The fragments were digested using restriction enzymes *NheI* and *BamHI* and were separately ligated into pcDNA3.1(+)-4xCox8-Halo-mCherry plasmid that underwent similar restriction enzyme digestion to generate the title plasmid.

#### \*pcDNA3.1(+)-4xCox8-Halo-mCherry

The DNA fragment of 2xCox8 was separately prepared from pKmc-2xCox8-Halo by PCR amplification using a forward primer 5'-GTAATTGGATCCGCCACCATGTCCGTCCTG-3' and a reverse primer 5'-TGTTAAGGATCCCCGAGCTTC-3'. The fragments were digested using a single restriction enzyme *BamHI* and were separately ligated into pcDNA3.1(+)-2xCox8-Halo-mCherry plasmid that underwent similar restriction enzyme digestion to generate the title plasmid.

#### \*pcDNA3.1(+)-2xCox8-Halo-mCherry

The DNA fragment of 2xCox8-Halo was separately prepared from pKmc-2xCox8-Halo<sup>102</sup> by PCR amplification using a forward primer 5'-GTACTTGCTAGCGCCACCATGTCCGTCCTGACGCC-3' and a reverse primer 5'-TGTTAACTCGAGACCGGAAATCTCCAGAGTAGACC-3'. The fragments were digested using restriction enzymes *NheI* and *XhoI* and were separately ligated into pcDNA3.1(+)-Halo-mCherry<sup>103</sup> plasmid that underwent similar restriction enzyme digestion to generate the title plasmid.

#### pET21b (+)-Halo-His

The DNA fragment of Halo was separately prepared from pcDNA3.1(+)-Halo-NLS<sup>102</sup> by PCR amplification using a forward primer 5'-GATTCGGCTAGCATGTCCGAAATCGGTACTGG-3' and a reverse primer 5'-GATTCGGCTAGCATGTCCGAAATCGGTACTGG-3'. The fragments were digested using a single restriction enzyme *NheI* and were separately ligated into pET21b (+) (Novagen) plasmid that underwent similar restriction enzyme

digestion to generate the title plasmid.

#### pcDNA3.1(+)-Halo-EGFR-mCherry

The DNA fragment of Halo was separately prepared from pcDNA3.1 (+)-Halo-NLS<sup>102</sup> by PCR amplification using a forward primers 5'-GATCGTGCTAGCATGTCCGAAATCGGTACTGG-3' and a reverse primer 5'-TGTTAAGCTAGCACCGGAAATCTCCAGAGTAGAC-3'. The fragments were digested using restriction enzyme *NheI* and were separately ligated into pcDNA3.1-BL(wt)-EGFR-mCherry plasmid that underwent similar restriction enzyme digestion to generate the title plasmid.

#### pcDNA3.1(+)-BL(wt)-EGFR-mCherry

The DNA fragment of mCherry was separately prepared from pcDNA3.1(+)-Halo-mCherry<sup>103</sup> by PCR amplification using a forward primers 5'-CTCGAGATGGTGAGCAAGGGCGAG-3' and a reverse primer 5'-GGACGAGCTGTACAAGTAATCTAGA-3'. The fragments were digested using restriction enzyme *XhoI* and *XbaI*, and were separately ligated into pcDNA3.1-BL-EGFR<sup>104</sup> plasmid that underwent similar restriction enzyme digestion to generate the title plasmid.

#### **\*Supplementary note to the construction of plasmids**

I prepared pcDNA3.1(+)-2xCox8-Halo-mCherry and pcDNA3.1(+)-4xCox8-Halo-mCherry for another study and performed mitochondrial imaging using pcDNA3.1(+)-Tom20-Halo-mCherry.

#### **Live-cell imaging**

---

HeLa or HEK293T cells were incubated in Dulbecco's Modified Eagle's Medium (DMEM) containing 10% fetal bovine serum (FBS) and transfected with 2500 ng of each plasmid or pcDNA3.1(+) (for negative control) plasmid using Lipofectamine 3000 transfection reagent (L3000015; Thermo Fisher Scientific) dissolved in Opti-MEM (Thermo Fisher Scientific) following the manufacturer's protocol. After transfection, the cells were incubated for 5 h, replaced medium with a new DMEM (only HeLa cells), and then incubated for 18 h at 37 °C with a continuous supply of 5% CO<sub>2</sub>. The cells were then washed twice with Hank's balanced salt solution (HBSS), incubated in DMEM including 1.0 μM HTL-Trp-BODIPY-FF (0.1% DMSO) for 20 min, and captured images using confocal fluorescence microscopies (FV10i; Olympus Corporation and Ti2-E; Nikon Corporation). FV10i recorded images with excitation/emission at 473/490–540 nm for HTL-Trp-BODIPY-FF detection and at 559/570–620 nm for mCherry detection. Ti2-E recorded images with excitation/emission at 488/499–551 nm for HTL-Trp-BODIPY-FF detection and at 561/571–625 nm for mCherry detection.

#### **Light irradiation setup for live cell imaging**

---

Light irradiation on living cells was conducted using a LED light source (CL-1501, Asahi Spectra Co., Ltd.) equipped with a timer (CL-TCN1, Asahi Spectra Co., Ltd.), a filter (CL-H1-365-9-1-B, Asahi Spectra Co., Ltd.), and a collective

lens (CL-H1LCB02, Asahi Spectra Co., Ltd.) for repetitive 365 nm irradiation (Light intensity: 10 mW/cm<sup>2</sup>, Irradiation time: 10 s per one cycle). Ti2-E equipped with a Plan Apochromat Lambda S 40XC silicon oil objective lens (NA 1.25, Nikon Corporation) or Plan Apo Lambda S 60XC silicone oil objective lens (NA 1.4, Nikon Corporation) and micro scanning stage was used to observe fluorescence images in living cells maintained at 37 °C with a continuous supply of 5% CO<sub>2</sub> by using a stage-top incubator (STXG-WSKMX-SET, Tokai Hit). After each cycle of 365 nm irradiation, images were taken at the rate of 1.01 (40X lens) or 1.76 (60X lens) fps with a quality of 0.86 (40X lens) or 0.58 (60X lens) μm/pixel for 20 s (20 (40X lens) or 11 (60X lens) images were captured per one cycle) by confocal laser scanning microscopy (AX-R, Nikon Corporation). All the images are recorded in a single z-stack plane. During the imaging, the fluorescence intensity of HTL-Trp-BODIPY-FF was recovered upon 488 and 561 nm excitation light stimulation. 365 nm irradiation (10 s) and 488 and 561 nm excitation (20 s) were repeated 10 times with a 1 s waiting time per each irradiation event.

### Image analyses

---

Image analyses were completed with commercial software ImageJ (Fiji) and NIS-Elements (Nikon Corporation). The fluorescence images were processed with the ImageJ software. Ratiometric images were obtained using both ImageJ (for image generation) and NIS-Elements software (for extracting signal intensities). Ratiometric images were generated using recorded images without background subtraction and masking. Before the analysis, all images were not processed with any contrast and brightness, because it may change the original signal intensities. For each experiment, I analyzed a random selection of 10 cells in three different cell plates (the number of replicates:  $N=3$ ). The signal intensities of green ( $I_{\text{Green}}$ ) and red channel ( $I_{\text{Red}}$ ) were measured using NIS-Elements software and calculated the ratio of green to red channel following Eq. 3-35.

$$\text{Ratio intensity, } I_{\text{Ratio}} = \frac{I_{\text{Green}}}{I_{\text{Red}}}$$

Equation 3-35

For measurement and analysis of the signal intensities, individual cells were automatically selected and defined as regions of interest (ROIs) using NIS-Elements software. The quenching efficiency in each cell was calculated using Eq. 3-36.

$$\text{Quenching efficiency, } E(n) = \frac{I_{\text{Ratio,on}}(n) - I_{\text{Ratio,off}}(n)}{I_{\text{Ratio,on}}(n)}$$

Equation 3-36

Here,  $I_{\text{Ratio,on}}(n)$  and  $I_{\text{Ratio,off}}(n)$  are the fluorescence ratio intensity before and after the  $n$ th 365 nm irradiation.

## Conclusions and Perspectives

Photoswitchable fluorescent molecules are valuable tools for versatile biological applications including super-resolution imaging technologies. However, owing to their hydrophobicity, synthetic PSFMs easily aggregate in aqueous solutions resulting in decreased photostability. To address this issue, I provided the solution for persistent reversible photoswitching using synthetic PSFMs in both fixed and live cells.

**In Chapter 1**, I have demonstrated that the novel type of PSFMs using AAP, namely SC molecules, exhibit reversible fluorescence switching in aqueous solution. This is the first example of PSFMs utilizing AAP's conformational change between *E*- and *Z*-isomers to control the distance of the fluorescence quencher to the fluorophore. Importantly, the SC molecules showed reversible photoswitching without any additive and resistance to photofatigue after repeated cycles of photoirradiation. I believe that these molecules will contribute to the new concept of design for PSFMs and provide useful tools for real-time tracking of biomolecules and super-resolution imaging in the future.

**In Chapter 2**, to explore the practical design for biological applications including intracellular imaging, I developed a FRET-based PSFM, FF-TMR, using FF as a photochromic quencher. FF-TMR exhibited changes in its fluorescence intensity upon light irradiation. Although, fulgimide chromophores have excellent photochromic properties with high photoisomerization efficiency and thermal stability, its biological applications have not been well investigated<sup>55</sup>. To the authors' knowledge, this is the first example of a FRET-based PSFM using a fulgimide chromophore that achieves both fixed- and live-cell bioimaging. Furthermore, I found that the photoswitching properties of FF-TMR depend on its surrounding environment. Most importantly, FF-TMR assisted by a protein-surface environment in a bioconjugate exhibits reversible and fast photoswitching performance in contrast to FF-TMR itself in an aqueous solution. The biological application of hydrophobic fluorophores (e.g., cyanine<sup>105</sup>) and photochromic chromophores (e.g., diarylethene<sup>5,39</sup> and spiropyran<sup>6,7</sup>) has been limited owing to their aggregation, which leads to poor photostability in an aqueous solution. The protein-surface-assisted strategy is a potential platform for future PSFM development to address this problem.

Modification of proteinogenic amino acids enabled FF-TMR-labeled antibodies to induce repetitive photoswitching in a specific localization of fixed cells. Catalyst-mediated selective amino acid modifications of the protein surface were recently extensively reported<sup>59,60</sup>. These amino acid modifications are attractive and powerful approaches that allow for engineering of biological properties and functions of proteins with minimal undesired chemical labeling. Protein-surface modifications with a PSFM will be widely applicable for existing catalyst-mediated amino acids labeling.

**In Chapter 3**, I have developed a PSFM, named Trp-BODIPY-FF, which has both fluorogenic and

photoswitching properties. Trp-BODIPY-FF exhibited fluorogenicity in hydrophobic environments including on protein-surfaces. Trp-BODIPY-FF enables reversible fluorescence switching upon repetitive light irradiation cycles when interacting with protein surfaces. To adapt Trp-BODIPY-FF to a protein labeling system for live-cell imaging, I have further developed a PSFM, named HTL-Trp-BODIPY-FF, which was created by the conjugation of a Halo-tag ligand to Trp-BODIPY-FF. HTL-Trp-BODIPY-FF successfully labeled Halo-tag with a significant increase in fluorescence intensity. Importantly, HTL-Trp-BODIPY-FF exhibits reversible fluorescence photoswitching in Halo-tag expressing live cells upon light irradiation and for more than 10 cycles. This work is the first example of a photoswitchable fluorogenic probe being used as a Halo tag system for reversible fluorescence control in living cells. Although there are concerns about the phototoxic effects of UV light irradiation on live cells with visible light responsive photochromic molecules such as indolyl fulgides<sup>55</sup>, hemi-indigos<sup>46</sup>, spironaphthoxazines<sup>44</sup>, and azobenzene derivatives,<sup>106,107</sup> I believe that these molecules have the potential to reduce the phototoxicity of PSFMs. The switching contrast of Trp-BODIPY-FF derivatives is still challenging for the final purpose of super-resolution imaging due to the low fluorescence switching contrast between ON and OFF state. Even though this drawback, I have demonstrated that synthesized based PSFMs exhibit excellent fluorogenicity and photoswitching efficiency that is superior to representative photoswitchable fluorescent proteins applicable for super-resolution imaging.

I demonstrated the methodology for reversible fluorescence control using no-wash fluorogenic labeling system. It is in principle applicable to other protein tags for versatile live-cell imaging technology. For example, SNAP<sup>61</sup> and CLIP tag<sup>108</sup> which may provide hydrophobic environments are also applicable for using this fluorogenic labeling system if the ligand is modified for each protein-tag. Moreover, I can also explore the fluorogenic fluorophores that can bind in the hydrophobic cavity of specific proteins as seen in PYP-tag<sup>109</sup> and would provide more compact probe designs. In conclusion, this study demonstrates a new scaffold for fluorescence photoswitching and opens avenues in the design of future live-cell super-resolution imaging.

## References

- (1) Chudakov, D. M.; Verkhusha, V. V.; Staroverov, D. B.; Souslova, E. A.; Lukyanov, S.; Lukyanov, K. A. Photoswitchable Cyan Fluorescent Protein for Protein Tracking. *Nat. Biotechnol.* **2004**, *22* (11), 1435–1439. <https://doi.org/10.1038/nbt1025>.
- (2) Chudakov, D. M.; Belousov, V. V.; Zairisky, A. G.; Novoselov, V. V.; Staroverov, D. B.; Zorov, D. B.; Lukyanov, S.; Lukyanov, K. A. Kindling Fluorescent Proteins for Precise in Vivo Photolabeling. *Nat. Biotechnol.* **2003**, *21* (2), 191–194. <https://doi.org/10.1038/nbt778>.
- (3) Sattarzadeh, A.; Saberianfar, R.; Zipfel, W. R.; Menassa, R.; Hanson, M. R. Green to Red Photoconversion of GFP for Protein Tracking in Vivo. *Sci. Rep.* **2015**, *5* (1), 11771. <https://doi.org/10.1038/srep11771>.
- (4) Kwon, J.; Hwang, J.; Park, J.; Han, G. R.; Han, K. Y.; Kim, S. K. RESOLFT Nanoscopy with Photoswitchable Organic Fluorophores. *Sci. Rep.* **2015**, *5* (1), 17804. <https://doi.org/10.1038/srep17804>.
- (5) Roubinet, B.; Bossi, M. L.; Alt, P.; Leutenegger, M.; Shojaei, H.; Schnorrenberg, S.; Nizamov, S.; Irie, M.; Belov, V. N.; Hell, S. W. Carboxylated Photoswitchable Diarylethenes for Biolabeling and Super-Resolution RESOLFT Microscopy. *Angew. Chem. Int. Ed.* **2016**, *55* (49), 15429–15433. <https://doi.org/10.1002/anie.201607940>.
- (6) Chai, X.; Han, H.-H.; Sedgwick, A. C.; Li, N.; Zang, Y.; James, T. D.; Zhang, J.; Hu, X.-L.; Yu, Y.; Li, Y.; Wang, Y.; Li, J.; He, X.-P.; Tian, H. Photochromic Fluorescent Probe Strategy for the Super-Resolution Imaging of Biologically Important Biomarkers. *J. Am. Chem. Soc.* **2020**, *142* (42), 18005–18013. <https://doi.org/10.1021/jacs.0c05379>.
- (7) Frawley, A. T.; Wycisk, V.; Xiong, Y.; Galiani, S.; Sezgin, E.; Urbančič, I.; Jentzsch, A. V.; Leslie, K. G.; Eggeling, C.; Anderson, H. L. Super-Resolution RESOLFT Microscopy of Lipid Bilayers Using a Fluorophore-Switch Dyad. *Chem. Sci.* **2020**, *11* (33), 8955–8960. <https://doi.org/10.1039/D0SC02447C>.
- (8) Frawley, A. T.; Leslie, K. G.; Wycisk, V.; Galiani, S.; Shrestha, D.; Eggeling, C.; Anderson, H. L. A Photoswitchable Solvatochromic Dye for Probing Membrane Ordering by RESOLFT Super-Resolution Microscopy. *ChemPhysChem* **2023**, *24* (12), e202300125. <https://doi.org/10.1002/cphc.202300125>.
- (9) Grimm, J. B.; English, B. P.; Choi, H.; Muthusamy, A. K.; Mehl, B. P.; Dong, P.; Brown, T. A.; Lippincott-Schwartz, J.; Liu, Z.; Lionnet, T.; Lavis, L. D. Bright Photoactivatable Fluorophores for Single-Molecule Imaging. *Nat. Methods* **2016**, *13* (12), 985–988. <https://doi.org/10.1038/nmeth.4034>.
- (10) Weber, M.; Khan, T. A.; Patalag, L. J.; Bossi, M.; Leutenegger, M.; Belov, V. N.; Hell, S. W. Photoactivatable Fluorophore for Stimulated Emission Depletion (STED) Microscopy and Bioconjugation Technique for Hydrophobic Labels. *Chem. – Eur. J.* **2021**, *27* (1), 451–458. <https://doi.org/10.1002/chem.202004645>.
- (11) Zhang, X.; Guan, D.; Liu, Y.; Liu, J.; Sun, K.; Chen, S.; Zhang, Y.; Zhao, B.; Zhai, T.; Zhang, Y.; Li, F.; Liu, Q. A Universal Photoactivatable Tag Attached to Fluorophores Enables Their Use for Single-Molecule Imaging. *Angew. Chem. Int. Ed.* **2022**, *61* (46), e202211767. <https://doi.org/10.1002/anie.202211767>.
- (12) Zhang, Y.; Zheng, Y.; Tomassini, A.; Singh, A. K.; Raymo, F. M. Photoactivatable Fluorophores for Bioimaging Applications. *ACS Appl. Opt. Mater.* **2023**, *1* (3), 640–651. <https://doi.org/10.1021/acsaom.3c00025>.
- (13) Lincoln, R.; Bossi, M. L.; Rimmel, M.; D’Este, E.; Butkevich, A. N.; Hell, S. W. A General Design of Caging-

- Group-Free Photoactivatable Fluorophores for Live-Cell Nanoscopy. *Nat. Chem.* **2022**, *14* (9), 1013–1020. <https://doi.org/10.1038/s41557-022-00995-0>.
- (14) Saladin, L.; Breton, V.; Dal Pra, O.; Klymchenko, A. S.; Danglot, L.; Didier, P.; Collot, M. Dual-Color Photoconvertible Fluorescent Probes Based on Directed Photooxidation Induced Conversion for Bioimaging. *Angew. Chem. Int. Ed.* **2023**, *62* (4), e202215085. <https://doi.org/10.1002/anie.202215085>.
- (15) Saladin, L.; Dal Pra, O.; Klymchenko, A. S.; Didier, P.; Collot, M. Tuning Directed Photooxidation-Induced Conversion of Pyrrole-Based Styryl Coumarin Dual-Color Photoconverters. *Chem. – Eur. J.* **2023**, *29* (20), e202203933. <https://doi.org/10.1002/chem.202203933>.
- (16) Cho, Y.; An, H. J.; Kim, T.; Lee, C.; Lee, N. K. Mechanism of Cyanine5 to Cyanine3 Photoconversion and Its Application for High-Density Single-Particle Tracking in a Living Cell. *J. Am. Chem. Soc.* **2021**, *143* (35), 14125–14135. <https://doi.org/10.1021/jacs.1c04178>.
- (17) Kwok, S. J. J.; Choi, M.; Bhayana, B.; Zhang, X.; Ran, C.; Yun, S.-H. Two-Photon Excited Photoconversion of Cyanine-Based Dyes. *Sci. Rep.* **2016**, *6* (1), 23866. <https://doi.org/10.1038/srep23866>.
- (18) van de Linde, S.; Heilemann, M.; Sauer, M. Live-Cell Super-Resolution Imaging with Synthetic Fluorophores. *Annu. Rev. Phys. Chem.* **2012**, *63* (1), 519–540. <https://doi.org/10.1146/annurev-physchem-032811-112012>.
- (19) Wysocki, L. M.; Grimm, J. B.; Tkachuk, A. N.; Brown, T. A.; Betzig, E.; Lavis, L. D. Facile and General Synthesis of Photoactivatable Xanthene Dyes. *Angew. Chem. Int. Ed.* **2011**, *50* (47), 11206–11209. <https://doi.org/10.1002/anie.201104571>.
- (20) Gong, Q.; Zhang, X.; Li, W.; Guo, X.; Wu, Q.; Yu, C.; Jiao, L.; Xiao, Y.; Hao, E. Long-Wavelength Photoconvertible Dimeric BODIPYs for Super-Resolution Single-Molecule Localization Imaging in Near-Infrared Emission. *J. Am. Chem. Soc.* **2022**, *144* (48), 21992–21999. <https://doi.org/10.1021/jacs.2c08947>.
- (21) Adhikari, S.; Moscatelli, J.; Smith, E. M.; Banerjee, C.; Puchner, E. M. Single-Molecule Localization Microscopy and Tracking with Red-Shifted States of Conventional BODIPY Conjugates in Living Cells. *Nat. Commun.* **2019**, *10* (1), 3400. <https://doi.org/10.1038/s41467-019-11384-6>.
- (22) Hofmann, M.; Eggeling, C.; Jakobs, S.; Hell, S. W. Breaking the Diffraction Barrier in Fluorescence Microscopy at Low Light Intensities by Using Reversibly Photoswitchable Proteins. *Proc. Natl. Acad. Sci.* **2005**, *102* (49), 17565–17569. <https://doi.org/10.1073/pnas.0506010102>.
- (23) Hell, S. W.; Wichmann, J. Breaking the Diffraction Resolution Limit by Stimulated Emission: Stimulated-Emission-Depletion Fluorescence Microscopy. *Opt. Lett.* **1994**, *19* (11), 780–782. <https://doi.org/10.1364/OL.19.000780>.
- (24) Rankin, B. R.; Kellner, R. R.; Hell, S. W. Stimulated-Emission-Depletion Microscopy with a Multicolor Stimulated-Raman-Scattering Light Source. *Opt. Lett.* **2008**, *33* (21), 2491–2493. <https://doi.org/10.1364/OL.33.002491>.
- (25) Balzarotti, F.; Eilers, Y.; Gwosch, K. C.; Gynnå, A. H.; Westphal, V.; Stefani, F. D.; Elf, J.; Hell, S. W. Nanometer Resolution Imaging and Tracking of Fluorescent Molecules with Minimal Photon Fluxes. *Science* **2017**, *355* (6325), 606–612. <https://doi.org/10.1126/science.aak9913>.

- (26) Aktalay, A.; Khan, T. A.; Bossi, M. L.; Belov, V. N.; Hell, S. W. Photoactivatable Carbo- and Silicon-Rhodamines and Their Application in MINFLUX Nanoscopy. *Angew. Chem. Int. Ed.* **2023**, *62* (41), e202302781. <https://doi.org/10.1002/anie.202302781>.
- (27) Rimmel, M.; Scheiderer, L.; Butkevich, A. N.; Bossi, M. L.; Hell, S. W. Accelerated MINFLUX Nanoscopy, through Spontaneously Fast-Blinking Fluorophores. *Small* **2023**, *19* (12), 2206026. <https://doi.org/10.1002/sml.202206026>.
- (28) Aktalay, A.; Lincoln, R.; Heynck, L.; Lima, M. A. do R. B. F.; Butkevich, A. N.; Bossi, M. L.; Hell, S. W. Bioorthogonal Caging-Group-Free Photoactivatable Probes for Minimal-Linkage-Error Nanoscopy. *ACS Cent. Sci.* **2023**, *9* (8), 1581–1590. <https://doi.org/10.1021/acscentsci.3c00746>.
- (29) Weber, M.; von der Emde, H.; Leutenegger, M.; Gunkel, P.; Sambandan, S.; Khan, T. A.; Keller-Findeisen, J.; Cordes, V. C.; Hell, S. W. MINSTED Nanoscopy Enters the Ångström Localization Range. *Nat. Biotechnol.* **2023**, *41* (4), 569–576. <https://doi.org/10.1038/s41587-022-01519-4>.
- (30) Weber, M.; Leutenegger, M.; Stoldt, S.; Jakobs, S.; Mihaila, T. S.; Butkevich, A. N.; Hell, S. W. MINSTED Fluorescence Localization and Nanoscopy. *Nat. Photonics* **2021**, *15* (5), 361–366. <https://doi.org/10.1038/s41566-021-00774-2>.
- (31) Habuchi, S.; Ando, R.; Dedecker, P.; Verheijen, W.; Mizuno, H.; Miyawaki, A.; Hofkens, J. Reversible Single-Molecule Photoswitching in the GFP-like Fluorescent Protein Dronpa. *Proc. Natl. Acad. Sci.* **2005**, *102* (27), 9511–9516. <https://doi.org/10.1073/pnas.0500489102>.
- (32) Grotjohann, T.; Testa, I.; Leutenegger, M.; Bock, H.; Urban, N. T.; Lavoie-Cardinal, F.; Willig, K. I.; Eggeling, C.; Jakobs, S.; Hell, S. W. Diffraction-Unlimited All-Optical Imaging and Writing with a Photochromic GFP. *Nature* **2011**, *478* (7368), 204–208. <https://doi.org/10.1038/nature10497>.
- (33) Grimm, J. B.; English, B. P.; Chen, J.; Slaughter, J. P.; Zhang, Z.; Revyakin, A.; Patel, R.; Macklin, J. J.; Normanno, D.; Singer, R. H.; Lionnet, T.; Lavis, L. D. A General Method to Improve Fluorophores for Live-Cell and Single-Molecule Microscopy. *Nat. Methods* **2015**, *12* (3), 244–250. <https://doi.org/10.1038/nmeth.3256>.
- (34) Sheng, W.; Nick, S. T.; Santos, E. M.; Ding, X.; Zhang, J.; Vasileiou, C.; Geiger, J. H.; Borhan, B. A Near-Infrared Photoswitchable Protein–Fluorophore Tag for No-Wash Live Cell Imaging. *Angew. Chem. Int. Ed.* **2018**, *57* (49), 16083–16087. <https://doi.org/10.1002/anie.201810065>.
- (35) Santos, E. M.; Sheng, W.; Esmatpour Salmani, R.; Tahmasebi Nick, S.; Ghanbarpour, A.; Gholami, H.; Vasileiou, C.; Geiger, J. H.; Borhan, B. Design of Large Stokes Shift Fluorescent Proteins Based on Excited State Proton Transfer of an Engineered Photobase. *J. Am. Chem. Soc.* **2021**, *143* (37), 15091–15102. <https://doi.org/10.1021/jacs.1c05039>.
- (36) Wang, L.; Frei, M. S.; Salim, A.; Johnsson, K. Small-Molecule Fluorescent Probes for Live-Cell Super-Resolution Microscopy. *J. Am. Chem. Soc.* **2019**, *141* (7), 2770–2781. <https://doi.org/10.1021/jacs.8b11134>.
- (37) Ye, Z.; Yu, H.; Yang, W.; Zheng, Y.; Li, N.; Bian, H.; Wang, Z.; Liu, Q.; Song, Y.; Zhang, M.; Xiao, Y. Strategy to Lengthen the On-Time of Photochromic Rhodamine Spirolactam for Super-Resolution Photoactivated Localization Microscopy. *J. Am. Chem. Soc.* **2019**, *141* (16), 6527–6536. <https://doi.org/10.1021/jacs.8b11369>.

- (38) Zheng, Y.; Ye, Z.; Zhang, X.; Xiao, Y. Recruiting Rate Determines the Blinking Propensity of Rhodamine Fluorophores for Super-Resolution Imaging. *J. Am. Chem. Soc.* **2023**, *145* (9), 5125–5133. <https://doi.org/10.1021/jacs.2c11395>.
- (39) Uno, K.; Bossi, M. L.; Irie, M.; Belov, V. N.; Hell, S. W. Reversibly Photoswitchable Fluorescent Diarylethenes Resistant against Photobleaching in Aqueous Solutions. *J. Am. Chem. Soc.* **2019**, *141* (41), 16471–16478. <https://doi.org/10.1021/jacs.9b08748>.
- (40) Kim, D.; Aktalay, A.; Jensen, N.; Uno, K.; Bossi, M. L.; Belov, V. N.; Hell, S. W. Supramolecular Complex of Photochromic Diarylethene and Cucurbit[7]Uril: Fluorescent Photoswitching System for Biolabeling and Imaging. *J. Am. Chem. Soc.* **2022**, *144* (31), 14235–14247. <https://doi.org/10.1021/jacs.2c05036>.
- (41) Uno, K.; Aktalay, A.; Bossi, M. L.; Irie, M.; Belov, V. N.; Hell, S. W. Turn-on Mode Diarylethenes for Bioconjugation and Fluorescence Microscopy of Cellular Structures. *Proc. Natl. Acad. Sci.* **2021**, *118* (14), e2100165118. <https://doi.org/10.1073/pnas.2100165118>.
- (42) Uno, K.; Bossi, M. L.; Belov, V. N.; Irie, M.; Hell, S. W. Multicolour Fluorescent “Sulfide–Sulfone” Diarylethenes with High Photo-Fatigue Resistance. *Chem. Commun.* **2020**, *56* (14), 2198–2201. <https://doi.org/10.1039/C9CC09390G>.
- (43) Xiong, Y.; Rivera-Fuentes, P.; Sezgin, E.; Vargas Jentzsch, A.; Eggeling, C.; Anderson, H. L. Photoswitchable Spiropyran Dyads for Biological Imaging. *Org. Lett.* **2016**, *18* (15), 3666–3669. <https://doi.org/10.1021/acs.orglett.6b01717>.
- (44) Xiong, Y.; Jentzsch, A. V.; Osterrieth, J. W. M.; Sezgin, E.; Sazanovich, I. V.; Reglinski, K.; Galiani, S.; Parker, A. W.; Eggeling, C.; Anderson, H. L. Spiroanthoxazine Switchable Dyes for Biological Imaging. *Chem. Sci.* **2018**, *9* (11), 3029–3040. <https://doi.org/10.1039/C8SC00130H>.
- (45) Li, J.; Ma, X.; Wang, Y.; Cheng, Y.; Qin, Y.; Zhai, J.; Xie, X. Proton-Coupled Photochromic Hemithioindigo: Toward Photoactivated Chemical Sensing and Imaging. *Anal. Chem.* **2023**, *95* (31), 11664–11671. <https://doi.org/10.1021/acs.analchem.3c01504>.
- (46) Berdnikova, D. V. Visible-Range Hemi-Indigo Photoswitch: ON–OFF Fluorescent Binder for HIV-1 RNA. *Chem. Commun.* **2019**, *55* (58), 8402–8405. <https://doi.org/10.1039/C9CC04270A>.
- (47) Ikegami, M.; Arai, T. Photochromic and Fluorescence Properties of a Hemiindigo in the Presence of Bovine Serum Albumin. *Chem. Lett.* **2005**, *34* (4), 492–493. <https://doi.org/10.1246/cl.2005.492>.
- (48) Torii, K.; Hori, Y.; Watabe, K.; Kikuchi, K. Development of Photoswitchable Fluorescent Molecules Using Arylazopyrazole. *Bull. Chem. Soc. Jpn.* **2020**, *93* (7), 821–824. <https://doi.org/10.1246/bcsj.20200077>.
- (49) Torii, K.; Hori, Y.; Kikuchi, K. Persistent Fluorescence Switching of a Probe Using a Photochromic Quencher with High Photostability Assisted by Protein-Surface Modification. *Anal. Chem.* **2023**, *95* (23), 8834–8841. <https://doi.org/10.1021/acs.analchem.3c00163>.
- (50) ALLY, K.; ÖZTÜRK, L.; KÖSE, M. Photochromic and Fluorescence Properties of Coumarin Fulgimides. *Turk. J. Chem.* **2020**, *44* (4), 1031–1042. <https://doi.org/10.3906/kim-2003-31>.
- (51) Walz, J.; Ulrich, K.; Port, H.; Wolf, H. C.; Wonner, J.; Effenberger, F. Fulgides as Switches for Intramolecular

- Energy Transfer. *Chem. Phys. Lett.* **1993**, *213* (3), 321–324. [https://doi.org/10.1016/0009-2614\(93\)85139-F](https://doi.org/10.1016/0009-2614(93)85139-F).
- (52) Torii, K.; Benson, S.; Hori, Y.; Vendrell, M.; Kikuchi, K. No-Wash Fluorogenic Labeling of Proteins for Reversible Photoswitching in Live Cells. *Chem. Sci.* **2024**, *15* (4), 1393–1401. <https://doi.org/10.1039/D3SC04953A>.
- (53) Weston, C. E.; Richardson, R. D.; Haycock, P. R.; White, A. J. P.; Fuchter, M. J. Arylazopyrazoles: Azoheteroarene Photoswitches Offering Quantitative Isomerization and Long Thermal Half-Lives. *J. Am. Chem. Soc.* **2014**, *136* (34), 11878–11881. <https://doi.org/10.1021/ja505444d>.
- (54) Yokoyama, Y. Fulgides for Memories and Switches. *Chem. Rev.* **2000**, *100* (5), 1717–1740. <https://doi.org/10.1021/cr980070c>.
- (55) Lachmann, D.; Lahmy, R.; König, B. Fulgimides as Light-Activated Tools in Biological Investigations. *Eur. J. Org. Chem.* **2019**, *2019* (31–32), 5018–5024. <https://doi.org/10.1002/ejoc.201900219>.
- (56) Giordano, L.; Jovin, T. M.; Irie, M.; Jares-Erijman, E. A. Diheteroarylethenes as Thermally Stable Photoswitchable Acceptors in Photochromic Fluorescence Resonance Energy Transfer (pcFRET). *J. Am. Chem. Soc.* **2002**, *124* (25), 7481–7489. <https://doi.org/10.1021/ja016969k>.
- (57) Soh, N.; Yoshida, K.; Nakajima, H.; Nakano, K.; Imato, T.; Fukaminato, T.; Irie, M. A Fluorescent Photochromic Compound for Labeling Biomolecules. *Chem. Commun.* **2007**, No. 48, 5206–5208. <https://doi.org/10.1039/B713663C>.
- (58) Takakusa, H.; Kikuchi, K.; Urano, Y.; Kojima, H.; Nagano, T. A Novel Design Method of Ratiometric Fluorescent Probes Based on Fluorescence Resonance Energy Transfer Switching by Spectral Overlap Integral. *Chem. – Eur. J.* **2003**, *9* (7), 1479–1485. <https://doi.org/10.1002/chem.200390167>.
- (59) Boutureira, O.; Bernardes, G. J. L. Advances in Chemical Protein Modification. *Chem. Rev.* **2015**, *115* (5), 2174–2195. <https://doi.org/10.1021/cr500399p>.
- (60) Lechner, V. M.; Nappi, M.; Deneny, P. J.; Folliet, S.; Chu, J. C. K.; Gaunt, M. J. Visible-Light-Mediated Modification and Manipulation of Biomacromolecules. *Chem. Rev.* **2022**, *122* (2), 1752–1829. <https://doi.org/10.1021/acs.chemrev.1c00357>.
- (61) Keppler, A.; Gendreizig, S.; Gronemeyer, T.; Pick, H.; Vogel, H.; Johnsson, K. A General Method for the Covalent Labeling of Fusion Proteins with Small Molecules in Vivo. *Nat. Biotechnol.* **2003**, *21* (1), 86–89. <https://doi.org/10.1038/nbt765>.
- (62) Keppler, A.; Pick, H.; Arrivoli, C.; Vogel, H.; Johnsson, K. Labeling of Fusion Proteins with Synthetic Fluorophores in Live Cells. *Proc. Natl. Acad. Sci.* **2004**, *101* (27), 9955–9959. <https://doi.org/10.1073/pnas.0401923101>.
- (63) Los, G. V.; Encell, L. P.; McDougall, M. G.; Hartzell, D. D.; Karassina, N.; Zimprich, C.; Wood, M. G.; Learish, R.; Ohana, R. F.; Urh, M.; Simpson, D.; Mendez, J.; Zimmerman, K.; Otto, P.; Vidugiris, G.; Zhu, J.; Darzins, A.; Klaubert, D. H.; Bulleit, R. F.; Wood, K. V. HaloTag: A Novel Protein Labeling Technology for Cell Imaging and Protein Analysis. *ACS Chem. Biol.* **2008**, *3* (6), 373–382. <https://doi.org/10.1021/cb800025k>.
- (64) Hori, Y.; Ueno, H.; Mizukami, S.; Kikuchi, K. Photoactive Yellow Protein-Based Protein Labeling System with

- Turn-On Fluorescence Intensity. *J. Am. Chem. Soc.* **2009**, *131* (46), 16610–16611. <https://doi.org/10.1021/ja904800k>.
- (65) Mendive-Tapia, L.; Zhao, C.; Akram, A. R.; Preciado, S.; Albericio, F.; Lee, M.; Serrels, A.; Kielland, N.; Read, N. D.; Lavilla, R.; Vendrell, M. Spacer-Free BODIPY Fluorogens in Antimicrobial Peptides for Direct Imaging of Fungal Infection in Human Tissue. *Nat. Commun.* **2016**, *7* (1), 10940. <https://doi.org/10.1038/ncomms10940>.
- (66) Mendive-Tapia, L.; Subiros-Funosas, R.; Zhao, C.; Albericio, F.; Read, N. D.; Lavilla, R.; Vendrell, M. Preparation of a Trp-BODIPY Fluorogenic Amino Acid to Label Peptides for Enhanced Live-Cell Fluorescence Imaging. *Nat. Protoc.* **2017**, *12* (8), 1588–1619. <https://doi.org/10.1038/nprot.2017.048>.
- (67) Subiros-Funosas, R.; Ho, V. C. L.; Barth, N. D.; Mendive-Tapia, L.; Pappalardo, M.; Barril, X.; Ma, R.; Zhang, C.-B.; Qian, B.-Z.; Sintes, M.; Ghashghaei, O.; Lavilla, R.; Vendrell, M. Fluorogenic Trp(redBODIPY) Cyclopeptide Targeting Keratin 1 for Imaging of Aggressive Carcinomas. *Chem. Sci.* **2020**, *11* (5), 1368–1374. <https://doi.org/10.1039/C9SC05558D>.
- (68) Mendive-Tapia, L.; Miret-Casals, L.; Barth, N. D.; Wang, J.; de Bray, A.; Beltramo, M.; Robert, V.; Ampe, C.; Hodson, D. J.; Madder, A.; Vendrell, M. Acid-Resistant BODIPY Amino Acids for Peptide-Based Fluorescence Imaging of GPR54 Receptors in Pancreatic Islets. *Angew. Chem. Int. Ed.* **2023**, *62* (20), e202302688. <https://doi.org/10.1002/anie.202302688>.
- (69) Mendive-Tapia, L.; Mendive-Tapia, D.; Zhao, C.; Gordon, D.; Benson, S.; Bromley, M. J.; Wang, W.; Wu, J.; Kopp, A.; Ackermann, L.; Vendrell, M. Rational Design of Phe-BODIPY Amino Acids as Fluorogenic Building Blocks for Peptide-Based Detection of Urinary Tract Candida Infections. *Angew. Chem. Int. Ed.* **2022**, *61* (17), e202117218. <https://doi.org/10.1002/anie.202117218>.
- (70) Barth, N. D.; Subiros-Funosas, R.; Mendive-Tapia, L.; Duffin, R.; Shields, M. A.; Cartwright, J. A.; Henriques, S. T.; Sot, J.; Goñi, F. M.; Lavilla, R.; Marwick, J. A.; Vermeren, S.; Rossi, A. G.; Egeblad, M.; Dransfield, I.; Vendrell, M. A Fluorogenic Cyclic Peptide for Imaging and Quantification of Drug-Induced Apoptosis. *Nat. Commun.* **2020**, *11* (1), 4027. <https://doi.org/10.1038/s41467-020-17772-7>.
- (71) Subiros-Funosas, R.; Mendive-Tapia, L.; Sot, J.; Pound, J. D.; Barth, N.; Varela, Y.; Goñi, F. M.; Paterson, M.; Gregory, C. D.; Albericio, F.; Dransfield, I.; Lavilla, R.; Vendrell, M. A Trp-BODIPY Cyclic Peptide for Fluorescence Labelling of Apoptotic Bodies. *Chem. Commun.* **2017**, *53* (5), 945–948. <https://doi.org/10.1039/C6CC07879F>.
- (72) Hirayama, S.; Hori, Y.; Benedek, Z.; Suzuki, T.; Kikuchi, K. Fluorogenic Probes Reveal a Role of GLUT4 N-Glycosylation in Intracellular Trafficking. *Nat. Chem. Biol.* **2016**, *12* (10), 853–859. <https://doi.org/10.1038/nchembio.2156>.
- (73) Sadhu, K. K.; Mizukami, S.; Lanam, C. R.; Kikuchi, K. Fluorogenic Protein Labeling through Photoinduced Electron Transfer-Based BL-Tag Technology. *Chem. – Asian J.* **2012**, *7* (2), 272–276. <https://doi.org/10.1002/asia.201100647>.
- (74) Kubin, R. F.; Fletcher, A. N. Fluorescence Quantum Yields of Some Rhodamine Dyes. *J. Lumin.* **1982**, *27* (4), 455–462. [https://doi.org/10.1016/0022-2313\(82\)90045-X](https://doi.org/10.1016/0022-2313(82)90045-X).

- (75) Yokoyama, Y.; Ogawa, K.; Iwai, T.; Shimazaki, K.; Kajihara, Y.; Goto, T.; Yokoyama, Y.; Kurita, Y. Study on the Conformation of an Isopropyl-Substituted Furylfulgide. Photochromic Coloring Reaction and Thermal Racemization. *Bull. Chem. Soc. Jpn.* **1996**, *69* (6), 1605–1612. <https://doi.org/10.1246/bcsj.69.1605>.
- (76) Slavov, C.; Bellakbil, N.; Wahl, J.; Mayer, K.; Rück-Braun, K.; Burghardt, I.; Wachtveitl, J.; Braun, M. Ultrafast Coherent Oscillations Reveal a Reactive Mode in the Ring-Opening Reaction of Fulgides. *Phys. Chem. Chem. Phys.* **2015**, *17* (21), 14045–14053. <https://doi.org/10.1039/C5CP01878A>.
- (77) Heo, J.; Murale, D. P.; Yoon, H. Y.; Arun, V.; Choi, S.; Kim, E.; Lee, J.-S.; Kim, S. Recent Trends in Molecular Aggregates: An Exploration of Biomedicine. *Aggregate* **2022**, *3* (2), e159. <https://doi.org/10.1002/agt2.159>.
- (78) Valdes-Aguilera, O.; Neckers, D. C. Aggregation Phenomena in Xanthene Dyes. *Acc. Chem. Res.* **1989**, *22* (5), 171–177. <https://doi.org/10.1021/ar00161a002>.
- (79) Casimiro, L.; Andreoni, L.; Groppi, J.; Credi, A.; Métivier, R.; Silvi, S. 4,4'-Dimethylazobenzene as a Chemical Actinometer. *Photochem. Photobiol. Sci.* **2022**, *21* (5), 825–833. <https://doi.org/10.1007/s43630-021-00162-3>.
- (80) Kuhn, H. J.; Braslavsky, S. E.; Schmidt, R. Chemical Actinometry (IUPAC Technical Report). *Pure Appl. Chem.* **2004**, *76* (12), 2105–2146. <https://doi.org/10.1351/pac200476122105>.
- (81) Nagasaka, T.; Sotome, H.; Yoshida, Y.; Yokoyama, Y.; Miyasaka, H. Cycloreversion Reaction of a Fulgide Derivative in Higher Excited States Attained by Femtosecond Two-Photon Pulsed Excitation. *J. Phys. Chem. C* **2018**, *122* (43), 24987–24995. <https://doi.org/10.1021/acs.jpcc.8b06271>.
- (82) Lakowicz, J. R.; Masters, B. R. Principles of Fluorescence Spectroscopy, Third Edition. *J. Biomed. Opt.* **2008**, *13* (2), 029901.
- (83) Casey, K. G.; Quitevis, E. L. Effect of Solvent Polarity on Nonradiative Processes in Xanthene Dyes: Rhodamine B in Normal Alcohols. *J. Phys. Chem.* **1988**, *92* (23), 6590–6594. <https://doi.org/10.1021/j100334a023>.
- (84) Ishida, H.; Tobita, S.; Hasegawa, Y.; Katoh, R.; Nozaki, K. Recent Advances in Instrumentation for Absolute Emission Quantum Yield Measurements. *Coord. Chem. Rev.* **2010**, *254* (21), 2449–2458. <https://doi.org/10.1016/j.ccr.2010.04.006>.
- (85) OECD. *Test No. 107: Partition Coefficient (n-Octanol/Water): Shake Flask Method*; Organisation for Economic Co-operation and Development: Paris, 1995.
- (86) Schindelin, J.; Arganda-Carreras, I.; Frise, E.; Kaynig, V.; Longair, M.; Pietzsch, T.; Preibisch, S.; Rueden, C.; Saalfeld, S.; Schmid, B.; Tinevez, J.-Y.; White, D. J.; Hartenstein, V.; Eliceiri, K.; Tomancak, P.; Cardona, A. Fiji: An Open-Source Platform for Biological-Image Analysis. *Nat. Methods* **2012**, *9* (7), 676–682. <https://doi.org/10.1038/nmeth.2019>.
- (87) Loudet, A.; Burgess, K. BODIPY Dyes and Their Derivatives: Syntheses and Spectroscopic Properties. *Chem. Rev.* **2007**, *107* (11), 4891–4932. <https://doi.org/10.1021/cr078381n>.
- (88) Liu, X.; Chi, W.; Qiao, Q.; Kokate, S. V.; Cabrera, E. P.; Xu, Z.; Liu, X.; Chang, Y.-T. Molecular Mechanism of Viscosity Sensitivity in BODIPY Rotors and Application to Motion-Based Fluorescent Sensors. *ACS Sens.* **2020**, *5* (3), 731–739. <https://doi.org/10.1021/acssensors.9b01951>.
- (89) Sunahara, H.; Urano, Y.; Kojima, H.; Nagano, T. Design and Synthesis of a Library of BODIPY-Based

- Environmental Polarity Sensors Utilizing Photoinduced Electron-Transfer-Controlled Fluorescence ON/OFF Switching. *J. Am. Chem. Soc.* **2007**, *129* (17), 5597–5604. <https://doi.org/10.1021/ja068551y>.
- (90) Wilhelm, J.; Kühn, S.; Tarnawski, M.; Gotthardt, G.; Tünnermann, J.; Tänzer, T.; Karpenko, J.; Mertes, N.; Xue, L.; Uhrig, U.; Reinstein, J.; Hiblot, J.; Johnsson, K. Kinetic and Structural Characterization of the Self-Labeling Protein Tags HaloTag7, SNAP-Tag, and CLIP-Tag. *Biochemistry* **2021**, *60* (33), 2560–2575. <https://doi.org/10.1021/acs.biochem.1c00258>.
- (91) Mitry, M. M. A.; Greco, F.; Osborn, H. M. I. In Vivo Applications of Bioorthogonal Reactions: Chemistry and Targeting Mechanisms. *Chem. – Eur. J.* **2023**, *29* (20), e202203942. <https://doi.org/10.1002/chem.202203942>.
- (92) Oliveira, B. L.; Guo, Z.; Bernardes, G. J. L. Inverse Electron Demand Diels–Alder Reactions in Chemical Biology. *Chem. Soc. Rev.* **2017**, *46* (16), 4895–4950. <https://doi.org/10.1039/C7CS00184C>.
- (93) Blizzard, R. J.; Backus, D. R.; Brown, W.; Bazewicz, C. G.; Li, Y.; Mehl, R. A. Ideal Bioorthogonal Reactions Using A Site-Specifically Encoded Tetrazine Amino Acid. *J. Am. Chem. Soc.* **2015**, *137* (32), 10044–10047. <https://doi.org/10.1021/jacs.5b03275>.
- (94) Borrmann, A.; Milles, S.; Plass, T.; Dommerholt, J.; Verkade, J. M. M.; Wießler, M.; Schultz, C.; van Hest, J. C. M.; van Delft, F. L.; Lemke, E. A. Genetic Encoding of a Bicyclo[6.1.0]Nonyne-Charged Amino Acid Enables Fast Cellular Protein Imaging by Metal-Free Ligation. *ChemBioChem* **2012**, *13* (14), 2094–2099. <https://doi.org/10.1002/cbic.201200407>.
- (95) Lang, K.; Davis, L.; Wallace, S.; Mahesh, M.; Cox, D. J.; Blackman, M. L.; Fox, J. M.; Chin, J. W. Genetic Encoding of Bicyclononynes and Trans-Cyclooctenes for Site-Specific Protein Labeling in Vitro and in Live Mammalian Cells via Rapid Fluorogenic Diels–Alder Reactions. *J. Am. Chem. Soc.* **2012**, *134* (25), 10317–10320. <https://doi.org/10.1021/ja302832g>.
- (96) Cheng, N.-S. Formula for the Viscosity of a Glycerol–Water Mixture. *Ind. Eng. Chem. Res.* **2008**, *47* (9), 3285–3288. <https://doi.org/10.1021/ie071349z>.
- (97) Duwé, S.; De Zitter, E.; Gielen, V.; Moeyaert, B.; Vandenberg, W.; Grotjohann, T.; Clays, K.; Jakobs, S.; Van Meervelt, L.; Dedecker, P. Expression-Enhanced Fluorescent Proteins Based on Enhanced Green Fluorescent Protein for Super-Resolution Microscopy. *ACS Nano* **2015**, *9* (10), 9528–9541. <https://doi.org/10.1021/acsnano.5b04129>.
- (98) Ando, R.; Mizuno, H.; Miyawaki, A. Regulated Fast Nucleocytoplasmic Shuttling Observed by Reversible Protein Highlighting. *Science* **2004**, *306* (5700), 1370–1373. <https://doi.org/10.1126/science.1102506>.
- (99) Konen, T.; Stumpf, D.; Grotjohann, T.; Jansen, I.; Bossi, M.; Weber, M.; Jensen, N.; Hell, S. W.; Jakobs, S. The Positive Switching Fluorescent Protein Padron2 Enables Live-Cell Reversible Saturable Optical Linear Fluorescence Transitions (RESOLFT) Nanoscopy without Sequential Illumination Steps. *ACS Nano* **2021**, *15* (6), 9509–9521. <https://doi.org/10.1021/acsnano.0c08207>.
- (100) Magde, D.; Wong, R.; Seybold, P. G. Fluorescence Quantum Yields and Their Relation to Lifetimes of Rhodamine 6G and Fluorescein in Nine Solvents: Improved Absolute Standards for Quantum Yields. *Photochem. Photobiol.* **2002**, *75* (4), 327–334. <https://doi.org/10.1562/0031->

- 8655(2002)0750327FQYATR2.0.CO2.
- (101) Kamikawa, Y.; Hori, Y.; Yamashita, K.; Jin, L.; Hirayama, S.; Standley, D. M.; Kikuchi, K. Design of a Protein Tag and Fluorogenic Probe with Modular Structure for Live-Cell Imaging of Intracellular Proteins. *Chem. Sci.* **2015**, *7* (1), 308–314. <https://doi.org/10.1039/C5SC02351C>.
- (102) Matsui, Y.; Funato, Y.; Imamura, H.; Miki, H.; Mizukami, S.; Kikuchi, K. Visualization of Long-Term Mg<sup>2+</sup> Dynamics in Apoptotic Cells Using a Novel Targetable Fluorescent Probe. *Chem. Sci.* **2017**, *8* (12), 8255–8264. <https://doi.org/10.1039/C7SC03954A>.
- (103) Kowada, T.; Arai, K.; Yoshimura, A.; Matsui, T.; Kikuchi, K.; Mizukami, S. Optical Manipulation of Subcellular Protein Translocation Using a Photoactivatable Covalent Labeling System. *Angew. Chem. Int. Ed.* **2021**, *60* (20), 11378–11383. <https://doi.org/10.1002/anie.202016684>.
- (104) Mizukami, S.; Watanabe, S.; Hori, Y.; Kikuchi, K. Covalent Protein Labeling Based on Noncatalytic  $\beta$ -Lactamase and a Designed FRET Substrate. *J. Am. Chem. Soc.* **2009**, *131* (14), 5016–5017. <https://doi.org/10.1021/ja8082285>.
- (105) Sun, W.; Guo, S.; Hu, C.; Fan, J.; Peng, X. Recent Development of Chemosensors Based on Cyanine Platforms. *Chem. Rev.* **2016**, *116* (14), 7768–7817. <https://doi.org/10.1021/acs.chemrev.6b00001>.
- (106) Shojaei, H.; Bossi, M. L.; Belov, V. N.; Hell, S. W. Bis-Rhodamines Bridged with a Diazoketone Linker: Synthesis, Structure, and Photolysis. *J. Org. Chem.* **2022**, *87* (1), 56–65. <https://doi.org/10.1021/acs.joc.1c01721>.
- (107) Gao, M.; Kwaria, D.; Norikane, Y.; Yue, Y. Visible-Light-Switchable Azobenzenes: Molecular Design, Supramolecular Systems, and Applications. *Nat. Sci.* **2023**, *3* (1), e220020. <https://doi.org/10.1002/ntls.20220020>.
- (108) Gautier, A.; Juillerat, A.; Heinis, C.; Corrêa, I. R.; Kindermann, M.; Beaufils, F.; Johnsson, K. An Engineered Protein Tag for Multiprotein Labeling in Living Cells. *Chem. Biol.* **2008**, *15* (2), 128–136. <https://doi.org/10.1016/j.chembiol.2008.01.007>.
- (109) Kumar, N.; Hori, Y.; Nishiura, M.; Kikuchi, K. Rapid No-Wash Labeling of PYP-Tag Proteins with Reactive Fluorogenic Ligands Affords Stable Fluorescent Protein Conjugates for Long-Term Cell Imaging Studies. *Chem. Sci.* **2020**, *11* (14), 3694–3701. <https://doi.org/10.1039/D0SC00499E>.



